

# **BIO-INSPIRED STRUCTURED COMPOSITES FOR LOAD-BEARING BONE GRAFT SUBSTITUTION**

To the Faculty of Mechanical, Process and Energy Engineering  
of the Technische Universität Bergakademie Freiberg

approved

## **THESIS**

to attain the academic degree of

Doktor-Ingenieur

(Dr.-Ing.)

submitted

by MSc Mat. Sc. Laëtitia Galea

born on the 20th of June, 1983, in Geneva, Switzerland

Reviewers: Prof. Dr. Marc Bohner, RMS Foundation, Bettlach, Switzerland

Prof. Dr. Thomas Graule, EMPA, Dübendorf, Switzerland

Prof. Dr. Christos G. Aneziris, TU Bergakademie Freiberg, Germany

March 3<sup>rd</sup>, 2015



# **BIO-INSPIRED STRUCTURED COMPOSITES FOR LOAD-BEARING BONE GRAFT SUBSTITUTION**

To the Faculty of Mechanical, Process and Energy Engineering  
of the Technische Universität Bergakademie Freiberg

approved

**THESIS**

to attain the academic degree of

Doktor-Ingenieur

(Dr.-Ing.)

submitted

by MSc Mat. Sc. Laëtitia Galea

born on the 20th of June, 1983, in Geneva, Switzerland

Reviewers: Prof. Marc Bohner, RMS Foundation, Bettlach, Switzerland

Prof. Thomas Graule, EMPA, Dübendorf, Switzerland

Prof. Christos G. Aneziris, TU Bergakademie Freiberg, Germany

March 3<sup>rd</sup>, 2015



*“Un objectif sans plan s’appelle un vœux.”*

Antoine de Saint-Exupéry



## **Declaration on Oath**

Herewith, I declare on oath that all parts of the present thesis were independently written by me, no other than indicated sources and aids were used and that all parts of the thesis, which have been taken over, either literally or in a general manner, have been accordingly indicated.

Any other persons have not contributed to the composition of the present thesis. The supervision of a doctoral promotion consultant has not been taken into provision. Third persons received no payment or nonmonetary benefits for any contribution.

The present thesis has not been submitted to any doctoral examination authority neither with national nor international location.

Laetitia Galea





# TABLE OF CONTENTS

<b>Acknowledgements</b>	<b>v</b>
<b>Summary</b>	<b>vii</b>
Background.....	vii
Thesis outline.....	viii
Part I: “Brick-and-mortar” structures with discrete reinforcement components.....	ix
Part II: “Textured” structures with continuous reinforcement components.....	x
<b>Zusammenfassung</b>	<b>xi</b>
Hintergrund.....	xi
Doktorarbeit Gliederung.....	xii
Teil I: “Ziegelmauer-Architektur” mit diskreten Verstärkungskomponenten.....	xiii
Teil II: “Texturierte” Strukturen mit kontinuierlichen Verstärkungskomponenten.....	xiv
<b>Chapter 1: General introduction</b>	<b>1</b>
Bone grafting.....	1
CaP ceramics.....	1
How to improve toughness of CaP ceramics?.....	2
Importance of structure design: bio-inspiration.....	2
What mechanical properties should be reached?.....	5
Specific aims.....	5
Two general approaches to reach the goal.....	6
Nacre-inspired “brick-and mortar” structures (Part I).....	6
Textured ceramic monoliths (Part II).....	6
References.....	7
<b>Chapter 2: Theoretical calculations</b>	<b>11</b>
Introduction.....	12
Theoretical tensile strength of $\beta$ -TCP platelets and critical size for flaw tolerance.....	13
Optimal aspect ratio.....	15
Composite strength and stiffness.....	17
Limitations.....	19
References.....	19
<b>PART I: NACRE-INSPIRED “BRICK-AND-MORTAR” STRUCTURES</b>	
<b>Chapter 3: Synthesis of sub-micrometer calcium phosphate platelets</b>	<b>23</b>
Introduction.....	24

Materials and Methods	25
Precipitation method	25
Reaction parameters	25
Characterization	26
Statistical analysis of results	28
Results	28
Reproducibility of standard experiments	28
Increase of the reagent volume to increase the productivity	30
Increase of the precursors concentration to increase the productivity and modify the particles	30
Increase of titration rate to simplify the process	32
Influence of temperature on the particles	35
Effect of the pH value on the particles	37
Effect of a longer reaction time on the particle stability	40
Study of the influence of variations of the Ca/P molar ratio	42
Discussion	43
Reproducibility	43
Productivity	44
CaP crystal shape	45
Crystal purity	47
Aspect ratio	48
Critical thickness	49
Uniformity of primary particles	50
Non agglomerated	51
General points	52
Conclusions	52
References	53
<b>Chapter 4: Kinetics study of the calcium phosphate platelets growth</b>	<b>57</b>
Introduction	58
Theory	58
Materials and methods	60
Materials and sample preparation	60
Characterization methods	61
Results	62
Visual observations during manipulations	62
SEM observations	62
XRD results	66
Size measurements	68
Kinetics calculations	70
Discussion	74
Nucleation and assembly mechanism	74
Reaction kinetics	76
Control of size and aspect ratio	76
Conclusions	77
References	78
<b>Chapter 5: Structural design of bio-inspired composites by solvent casting</b>	<b>81</b>
Foreword	82
Introduction	82
Experimental section	84

Synthesis of resorbable ceramic platelets.....	84
Solvent casting to prove the reinforcement efficiency of DCP platelets.....	84
Magnetization of the platelets.....	85
Maintaining the orientation during drying of an hydrogel matrix.....	86
Results.....	87
Synthesis of resorbable ceramic platelets.....	87
Solvent casting to prove the reinforcement efficiency of CaP platelets.....	87
Magnetization of the platelets.....	91
Maintaining the orientation during drying of an hydrogel matrix.....	93
Discussion.....	95
Detrimental effect of $\beta$ -TCP platelets in chitosan.....	95
Efficient reinforcement with DCP platelets up to a given volume fraction.....	96
Threshold value for strength improvement.....	97
Fitting the experimental results with theoretical equations.....	98
Conclusions.....	101
References.....	101

## **Chapter 6: Biodegradable, strong and tough nacre-inspired structures obtained by freeze-casting** **105**

Introduction.....	106
Experimental section.....	108
Synthesis of resorbable ceramic platelets.....	108
Preliminary freeze-casting tests with $\beta$ -TCP-based slurries.....	108
Determination of adequate freeze-casting parameters for hydrogels-CaP slurries.....	108
Integration of CaP platelets and local planar alignment.....	109
Attempts to globally align porosity in two directions.....	109
Densification and consolidation.....	110
Tensile testing.....	110
Results.....	111
Preliminary freeze-casting tests with $\beta$ -TCP-based slurries.....	111
Determination of adequate freeze-casting parameters for hydrogels-CaP slurries.....	112
Integration of CaP platelets and local planar alignment.....	113
Attempts to globally align porosity in two directions.....	119
Densification and consolidation.....	121
Tensile testing.....	121
Discussion.....	122
Conclusions.....	124
References.....	125

## **PART II: TEXTURED CERAMIC MONOLITHS**

### **Chapter 7: Micro-texturing by recrystallization of calcium phosphate blocks in hydrothermal conditions** **127**

Introduction.....	128
Materials and Methods.....	130
Samples characterization.....	132
Results.....	133
Macroscopic observations.....	133
Microstructural changes (SEM).....	133
Crystalline phase conversion (XRD).....	139

Mechanical properties.....	142
Fractured surfaces.....	142
Discussion.....	145
Conclusions.....	150
References.....	150
<b>Chapter 8: Toughening of textured calcium phosphate blocks by polymer impregnation</b>	<b>155</b>
Foreword.....	156
Introduction.....	156
Materials and Methods.....	157
Samples preparation.....	157
Characterization.....	158
Results.....	158
Porosity and microstructure.....	158
Composition.....	161
Mechanical properties.....	161
Discussion.....	162
Conclusions.....	164
References.....	164
<b>Chapter 9: Synthesis and outlook</b>	<b>167</b>
<b>Curriculum Vitae</b>	<b>171</b>

# ACKNOWLEDGMENTS

I would like to express my gratitude to Dr. Marc Bohner and Dr. Beat Gasser for giving me the opportunity to perform my PhD thesis in the RMS Foundation. A special thanks to Marc for his commitment and patient supervision, numerous advices and passionate discussions on any kind of topics, from science to running, through men-women equality (!).

Many thanks to my co-examiner Prof. Dr. Thomas Graule for believing in my project, accepting supervising me and introducing me to my examiner, Prof. Dr. Aneziris.

I would like to thank many people who collaborated with me during this project and brought many ideas but also concrete help: Prof. Dr. Andre Studart, Jürg Thüning, Prof. Dr. Lennart Bergström, Dr. Christina Schütz, Prof. Dr. Markus Niederberger, Dr. David Eglin. I want to thank in particular Dr. Randall Erb, Arto Ojuva and Dr. Marianna Peroglio for introducing me to their respective expertise fields and the thorough help in the lab. Dr. Nicola Döbelin deserves my deep gratitude for his constructive and numerous corrections of my papers and part of this manuscript, but also for the assistance with XRD analysis, among other.

Special thanks to the students and trainees who helped me in different parts of the thesis: Dmitriy Alexeev, Vivian Moser and Katharina Thiers.

For helping me improving my redaction skills and for her interesting external vision on my project, I wish to thank Dr. Catherine Schütz.

Thanks to Jong Seto for the fascinating talks at diverse conferences and the invitation to present my work at Konstanz University.

I am grateful to my sister and my friends for supporting me during my time as a PhD student. Oscillating between workaholic frenzy and demotivated laziness with all possible intermediate mind state, those last 3 ½ years were certainly not easy for my entourage! Thank you all for your encouragements and for distracting me when necessary, or simply for your faithful presence.



March 2015

*Laëtitia Galea*



# SUMMARY

## Background

In the occurrence of a defect, bone tissue can heal by itself, on some extent. If the defect is too large, the healing process is too slow and usually soft tissues grow faster and fill the gap, impairing further bone ingrowth and regeneration. To avoid the formation of this weak material, filler materials can be plugged in. If the material is resorbable, bone can then grow and replace progressively the material. Bone auto- and allografts are considered as the gold standard for bone void filling by many surgeons, but they have some important drawbacks: high costs and risks of disease transmission in the case of allografts, limited availability, additional pain and an increased risk of side-effects for autografts. In the past decades synthetic bone graft substitutes have become a viable alternative to bone auto- and allografts.

Therefore, there is a trend towards the use of synthetic bone graft substitutes, and particularly calcium orthophosphates (CaP) are widely used as bone graft substitutes because they are attractive due to their chemical similarity with the mineral part of bone. However, calcium phosphates (CaPs) are inherently brittle, hence restricting their use to mechanically protected environments. **Improving the toughness of CaP based bone scaffolds is thus of paramount importance and is the goal of this PhD research work.** The most common technique used to toughen ceramics – in particular in the bone substitutes field – is to combine them with a tough polymeric phase. However, beside this addition of a second phase, the toughness of a ceramic can already be increased by structural changes.

Hence, the general procedure in this thesis was to first deeply investigate the ceramic part – from the individual components features (particle size and shape, composition, ...), to their micro- and macroscopic 3D arrangement – and second combine them with a tough polymer phase. In the aim to **obtain CaP based materials with designed structures combining strength, toughness and biodegradability**, two types of composites were investigated in two different parts of this thesis: on one side composite with discrete ceramic reinforcements (Part I: “brick-and-mortar” structures, chapters 3 to 6) and on the other side composites based on continuous long reinforcements (Part II: “textured ceramic monoliths”, chapters 7 and 8).

## Summary

To achieve the highest possible mechanical properties in “brick-and-mortar” composites, some features of CaP ceramics particles had to be controlled as precisely as possible: uniform size and shape, no agglomeration, adequate aspect ratio (elongation) and thickness. To do so, numerous parameters of the synthesis process, i.e. precipitation in organic media, were thoroughly investigated (Chapters 3 and 4). These particles were then incorporated in polymeric matrices using different alignment methods to achieve the desired structural design (Chapters 5 and 6).

Similarly, for the second approach, the first stages also focused on the structure of the pure CaP parts (Chapter 7). Their architecture was modified from nano- to macroscale aiming at increasing the work of fracture, even without addition of a polymer phase. The obtained microstructures were analogous to those of shell or enamel (but without polymer phase), with 5 hierarchical structure levels: (1) hydroxyapatite crystals, (2) in the form of needles, (3) aligned in bundles (4) which are isotropically stacked, to finally form (5) the macroscopic tough ceramic blocks. Size refinement and texturing of a ceramic is undeniably an effective way to improve its strength and particularly its toughness. Indeed, rupture surfaces revealed intergranular tortuous crack paths, which dissipate much more energy than the transgranular cracks observed in sintered samples. The toughness, and surprisingly also the strength, could further be improved by polymer impregnation.

In summary, brick-and-mortar structures were achievable with strength and strain values similar to cortical bone but were in limited sizes (Chapter 3 to 6). Macroscopic CaP monoliths with hierarchical structure showed improved toughness and strength compared to conventional sintered ceramics, but were still inferior to cortical bone values (Chapter 7 and 8). In conclusion, obtaining strong, tough and biodegradable scaffolds for bone substitution in load-bearing location remains a compromise between macroscopic size and appropriate features, but is getting closer to success in regards to the present PhD thesis outcomes.

## Thesis outline

Chapter 1 gives a general introduction to bone substitution, advantages and current limitations of calcium phosphates, bio-inspiration for microstructures and how we intended to apply principles found in natural materials to engineered ones.

Chapter 2 details the theoretical calculations that have been done to estimate the ideal dimensions of calcium phosphate ceramic components to maximize their intrinsic strength and their efficiency as reinforcement elements in composite structures. Then, considering a specific matrix



material, optimum size and shape for a compromise between strength improvement and preservation of toughness was determined. Finally, the theoretical mechanical properties of the perfect composite were predicted in function of the fractions of phases.

### **Part I: “Brick-and-mortar” structures with discrete reinforcement components**

Part I describes how to obtain nacre-like structures, from the raw materials synthesis (Chapters 3 and 4) to assembly within macroscopic samples (Chapters 5 and 6).

Chapter 3 details the synthesis procedure used to obtain sub-micrometric CaP platelets. This involved the precipitation of CaP particles in ethylene glycol at moderate temperatures (90 - 170 °C) and the variation of different reaction parameters (temperature, precursors concentration, pH, titration rate, etc). As a result, two main CaP phases were obtained as sub-micrometric, well-dispersed and highly uniform platelets in the form of: (i)  $\beta$ -tricalcium phosphate ( $\beta$ -TCP) hexagonal prisms with an aspect ratio of about 6 and a narrow size dispersion of < 5 % (standard deviation/mean) and (ii) monetite (DCP) flat parallelepipeds with an aspect ratio up to 25 but a larger size dispersion (about 20 %). The thickness of both platelets type was below 300 nm which should be ideal for the synthesis of strong CaP-based composites.

Chapter 4 is dedicated to deeper understanding of the growth kinetics of CaP – and in particular  $\beta$ -TCP – platelets, in order to eventually better control their size and aspect ratio. The growth curves could be either fitted by diffusion- or reaction-controlled models. However, the high activation energies calculated suggested reaction-controlled mechanisms. Hence, the best way to influence the crystal size and shape would be to increase the precursors concentration. However, solubility is limited and aspect ratios larger than 6 remained unachievable for  $\beta$ -TCP platelets.

Chapter 5 relates how CaP platelets, as obtained in the previous chapters, were used to reinforce chitosan matrices. Incorporation of the ceramic particles was done in chitosan solutions that were casted and dried. Solvent evaporation led to film formation that forced the incorporated CaP platelets to lie down in the film plane. The use of DCP platelets was more successful than  $\beta$ -TCP, thanks to better interface and alignment due to higher aspect ratio. Alignment of the platelets was further improved by decorating the CaP platelets with nano iron oxide particles and orienting them in a rotating magnetic field. Hence, strength increase without large ductility decrease was observed up to 20 vol-% of ceramic. Above this threshold value, percolation occurred and strength abruptly decreased, sometimes even under the strength of pure matrix material. However, a ceramic fraction higher than 20 vol-% would be desirable in regard to the better biocompatibility of CaP than most degradable polymers. Hence, better alignment is necessary to add more than 20 vol-% without reduction of the mechanical strength and toughness.

Chapter 6 demonstrates the feasibility of using directional freezing (also named freeze-casting) with CaP platelets in hydrogel matrices. The growing ice crystals pushed the platelets in the pore walls, where they aligned in the plane and were bonded by the dry polymeric matrix. Volume fraction up to 50 % led to apparently proper embedding of the platelets and good spatial arrangement. Further developments were investigated to compress 2D-oriented lamellar samples into dense, nacre-like structures, and to stabilize the chitosan matrix by acetylation. Such films could then be tensile tested and compared with the ones obtained by solvent casting with and without magnetic alignment, however the acetylation process release some acetic acid that dissolved the CaP platelets.

### **Part II: “Textured” structures with continuous reinforcement components**

Part II relates an *in situ* texturing method rather than an assembly approach like in Part I. This method was supposed to be rather an engineering approach than bio-inspired. However obtained structures were close to observed natural ones.

In Chapter 7, hydrothermal incubation of sintered CaP blocks led to phase transformation, with *in situ* recrystallization into finer, elongated and aligned crystals. Brazilian tests were used to determine the diametral tensile strength,  $\sigma_{dts}$ , and the work-of-fracture, WOF. Hydrothermal incubation significantly increased  $\sigma_{dts}$  and WOF of the ceramic blocks. Since the mechanical properties of  $\alpha$ -TCP and CDHA are very similar, the observed improvements have to be attributed to the fine and entangled crystal structure obtained after incubation. Hence, refining the microstructure and texturing a ceramic material is an effective way to improve its strength but also its toughness, with a structural toughening mechanism, as observed in natural composite materials.

Chapter 8 aims at further increasing the toughness by addition of a ductile phase within the microstructure. More specifically, poly( $\epsilon$ -caprolactone) (PCL) impregnation of ceramic blocks, hydrothermally treated or not, covered micro- and macropores walls and led to work-of-fracture enhancement thanks to polymer fibrils formation. Surprisingly, even the strength was increased when textured ceramic scaffolds were impregnated, presumably due to filling of surface defects of the ceramic and a very good contact, hence stress transfer, between both phases. In consequence, texturing of ceramics increases toughness thanks to failure mode change; but also increases global strength when impregnated thanks to large and strong binding interfaces between both phases.

# ZUSAMMENFASSUNG

## Hintergrund

In den vergangenen Jahrzehnten haben sich synthetische Knochenersatzmaterialien als interessante Alternative zu autologen und allogenen Knochentransplantaten etabliert. Zwar werden Transplantate von vielen Chirurgen nach wie vor als Stand der Technik zur Heilung grosser Knochendefekte betrachtet, dennoch sind einige gravierende Nachteile nicht von der Hand zu weisen: Allografts sind mit hohen Kosten verbunden und bergen das Risiko von Krankheitsübertragungen, wohingegen Autografts nur in limitierter Menge verfügbar sind und an der Entnahmestelle zusätzliche Schmerzen und Komplikationen verursachen können.

Aus den genannten Gründen gewinnen synthetische Knochenersatzmaterialien zunehmend an Bedeutung, und in den vergangenen Jahrzehnten wurde eine Vielzahl unterschiedlicher Materialien eingesetzt, darunter Polylactid-basierte Polymere, Magnesium-basierte Metalle, bioaktive Gläser sowie Kalzium-basierte Keramiken. Als besonders interessant erwiesen sich Kalzium-Orthophosphate (CaP), da ihre chemische Zusammensetzung derjenigen von Knochenmineral sehr ähnlich ist.

Die heutzutage weit verbreiteten Kalziumphosphat-Knochenersatzmaterialien (CaP) sind spröde und dürfen deshalb nur in vor mechanischer Belastung geschützten Defekten eingesetzt werden. **Das Ziel dieser Doktorarbeit ist daher eine Verbesserung der Zähigkeit CaP-basierter Knochenersatz-Gerüste, um in Zukunft Anwendungen in lasttragenden Situationen zu ermöglichen.** Dies würde einen Meilenstein in der Entwicklung synthetischer Knochenersatzmaterialien darstellen. Zusätzlich zum bekannten intrinsischen Verstärkungseffekt durch die Kombination von CaP-Keramik mit einer zähen Polymer-Phase wurde untersucht, ob eine Änderung der Struktur ebenfalls zu einer extrinsischen Verstärkung führt. Es wurden zwei unterschiedliche Ansätze **zur Verbesserung der Festigkeit und Zähigkeit biodegradierbarer CaP-Keramiken durch Optimierung der Architektur und Struktur** untersucht: Herstellung von Proben mit Ziegelmauer-Architektur (Teil I: Kapitel 3 bis 6) und Verfeinerung und Texturierung der CaP-Monolithe (Teil II: Kapitel 7 und 8).

Grundsätzlich, kann die höchste mechanische Stabilität einer sogenannten Compositestruktur nach dem Vorbild einer Backsteinmauer nur erreicht werden wenn die CaP-Partikel folgende, exakt kontrollierte Eigenschaften aufweisen: Sie müssen einheitlich in Form und Grösse, nicht agglomeriert, sowie von länglicher dünner Kristallform sein. Im ersten Teil dieser Arbeit wurde daher eine neue Methode zur Herstellung solcher Partikel entwickelt und optimiert. Die synthetisierten

Partikel wurden anschliessend in eine Polymermatrix integriert und mit verschiedenen Methoden orientiert, um eine geordnete strukturelle Architektur des Compositematerials zu erhalten.

Neben der Arbeit mit orientierten CaP-Partikeln in einer Polymermatrix wurde untersucht, ob die Kristalle innerhalb monolithischer CaP-Proben orientiert werden können, um auch ohne Polymerzugabe eine Verstärkung der Brucharbeit erzielen zu können. Die so hergestellten Proben glichen in ihrer Architektur der Struktur von natürlichen Schalen oder Zahnschmelz, hierarchisch organisiert in 5 Ebenen: (1) Hydroxylapatit-Kristalle, (2) die nadelförmig sind, und (3) in Bündeln gemeinsam ausgerichtet werden, die selbst (4) isotrop zusammengebaut werden, um abschliessend einen zähen (5) makroskopischen Keramikblock zu bilden. Die Optimierung der Kristallgrösse und -textur ist somit eine effektive Methode, um die Festigkeit, vor allem aber die Zähigkeit von Keramiken zu verbessern. Bruchflächen zeigten in der Tat gewundene intergranulare Bruchverläufe, die deutlich mehr Energie absorbieren als die transgranularen Brüche, wie sie normalerweise in gesinterten Proben auftreten. Interessanterweise konnte die Härte und Zähigkeit solcher hierarchischer Strukturen durch die Zugabe geringer Mengen eines Polymers stärker erhöht werden als in vergleichbaren untexturierten Keramikproben. Dies ist vermutlich auf eine grössere Kontaktfläche und damit verbundene bessere Kraftübertragung zurückzuführen.

Zusammengefasst wurden einerseits Proben mit Backsteinmauer-Architektur hergestellt, die zwar ein beachtliches Potenzial bezüglich der mechanischen Eigenschaften aufwies (Kapitel 3 bis 6) (die Festigkeit lag im Bereich derjenigen von kortikalem Knochen, und die Bruchdehnung lag bei einigen Prozent), jedoch in der Grösse limitiert waren. Andererseits wurden makroskopische CaP-Monolithe mit 5 hierarchischen Ebenen vom sub-Mikrometer bis makroskopischen Bereich hergestellt, deren Zähigkeit und Festigkeit deutlich über derjenigen von konventionell gesinterten Keramiken lag (Kapitel 7 und 8), allerdings wurde die Werte von kortikalem Knochen nicht erreicht. Somit bleibt die Herstellung fester, zäher, abbaubarer Gerüste zur Füllung von Knochendefekten in lasttragenden Situationen vorerst ein Kompromiss zwischen makroskopischer Grösse und geeigneten Eigenschaften. Die Resultate dieser Doktorarbeit stellen jedoch einen beträchtlichen Schritt in Richtung Realisierbarkeit solcher Materialien dar.

## **Gliederung der Doktorarbeit**

Kapitel 1 liefert eine generelle Einleitung zum Thema Knochenersatz und diskutiert die Vor- und Nachteile von aktuell verfügbaren Kalziumphosphat-Materialien, die Bedeutung von bio-

inspirierten Mikrostrukturen, und unsere Strategie um solche natürlichen Prinzipien auf synthetische Materialien zu übertragen.

Kapitel 2 diskutiert die theoretischen Berechnungen zur Bestimmung der idealen Dimensionen keramischer Partikel im Hinblick auf hohe Festigkeit und Zähigkeit.

## **Teil I: “Ziegelmauer-Architektur” mit diskreten Verstärkungskomponenten**

Abschnitt I beschreibt den Ansatz der Ziegelmauer-Architektur nach dem Vorbild natürlichen Perlmutts, beginnend mit der Synthese der Keramikpartikel (Kapitel 3 und 4), gefolgt von der Herstellung makroskopischer Komposit-Proben (Kapitel 5 und 6).

Kapitel 3 diskutiert die Synthese zur Herstellung von CaP-Kristallen im sub-Mikrometer-Bereich. Dies beinhaltet die Ausfällung von CaP-Partikeln in Ethylenglykol bei moderaten Temperaturen (90 – 170 °C) und die Variation verschiedener Reaktionsparameter (Temperatur, Konzentration der Ausgangsmaterialien, pH, Titrationsrate, usw.). Als Resultat erhielten wir zwei unterschiedliche CaP-Phasen, jeweils als gut dispergierte, gleichförmige sub-Mikrometer-Plättchen: (i) hexagonale Prismen aus  $\beta$ -Trikalziumphosphat ( $\beta$ -TCP) mit einem Seitenverhältnis von ca. 6 und einer engen Partikelgrößenverteilung von < 5 % (Standardabweichung/Mittelwert), und (ii) flache Parallelepipede aus Monetit (DCP) mit einem Seitenverhältnis von bis zu 25, jedoch einer etwas weiteren Partikelgrößenverteilung (ca. 20 %). Die Dicke beider Typen von Plättchen lag unter 300 nm, was ideale Voraussetzungen für die Herstellung fester CaP-basierter Komposite darstellte.

In Kapitel 4 wurde die Wachstumskinetik von CaP, speziell von  $\beta$ -TCP, im Detail untersucht, um ein besseres Verständnis und mehr Kontrolle über Grösse und Seitenverhältnis der Kristalle zu erhalten. Die Wachstumskurven konnten sowohl mit Gleichungen für diffusionskontrollierte als auch für reaktionskontrollierte Wachstumsmodelle angepasst werden. Die hohen berechneten Aktivierungsenergien deuten jedoch eher auf einen reaktionskontrollierten Mechanismus hin. Somit liesse sich die Kristallgrösse und -form am besten über die Konzentration der Ausgangsmaterialien kontrollieren. Ein Seitenverhältnis grösser als 6 wurde jedoch aufgrund der begrenzten Löslichkeit der Ausgangsmaterialien nicht erreicht.

In Kapitel 5 wurde mit vorgängig produzierten CaP-Plättchen eine Chitosan-Matrix verstärkt. Die Plättchen wurden einer Chitosan-Lösung beigemischt, welche anschliessend in eine Form gegossen und getrocknet wurde. Durch Verdunsten des Lösungsmittels bildete sich ein Film, in dessen Ebene sich die CaP-Plättchen ausrichteten. Mit DCP wurde aufgrund grösserer Seitenverhältnisse und Kontaktflächen eine homogenere Ausrichtung erreicht als mit  $\beta$ -TCP. Die Ausrichtung konnte weiter verbessert werden, indem die Plättchen vorgängig mit Eisenoxid-Nanopartikeln beschichtet und in einem rotierenden Magnetfeld orientiert wurden. Keramikgehalte

von bis zu 20 Vol-% führten zu einer Verbesserung der Festigkeit ohne deutliche Verschlechterung der Duktilität. Höhere Keramikgehalte führten zu Perkolation und zu einer abrupten Verschlechterung der Festigkeit, teilweise sogar zu tieferen Werten als denjenigen der reinen Matrix. Ein Keramikanteil von mehr als 20 Vol-% wäre aufgrund der besseren Biokompatibilität der Keramikphasen gegenüber den meisten abbaubaren Polymeren wünschenswert. Dies erfordert jedoch eine noch bessere Ausrichtung der Partikel, um anstelle einer drastischen Reduktion der Festigkeit eine Verstärkung zu erzielen.

Kapitel 6 untersucht die Machbarkeit eines gerichteten Gefriergiessens („Freeze-casting“) von CaP-Plättchen in einer Hydrogel-Matrix. Die wachsenden Eiskristalle drücken die Plättchen in die Porenwände, wo sie ausgerichtet und durch die Polymer-Matrix verklebt werden. Keramikanteile von bis zu 50 Vol-% konnten so in die Matrix eingebettet und ausgerichtet werden. Weitere Untersuchungen wurden gemacht, um die 2D-orientierten lamellaren Proben in dichte, Perlmutter-ähnliche Strukturen zu komprimieren und die Chitosan-Matrix durch Acetylation zu stabilisieren. Die Proben konnten dann auf Zugfestigkeit geprüft und mit vorhergehenden Proben, mit oder ohne magnetische Ausrichtung, verglichen werden. Leider wurde wegen der Acetylation Essigsäure freigesetzt, was die CaP Plättchen aufgelöst hat.

## Teil II: „Texturierte“ Strukturen mit kontinuierlichen Verstärkungskomponenten

Abschnitt II beschreibt eine Methode zur Ausrichtung der Kristalle *in-situ*, welche sich deutlich von den in Abschnitt I beschriebenen mischungsbasierten Methoden unterscheidet. Obwohl der Prozess rein technischer Natur und nicht bio-inspiriert ist, wiesen die so hergestellten Strukturen erstaunliche Ähnlichkeiten mit natürlich vorkommenden Strukturen auf.

In Kapitel 7 wurden gesinterte CaP-Blöcke hydrothermal inkubiert, um durch eine Phasentransformation *in-situ* eine Rekristallisation zu feineren, länglichen und ausgerichteten Kristallen zu erreichen. Keilbruchversuche („Brazilian tests“) wurden durchgeführt, um die diametrale Zugfestigkeit  $\sigma_{dts}$  und die Brucharbeit („work of fracture“, WOF) zu bestimmen. Durch die Inkubation wurden die  $\sigma_{dts}$  und WOF der Keramikblöcke signifikant erhöht. Da die mechanischen Eigenschaften von  $\alpha$ -TCP und CDHA ähnlich hoch sind, kann die Verbesserung der feiner verwachsenen Struktur der Kristalle nach der Inkubation zugeschrieben werden. Somit stellt die Optimierung der Mikrostruktur und Ausrichtung der Kristalle in einem keramischen Material eine effektive Methode zur Verbesserung der Festigkeit und Zähigkeit dar.

In Kapitel 8 wurde die Zähigkeit der in Kapitel 7 hergestellten Proben durch Imprägnierung mit einer duktilen Phase weiter verstärkt. Dazu wurde die keramische Struktur vor und nach der Hydrothermalbehandlung mit Poly( $\epsilon$ -caprolacton) (PCL) infiltriert, welches sich an den Wänden der

Mikro- und Makroporen anlagerte und die Brucharbeit durch Bildung von Polymerfibrillen erhöhte. Erstaunlicherweise verbesserte sich im Falle der texturierten Proben durch die Imprägnation auch die Festigkeit, was auf einen sehr guten Kontakt und somit gute Kraftübertragung zwischen Keramik und Polymer schliessen lässt. Zusammengefasst lässt sich schlussfolgern, dass die Texturierung von Keramiken die Zähigkeit durch eine Änderung der Rissausbreitung (Bruchmodus) erhöht. Gleichzeitig erhöht die Imprägnation mit einer duktilen Phase die Festigkeit von texturierten Keramiken aufgrund der grossen Kontaktfläche und starken Bindungskräfte beider Phasen.





## CHAPTER 1:

### GENERAL INTRODUCTION

#### Bone grafting

Bone defects may arise from accidents (trauma), but also from tumour or cysts removal, burr holes or osteotomies [1]. Bone has a large self-healing and regeneration capacity, however limited to a given size depending on different biological factors (age, sex, or health) [2, 3]. When bone defect exceeds a certain size – so called “critical size defects” – bridging is impossible or delayed and bone grafting has to be applied to prevent the faster filling by soft tissue only.

The most common source of bone graft is from the patient’s iliac crest, but availability of autologous material is limited and the harvesting procedure causes longer operation times and increased risk of side-effects and pain at the donor site [4, 5]. Moreover, the harvesting site may also become a critical size defect that has to be filled. Allografts might be used to replace or complement the autograft, but this approach bears ethical concerns and may lead to disease transmission [6, 7].

In the past decades synthetic bone graft substitutes have become a viable complement or even alternative to bone auto- and allografts [8], although still being considered the gold standard for bone void filling by many surgeons.

#### CaP ceramics

Calcium phosphates (CaP) ceramics are widely used as a synthetic alternative due to their chemical similarity to the mineral part of bone [9, 10]. There is a broad range of CaP materials used for bone substitution. The most common ones are sintered CaP, such as hydroxyapatite (HA,  $\text{Ca}_5(\text{PO}_4)_3\text{OH}$ ),  $\beta$ -tricalcium phosphate ( $\beta$ -TCP,  $\text{Ca}_3(\text{PO}_4)_2$ ) and their mixtures called biphasic calcium phosphates (BCP). Initially, researchers strongly focused on hydroxyapatite because the mineral part of bone is a low crystalline carbonated hydroxyapatite phase [11]. However, synthetic hydroxyapatite is often

obtained by sintering at high temperature and this highly crystalline phase is extremely slowly resorbable. For example, Linhart et al. could not detect any resorption after 7 years implantation [12].

$\beta$ -TCP is of particular interest as it is generally considered to be an excellent bone substitute, not only presenting a high osteoconductivity but also a cell-mediated resorption [10, 13]. Thanks to its higher solubility it is completely resorbed within a couple of months [14], depending on the implant size. Moreover, calcium and phosphate ions released during the resorption can be used to mineralize new bone in the bone remodelling process [15].

Non-sintered CaP phases such as brushite (DCPD,  $\text{CaHPO}_4 \cdot \text{H}_2\text{O}$ ) and monetite (DCP,  $\text{CaHPO}_4$ ) have recently raised the interest of researchers due to their good biocompatibility and fast osteotransduction [16-19]. These phases are even more soluble than  $\beta$ -TCP and their degradation pathway is supposed to be similar to that of  $\beta$ -TCP but it has been less studied as for  $\beta$ -TCP due to their younger history as implant materials.

A major drawback of synthetic CaP bone substitutes is their brittleness [20], which excludes their use in load-bearing applications [7] and requires supplementary fixation with osteosynthesis fixation devices like metallic plates and screws [20, 21].

## **How to improve toughness of CaP ceramics?**

To overcome this problem, the current trend is to associate CaP particles with a degradable polymer [7, 21, 22]. Ideally, composite structures combine the best of both materials: the ceramic particles provide strength and stiffness to the composites, while the polymer phase brings toughness [23]. However, to the best of our knowledge, no synthetic material combines biodegradability with strength and toughness values similar to those of cortical bone. The usual default of the materials reported in the literature is the lack of structure design, impairing high ceramic fractions and limiting strength and/or toughness.

## **Importance of structure design: bio-inspiration**

One approach to obtain strong and tough composites based on calcium phosphate ceramics is to mimic the structure of certain natural materials like bone and nacre (Figure 1-1) [23-25]. Such materials can be seen as a ductile organic matrix reinforced with sub-micron ceramic particles or as inorganic particles held together by an organic “glue”.

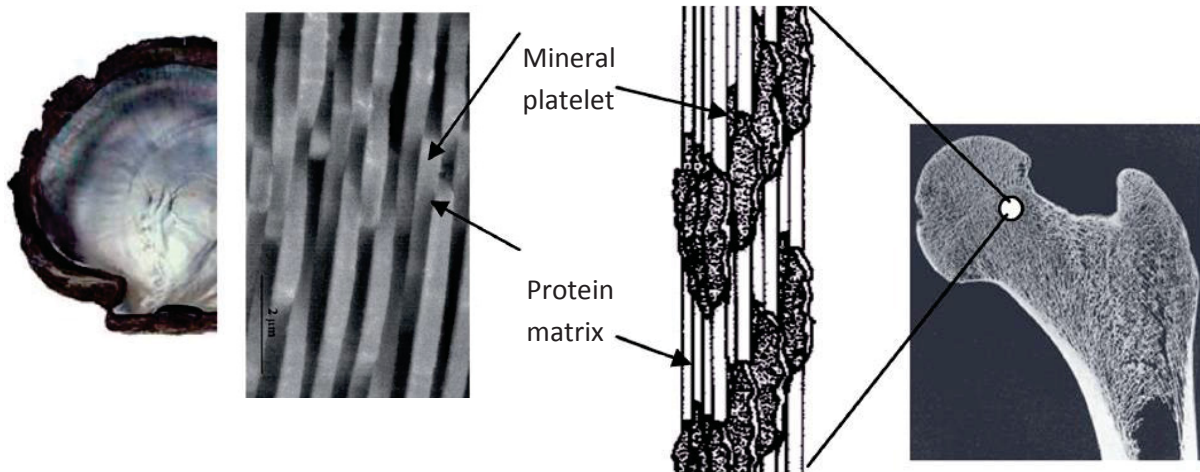


**Figure 1-1** Natural composite materials made of mineral platelets in an organic matrix: a) macroscopic nacre, b) microstructure of nacre (TEM), c) scheme of the nanostructure of bone and d) macroscopic bone. [26].

Their architecture is very important and very well controlled [27-29]. For example, the ceramic particles must have a thickness below a critical value and they must present a large aspect ratio (= particle length/thickness) [30]. Indeed, limiting the size of the ceramics is the most efficient way to increase their strength (Griffith's law) [31]. Also, a high aspect ratio provides large interfaces allowing a good load transfer between organic matrix and ceramic particles.

In consequence it appears crucial that the reinforcement particles must have very precise features to optimize the mechanical reinforcement in composites, especially when based on biodegradable materials, i.e. chemically weak.

- (i) They must be non-agglomerated to prevent voids [32] and crack propagation by weak and brittle particle interactions [33]; in addition agglomerates locally impair alignment of the particles.
- (ii) They must have one or preferably two dimensional geometries (fibers or platelets) to eventually provide a unidirectional or preferentially planar reinforcement of the composite [34, 35].
- (iii) They must have a high aspect ratio to provide a large contact area and optimal load transfer between polymer matrix and ceramic particles [36].
- (iv) They must be thinner than a critical size under which ceramic particles reach their maximum mechanical properties [31].
- (v) They must be uniform in size (= monodisperse) and shape to achieve homogeneous properties. A regular shape and size also helps to achieve high packing density and consequently high ceramic fractions, as observed in tough natural materials like nacre [27].

To summarize, in order to efficiently combine the ductility and resilience of a matrix, with the strength and stiffness of its reinforcement elements, the whole composite structure has to be properly designed [37], implying:

- a. An appropriate ratio of both phases
- b. A strong interface between both phases to efficiently transmit shear forces
- c. An optimum aspect ratio of the reinforcement elements, which depends on the organic matrix properties and the interface strength between both materials, as explained hereafter and
- d. A high ordering/alignment.

When the aspect ratio of the reinforcing phase is too small, the stresses are not correctly transmitted to the reinforcing phase and the matrix fails first; for too large aspect ratios, the load-transfer is too high and the reinforcing phase is exposed to too high stresses and breaks before the matrix, leading to brittle, catastrophic failure [23, 38]. In an optimal composite, matrix and reinforcing phase should fail at the same time, ideally by pull-out mode of the fibers/plates to dissipate as much as possible of fracture energy. Hence, an optimal aspect ratio exists, but depends on both materials and their bonding strength [36]. For abalone nacre, the critical aspect ratio of the calcium carbonate crystals is close to 9 and the observed value is 8 [23, 39]. For stronger ceramics like alumina platelets in biopolymers, the critical aspect ratio is close to 50 [23].

When all these factors (phase ratio, interface strength, platelets features like size and aspect ratio, and designed architecture) are optimized, tough and strong materials can be obtained, even made of individually weak constituents. However, well-organized layered structures with high ceramic fractions are only conceivable with non-agglomerated, monodisperse platelets with well-defined shape and size, which is not common for calcium phosphate materials, mainly due to their synthesis methods [40-44].

Many attempts have already been done to combine CaP particles with a polymeric matrix [45-50]. Investigations with irregular particles have shown very little potential regarding target mechanical properties, i.e. those of cortical bone [21]. As already mentioned above, composites based on plate-like reinforcement particles have already been done, but never with resorbable materials [23, 32, 51-53]. Many different methods have been investigated to reach the high particle alignment required for high reinforcement. Solvent casting for example has shown good potential also within a magnetic field [53]. Freeze-casting also led to high spatial arrangement of the particles [52, 54]. Tape-casting was recently investigated and was less efficient, but showed ease of use and high production rate [55].

Beside the bio-inspired approach to make CaP-based composites based on discrete short CaP particles embedded within a continuous polymeric matrix, another approach has also been widely investigated: impregnation of continuous ceramic blocks by a soft polymeric phase. The interpenetration of both phases increases the work of fracture compared to the pure ceramic blocks. However, even if the improvement is consequent (7- to 13-fold increase of fracture energy [56]), the values reached remain below those of natural composites. Moreover, the surface of the implant ends completely covered by the polymer, which tends to decrease the osteointegration.

## **What mechanical properties should be reached?**

Ideally, a bone graft substitute materials should have similar mechanical properties than native bone, i.e. a tensile strength of 70 - 150 MPa [27, 57, 58], a yield strength of 30 - 70 MPa [58], a stiffness of 3 - 30 GPa [27, 57-59] and a fracture toughness of 2 - 12 MPa·m<sup>½</sup> [27, 57, 59]. Higher strength and stiffness would also be suitable in a mechanical point of view, however bone regeneration is often hindered when stress shielding occurs, i.e. when too many stresses are undertaken by the implant and the bone remains unloaded.

More interest was given to tensile than compression properties, which is uncommon in the field of bioceramics. However, ceramic materials, especially dense ones, are rather good in compression, and when they fail, even in compression mode, it is because of shear forces, i.e. tensile components in the internal stresses. Hence, only tensile properties were looked at and optimized in the present thesis. This makes comparison with other results found in the literature difficult. Indeed, testing in compression mode is mostly tested either because it is much easier than tensile mode testing with ceramic, and/or because it is usually, but wrongly, admitted that bones are only submitted to compressive loading.

## **Specific aims**

The goal of the present PhD thesis was to obtain bio-inspired CaP based materials with designed structures in the aim to combine strength, toughness and biodegradability. In this aim, new materials forms and synthesis processes were developed. In particular, strong focus was set on alignment methods for sub-micro-metric particles.

The application target is bone repair in load-bearing locations. However, the newly developed composites materials not only aim at providing scaffolds or void filler, but also to furnish adequate

materials for the fabrication of mechanically stable but resorbable osteosynthesis elements like plates and screws.

## Two general approaches to reach the goal

Two approaches were investigated here, following both directions already widely found in the literature, but also based on 2 conventional composite types: (i) reinforcement of a continuous matrix with short, discrete particles and (ii) continuous reinforcement acting as a skeleton.

### Nacre-inspired “brick-and mortar” structures (Part I)

The first part (chapters 3 to 6) of this thesis aimed at building structures inspired by nacre structure using a “brick-and-mortar” approach. Since CaP platelets with the above mentioned features could not be found, they were produced. The synthesis and characterization of such platelets is presented in chapter 3, while their growth kinetics is investigated in chapter 4. The assembly of the platelets with a polymer matrix and alignment by solvent evaporation technique and in a magnetic field is described in chapter 5. The use of freeze-casting (also called ice-templating [60]) to improve the alignment of the structure is the topic of chapter 6. Attention was particularly paid on the structure-properties (mechanical) relationship.

### Textured ceramic monoliths (Part II)

In parallel to the bio-inspired “brick-and-mortar” structures, another – more classical engineering – strategy was also investigated and is reported in the second part (chapters 7 and 8). In this case, the synthesis started by the production of standard sintered monolithic 3D ceramics, followed by recrystallization to refine and structure the grains (chapter 7) and subsequent polymer impregnation (chapter 8). Hence, structuration of the reinforcement phase is done before composite elaboration, similarly to woven or mat-based composites. Such a material is supposed to fulfil most of the requirements listed above:

- (i) Agglomeration is not relevant, since the synthesis starts from a dense ceramic and not with loose particles. However, if a non-continuous ceramic phase can be achieved, it would allow deep polymer impregnation, i.e. high synergy between both phases.
- (ii) Hydrothermal treatments of CaP tend to produce needle-like HA particles,
- (iii) with aspect ratios between 10 and 30 and
- (iv) thickness under 400nm.

- (v) Since the starting material before recrystallization is already dense, it is expected that it triggers homogeneous structures.

## References

- [1] Sullivan F. European Markets for bone grafts and bone. 2008.
- [2] Lu C, Miclau T, Hu D, Hansen E, Tsui K, Puttlitz C, et al. Cellular basis for age-related changes in fracture repair. *J Orthop Res*. 2005;23:1300-7.
- [3] Kalfas IH. Principles of bone healing. *Neurosurg Focus*. 2001;10.
- [4] Banwart JC, Asher MA, Hassanein RS. Iliac crest bone graft harvest donor site morbidity. A statistical evaluation. *Spine*. 1995;20:1055-60.
- [5] Younger EM, Chapman MW. Morbidity at bone graft donor sites. *J Orthop Trauma*. 1989;3:192-5.
- [6] Hofmann GO, Kirschner MH, Wangemann T, Falk C, Mempel W, Hammer C. Infections and immunological hazards of allogeneic bone transplantation. *Arch Orthop Trauma Surg*. 1995;114:159-66.
- [7] Laurencin C, Khan Y, El-Amin SF. Bone graft substitutes. *Expert Review of Medical Devices*. 2006;3:49-57.
- [8] Giannoudis PV, Dinopoulos H, Tsiridis E. Bone substitutes: an update. *Injury*. 2005;36 Suppl 3.
- [9] LeGeros RZ. Properties of osteoconductive biomaterials: calcium phosphates. *Clin Orthop*. 2002:81-98.
- [10] Bohner M. Resorbable biomaterials as bone graft substitutes. *Materials Today*. 2010;13:24-30.
- [11] Constantz BR, Ison IC, Fulmer MT, Poser RD, Smith ST, VanWagoner M, et al. Skeletal repair by in situ formation of the mineral phase of bone. *Science*. 1995;267:1796-9.
- [12] Linhart W, Briem D, Amling M, Rueger JM, Windolf J. Mechanical failure of a porous hydroxyapatite ceramic 7.5 years after treatment of a fracture of the proximal tibia. *Unfallchirurg*. 2004;107:154-7.
- [13] Egli PS, Muller W, Schenk RK. Porous hydroxyapatite and tricalcium phosphate cylinders with two different pore size ranges implanted in the cancellous bone of rabbits. A comparative histomorphometric and histologic study of bony ingrowth and implant substitution. *Clin Orthop*. 1988:127-38.
- [14] Gatti AM, Zaffe D, Poli GP. Behaviour of tricalcium phosphate and hydroxyapatite granules in sheep bone defects. *Biomaterials*. 1990;11:513-7.
- [15] Kanatani M, Sugimoto T, Fukase M, Fujita T. Effect of elevated extracellular calcium on the proliferation of osteoblastic MC3T3-E1 cells: its direct and indirect effects via monocytes. *Biochem Biophys Res Commun*. 1991;181:1425-30.
- [16] Bohner M, Theiss F, Apelt D, Hirsiger W, Houriet R, Rizzoli G, et al. Compositional changes of a dicalcium phosphate dihydrate cement after implantation in sheep. *Biomaterials*. 2003;24:3463-74.
- [17] Galea LG, Bohner M, Lemaitre J, Kohler T, Muller R. Bone substitute: Transforming  $\beta$ -tricalcium phosphate porous scaffolds into monetite. *Biomaterials*. 2008;29:3400-7.
- [18] Tamimi F, Torres J, Bassett D, Barralet J, Cabarcos EL. Resorption of monetite granules in alveolar bone defects in human patients. *Biomaterials*. 2009;31:2762-9.

- [19] Tamimi F, Sheikh Z, Barralet J. Dicalcium phosphate cements: Brushite and monetite. *Acta Biomaterialia*. 2012;8:474-87.
- [20] Wagoner Johnson AJ, Herschler BA. A review of the mechanical behavior of CaP and CaP/polymer composites for applications in bone replacement and repair. *Acta Biomaterialia*. 2011;7:16-30.
- [21] Rezwani K, Chen QZ, Blaker JJ, Boccaccini AR. Biodegradable and bioactive porous polymer/inorganic composite scaffolds for bone tissue engineering. *Biomaterials*. 2006;27:3413-31.
- [22] Kolk A, Handschel J, Drescher W, Rothamel D, Kloss F, Blessmann M, et al. Current trends and future perspectives of bone substitute materials - From space holders to innovative biomaterials. *J Cranio-Maxillofac Surg*. 2012;40:706-18.
- [23] Bonderer LJ, Studart AR, Gauckler LJ. Bioinspired design and assembly of platelet reinforced polymer films. *Science*. 2008;319:1069-73.
- [24] Tang Z, Kotov NA, Magonov S, Ozturk B. Nanostructured artificial nacre. *Nat Mater*. 2003;2:413-8.
- [25] Dimas LS, Bratzel GH, Eylon I, Buehler MJ. Tough composites inspired by mineralized natural materials: Computation, 3D printing, and testing. *Advanced Functional Materials*. 2013;23:4629-38.
- [26] Ji B. A study of the interface strength between protein and mineral in biological materials. *Journal of Biomechanics*. 2008;41:259-66.
- [27] Ji B, Gao H. Mechanical properties of nanostructure of biological materials. *J Mech Phys Solids*. 2004;52:1963-90.
- [28] Barthelat F, Tang H, Zavattieri PD, Li CM, Espinosa HD. On the mechanics of mother-of-pearl: A key feature in the material hierarchical structure. *Journal of the Mechanics and Physics of Solids*. 2007;55:306-37.
- [29] Kamat S, Su X, Ballarini R, Heuer AH. Structural basis for the fracture toughness of the shell of the conch *Strombus gigas*. *Nature*. 2000;405:1036-40.
- [30] Meyers MA, Chen PY, Lin AYM, Seki Y. Biological materials: Structure and mechanical properties. *Progress in Materials Science*. 2008;53:1-206.
- [31] Griffith AA. The Phenomena of Rupture and Flow in Solids. *Philosophical Transactions of the Royal Society of London Series A, Containing Papers of a Mathematical or Physical Character*. 1921;221:163-98.
- [32] Podsiadlo P, Kaushik AK, Arruda EM, Waas AM, Shim BS, Xu J, et al. Ultrastrong and stiff layered polymer nanocomposites. *Science*. 2007;318:80-3.
- [33] Thornton C, Yin KK, Adams MJ. Numerical simulation of the impact fracture and fragmentation of agglomerates. *J Phys D: Appl Phys*. 1996;29:424-35.
- [34] Zhang Y, Evans JRG. Approaches to the manufacture of layered nanocomposites. *Applied Surface Science*. 2012;258:2098-102.
- [35] Rexer J, Anderson E. COMPOSITES WITH PLANAR REINFORCEMENTS (FLAKES, RIBBONS) - A REVIEW. *Polym Eng Sci*. 1979;19:1-11.
- [36] Gao H. Application of fracture mechanics concepts to hierarchical biomechanics of bone and bone-like materials. *International Journal of Fracture*. 2006;138:101-37.
- [37] Vinson JR, Sierakowski RL. *The Behavior of Structures Composed of Composite Materials*: Kluwer Academic Publishers; 2002.



- [38] Gao H, Ji B, Jäger IL, Arzt E, Fratzl P. Materials become insensitive to flaws at nanoscale: Lessons from nature. *Proceedings of the National Academy of Sciences of the United States of America*. 2003;100:5597-600.
- [39] Jackson AP, Vincent JFV, Turner RM. The Mechanical Design of Nacre. *Proceedings of the Royal Society of London Series B Biological Sciences*. 1988;234:415-40.
- [40] LeGeros RZ, LeGeros JP. Calcium phosphate Bioceramics: Past, present and future. *Key Eng Mat* *Key Eng Mat*. 2003;240-2:3-10.
- [41] Gibson IR, Ke S, Best SM, Bonfield W. Effect of powder characteristics on the sinterability of hydroxyapatite powders. *J Mater Sci-Mater M* *J Mater Sci-Mater M*. 2001;12:163-71.
- [42] Layrolle P, Lebugle A. Characterization and Reactivity of Nanosized Calcium Phosphates Prepared in Anhydrous Ethanol. *Chem Mater*. 1994;6:1996-2004.
- [43] Layrolle P, Lebugle A. Synthesis in pure ethanol and characterization of nanosized calcium phosphate fluoroapatite. *Chem Mater*. 1996;8:134-44.
- [44] Wang P, Li C, Gong H, Jiang X, Wang H, Li K. Effects of synthesis conditions on the morphology of hydroxyapatite nanoparticles produced by wet chemical process. *Powder Technology*. 2010;203:315-21.
- [45] Bonfield W, Grynpas M, Tully AE, Bowman J, Abram J. Hydroxyapatite reinforced polyethylene--a mechanically compatible implant material for bone replacement. *Biomaterials*. 1981;2:185-6.
- [46] Shikinami Y, Okuno M. Bioresorbable devices made of forged composites of hydroxyapatite (HA) particles and poly-L-lactide (PLLA): Part I. Basic characteristics. *Biomaterials*. 1999;20:859-77.
- [47] Venkatesan J, Kim SK. Chitosan composites for bone tissue engineering - An overview. *Mar Drugs*. 2010;8:2252-66.
- [48] Baji A, Wong SC, Srivatsan TS, Njus GO, Mathur G. Processing methodologies for polycaprolactone-hydroxyapatite composites: A review. *Mater Manuf Process*. 2006;21:211-8.
- [49] Kim SS, Sun Park M, Jeon O, Yong Choi C, Kim BS. Poly(lactide-co-glycolide)/hydroxyapatite composite scaffolds for bone tissue engineering. *Biomaterials*. 2006;27:1399-409.
- [50] Hu Q, Li B, Wang M, Shen J. Preparation and characterization of biodegradable chitosan/hydroxyapatite nanocomposite rods via in situ hybridization: A potential material as internal fixation of bone fracture. *Biomaterials*. 2004;25:779-85.
- [51] Munch E, Launey ME, Alsem DH, Saiz E, Tomsia AP, Ritchie RO. Tough, bio-inspired hybrid materials. *Science*. 2008;322:1516-20.
- [52] Launey ME, Munch E, Alsem DH, Barth HB, Saiz E, Tomsia AP, et al. Designing highly toughened hybrid composites through nature-inspired hierarchical complexity. *Acta Materialia*. 2009;57:2919-32.
- [53] Erb RM, Libanori R, Rothfuchs N, Studart AR. Composites reinforced in three dimensions by using low magnetic fields. *Science*. 2012;335:199-204.
- [54] Munch E, Saiz E, Tomsia AP, Deville S. Architectural control of freeze-cast ceramics through additives and templating. *Journal of the American Ceramic Society*. 2009;92:1534-9.
- [55] Libanori R, Münch FHL, Montenegro DM, Studart AR. Hierarchical reinforcement of polyurethane-based composites with inorganic micro- and nanoplatelets. *Composites Science and Technology*. 2012;72:435-45.
- [56] Peroglio M, Gremillard L, Chevalier J, Chazeau L, Gauthier C, Hamaide T. Toughening of bio-ceramics scaffolds by polymer coating. *Journal of the European Ceramic Society*. 2007;27:2679-85.

[57] Roeder RK, Converse GL, Kane RJ, Yue W. Hydroxyapatite-reinforced polymer biocomposites for synthetic bone substitutes. *JOM*. 2008;60:38-45.

[58] Cooke FW. Bulk properties of materials. In: Ratner BD, Hoffman AS, Schoen FJ, Lemons JE, editors. *Biomaterials science - an introduction to materials in medicine*. San Diego: ACADEMIC PRESS; 1996. p. 11-21.

[59] Currey JD, Zioupos P, Davies P, Casinos A. Mechanical properties of nacre and highly mineralized bone. *Proceedings of the Royal Society B: Biological Sciences*. 2001;268:107-11.

[60] Wegst UGK, Schechter M, Donius AE, Hunger PM. Biomaterials by freeze casting. *Philos Trans R Soc A Math Phys Eng Sci*. 2010;368:2099-121.

## CHAPTER 2: THEORETICAL CALCULATIONS

### ***Abstract***

Following a few mechanical principles, it is possible to design new composite materials aiming at sustaining a given loading mode and intensity. Hence, the ideal features of calcium phosphate based composites for bone substitution were predicted using different calculations based on rules from the classical composite technology but also on structure-properties relationships observed in natural materials.

Theoretical calculations were done to estimate the ideal dimensions of calcium phosphate ceramic components to maximize their intrinsic strength and their efficiency as reinforcement elements in composite structures. Then, considering a specific matrix material, optimum size and shape for a compromise between strength improvement and preservation of toughness was determined. Finally, the theoretical mechanical properties of composites were predicted in function of the phase's fractions and the adequate features (particles size and aspect ratio, volume fractions) for bone substitution were predicted.

Published in part as supplementary data in:

Galea L, Bohner M, Thuering J, Doebelin N, Ring TA, Aneziris CG, Graule T. *Growth kinetics of hexagonal sub-micrometric  $\beta$ -tricalcium phosphate particles in ethylene glycol*. **Acta Biomateriala**, 10, 3922-3930 (2014).

## Introduction

Combining two or more materials in composite structures is a common way to combine properties of both phases, usually with some compromise. Usually, the final properties are proportional to the individual properties of each phase and their respective fractions. In certain case, the properties might even be higher than expected from the mixing law; but they can also be lower, often because of poor interfaces but also because of various structural mistakes. The ideal dimensions of each phase of a composite can be designed theoretically, as well as the way they have to be arranged in the 3D solid constructs to reach the desired properties to sustain a given loading mode. Those calculations are based on a few mechanical principles, actually known from the classical composites field and also from structure-properties relationships observed in natural materials.

Indeed, during the past two decades, many studies have been conducted on natural materials, particularly on nacre and bone, usually with the aim to translate those design principles to artificial materials [1-3]. Gao et al. for example extensively studied the structure and the features of individual phases of natural materials, in particular nacre [4-7]. Their work supports the hypothesis that the sub-micrometer scale in natural composites like bone and nacre is the result of an optimisation to tolerate crack-like flaws. Simulations of brick-and-mortar structures with nacre's constituents led to the same conclusion: the optimal geometries found are those of natural nacre. Moreover, the enormous difference in toughness between pure calcium carbonate ceramic and nacre could be explained by the complex hierarchical structures achieved [5, 8].

Those design principles were applied in a few engineered composite, like by Studart's research group [9-13] or Deville and co-workers [14-17]. The first ones used planar synthesis methods (solvent casting, dip-coating, etc.) leading to dense films whereas the second ones obtained 3D porous constructs by freeze-casting. The mechanical properties achieved were outstanding compared to those obtained with similar raw materials but without paying attention to particle size, shape and orientation.

Wagner and Bar-On also thoroughly investigated the links between architectural features and mechanical properties [18-21]. They specifically elucidated the relations between elastic modulus and staggering characteristics like overlapping [20] or thickness of layers [19]. In particular, they highlighted that the stiffness of a composite in the axial direction (relative to platelets length) strongly increases once the platelets start to overlap. Hence, for a constant ceramic fraction, the axial stiffness can actually be increased by increasing the thickness of the organic layers (in the orthogonal direction).

The aim of the present chapter was thus to assemble various mechanical principles to first optimize the reinforcement particles and second predict the ideal synthetic structures to approach the mechanical properties of cortical bone with resorbable materials. Hence, after estimating the ideal size and shape for the platelets to reach their intrinsic optimum and to reinforce efficiently composite structures, the mechanical properties of well-ordered composite structures were calculated. If all optimal dimensions and microstructural aspects can be experimentally combined, synthetic materials with outstanding performances could be developed.

## Theoretical tensile strength of $\beta$ -TCP platelets and critical size for flaw tolerance

The theoretical strength,  $\sigma_{th}$ , of a material theoretically ranges between 1 and 10 % of the Young's modulus [6], but this strength is never reached in macroscopic ceramics. Indeed the presence of pre-existing defects strongly weakens the material and leads to catastrophic failure by crack propagation. The Griffith's criterion [22] describes the relationship between tensile strength and defect size. Specifically, the tensile strength of a brittle material,  $\sigma_p$ , can be expressed as a function of the material Young's modulus,  $E$ , the surface energy,  $\gamma$ , the Poisson's ratio,  $\eta$ , and the size of the largest surface flaw,  $c$ , assumed to be the half of the mineral platelet thickness,  $h$  (Eq. 1, Figure 2-1):

$$\sigma_{p,1} = \sqrt{\frac{4 \cdot E \cdot \gamma}{\pi \cdot \eta \cdot h}} \quad [22] \quad \text{Equation 1}$$

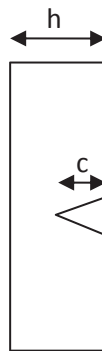


**Figure 2-1** a strip of width  $h$  with an edge crack of length  $c$ .

Considering an elastic modulus of 110 GPa for  $\beta$ -TCP, a Poisson's ratio of 0.276 and a surface energy of  $0.842 \text{ J/m}^2$  [23], for largest surface flaw of  $c = h/2$ , the tensile strength varies from 0.9 GPa to 2.9 GPa for 500 nm to 50 nm thick crystals, respectively (Figure 2-2).

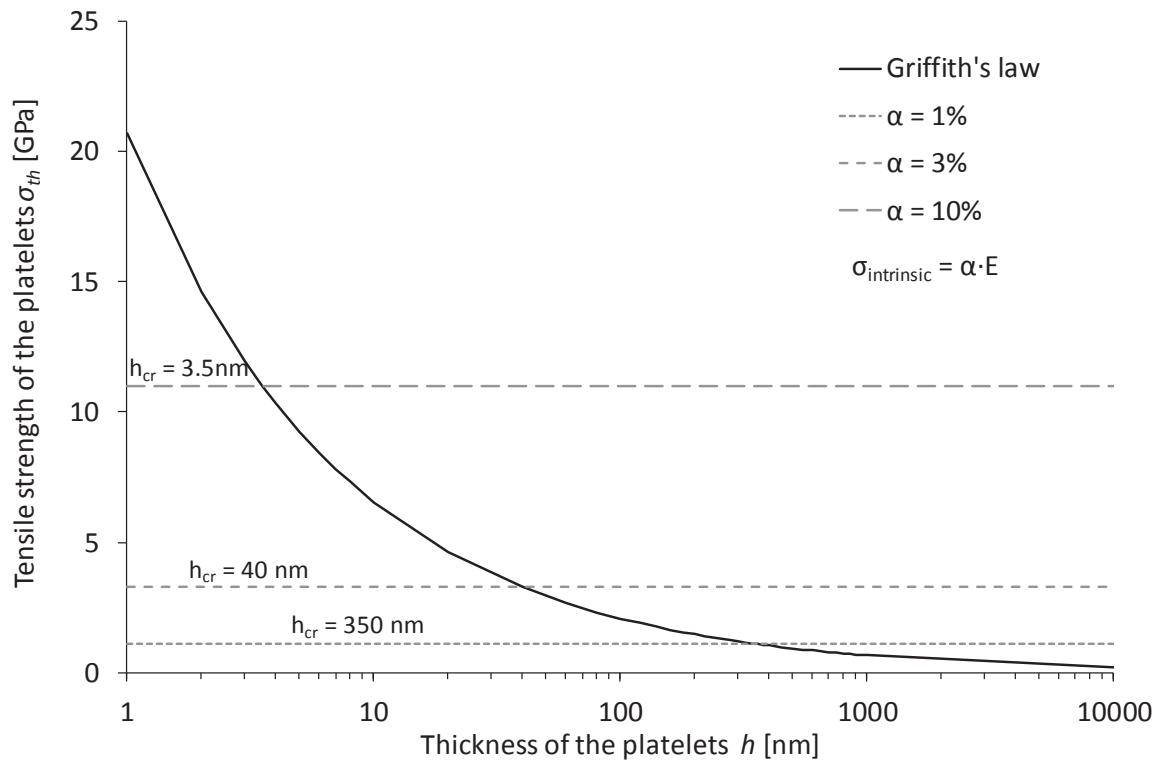


**Figure 2-2** Calculated tensile strength in function of  $\beta$ -TCP platelets thickness and theoretical strength of  $\beta$ -TCP (1, 3 or 10 % of  $E=110$  GPa).

However, the crystals strength cannot decrease infinitely when decreasing in size. The maximum theoretical strength or intrinsic strength,  $\sigma_{int}$ , of a perfect crystal is generally considered to amount 1 to 10 % ( $\alpha$ ) of its elastic modulus ( $\sigma_{int} = \alpha \cdot E$ ). There is thus a critical crystal size,  $h_{cr}$ , below which the strength is at its maximum and the material fails by uniform rupture. Above this critical size, the material is not flaw tolerant anymore and breaks by crack propagation. Hence, to tolerate crack flaws of all sizes a crystal has to be smaller than  $h_{cr}$ . It can be expressed by reversing Equation 1:

$$h_{cr,1} = \frac{4 \cdot E \cdot \gamma}{\pi \cdot \eta \cdot \sigma_{int}^2} = \frac{4 \cdot \gamma}{\pi \cdot \eta \cdot \alpha^2 \cdot E} \quad \text{Equation 2}$$

The following calculations will be done with  $\alpha$  values of 1 %, 3 % and 10 %, even if proportions higher than 1 % are rare for ceramic crystals. Indeed, a strength of 3 GPa seems unrealistic for materials with such weak crystallographic structure as CaP. Using the above mentioned values from Liang et al. for  $\beta$ -TCP [23], with  $\alpha = 1 \% / 3 \% / 10 \%$ , **the platelets retain their intrinsic or maximum strength below 350 nm / 40 nm / 3.5 nm** (Figure 2-2). In a conservative point of view an intrinsic strength of 1 % of the stiffness will further be considered.

From equation 2 it is obvious that the stronger a material is, the smaller it has to be to reach its intrinsic limiting strength. Biological materials with low Young's modulus and no perfect lattice

structures or pure chemical composition can become insensitive to crack-like flaws at quite large size scales. For materials with low Young's modulus like calcium carbonate – which Young's modulus can be as low as 50 GPa – the critical size is as large as a few hundred nanometers. Indeed, aragonite crystals in nacre are 200-500 nm thick [24]. However, for hydroxyapatite, Gao [6] assumed  $\gamma = 1 \text{ J/m}^2$ ,  $E = 100 \text{ GPa}$ , and  $\sigma_{th} = E/30$ , leading to a critical crystal size of 18 nm, to explain that crystals in cortical bone are only a few nanometers thick. It is however questionable if the size of the HA crystals is not limited by other factors.

These calculations support the hypothesis that the sub-micrometer scale in natural composites like bone and nacre is the result of an optimization to tolerate crack-like flaws. This principle has to be followed in bio-inspired materials.

Other equations than Griffith's one (Equation 1) have been used by different research groups. Using  $\eta = 0.3$  and the approximation  $\eta \cdot \pi \approx 1$ , Gao [6] proposed a simplified equation

$$\sigma_{p,2} = \sqrt{\frac{4 \cdot E \cdot \gamma}{h}} \quad \text{Equation 3}$$

leading to the following estimation of the critical size

$$h_{cr,2} = \frac{4 \cdot E \cdot \gamma}{\sigma_{int}^2} \quad \text{Equation 4}$$

Bonderer et al. [9] used a variation of the Griffith's criterion to estimate the tensile strength of brittle platelets where they neglected the Poisson's ratio.

$$\sigma_{p,3} = \sqrt{\frac{2 \cdot E \cdot \gamma}{\pi \cdot c}} \quad \text{Equation 5}$$

In spite of these differences, the size order for critical crystal sizes was similar.

## Optimal aspect ratio

In a composite structure, the tensile stresses applied on the whole structure are transferred from the organic matrix to the reinforcing particles by shear stresses at the organic-inorganic interface. In consequence, the larger is the contact surface between both materials (in the direction of the stresses) relative to the volume occupied by the particles, the larger is the stress transfer from the soft matrix to the strong mineral part, and thus the stronger is the composite. Particles with large aspect ratio are thus preferred to improve the strength of a material. Nevertheless, if the platelets are too long, the stress transfer is too high and the mineral reinforcement breaks first, leading to

catastrophic brittle failure of the composite, i.e. low toughness. On the other hand, too short particles do not carry enough of the stresses and the matrix breaks first, using mechanisms like platelets debonding, crack deflection, etc. There is thus an optimum aspect ratio,  $s_{cr}$ , of the mineral platelets which corresponds to the condition that organic matrix and ceramic phase fail at the same time [4]. Hence, to obtain a composite with the highest possible strength while preserving a certain toughness of the matrix, the aspect ratio of the particles should be as close as possible but slightly under the critical aspect ratio.

In the case of a perfect interface that transmits all stresses from the matrix to the platelets, the tensile stress in the mineral platelets,  $\sigma$ , is equal to the product of the mineral aspect ratio,  $s$ , with the shear stress at the interface, which is equal to the shear stress in the organic matrix,  $\tau$ ,

$$\sigma = s \cdot \tau \quad \text{Equation 6}$$

Hence, the optimum aspect ratio,  $s_{cr}$ , is a function of the ceramic strength and of the shear strength of the interface,  $\tau_i$ , or of the organic matrix,  $\tau_m$  [6].

$$s_{cr} = \frac{\sigma_p}{\tau_i} = \frac{\sigma_p}{\tau_m} \quad \text{Equation 7}$$

The higher the mineral strength is compared to the shear strength, the larger is the critical aspect ratio and high loads can be transferred to the mineral part without brittleness [9]. Contrarily, weak materials like carbonates have a low optimal aspect ratio and have to be quite short to avoid brittle fracture of the composite, limiting the reinforcing capacity of calcium carbonate on the composite. Indeed, the calcium carbonate platelets in nacre have an aspect ratio of about 8 [25].

Using the tensile strength of the platelets calculated above with the Griffith's criterion and a shear strength of about 40 MPa for chitosan [9], the optimal aspect ratio of a  $\beta$ -TCP-chitosan composite would be 28 for platelets thinner than 350 nm (i.e. under the critical size for  $\beta$ -TCP, considering an intrinsic strength of 1% of its stiffness) and lower for thicker crystals (Figure 2-3). If  $\beta$ -TCP would intrinsically be stronger as 1.1 GPa, the critical aspect ratio would increase for thinner platelets. On the opposite, if no  $\beta$ -TCP platelets thinner than  $\beta$ -TCP's critical size can be obtained, their strength will be lower than expected due to flaw sensitivity and the corresponding critical aspect ratio will be lower.



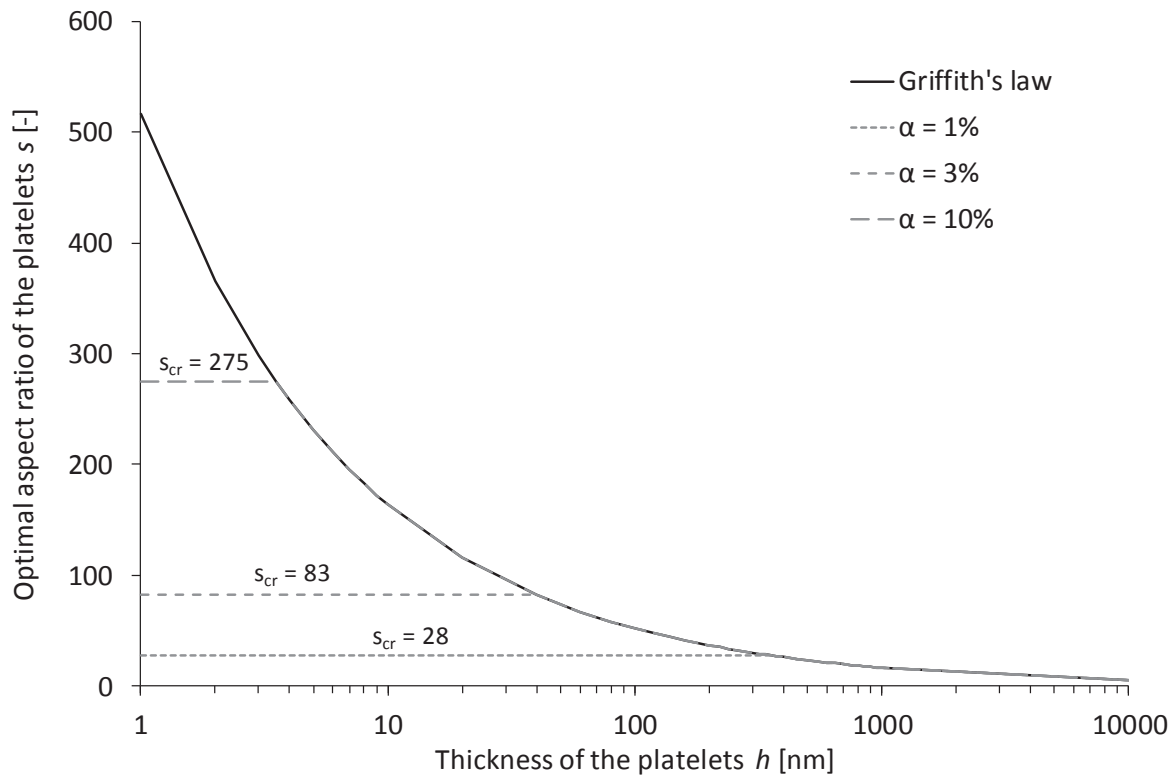


**Figure 2-3** Optimal aspect ratio for  $\beta$ -TCP platelets in function of their thickness and their intrinsic strength (1, 3 or 10 % of their stiffness).

## Composite strength and stiffness

In a composite structure with well oriented reinforcement elements and perfect bonding between both phases, the applied loads create stresses in the matrix that are transferred to the platelets by shearing [4]. The ultimate tensile strength of a composite,  $\sigma_{comp}$ , is a function of the platelets volume fraction,  $\phi_p$ , platelets aspect ratio,  $s$ , and tensile strength of both phases,  $\sigma_p$  and  $\sigma_m$  [9] (Figure 2-4).

$$\sigma_{comp} = \alpha \cdot \phi_p \cdot \sigma_p + (1 - \phi_p) \cdot \sigma_m \quad \text{Equation 8}$$

with

$$\text{for } s < s_{cr}: \quad \alpha = \frac{\tau_m \cdot s}{2 \cdot \sigma_p} \quad \text{Equation 9}$$

$$\text{or for } s > s_{cr}: \quad \alpha = 1 - \frac{\sigma_p}{2 \cdot \tau_m \cdot s} \quad \text{Equation 10}$$

In the case of  $s < s_{cr}$ , the continuous matrix yields before platelets break, leading to toughening mechanisms like platelet pull-out and matrix flow. For  $s > s_{cr}$ , the composite fails in a brittle way due to platelets fracture.

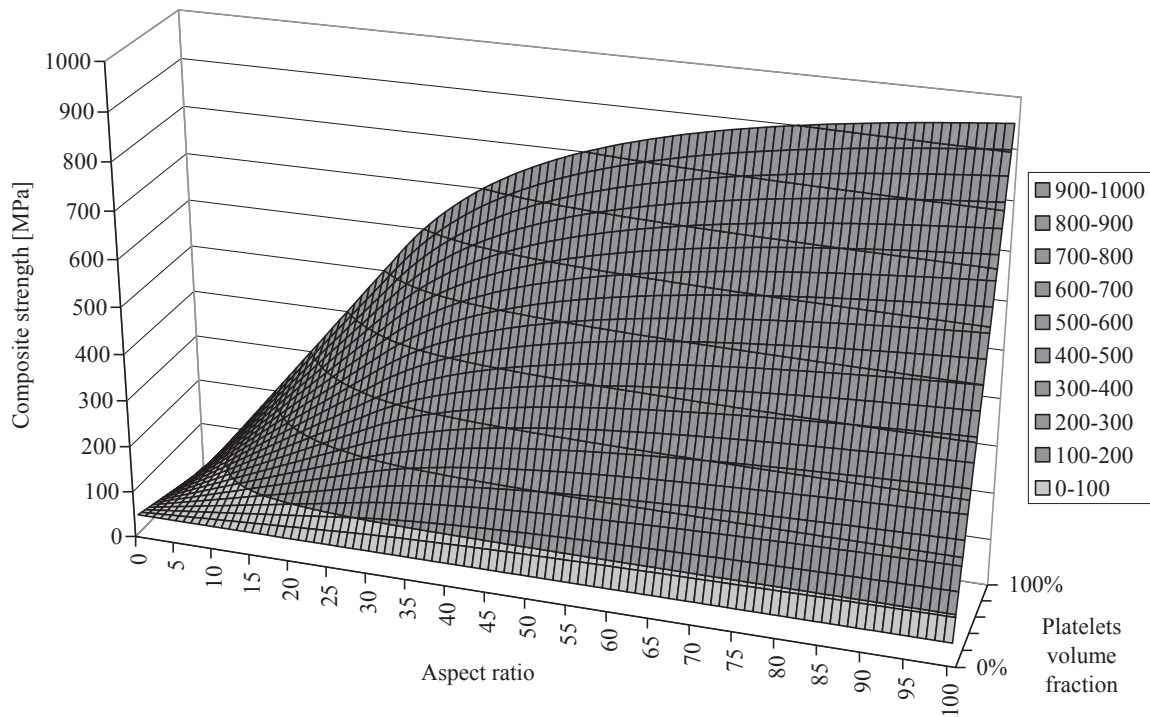


**Figure 2-4** Ultimate tensile strength of the composite for different platelets volume fraction and platelets with different aspect ratios.

Hence, considering platelets of a given strength  $\sigma_p$  and aspect ratio  $s$  smaller than the optimal aspect ratio  $s_{cr}$ , the strength of the composite  $\sigma_{comp}$  can be rewritten as

$$\sigma_{comp} = \frac{\tau_m \cdot s}{2} \cdot \phi_p + (1 - \phi_p) \cdot \sigma_m \quad \text{Equation 11}$$

or using equation 7

$$\sigma_{comp} = \frac{s}{2 \cdot s_{cr}} \cdot \phi_p \cdot \sigma_p + (1 - \phi_p) \cdot \sigma_m \quad \text{Equation 12}$$

The fraction of composite strength due to the platelets is thus proportional to the ratio between aspect ratio and optimal aspect ratio. Hence with an aspect ratio of 6, 75 vol-% of  $\beta$ -TCP platelets are necessary to reach 100 MPa in a chitosan matrix ( $\sigma_m = 50$  MPa,  $\tau_m = 40$  MPa [Bonderer 2008]). When the aspect ratio is increased to 20, the required ceramic fraction to reach 100 MPa drops to 15 vol-%.

More generally, the relative strength,  $\sigma_{rel}$  can be expressed as

$$\sigma_{rel} = \frac{\sigma_{comp}}{\sigma_m} = \frac{\tau_m \cdot S}{2 \cdot \sigma_m} \cdot \phi_p + (1 - \phi_p). \quad \text{Equation 13}$$

Since in theory, the shear strength of a polymer is about 1/3 of its tensile strength, the equation can be simplified:

$$\sigma_{rel} = \frac{S}{6} \cdot \phi_p + (1 - \phi_p). \quad \text{Equation 14}$$

With this simplified equation, it appears obvious that **ceramic platelets should have an aspect ratio larger than 6** to increase the strength of the composite structure, proportionally to their fraction.

Adding strong reinforcement particles to a softer matrix should not only increase the strength, but also the stiffness of the composite. The elastic modulus of a composite is a function of the modulus of the individual components and their respective fraction, but also of the overlapping degree of the reinforcing elements also has to be taken into account [20]. The higher the overlapping, the stiffer is the composite. On the opposite, the stiffness remains close to the one of the pure ceramic when there is no overlapping. Hypothesizing that 20 vol-% of CaP platelets can be added to a chitosan matrix, and placed such that they are close to overlap, the stiffness could be increase to 20 GPa whereas the pure chitosan only has a stiffness of about 3 GPa.

## Limitations

These calculations suppose that the particles are well dispersed and have a perfect bonding with the matrix. In addition, to reach high particle volume fraction, they have to be well organized, i.e. all in the same direction to allow maximum stacking. In his study, Bonderer [9] obtained considerable improvement at low (< 10 - 15 wt-%) platelet concentration, but lower than expected at higher platelets concentrations, due to difficulties like dispersion or poor bonding.

## References

- [1] Barthelat F, Tang H, Zavattieri PD, Li CM, Espinosa HD. On the mechanics of mother-of-pearl: A key feature in the material hierarchical structure. *Journal of the Mechanics and Physics of Solids*. 2007;55:306-37.
- [2] Barthelat F. Nacre from mollusk shells: A model for high-performance structural materials. *Bioinspiration and Biomimetics*. 2010;5.

- [3] Mayer G. New classes of tough composite materials-Lessons from natural rigid biological systems. *Materials Science and Engineering C*. 2006;26:1261-8.
- [4] Gao H, Ji B, Jäger IL, Arzt E, Fratzl P. Materials become insensitive to flaws at nanoscale: Lessons from nature. *Proceedings of the National Academy of Sciences of the United States of America*. 2003;100:5597-600.
- [5] Ji B, Gao H. Mechanical properties of nanostructure of biological materials. *J Mech Phys Solids*. 2004;52:1963-90.
- [6] Gao H. Application of fracture mechanics concepts to hierarchical biomechanics of bone and bone-like materials. *International Journal of Fracture*. 2006;138:101-37.
- [7] Zhang Z, Zhang Y-W, Gao H. On optimal hierarchy of load-bearing biological materials. *Proceedings of the Royal Society B: Biological Sciences*. 2010.
- [8] Ballarini R, Kayacan R, Ulm FJ, Belytschko T, Heuer AH. Biological structures mitigate catastrophic fracture through various strategies. *International Journal of Fracture*. 2005;135:187-97.
- [9] Bonderer LJ, Studart AR, Gauckler LJ. Bioinspired design and assembly of platelet reinforced polymer films. *Science*. 2008;319:1069-73.
- [10] Erb RM, Libanori R, Rothfuchs N, Studart AR. Composites reinforced in three dimensions by using low magnetic fields. *Science*. 2012;335:199-204.
- [11] Libanori R, Münch FHL, Montenegro DM, Studart AR. Hierarchical reinforcement of polyurethane-based composites with inorganic micro- and nanoplatelets. *Composites Science and Technology*. 2012;72:435-45.
- [12] Sommer MR, Erb RM, Studart AR. Injectable materials with magnetically controlled anisotropic porosity. *ACS Applied Materials and Interfaces*. 2012;4:5086-91.
- [13] Studart AR. Turning brittleness into toughness. *Nature Materials*. 2014;13:433-5.
- [14] Deville S, Saiz E, Nalla RK, Tomsia AP. Freezing as a path to build complex composites. *Science*. 2006;311:515-8.
- [15] Deville S, Saiz E, Tomsia AP. Freeze casting of hydroxyapatite scaffolds for bone tissue engineering. *Biomaterials*. 2006;27:5480-9.
- [16] Munch E, Saiz E, Tomsia AP, Deville S. Architectural control of freeze-cast ceramics through additives and templating. *Journal of the American Ceramic Society*. 2009;92:1534-9.
- [17] Bouville F, Maire E, Meille S, Van de Moortèle B, Stevenson AJ, Deville S. Strong, tough and stiff bioinspired ceramics from brittle constituents. *Nature Materials*. 2014.
- [18] Bar-On B, Wagner HD. Mechanical model for staggered bio-structure. *Journal of the Mechanics and Physics of Solids*. 2011;59:1685-701.
- [19] Bar-On B, Wagner H. Structural motifs and elastic properties of hierarchical biological tissues - A review. *J Struct Biol*. 2013;183:149-64.
- [20] Bar-On B, Wagner HD. The emergence of an unusual stiffness profile in hierarchical biological tissues. *Acta Biomaterialia*. 2013;9:8099-109.
- [21] Wagner HD, Lustiger A. Optimized toughness of short fiber-based composites: The effect of fiber diameter. *Composites Science and Technology*. 2009;69:1323-5.
- [22] Griffith AA. The Phenomena of Rupture and Flow in Solids. *Philosophical Transactions of the Royal Society of London Series A, Containing Papers of a Mathematical or Physical Character*. 1921;221:163-98.
- [23] Liang L, Rulis P, Ching WY. Mechanical properties, electronic structure and bonding of  $\alpha$ - and  $\beta$ -tricalcium phosphates with surface characterization. *Acta Biomaterialia*. 2010;6:3763-71.

[24] Espinosa HD, Rim JE, Barthelat F, Buehler MJ. Merger of structure and material in nacre and bone - Perspectives on de novo biomimetic materials. *Progress in Materials Science*. 2009;54:1059-100.

[25] Jackson AP, Vincent JFV, Turner RM. The Mechanical Design of Nacre. *Proceedings of the Royal Society of London Series B Biological Sciences*. 1988;234:415-40.



## Part I: Nacre-inspired brick-and-mortar structures

### CHAPTER 3:

## SYNTHESIS OF SUB-MICROMETER CALCIUM PHOSPHATE

### PLATELETS

#### ***Abstract***

Calcium phosphates (CaPs) are widely used as bone graft substitutes but are inherently brittle, hence restricting their use to mechanically protected environments. Combining them with a tough polymer matrix could potentially lead to a composite with load-bearing properties. However, the highest mechanical properties can only be achieved if the CaP particles possess very precise features: they should be uniform in size and shape, non-agglomerated, elongated and thin. The aim of the present study therefore was to assess a novel method to produce such particles. This involved the precipitation of CaP particles in ethylene glycol at moderate temperatures (90-170°C) and the variation of different reaction parameters (temperature, concentration, pH, etc) to study their influence on particle composition, size, shape and dispersion was studied. As a results, two main CaP phases were obtained as well-dispersed and highly uniform platelets in the form of: (i)  $\beta$ -tricalcium phosphate ( $\beta$ -TCP) hexagonal prisms and (ii) monetite (DCP) flat parallelepipeds. The size dispersion was the narrowest for  $\beta$ -TCP (standard deviation/mean <5%) whereas the aspect ratio was the highest for DCP (up to 25). In both cases, the thickness of the platelets was below 300 nm which should be ideal for the synthesis of strong CaP-based composites.

Published in part as:

Galea L, Bohner M, Thuering J, Doebelin N, Aneziris CG, Graule T. *Control of the size, shape and composition of highly uniform, non-agglomerated, sub-micrometer  $\beta$ -tricalcium phosphate and dicalcium phosphate platelets.* **Biomaterials**, 34, 6388-6401 (2013).

## Introduction

As presented in the introduction chapter, the first approach chosen here to obtain calcium phosphate based materials combining strength, toughness and bioresorbability was to build nacre-inspired brick-and-mortar composites. The first requirement was the availability of “bricks” and a “mortar”, i.e. ceramic platelets and polymeric glue. Concerning the last component, many biodegradable and tough polymers exist and could theoretically be tried without material development. However, biodegradable platelets are not common. The first part of this research project hence consisted in synthesizing the adequate “bricks”, i.e. calcium phosphate platelets with suitable size and shape, narrow size dispersion, and non-agglomerated. Good control of those features has never been achieved with current manufacturing processes for CaP.

CaP powders are usually obtained by either high temperature processes (solid-state reaction, thermal conversion) or wet chemical routes (precipitation, hydrolysis). When produced by sintering or by solid-state reaction at high temperature ( $\alpha$ -TCP,  $\beta$ -TCP, HA), the particles are agglomerated, have a low aspect ratio and broad size distributions [1]. Contrarily, when synthesized by precipitation, higher aspect ratios can be achieved but still a high degree of agglomeration and large size and geometry variations are observed [2-5]. Less agglomeration is generally reported for hydrothermally produced CaP particles. Needles or whiskers are commonly observed but the particle size distribution remains quite broad [6-11]. For example, Zhang and Darvell [6, 7] obtained needles with a size dispersion estimated at 0.2-0.3 (standard deviation/mean). Zhang et al. [11] obtained HA platelets with a length between 25 and 160 nm, i.e. a size dispersion (= standard deviation/mean) of about 0.5. Monodispersity is usually defined as  $< 0.10$  [12].

Recently Tao et al. [13, 14] proposed to synthesize single hexagonal  $\beta$ -TCP crystals by precipitation in ethylene glycol. This study describes the precipitation of nearly uniform, non-agglomerated, sub-micrometer CaP particles. The loose, homogeneous and well defined particles obtained by Tao et al. [13, 14] would allow a high packing density in a composite material, but would not be sufficient to efficiently reinforce a polymer matrix because of their low aspect ratio (3 to 4). In order to optimize the mechanical properties of the composite, it is necessary to increase the length and aspect ratio of the crystals. Therefore the aim of the present study was to extend Tao's work in order to synthesize CaP particles of controlled thickness, aspect ratio and composition, a low degree of agglomeration and high productivity. A more specific aim was to obtain CaP particles with considerably higher aspect ratios (typically  $> 20$ ) as those observed by Tao et al. (3 - 4), irrespective of the CaP crystalline phase. For that purpose, various parameters were systematically modified and the



yielded crystals were characterized extensively, while particular attention was paid to the reproducibility of the experiments.

## Materials and Methods

### Precipitation method

The precipitation reaction used here was inspired by Tao et al. [13]. Briefly, an ethylene glycol ( $C_2H_6O_2$ , Reag.Ph.Eur., art. n° 85512.360, VWR, Nyon, Switzerland) solution containing phosphate ions ( $Na_2HPO_4 \cdot 2H_2O$ , purum p.a., art. n° 71645, Fluka, Buchs, Switzerland) was poured into a pre-heated ethylene glycol solution that contained calcium ions ( $CaCl_2 \cdot 2H_2O$ , Reag.Ph.Eur., art. n° 1.02382, MERCK, Darmstadt, Germany). After 1.5 h reaction, the solution was cooled down and centrifuged at 4000 rpm for 30 min to separate the solid phase from the filtrate. The precipitate was then washed by mixing and centrifugation cycles in alternating demineralised water and ethanol ( $C_2H_6O$ , absolute 99.8%, art. n° G003, Grogg, Switzerland). After washing, the precipitate was dispersed again in ethanol and small amounts of this suspension were used for scanning electron microscopy (SEM), X-ray diffraction (XRD) and particle size measurements. The remains were dried at 30°C under vacuum (vacuum drying oven from Binder, Tuttlingen, Germany) for 24h. A standard experiment was defined as having a total volume of 70 mL, a titration rate of around 600 mL/min (= highest rate that can be achieved by manually pouring the phosphate solution into the calcium solution), a reaction temperature of 150 °C, a total precursors' concentration (sum of phosphate and calcium ions) of 16 mM, a reaction time of 1.5 h, a Ca/P molar ratio of 1.5 and a pH of the phosphate solution of 9.5 (adjusted at 95°C with NaOH, puriss. p.a., art. n° 71690, Fluka, Buchs, Switzerland) (Table 3-1).

### Reaction parameters

Several parameters were modified to achieve various aims (Table 3-1): (i) increase the productivity, by increasing the reagent volume (from 70 to 500 mL) or the total precursors concentration (from 1.6 to 64 mM) (ii) ease the production procedure by increasing the addition rate of the phosphate precursor (from 0.5 to 800 mL/min), or by reducing the production temperature below 100°C to allow the replacement of an oil bath with a water bath, save energy and avoid long heating times, or (iii) influence the composition, size and shape of the precipitated particles by varying the solution's pH (from 4 to 10), the precursors concentration (from 1.6 to 64 mM), the reaction temperature (from 90 to 170 °C), the reaction time (from 1.5 to 24h) or the Ca/P molar ratio (from 0.5 to 2.0).

**Table 3-1** Description of the experiments performed in this study to assess the effects of reaction volume, titration rate, reaction temperature, precursors' concentration and pH. The parameters that were varied in each sub-study are marked in bold. The standard experiment is the reference that was used for comparison in each sub-study.

		Volume [ml]	Precursors concentration [mM]	Titration rate [mL/min]	Reaction temperature [°C]	pH of PO <sub>4</sub> <sup>3-</sup> solution	Reaction time [h]	Ca / P molar ratio	n =
	Standard experiment	70	16	≈600	150	9.5	1.5	1.5	5
Study of the effect of...	... volume	<b>70, 500</b>	16	≈600	150	9.5	1.5	1.5	7
	... precursors concentration	<b>500</b>	<b>1.6, 4, 8, 16, 32, 64</b>	≈800	150	9.5	1.5	1.5	1 (2)
	... titration rate	<b>70, 500</b>	16	<b>0.5, 20*, ≈600-800</b>	150	9.5	1.5	1.5	2
	... reaction temperature	70	16	≈600	<b>90, 110, 130, 150, 170</b>	9.5	<b>1.5, 24</b>	1.5	5 (3@ 170°C)
	... pH	70	<b>16, 32</b>	≈600	<b>90, 150</b>	<b>4, 7, 7.5, 8, 9.5, 10</b>	1.5	1.5	1 (2)
	... reaction time	70	16	≈600	<b>90, 150</b>	<b>4, 9.5, 10</b>	<b>1.5, 24</b>	1.5	2
	... Ca / P ratio	70	16	≈600	150	9.5	1.5	<b>0.5, 1.0, 1.1, 1.2, 1.3, 1.4, 1.5, 1.67, 2.0</b>	2

\* and one experiment without stirring

## Characterization

Various characterization methods were applied to the particles. The size and morphology of the precipitate were analysed by scanning electron microscopy (SEM). Rietveld refinement of X-ray diffraction (XRD) measurements was used to quantify the relative amounts of crystalline phases. Finally, the particle size distribution (PSD) was measured by laser diffraction.

For SEM, a drop of the diluted ethanol suspension was spread on a SEM aluminium sample holder. After complete evaporation of the solvent, the samples were coated with a 10 nm thick platinum layer (sputter time 60 s at 40 mA) and observed with an EVO MA25 microscope (Zeiss,

Germany) using a voltage of 20 kV and a working distance of 7-8 mm. The particle size was assessed by image analysis (Image Access 11 Premium, Imagic Bildverarbeitung AG, Glattbrugg, Switzerland) of SEM pictures at 10'000 fold enlargement. The dimensions of at least 20 particles were used to calculate the mean diameter, length and width. As most particles were lying flat, only a minimum of 6 measurements was used to determine the particle thickness. The diameter,  $d$ , of hexagonal prisms was defined as the diameter of the inscribed circle (Figure 3-1, left); for parallelepiped particles, the length,  $l$ , and width,  $w$ , were measured as the length and width of the circumscribed rectangle (Figure 3-1, right). The aspect ratio,  $s$ , was defined as the diameter or the length divided by the thickness. The ratio between the standard deviation and the mean of the longest dimension (diameter or length) was used to estimate the size dispersion.

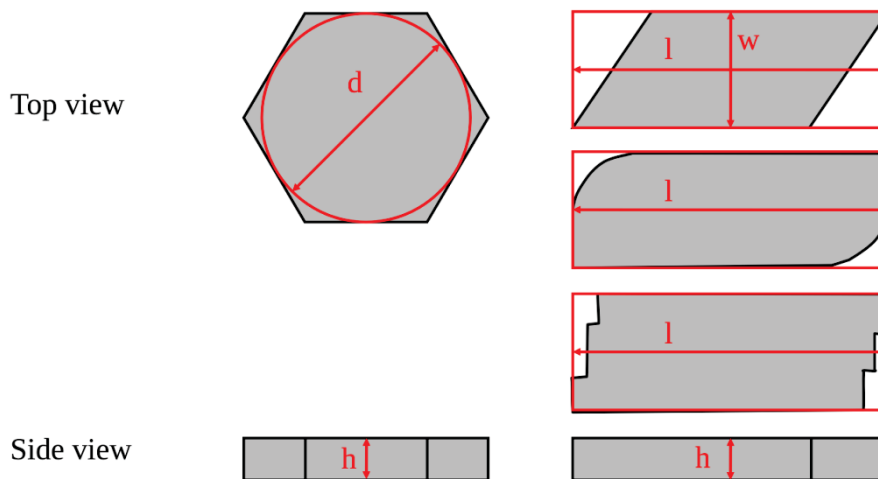


**Figure 3-1** Description of the measurement methods used to determine the dimensions of the hexagonal  $\beta$ -TCP platelets (left) and the parallelepiped DCP platelets (right). The aspect ratio is calculated as  $s=d/h$  or  $s=l/h$ .

For X-ray diffraction measurements (XRD), a concentrated ethanol suspension was dried on a glass plate, scratched off and spread on a silicon single crystal sample holder to minimize preferred orientation. XRD data were collected in reflective geometry on an X-Pert diffractometer (X'Pert Pro MPD, Panalytical, Almelo, the Netherlands). Ni-filtered  $\text{CuK}\alpha$  radiation, a step size of  $0.016^\circ$  and a measuring angle from  $4.01^\circ$  to  $59.99^\circ$   $2\theta$  were used for all XRD characterizations. Semi-quantitative phase analysis was done by Rietveld refinement and the FullProf.2k software (Version 5.00) [15] using a previously determined instrument resolution function. Crystalline models for  $\beta$ -tricalcium phosphate ( $\beta$ -TCP), monetite (DCP) and chlorapatite (Cl-HA) were taken from Dickens et al. [16], Dickens et al. [17] and Sudarsanan and Young [18], respectively.

Particle size distribution (PSD) was measured with a laser diffraction particle size analyser (LS 13 320, Beckman-Coulter, Krefeld, Germany). The concentrated ethanol suspension of platelets was added drop by drop into the reservoir of the device filled with ethanol until an adequate

concentration was reached. Sonication was applied for 30 s before each measurement with a sonication control unit (Beckman-Coulter, Krefeld, Germany).

### Statistical analysis of results

Dimension values are given as mean  $\pm$  one standard deviation. The significance of differences was evaluated by Student t-test or by ANOVA and was set at a maximum error risk of 5 %.

## Results

### Reproducibility of standard experiments

One of the aims of this study was to test the reproducibility of the synthesis. For that purpose, a synthesis in “standard” conditions was performed 5 times. The standard experiment (Table 3-1) led to hexagonal platelets with average diameter and thickness of  $853 \pm 73$  nm and  $164 \pm 11$  nm, respectively (Figure 3-2). As a result, the size dispersion was 0.09 and the average aspect ratio was  $5.5 \pm 0.7$ . However, it is important to mention that the size dispersion in each batch was lower than 0.05. Significant but small differences were not only seen in the mean size but also in the appearance of the platelets: variations of porosity and surface roughness were observed between batches (Figure 3-2).

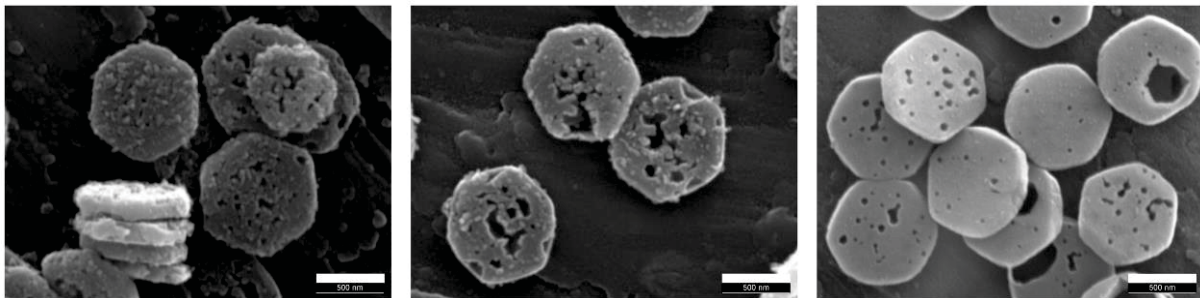


**Figure 3-2** Three representative batches of hexagonal platelets obtained with the standard conditions. Scale bar is 500nm.

According to laser diffraction, most of the particles were non agglomerated, but the presence of a few  $1.3 \mu\text{m}$  large particles was detected (Figure 3-3). The median particle size ( $D_{50}$ ) in number was  $0.33 \mu\text{m}$ , i.e. much smaller than the diameter measured on SEM images. This discrepancy might be explained by artefacts in laser diffraction measurements due to the non-spherical shape of the particles, whereas the model is based on spherical particles. Hence the obtained value is an equivalent diameter, not the absolute diameter. Indeed, laser diffraction is known to have problems estimating the size of particles with large aspect ratios, because the diameter depends on the

particle orientation. However, this does not impair comparison between experiments and identification of agglomerates.

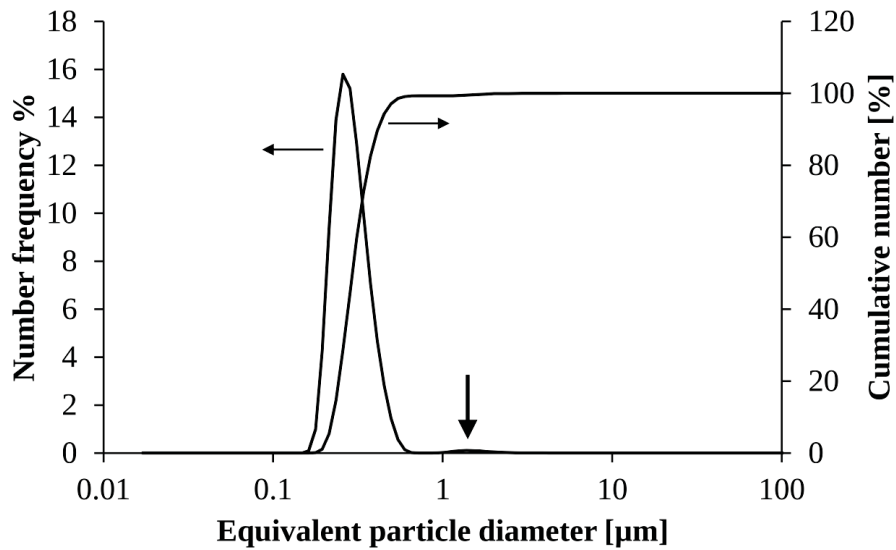


**Figure 3-3** Particle size distribution obtained by laser diffraction in volume percent. The arrow shows the small peak at 1.3 $\mu\text{m}$ .

The crystalline phase composition obtained by Rietveld refinement of XRD measurements was mainly  $\beta$ -TCP with traces (<1 %) of chloroapatite (Figure 3-4). However, the fit was difficult due to a preferential orientation of the  $\beta$ -TCP platelets along the c-axis (001 direction), as well as insufficient sample area and thickness on account of limited availability of material.

After drying, 20 to 30 mg of  $\beta$ -TCP platelets were obtained, corresponding to about 30-40 % of the total amount of calcium and phosphate ions initially present in the solution.

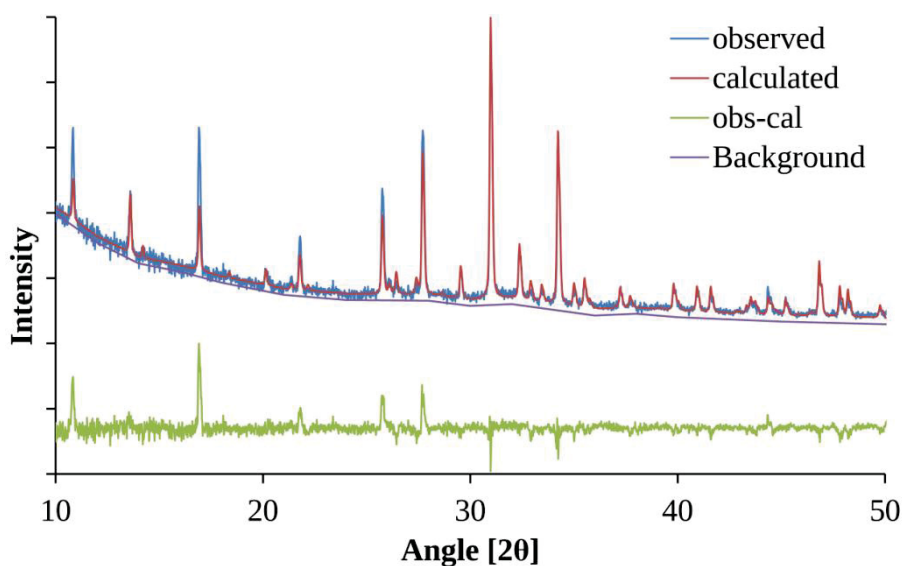


**Figure 3-4** Representative XRD of a standard experiment. The diagram corresponds to  $\beta$ -TCP with traces of chloroapatite. The differences (green line) between observed values (blue line) and the calculated model (red line) are due to a high crystalline orientation.

### Increase of the reagent volume to increase the productivity

A second aim of this study was to increase the productivity. One possibility to reach this goal was to increase the batch size. Fortunately, the change of reaction volume from 70 to 500 mL did not have a significant effect on the output morphology (Figure 3-5), however the production in 500 mL-batches better preserved the samples and reduced their porosity. The amount of obtained platelets was between 150 and 200 mg, which is a similar productivity than with smaller volumes, i.e. 30-40 % of the total amount of calcium and phosphate ions initially present in the solution.

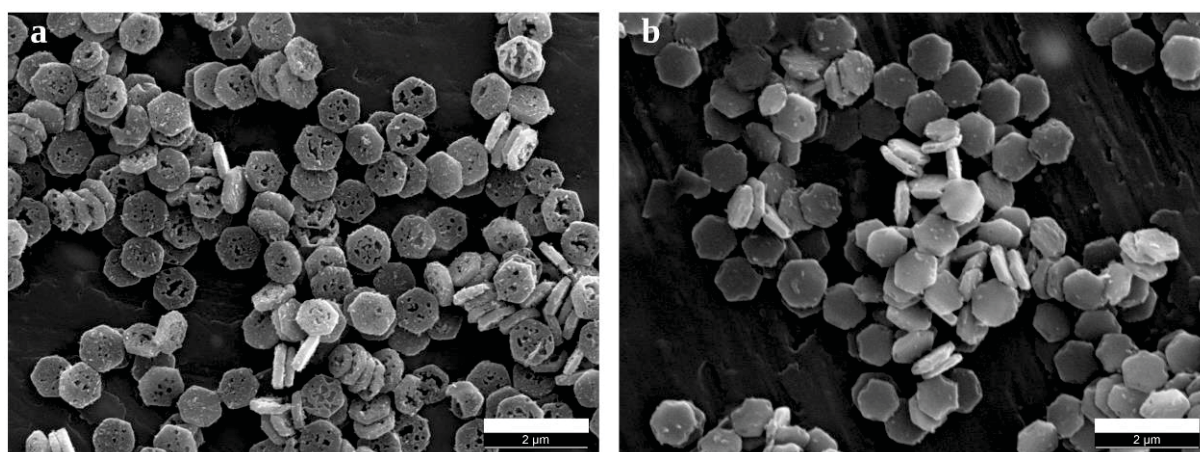


**Figure 3-5** Representative SEM images of batches with a) small volume (70ml); b) large volume (500ml). Scale bar is 2µm.

### Increase of the precursors concentration to increase the productivity and modify the particles

A second way to increase the productivity was to increase the precursors' concentration. However, since this parameter might also affect the particle appearance (geometry, size), a large range of concentrations was tested, from 10 to 400 % of the standard concentration (16 mM). At 1.6 mM, hollow regular octahedron particles were obtained (Figure 3-6a). At 4 mM, the obtained particles had a similar shape and were still hollow but larger (Figure 3-6b). The size further increased by raising the precursors' concentration, but from 8 mM the particles became hexagonal prisms and were not hollow anymore, but porous (Figure 3-6c and d). From 32 mM onwards, larger (> 1 µm) parallelepiped particles appeared (Figure 3-6e) and prevailed at 64 mM (Figure 3-6f). Furthermore fine particles covering the surface of the prisms could also be detected at 64 mM.

The hexagonal prisms diameter enlarged with increasing precursors' concentration while the thickness tended to decrease (Figure 3-7). In consequence, the aspect ratio increased from 1 to 10 (Figure 3-7). Contrarily, a change in concentration did not affect the size of the parallelepiped particles that appeared at 32 mM and 64 mM. These particles were  $3.3 \pm 0.9 \mu\text{m}$  long,  $1.3 \pm 0.4 \mu\text{m}$  wide and  $0.23 \pm 0.05 \mu\text{m}$  thick, leading to an aspect ratio of  $14 \pm 5$  and a size dispersion of 0.2.

The crystalline phase composition measured by Rietveld refinement of XRD results varied with the precursors concentration. Up to 16 mM, the samples solely consisted of  $\beta$ -TCP. At a concentration of 32 mM,  $\beta$ -TCP was mixed with 15 wt-% DCP and 45 wt-% chloroapatite and at 64 mM DCP was mixed with 33 wt-% chloroapatite and 1 wt-%  $\beta$ -TCP (Figure 3-8).

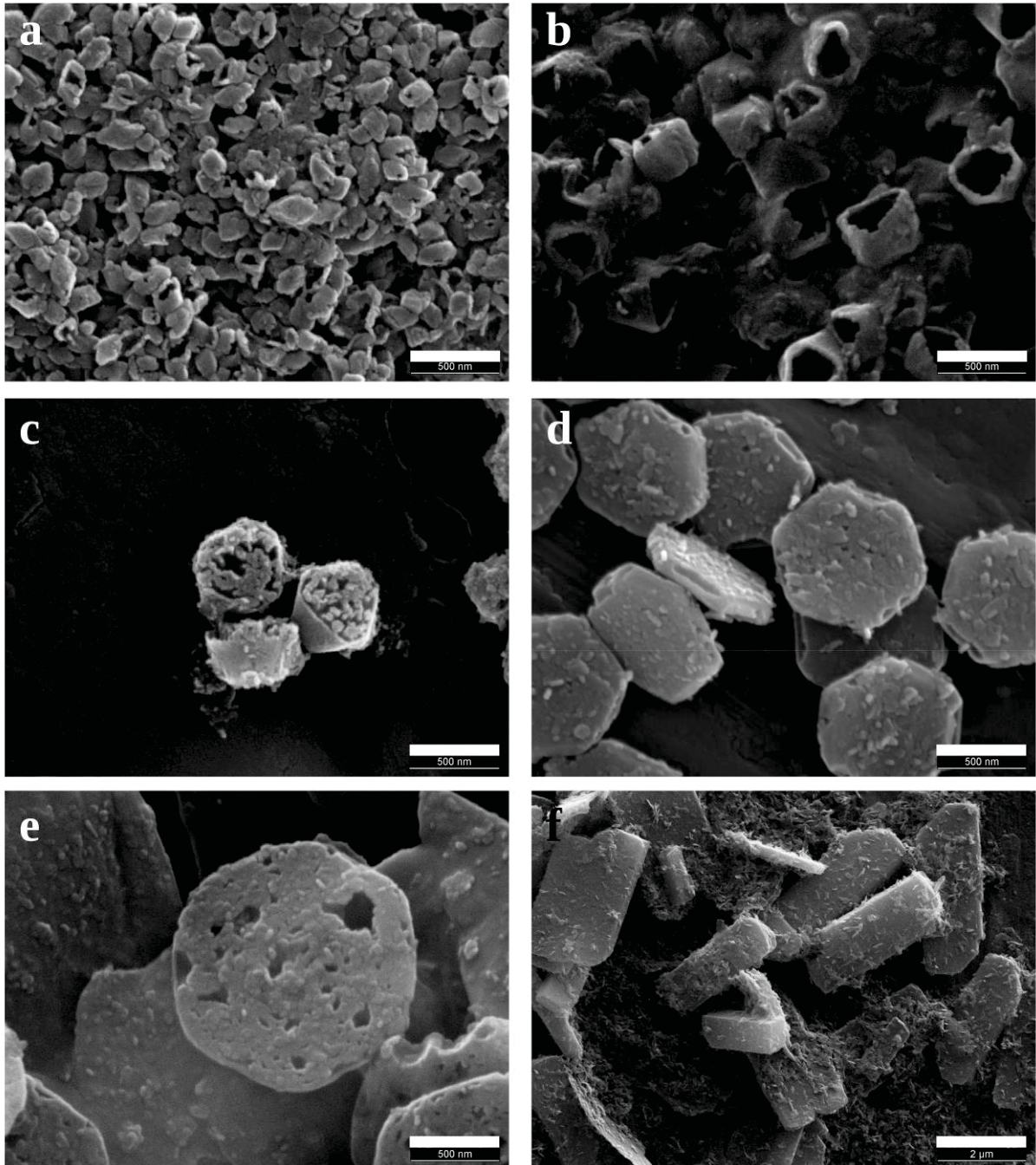


**Figure 3-6** Representative SEM images at different precursors concentration: a) 1.6 mM; b) 4 mM; c) 8 mM; d) 16 mM; e) 32 mM; f) 64 mM. Scale bar is 500 nm for a-e and 2  $\mu$ m for f.

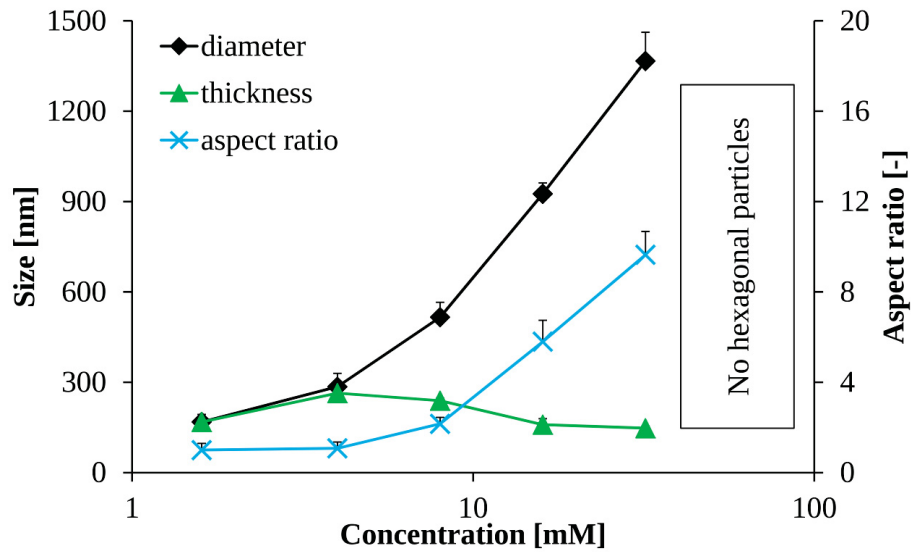


**Figure 3-7** Effect of the precursors concentrations on the dimensions of the hexagonal platelets: diameter (diamonds, left axis), thickness (triangles, left axis) and aspect ratio (cross, right axis).

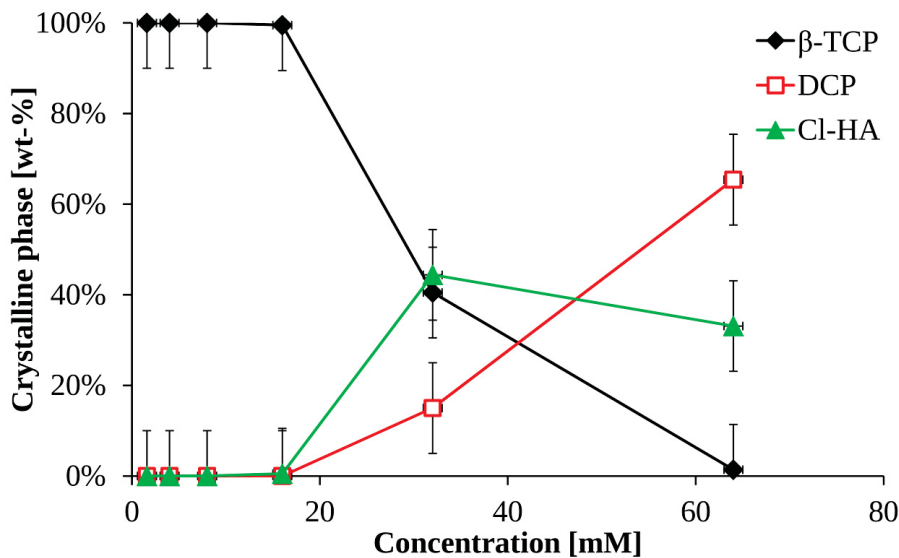


**Figure 3-8** Effect of the precursors concentrations on the crystalline phase.

### Increase of titration rate to simplify the process

In the aim to simplify the production process, the titration rate was increased to a maximum, i.e. the phosphate solution was added into the calcium solution at once, but not without beforehand studying the effect of this parameter on the size and degree of agglomeration of the particles. In addition, variations of addition rate were investigated at two different volumes, 70 and 500 mL, although the addition rate was not scaled with the volume. Hence, the titration rates are not directly comparable, since adding a solution at the same speed in a large volume increases slower the concentration than in a small volume. In consequence, for comparison, the titration rates were



reported to the volume and expressed in  $[\text{min}^{-1}]$ . The lowest titration rate of 0.5 mL/min in a large volume led to agglomerated, thick and round particles (Figure 3-9a); at all higher titration rates, hexagonal platelets were observed. The agglomeration decreased and the particle size and aspect ratio increased with increasing titration rate Figure 3-9b to e) until no more changes were observed at the highest titration rate between both volumes (Figure 3-9c and f). Displaying the size dispersion over the titration rate relative to the total volume showed a negative tendency (Figure 3-10a), i.e. the faster the addition rate, the narrower the size dispersion.

Without consideration of titration rate, the volume affected the particles appearance: when synthesized in a smaller volume, the platelets tended to be porous (Figure 3-9b-c), while their surfaces were denser and smoother with a larger volume (Figure 3-9e-f).

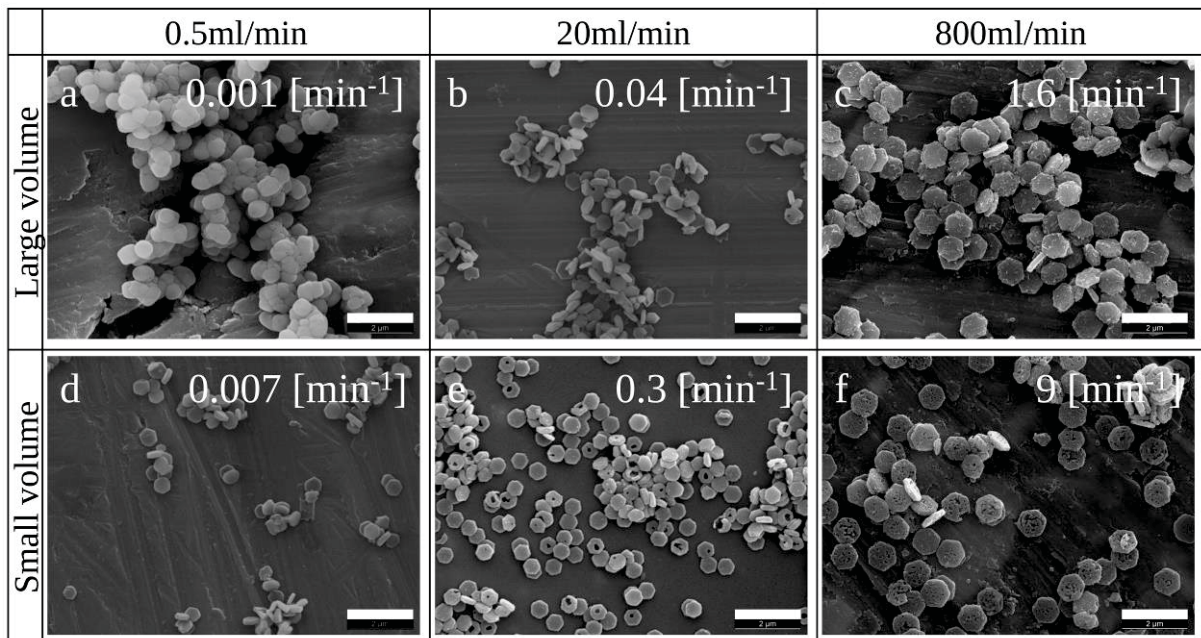


**Figure 3-9** SEM images of precipitates obtained in a) to c) large volume, d) to f) small volume, with a titration rate of a) and d) 0.5 mL/min; b) and e) 20 mL/min; c) and f) maximum titration rate (about 600 mL/min for small volume, about 800 mL/min for large volume). Scale bar is 2  $\mu\text{m}$ . The values on the pictures correspond to the titration rate reported to the volume.

PSD measurements by laser diffraction confirmed the broadening of PSD (Figure 3-9b) and the reduction of the median particle size with decrease of addition rate (results not shown). Importantly, after dispersion in ethanol and ultrasonication no agglomerates were measured.

Two experiments were conducted with an addition rate of 20 mL/min but without stirring. The resulting particle size distribution was 0.16 (Figure 3-11).

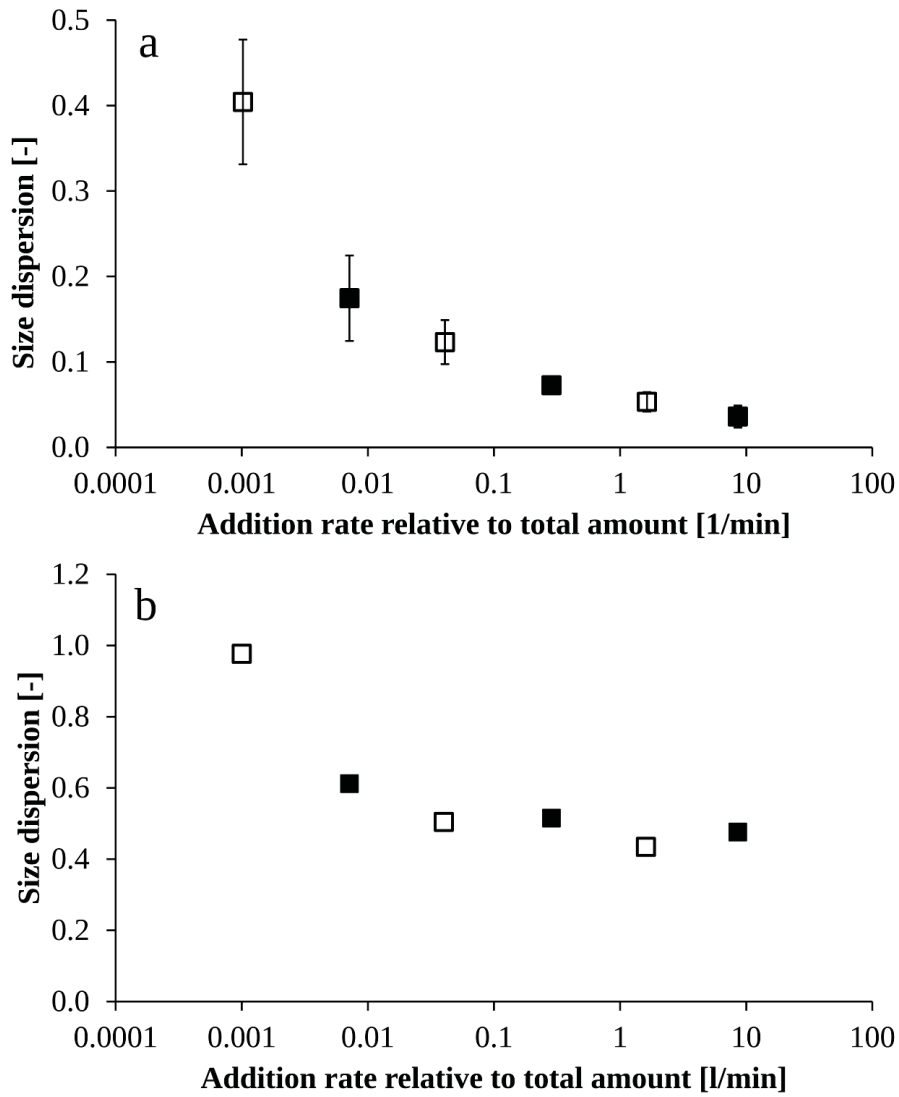


**Figure 3-10** a) Effect of the addition rate relative to total volume on the size dispersion measured by SEM images analysis; b) particle size distribution obtained by laser diffraction in function of addition rate. Narrowing (decrease of size dispersion) and displacement to higher values with increase of addition rate are obvious.

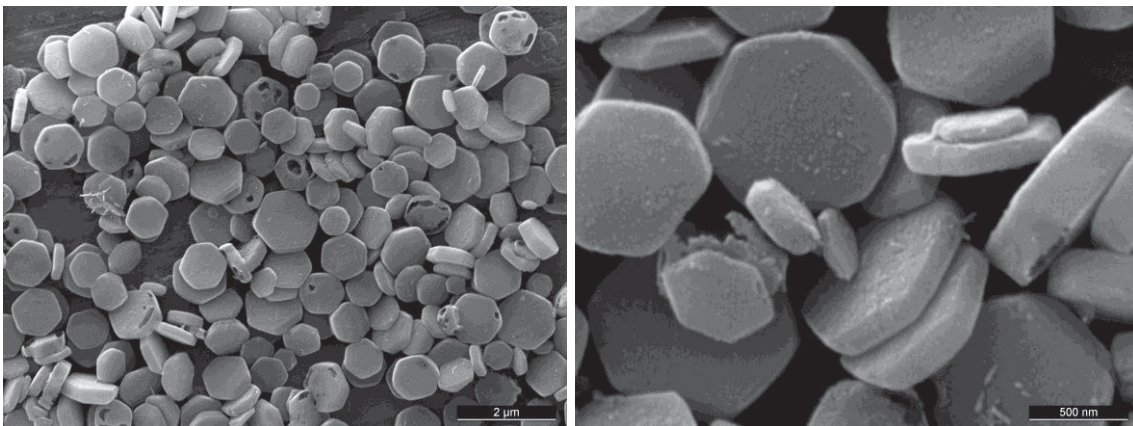


**Figure 3-11** Slow mixing of solution leading to large particle size distribution.

### Influence of temperature on the particles

Another way to ease the platelets synthesis is to decrease the reaction temperature. This would for instance avoid using an oil bath, save energy and reduce heating times. But the reaction temperature might affect the particles. Hence, the effect of a temperature change from 90 °C up to 170 °C was investigated. At 90 °C (Figure 3-12a), the samples mostly consisted of large parallelepiped platelets with blunt edges and a sheet structure. Some small circular to hexagonal platelets were also observed. Increasing the temperature decreased the relative amount of the parallelepiped particles while the shape of both types of particles became better defined, i.e. less round and more hexagonal in the case of the small ones and the large ones developed towards a rectangular and less sheet-like shape (Figure 3-12). No more parallelepipeds were observed at 150 and 170 °C.

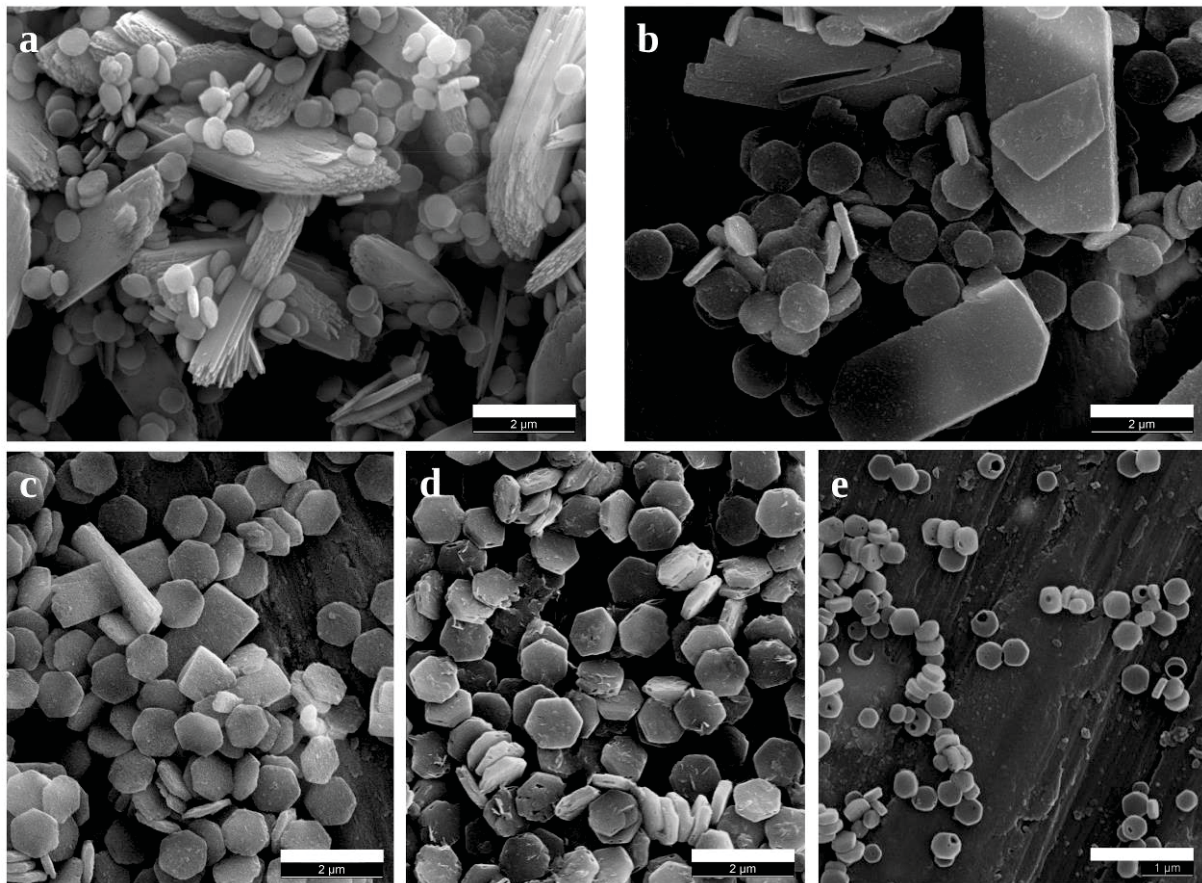


**Figure 3-12** Representative SEM pictures of samples synthesized at a) 90 °C; b) 110 °C; c) 130 °C; d) 150 °C; e) 170 °C.

Quantitatively, the length and width of the parallelepiped platelets were significantly smaller at 130 °C than at 90 and 110 °C (Figure 3-13a). Since their thickness did not vary significantly, the aspect ratio of the platelets significantly decreased from  $12 \pm 3$  to  $9 \pm 3$  (Figure 3-13a). The size dispersion in length and width also significantly decreased with the temperature from 0.30 at 90 °C to 0.14 at 130 °C. Similar observations were made with hexagonal platelets. The diameter of the

hexagonal prisms (Figure 3-13b) increased significantly from 600 to 800 nm between 90 and 110 °C and was stable between 110 and 150 °C. It then decreased to 600 nm at 170 °C, though this change was not significant ( $p = 0.14$ ). The thickness (Figure 3-13b) continuously increased with the temperature between 90 and 150 °C, from 120 nm to 180 nm and the decrease observed at 170 °C was not significant. However, the aspect ratio (Figure 3-13b) did not vary significantly between 90 and 170 °C. The size dispersion per batch of the hexagonal platelets was narrow for all temperatures and was the lowest at 130 and 150 °C (0.03 - 0.10 for single batches, 0.11 - 0.20 across multiple batches,  $n = 5$ ).

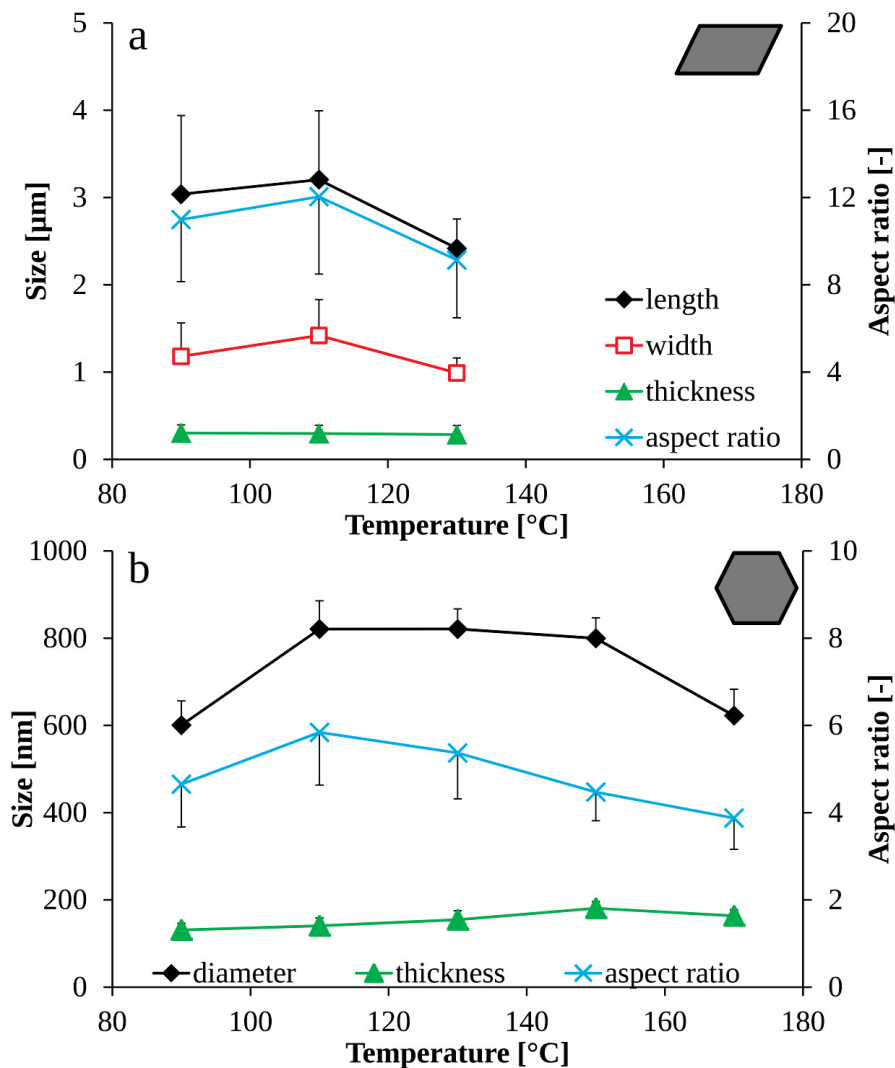


**Figure 3-13** Effect of the reaction temperature on the dimensions of a) parallelepiped crystals and b) hexagonal b-TCP platelets measured on SEM images. Left axis: Length, diameter and thickness. Right axis: aspect ratio.

According to Rietveld refinement of XRD data, most of the precipitates produced at 90 °C consisted of monetite (DCP) with about one third of  $\beta$ -TCP and a few percent of chlorapatite (Cl-HA). The amounts of DCP and Cl-HA decreased with increasing temperature and were negligible at 150 and 170 °C (Figure 3-14).

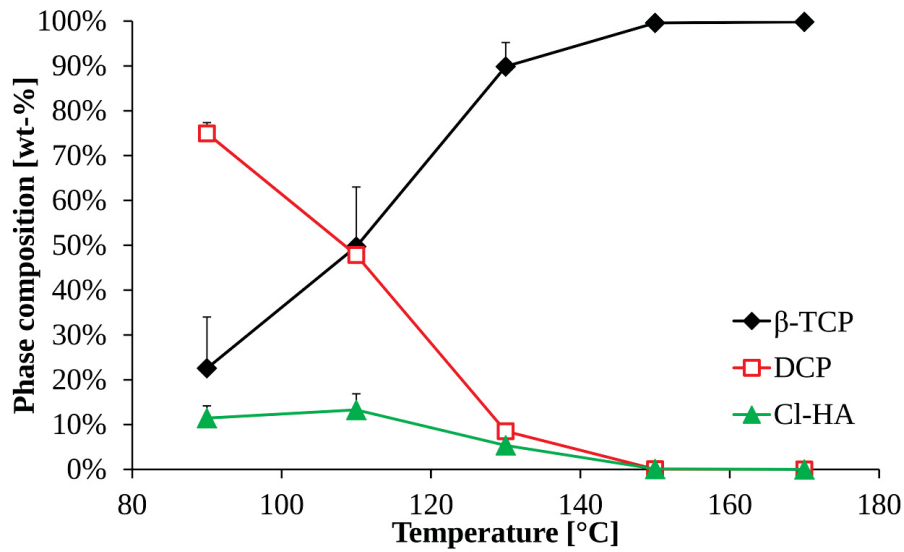


**Figure 3-14** Effect of the synthesis temperature on the crystalline phase (obtained from Rietveld refinement of XRD measurements).

The precursors' concentration and reaction temperature were investigated in order to increase the productivity and ease the production, respectively. These parameters were seen to affect the particles size, shape and composition. In both investigations, beside  $\beta$ -TCP hexagonal particles, monetite particles appeared which are usually more stable at lower pH values than  $\beta$ -TCP. Possibly, variations of pH might as well affect the particles shape, size and composition.

### Effect of the pH value on the particles

The effect of the pH was investigated from pH 4 to pH 10 at temperatures of 90 and 150 °C. The first difference from standard conditions was the appearance of a gel-like substance in the centrifugation tubes at the highest pH values (pH 9.5 and 10 at 90 °C and pH 10 at 150 °C), which was not observed at pH 9.5 and 150 °C. SEM observations revealed the formation of star-like particles at 90 °C and pH 4 (Figure 3-15a). At 90 °C, pH 7 elongated plate-like particles were formed. These particles tended to be thicker with better defined edges when further increasing the pH (Figure 3-15b and c). From pH 9.5 onwards, hexagonal platelets and a continuous phase started to appear (Figure 3-15d) and remained the only phase detected at pH 10 (Figure 3-15e). A similar behaviour was observed at a temperature of 150 °C. Specifically, parallelepiped platelets were observed at pH 4 and pH 7 (Figure 3-15f to g). At pH 8, hexagonal platelets already appeared (Figure 3-15h to j) and prevailed at pH 9.5 and pH 10. At pH 10, the continuous phase was noticed, as observed at 90 °C.

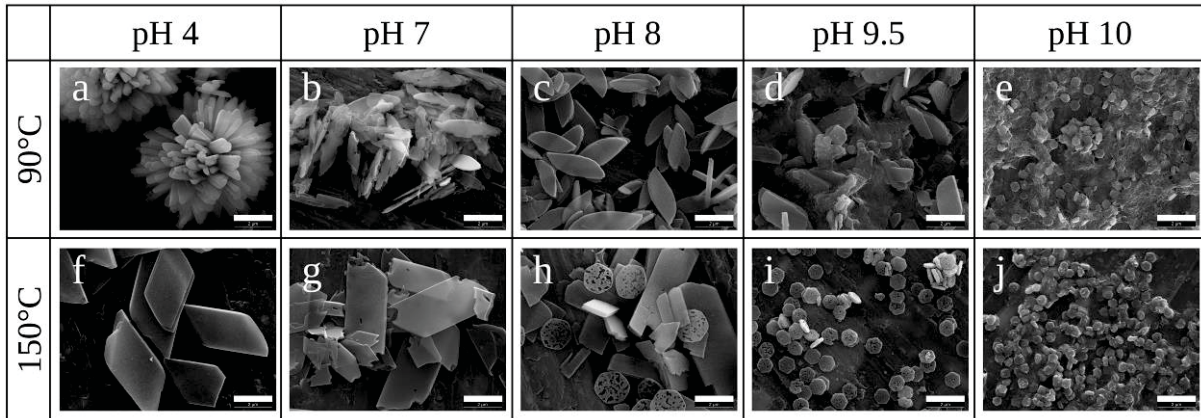


**Figure 3-15** SEM images of particles obtained at 90 °C (a-e) or 150 °C (f-j), and pH 4 (a+f), pH 7 (b+g), pH 8 (c+h), pH 9.5 (d+i) or pH 10 (e+j). Scale bar is 2 micrometers on all images.

The size of the different types of particles was measured on the SEM images. The star-like particles obtained at 90 °C and pH 4 had a diameter of  $2.8 \pm 0.7 \mu\text{m}$ . The size of the parallelepiped particles obtained at 90 °C varied significantly as a function of pH (Figure 3-16a). They were significantly longer and thinner at pH 7 than at pH 8 and pH 9.5 although the width and the size dispersion remained similar. Hence, the aspect ratio reached  $23 \pm 4$  at pH 7, but decreased to  $16 \pm 4$  at pH 8 and pH 9.5. Contrarily, the size of the parallelepiped particles obtained at 150 °C did not vary significantly with the change of pH, except for a 20 % decrease of width between pH 7 and pH 8 (Figure 3-16c). Turning to the hexagonal platelets, no variation of size was observed at 90 °C (Figure 3-16b). However, at 150 °C the hexagonal prisms shrunk with a pH increase (Figure 3-16d). At pH 8, all platelets laid flat, so their thickness could not be measured. Hence, a comparison of the aspect ratio was not feasible. However, the platelets seemed very thin, possibly thinner than at higher pH values. Consequently, the aspect ratio was likely higher than 10.

XRD measurements and Rietveld refinement revealed that at 90 °C, up to a pH of 8, the samples consisted of pure monetite. An increase of the pH led to a mix of monetite and  $\beta$ -TCP and finally at pH 10 to a mix of  $\beta$ -TCP (77 wt-%) and chloroapatite (23 wt-%) (Figure 3-17). The larger diffraction peaks obtained with this sample and the broad and high background indicated the presence of an amorphous phase (Figure 3-18), probably the continuous phase observed in SEM. Rietveld refinement indicated a strong preferential orientation of both types of crystals, explaining the observed difference in intensity (Figure 3-18). The same phase change from monetite to  $\beta$ -TCP was observed at 150 °C, but slightly shifted towards lower pH values (Figure 3-17). At high pH values, an amorphous phase also appeared, but without occurrence of chloroapatite.

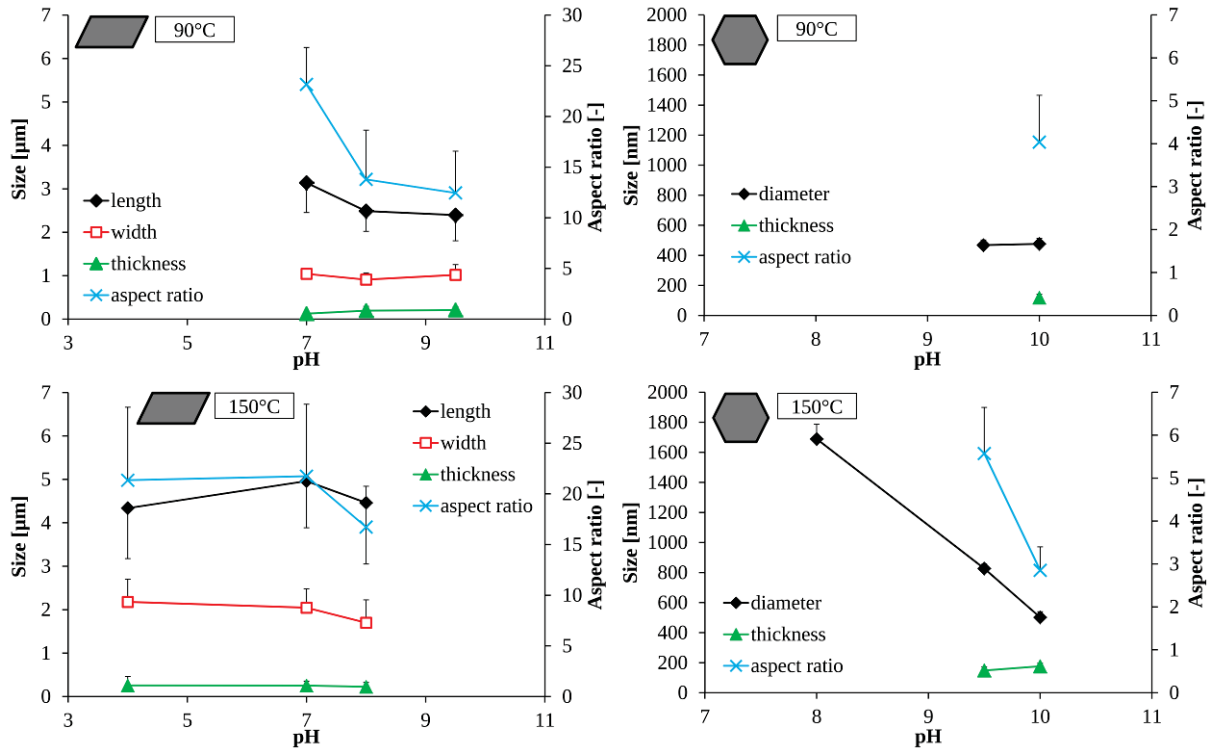


**Figure 3-16** Effect of the pH on the dimensions of a) and c) parallelepiped crystals and b) and d) hexagonal crystals at a) and b) 90 °C and c) and d) 150 °C: diameter or length (diamonds, left axis), width (squares, left axis), thickness (triangles, left axis) and aspect ratio (cross, right axis).

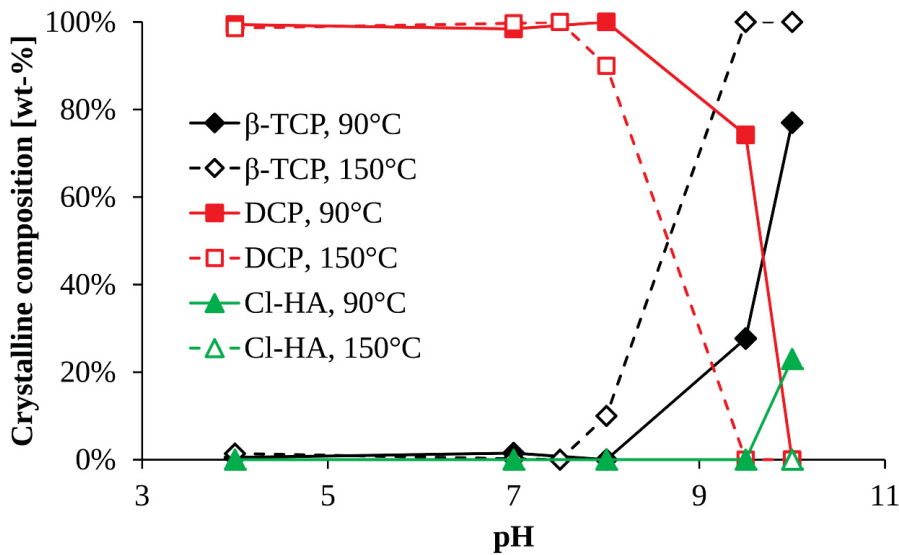


**Figure 3-17** Effect of the pH on the crystalline phase: at low pH, monetite is formed.  $\beta$ -TCP then appears, at lower pH at 150 °C (dashed lines) than at 90 °C (continuous lines). Hence 100 %  $\beta$ -TCP is reached with a pH of 9.5 at 150 °C whereas a slightly higher pH (10) is required at 90 °C to avoid DCP.

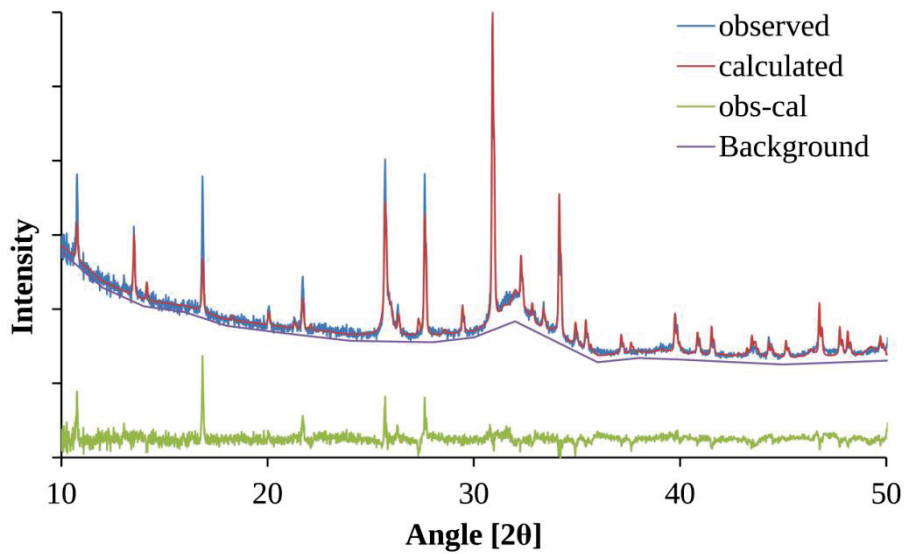


**Figure 3-18** XRD diagram of the sample precipitated at 90 °C pH 10. The observed diffraction diagram (blue line) was fitted with a calculated model (red line). The large differences (green line, “obs-cal”) at peak positions are due to a strong crystalline orientation. The  $\beta$ -TCP and chlorapatite peaks were identified and refined with Rietveld analysis. The broad peaks and the high background (purple line) indicate the presence of an amorphous phase.

Since an increase of the pH decreased the occurrence of the DCP phase, 2 experiments were conducted at 150 °C with a concentration of 32 mM and pH 10 to compare it with the results obtained at pH 9.5 (Figure 3-6e and Figure 3-8). SEM observations showed and impaired precipitation with the presence of amorphous phase (Figure 3-19).

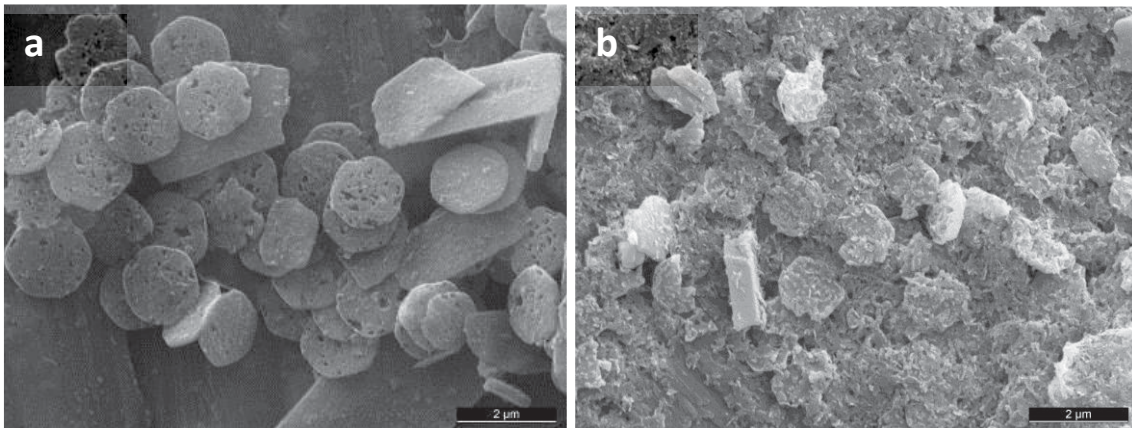


**Figure 3-19** With a concentration in precursor of 32 mM, a) at pH 9.5, precipitation of hexagonal  $\beta$ -TCP platelets and DCP parallelepipeds occurred b) but was hindered at pH 10. Scale bar is 2 $\mu$ m.

### Effect of a longer reaction time on the particle stability

In standard conditions, the platelets did not grow further when increasing the reaction time from 1.5 to 24h, suggesting that the reaction was terminated very rapidly (Figure 3-20). Similarly, the particles shape did not change, neither the crystallinity, as observed on XRD diagrams. Positively, the platelets were not more agglomerated after 24h than after 1.5h.



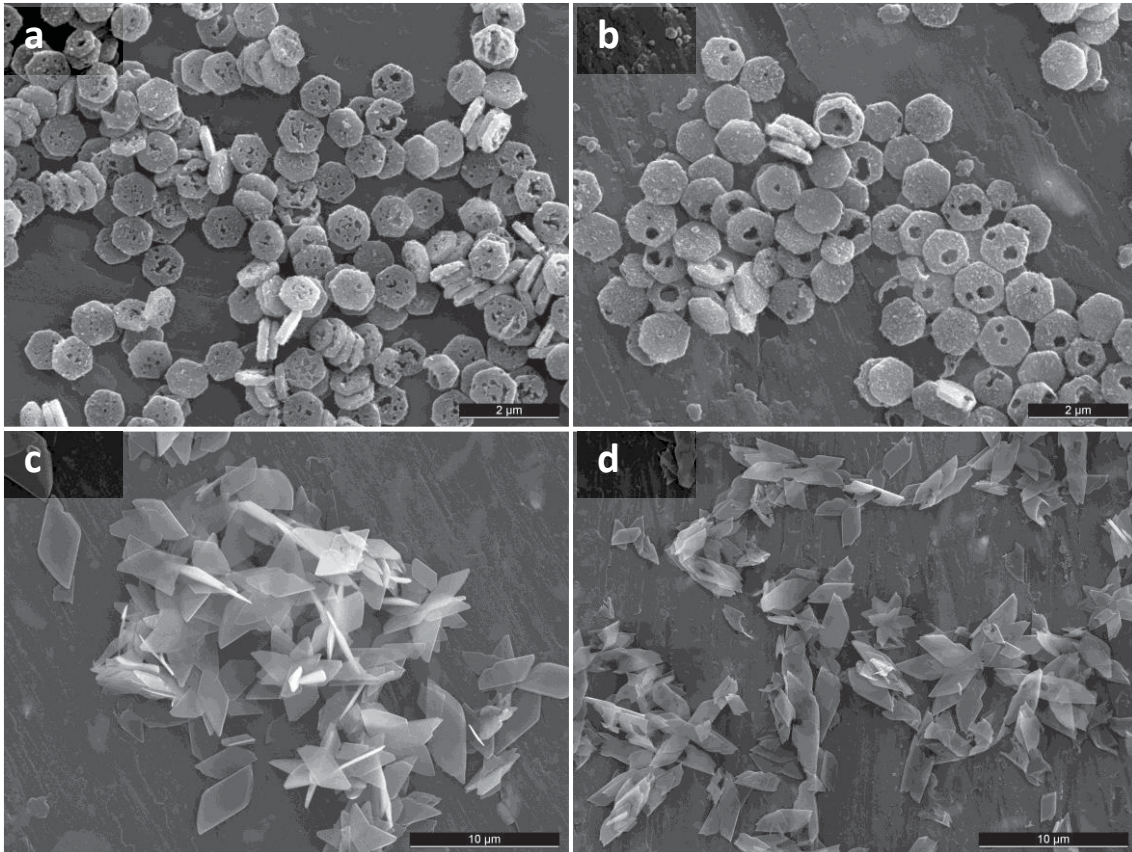


**Figure 3-20** Samples of b-TCP hexagons (a and b) and DCP parallelepipeds (c and d) after 1.5h of reaction (a and c) and 24h of reaction (b and d). Scale bars are 2 μm in a and b and 10 μm in c and d.

At 90 °C, increasing the pH to 10 allowed avoiding the DCP phase, but some amorphous phase remained after 1.5h of reaction (Figure 3-15e and Figure 3-17). To verify if a prolonged reaction would lead to a complete crystallization, an additional precipitation experiment was done during 24h at 90 °C, pH 10. This effectively led to a complete crystallization, but DCP was also formed (Figure 3-21).

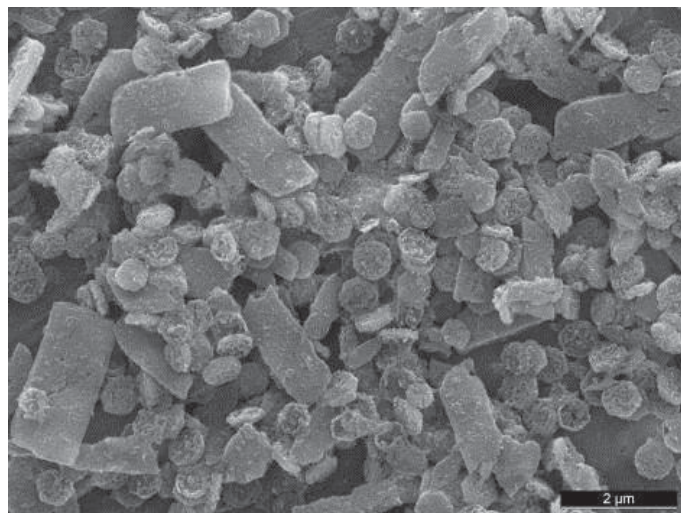


**Figure 3-21** Results of the prolonged (24h) precipitation at 90 °C, pH 10.

### Study of the influence of variations of the Ca/P molar ratio

A change of Ca/P molar ratio had either no massive effect on the particles size and shape or impaired completely the crystallization. Indeed, a Ca/P ratio of 0.5 and 1.0 led to an amorphous gel-like substance but no crystallization occurred (Figure 3-22). With and above a Ca/P ratio of 1.1 hexagonal  $\beta$ -TCP platelets were exclusively obtained (Figure 3-22).

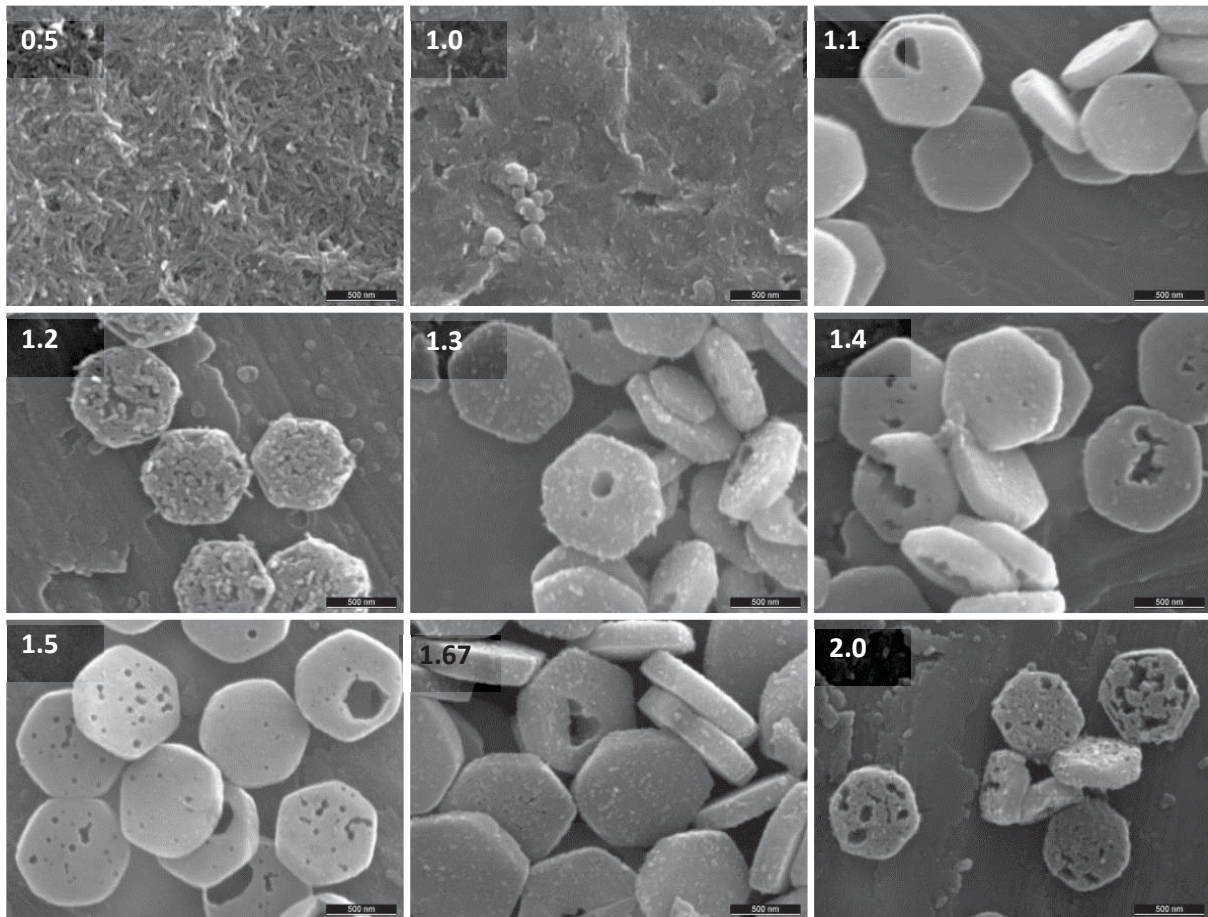


**Figure 3-22** SEM images of reaction products at different Ca/P ratios (indicated on the corner of the images). The scale bar is 500nm

The particle size did not vary significantly between a Ca/P ratio of 1.1 and of 1.5. The largest diameter (925 nm) was obtained at Ca/P = 1.67 and the smallest (625 nm) at Ca/P = 2.0 (blue diamonds in Figure 3-23). The thickness was always under 200 nm (green triangles in Figure 3-23). In consequence, the aspect ratio was similar, i.e. 5.5, between Ca /P ratios of 1.1 and 1.67 and smaller with a Ca/P ratio of 2.0 (purple crosses in Figure 3-23). No new crystalline phase was observed. Mix with Ca/P ratios smaller than 1.1 did not crystallized (Figure 3-22). Hence,  $\beta$ -TCP could crystallize with a calcium ions lack up to 25%, but not further.

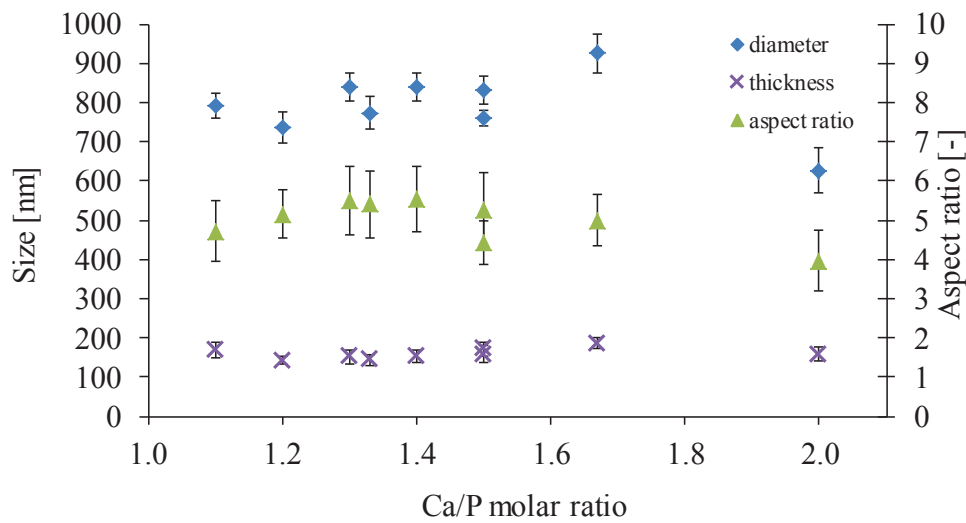


**Figure 3-23** Diameter (squares, left axis), thickness (diamonds, left axis) and aspect ratio (triangles, right axis) of the platelets according to the Ca/P molar ratio.

## Discussion

The aim of this study was to produce reproducible CaP platelets of controlled thickness, aspect ratio and composition, a low degree of agglomeration and high productivity. For this purpose,  $\text{CaCl}_2$  and  $\text{Na}_2\text{HPO}_4$  salts were dissolved in ethylene glycol and these solutions were mixed and aged under controlled conditions. The effects of several parameters were investigated: pH, temperature, titration rate and concentration of precursors. The particles composition and dimensions were measured.

### Reproducibility

Before investigating the effect of several parameters on the yielded particles, it was important to verify the reproducibility of the experiment. This was done by replicating 5 times the standard experiment (Table 3-1), which yielded hexagonal  $\beta$ -TCP platelets (prisms).

A high reproducibility between replicas was found (Table 3-2). Some size variations were observed from batch to batch, but these differences remained small (size dispersion < 10%). When looking at the literature, the particles produced here were slightly larger and thinner (diameter =  $853 \pm 73$  nm, thickness =  $164 \pm 11$  nm, Figure 3-2) than those obtained by Tao et al. (diameter = 750 - 800 nm, thickness = 200 - 250 nm [13]), but differences were marginal. Besides the variations of size, differences of surface appearance of the  $\beta$ -TCP crystals were noticed, particularly at different batch volumes: in large batches, the platelets were very smooth (Figure 3-5b), whereas platelets produced

in small volumes were rough or even porous (Figure 3-2 and Figure 3-5a). The pores and roughness were similar to the dissolution patterns observed by Tao et al. [13]. This suggests that the  $\beta$ -TCP platelets were dissolved during washing. In fact, the differences observed from batch to batch and in different conditions can be easily explained by the fact that the washing conditions were not the same for all samples. Indeed, some batches could be cleaned directly after precipitation, while others had to be stored for a while in solution (water or ethanol) before centrifugation due to lab use constraints. Moreover, the washing procedure was not the same for large and small batches. Specifically, the platelets produced in large volumes were 3 times more concentrated during washing.

Despite these variations, the reproducibility of the synthesis method can be considered to be excellent, even if different synthesis conditions are used (Table 3-2), not only in terms of particle size but also in terms of chemistry.

**Table 3-2** Dimensions of the platelets obtained with different volumes and titration rates (n=1). The titration rate can be expressed either as volume of solution per unit of time (ml/min) or relatively to the total volume (min<sup>-1</sup>).

Volume [mL]	Titration rate		n	Diameter [nm]	Size dispersion	Thickness [nm]	Aspect ratio
	[mL/min]	[min <sup>-1</sup> ]					
70	0.5	0.007	1	447 ± 95	0.21	135 ± 30	3.3 ± 1.4
70	20	0.3	1	527 ± 38	0.07	147 ± 15	3.6 ± 0.6
70	600	9	5	853 ± 33	0.04 ± 0.01	164 ± 18	5.0 ± 0.7
500	0.5	0.001	1	415 ± 178	0.43	415 ± 178	1.0 ± 0.9
500	20	0.04	1	501 ± 53	0.11	128 ± 16	3.9 ± 0.9
500	800	1.6	6	844 ± 45	0.05 ± 0.01	151 ± 19	5.6 ± 1.0

## Productivity

One of the problems related to the production method used here, is the very low productivity of the reaction. Indeed, only 0.3 - 0.4 g/L CaP particles ( $\beta$ -TCP and/or DCP) were produced in the best conditions. Concerning  $\beta$ -TCP, obtained at high pH, an attempt was made to increase the concentrations, but the solubility of the phosphate precursor is limited to about 1.33 M in ethylene glycol. Furthermore, a concentration increase at high pH led to a change of precipitated phase: whereas  $\beta$ -TCP was the main phase obtained in standard conditions (16 mM), only a mixture of DCP and apatite was obtained at 64 mM (Figure 3-12 and Figure 3-13). Since DCP is a more acidic phase than  $\beta$ -TCP, it was supposed that the use of a higher pH might hinder DCP precipitation and favour  $\beta$ -

TCP. Unfortunately, an increase of the pH at pH10 impaired the precipitation, maybe due to competition between free OH groups in the solution and the stabilizing OH groups of the ethylene glycol molecules (Figure 3-19). Nevertheless, it was possible to increase the reaction volume from 70 to 500 mL without significant changes in particle size, size dispersion and agglomeration (Figure 3-5). In other words, upscaling the precipitation synthesis seems to be feasible. It is surprising that the yield is only 30 % at 16 mM, even though precipitates were still observed at 1.6 mM. If precipitation is observed for a solution of 1.6 mM, a 10-fold increase of the concentration would be expected to result in a yield much higher than 30 %. This suggests that the solubility of  $\beta$ -TCP is very low in ethylene glycol, but that a lot of precipitates must be lost during processing, for example during centrifugation. For comparison, large batches at 150 °C and low pH (pH 4) also yielded 0.3 - 0.4 g/L of DCP platelets. However the precursors' concentration could easily be doubled without occurrence of another crystalline phase and the productivity was increased to 0.8 - 0.9 g/L without influence on crystal size and composition.

### CaP crystal shape

Since the CaP platelet synthesis was reproducible and feasible in reasonable amounts, the next important requirement was first to relate crystal shape and composition, and then explain the crystal habit based on the crystalline structure. SEM observations (Figure 3-8 and Figure 3-14) suggest that the DCP crystals identified by XRD always crystallized in the form of parallelepipeds, whereas the  $\beta$ -TCP crystals precipitated as almost regular octahedrons or hexagonal prisms. Regarding the crystal habit, DCP crystallizes in the triclinic crystal system and is known to adopt a parallelepiped shape [19] as observed here. The crystal habits of  $\beta$ -TCP crystals are more surprising. The lattice system of  $\beta$ -TCP is rhombohedral which belongs to the trigonal crystal system and the hexagonal crystal family. The most common crystal form of whitlockite – the naturally occurring phase isostructural to  $\beta$ -TCP – is represented in Figure 3-24a. The [001] planes can become regular hexagons (Figure 3-24b) if the side faces (e.g. [104] and [102] planes) grow at similar rates. Similarly, platelets are formed when the [001] planes (identified by preferred orientation in XRD) have the slowest growth rate. Hexagonal prisms crystalline habits are thus not surprising. No SAED patterns were measured in the present study, hence the side planes were not identified. Tao et al. stated that the side faces of the hexagons were perpendicular to the [001] planes [14], but considering the rounded edges observed in the present study on SEM images and the crystal habit of whitlockite, the planes of the crystal side faces might be other family planes.

The formation of regular octahedrons is more surprising in a trigonal crystal system. It is assumed that the crystals are pseudo-octahedrons and that they are formed when the [001] planes and some of the side planes grow slowly at equal growth rates (Figure 3-24c). The indices of those

planes were not investigated here. Tao et al. proposed [111], [101] or [001] planes. However, these authors did not obtain  $\beta$ -TCP octahedrons by changing the precursor concentration but by using other precursors.

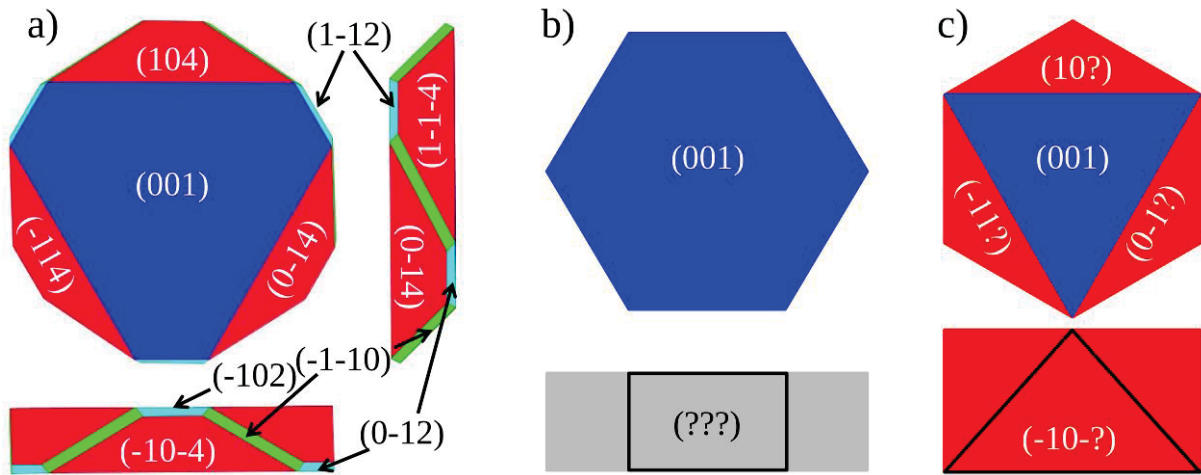


**Figure 3-24** a) Trigonal crystal habit of the whitlockite (webmineral.com) from the top and the sides. Indices of dark blue faces is (001), of red is (104), of cyan is (102) and of green is (110). b) hexagonal prisms derived from the trigonal crystal habit in a, top and side view. c) regular hexagon derived from the trigonal crystal habit in a, top and side view.

In the present study, there is a slow transition from a globular / compact shape at low concentration (pseudo-regular octahedrons) to a planar shape at high concentration (hexagonal prisms; Figure 3-6). At intermediate concentration (8 mM), transitional shapes between hexagonal prism and regular octahedron were observed. This concentration dependence of the crystal shape is typical for precipitation reactions [20]. At low concentrations the shape is dominated by nucleation requirements (nearly spherical but still faceted shapes, minimizing the surface per volume). According to [21], an increase of the supersaturation favors the growth of specific crystal faces, leading to more elongated crystals.

Tao et al. explained the precipitation of  $\beta$ -TCP in the form of hexagonal prisms in the solution  $\text{CaCl}_2\text{-Na}_2\text{HPO}_4\text{-EG}$  by surface energy calculations [14]. They showed that the octahedron formation in  $\text{CaCl}_2\text{-Na}_2\text{HPO}_4\text{-EG}$  solution is thermodynamically unfavorable for its relatively large interfacial energy, but the smallest specific surface of the octahedral crystals is apparently favored at lower concentrations. However, these authors did not make calculations using different precursor concentrations.

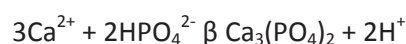
For both phases, the particles became more angular and adopted a more idiomorphic crystal form with increasing temperature (Figure 3-12), similar to the observation of Tao et al. for  $\beta$ -TCP [14]. However, the particles size and shape did not change when the reaction time was increased from 1.5 h to 24 h (Figure 3-20), suggesting that the hexagonal and parallelepiped shapes were

already the least energetic configuration for  $\beta$ -TCP and DCP crystals, respectively. Moreover, ethylene glycol is an efficient medium to disperse  $\beta$ -TCP and DCP particles since the particles were stable in size and shape over time and the agglomeration rate did not increase after 24h of reaction.

### Crystal purity

Four different CaP phases were obtained in all precipitation experiments performed in this study: DCP,  $\beta$ -TCP, chlorapatite, and an amorphous phase. From these four CaP phases, DCP and  $\beta$ -TCP constituted almost 100 % of all precipitates retrieved in the various experiments (Figure 3-4, Figure 3-8, Figure 3-14 and Figure 3-18). Except for a few exceptions, as at high concentrations, the other phases only occurred in trace amounts.

Contrary to  $\beta$ -TCP, DCP formation was favored at a low pH value (Figure 3-17), low temperature (Figure 3-14, and even at high pH: Figure 3-21) and a high concentration (Figure 3-8). The predominance of DCP at low pH values is logical considering the respective solubilities of DCP and  $\beta$ -TCP phases. For example, Vereecke and Lemaître [22] calculated that in the system  $\text{Ca}(\text{OH})_2\text{-H}_3\text{PO}_4\text{-KOH-HNO}_3\text{-CO}_2\text{-H}_2\text{O}$ , DCP was more stable than  $\beta$ -TCP below a pH value of 6.3 - 6.4. Interestingly, their data also showed that the pH stability range of  $\beta$ -TCP (compared to DCP) enlarged with an increase of temperature. Assuming that this type of behavior can be extrapolated to ethylene glycol,  $\beta$ -TCP formation should not only be favored at high pH but also at high temperature, which was observed in our study. However, it is questionable to extrapolate data from an aqueous to a non-aqueous system. Indeed, whereas three CaP phases precipitate in physiological conditions (DCP at low pH (< 6), OCP at intermediate pH (~ 6-7) and HA in basic conditions, usually only two main phases formed in ethylene glycol: DCP and  $\beta$ -TCP. Furthermore, one of these two phases,  $\beta$ -TCP, has never been reported to form in aqueous conditions. Tao *et al* proposed that ethylene glycol slowly released calcium and phosphate ions, hence maintaining a low but stable driving force during precipitation [13]. This promoted the formation of the well-crystallized  $\beta$ -TCP crystals which normally do not appear in aqueous solution. Indeed it is known that the divalent calcium ions can be chelated by ethylene glycol [23, 24]. In addition to low pH and temperature, an increase in precursor concentration also favored DCP formation. This can be expected looking at the chemical reaction:



During  $\beta$ -TCP formation, hydronium ions are released leading to an acidification of the solution. Therefore, the higher the precursor concentration is, the more  $\text{H}^+$  ions are released, favoring the acidic monetite phase.

Besides DCP and  $\beta$ -TCP, chlorapatite was also observed (e.g. 90 °C, pH 10), but the amounts usually remained low (Figure 3-14 and Figure 3-17). The formation of an apatite compound is

expected, especially at high pH, considering that HA is the most stable CaP phase in neutral and basic aqueous solutions [22]. Furthermore, Weng et al. [25] and Gopi et al. [26] have reported the precipitation of apatite in ethylene glycol using other precursors but obtained agglomerated particles with irregular or globular morphology.

The last phase that was observed was amorphous calcium phosphate. The occurrence of an amorphous precursor at the beginning of a biomineralization process is not surprising [27]. Its presence in some samples thus indicates an incomplete crystallization.

Interestingly, changing the Ca/P molar ratio while maintaining constant the overall precursors concentration did neither affect the crystalline phase nor the morphology or the size (Figure 3-22 and Figure 3-23). Only at too low Ca/P ratios the precipitation of  $\beta$ -TCP was impaired, probably due to the lack of calcium ions which increases the pH. Since no phosphate ions lack higher than 25 % was tested, it is not possible to confirm the same behaviour with phosphate ions. The composition, size and geometry of the platelets were thus very similar over a large Ca/P ratio range, showing once more the robustness of this synthesis method.

Hence, only two crystal phases were produced pure:  $\beta$ -TCP and DCP. Since DCP and  $\beta$ -TCP platelets have very different morphologies, it is essential to either produce pure  $\beta$ -TCP or pure DCP. Indeed, a mixture of these two phases would lead to a bi-modal size distribution and therewith to a less ideal composite structure. Currently, it is difficult to say which phase would be the most efficient to reinforce a composite. Regarding the mechanical properties, ab initio calculations were published for  $\beta$ -TCP [28], but not for monetite. However, considering the higher thermodynamical stability of  $\beta$ -TCP compared to that of DCP (lower solubility, higher melting point),  $\beta$ -TCP is expected to be stronger than DCP. Nevertheless, not only the tensile strength but also the aspect ratio affects the mechanical properties of the composite [29].

### **Aspect ratio**

In general, the DCP parallelepiped platelets presented higher aspect ratios than  $\beta$ -TCP platelets. The values for DCP platelets varied between 8 and 25, whereas the highest aspect ratio obtained with  $\beta$ -TCP platelets was 10 (Figure 3-7). Pure  $\beta$ -TCP platelets, on the other hand, were only obtained with an aspect ratio of max. 6. In comparison, Tao et al. [14] did not obtain DCP platelets and did not report aspect ratios superior to 4 for  $\beta$ -TCP.

The aspect ratio could be influenced by different reaction parameters such as titration rate (for  $\beta$ -TCP), temperature (for both phases), concentration (for  $\beta$ -TCP) and pH value (for both phases). The most effective parameters were the concentration and the pH value. For example,  $\beta$ -TCP aspect ratio increased from 1 to 10 with a concentration increase from 1.6 to 32 mM (Figure 3-7). Similarly, DCP



aspect ratio increased from 12 to 25 when the pH value was reduced from 9.5 to 7.0 (Figure 3-16a). As previously explained, the effect of concentration on the  $\beta$ -TCP aspect ratio (Figure 3-7) is related to the general trend that platelets grow wider and thinner with increasing supersaturation [20]. The effect seen for pH alterations might be due to modifications of crystal surface charges [20] or to supersaturation changes with pH [30]. An increase of the temperature also slightly reduced the aspect ratio of the crystals (Figure 3-13). This suggests that the solubility increased with the temperature, which increased the nucleation rate but limited crystal growth [30]. Indeed, a rise of solubility reduces the supersaturation and in consequence the differences in growth rates between side and surface faces decreased and with it the aspect ratio decreased [20].

Ideally, a large aspect ratio is required to efficiently reinforce a polymer-ceramic composite as it allows an adequate stress transfer between the polymer matrix and the ceramic reinforcement [29]. Based on the present results, the DCP platelets produced with an aspect ratio of 25 appear to be the most interesting.

### Critical thickness

Ceramic materials break in a brittle manner by catastrophic crack propagation. Pre-existing defects, particularly large ones, act like a stress concentrator. As a result, the experimental strength hardly reaches the theoretical strength of the material. For example, dense polycrystalline  $\beta$ -TCP reaches a tensile strength of 154 MPa [31], whereas its theoretical strength lies between 1 and 10 GPa, i.e. 1 to 10% of the theoretical Young's Modulus value of 110 GPa [28]. When the size of the ceramic parts is reduced, the size of the largest defects is also reduced. Consequently, rupture happens at higher stresses. Whereas when the largest defects become smaller than a critical value (Griffith criterion) [32], they are not able to concentrate stresses and the theoretical rupture strength is reached. In case of  $\beta$ -TCP, the critical thickness was estimated to be close to 350 nm, based on theoretical mechanical properties [28] (see theoretical calculations in chapter 2). An estimation for DCP was not possible, because no *ab initio* calculated mechanical properties could be found in the literature. However, as previously mentioned DCP Young's modulus is certainly similar or smaller than the  $\beta$ -TCP modulus. Since the weaker a ceramic is, the larger is its critical thickness [Gao 2006], the critical thickness of DCP is certainly close to or above the one of  $\beta$ -TCP, i.e.  $\geq 350$  nm. In the present study, both types of obtained platelets were thinner than 300 nm, i.e. thin enough to reach the theoretical strength.

The optimum thickness and aspect ratio of ceramic reinforcement are prerequisite to achieve an efficient reinforcement of a ductile matrix, but not only. In addition it is necessary that the reinforcement particles have homogeneous properties, otherwise local variations may weaken the structure. For example, particles from a weaker phase might break first leading to local catastrophic

failure. Therefore, the size dispersion of the primary particles should be as narrow as possible and they should not be agglomerated.

### Uniformity of primary particles

In the present study, the size dispersion was generally below 0.10 for  $\beta$ -TCP particles, and between 0.20 and 0.30 for parallelepiped platelets (Figure 3-3, Figure 3-7, Figure 3-10, Figure 3-13 and Figure 3-16). As monodispersity is generally defined as  $< 0.10$  [33], only  $\beta$ -TCP crystals can be considered to be monodisperse. Such a narrow particle size distribution is typical for diffusion-controlled reactions [12, 34] and often seen for the synthesis of oxides in organic media [35, 36]. A comparison with the literature is difficult because particle size distribution measurements are rarely performed – or mentioned – for CaP powders, perhaps because the size distribution is too broad and/or the particles often are strongly agglomerated. For example, the lowest size dispersion that could be estimated on SEM pictures from the literature was 0.2 - 0.3 [6, 7].

The precipitation of very uniform particles can be explained by a combination of the LaMer model [37, 38] and a diffusion-controlled growth. In the LaMer model, nucleation is so rapid that a high supersaturation, occurring for example after quickly adding the phosphate solution into the calcium solution, is only transitory (Figure 3-25, adapted from [37] and [12]). In other words, all nuclei form simultaneously, resulting in a rapid drop of the concentration, therewith impairing further nucleation. The subsequent growth history is then identical for all nuclei.

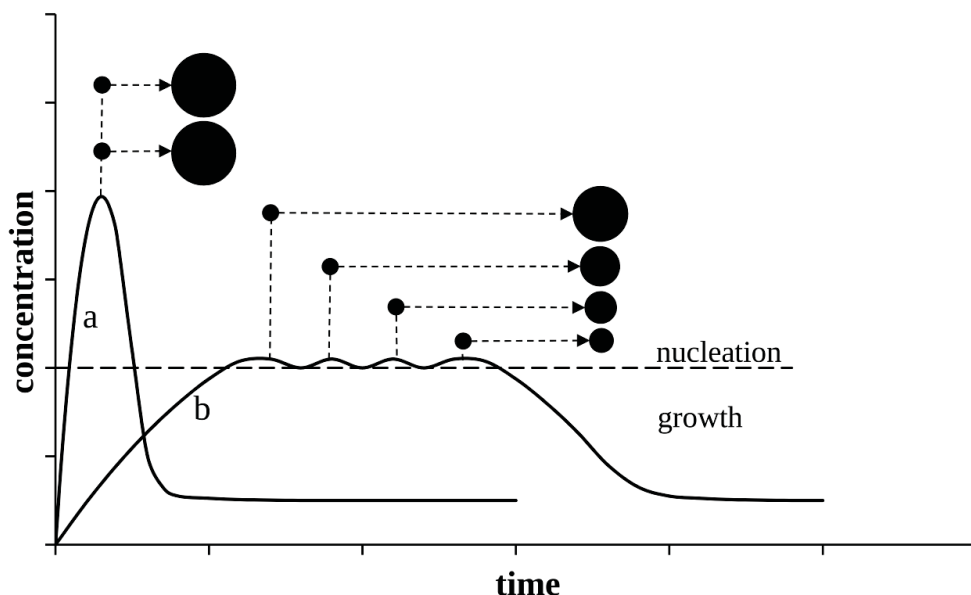


**Figure 3-25** Nucleation and growth mechanism with a) fast and b) slow concentration increase leading to narrow and broad particle size distribution, respectively (adapted from [37] and [12]).

On the other hand, when titration is slow, nucleation occurs during the whole titration period, hence leading to various growth histories (Figure 3-25), i.e. various particle sizes. The LaMer-type nucleation is not the only pre-requisite to obtain a narrow size distribution. It is also necessary to have a diffusion-controlled growth for which the concentration gradient (and hence the growth rate) is inversely proportional to the particle radius. In other words, small particles grow faster than large particles [21], thus preventing coarsening or ripening [39] and resulting in a narrowing of the PSD. According to the theory, this effect is particularly strong at high concentrations but the present results demonstrate that uniform particles can be obtained at low concentrations (Figure 3-7). Additional experiment further confirmed that the growth of the present system is diffusion-controlled. By lowering the stirring rate, the concentration was less homogeneous and in consequence the particle size distribution increased (Figure 3-11). This is typical for diffusion-controlled processes [30].

Interestingly, the narrow size distribution of  $\beta$ -TCP crystals obtained at high titration rate remained stable over time, suggesting that Ostwald ripening (dissolution of the smallest particles to feed the growth of the largest ones) was negligible [12] (Figure 3-20).

The DCP size dispersion is slightly larger than that of  $\beta$ -TCP, suggesting that the nucleation and/or growth mechanisms are not fully identical, but currently only speculations can be made about this difference. To get more insights, growth kinetics studies should be performed, but these will be done in a subsequent stage.

### **Non agglomerated**

Last, but not least, to ensure optimal performances of a composite material, agglomeration of the reinforcement particles should be minimal. Luckily, most particles appeared to be fairly well dispersed. This was expressed by the narrow monomodal size dispersion measured by laser diffraction. However, one parameter seemed to negatively affect the degree of agglomeration. A slow titration rate of the phosphate precursor tended to promote the formation of agglomerates [40], as observed on SEM images (Figure 3-9a, b and d), which could however be separated by ultrasonication (as observed by laser diffraction measurements). Since nuclei are formed during the entire titration period, it is assumed that at slow titration rates, pre-existing particles served as seeds for new particles, hence forming agglomerates [40]. Moreover, phosphate ions are known to act as dispersant. Hence adding them slowly increases agglomeration. In other words, high titration rates ensured a low degree of agglomeration.

The platelets were not more agglomerated after 24 h than after 1.5 h, demonstrating the efficiency of ethylene glycol to disperse and stabilize  $\beta$ -TCP particles and thus maintaining a constant

particle size and shape over time (Figure 3-20). This stabilizing effect is attributed to the formation of chelates between the OH groups of the ethylene glycol molecules and calcium ions [41].

### General points

The aim of this study was to synthesize reproducible CaP particles of controlled thickness, aspect ratio and composition, with a low degree of agglomeration and high productivity. The results show that it is indeed possible to achieve most requirements. However, pure  $\beta$ -TCP platelets could not be produced with an aspect ratio larger than 6 and DCP platelets tended to be agglomerated and presented a non-uniform particle size distribution. In a ceramic-reinforced polymer composite, a low aspect ratio and a high degree of agglomeration of ceramic particles are expected to be detrimental to the tensile properties. Therefore, based on the present study, a choice has to be made between  $\beta$ -TCP particles with high uniformity and low aspect ratios and monetite particles with low uniformity but high aspect ratios. Such a choice may not only affect the mechanical properties of the composite, but also its biological properties.  $\beta$ -TCP is indeed less soluble than DCP in physiological conditions and hence is expected to resorb slower [42]. However, to our knowledge, there is no in vivo study demonstrating a difference between these two materials.

The present study shows that  $\beta$ -TCP platelets with aspect ratio  $> 6$  can be obtained at pH 8 and at a high concentration but with concomitant formation of DCP. Since the pH was only controlled at the start of the reaction, it might be of interest to monitor and control the pH value during the reaction.

One of the problems raised by the present study is the difficulty to increase the productivity. The solubility of the raw materials is very low, hence limiting the productivity to 0.3 - 0.4 g/L. Even though the volume can be increased, uniform particles can only be obtained at high titration rates (Figure 3-10), which is likely to be a problem for much bigger batches. Tubular reactors may be considered. These types of reactors are particularly interesting for reactions finished within a few minutes, as suggested by Tao et al. [14].

## Conclusions

Precipitating CaP particles in ethylene glycol is a very effective method to obtain non-agglomerated CaP particles with well-defined composition, size and shape. In the best conditions, the particle size dispersion sank below 5 % for  $\beta$ -TCP and below 20 % for DCP. The size and shape were tuneable by means of precursors' concentration, pH and temperature. Samples of pure uniform hexagonal  $\beta$ -TCP platelets were obtained at high pH and high temperature. The diameter and aspect ratio ranged from

170 nm to 870 nm and from 1 to 5, respectively. When mixed with DCP, aspect ratios superior to 10 were obtained. Pure monetite platelets were obtained in acidic and neutral pH conditions, with some variations in particle shape and size according to the temperature and pH. The particles showing the largest aspect ratio (close to 25) were monetite parallelepiped platelets obtained at 90 °C and at pH 7. However, these particles had a broader size dispersion than  $\beta$ -TCP hexagonal platelets and appeared more agglomerated.

The ideal platelets for “brick-and-mortar” composites are a trade-off between a large aspect ratio, a pure composition, uniformity (monodispersity), sub-micrometric dimensions and a low degree of agglomeration but these properties are affected by reaction temperature, pH, titration rate and precursors’ concentration. A deeper understanding of the nucleation and growth mechanisms might help better control the purity and size, to obtain either  $\beta$ -TCP platelets with an aspect ratio large enough to efficiently reinforce a biopolymer matrix, or DCP platelets better dispersed and more uniform.

## References

- [1] LeGeros RZ, LeGeros JP. Calcium phosphate Bioceramics: Past, present and future. *Key Eng Mat.* 2003;240-2:3-10.
- [2] Layrolle P, Lebugle A. Characterization and Reactivity of Nanosized Calcium Phosphates Prepared in Anhydrous Ethanol. *Chem Mater.* 1994;6:1996-2004.
- [3] Layrolle P, Lebugle A. Synthesis in pure ethanol and characterization of nanosized calcium phosphate fluoroapatite. *Chem Mater.* 1996;8:134-44.
- [4] Gibson IR, Ke S, Best SM, Bonfield W. Effect of powder characteristics on the sinterability of hydroxyapatite powders. *J Mater Sci-Mater M.* 2001;12:163-71.
- [5] Wang P, Li C, Gong H, Jiang X, Wang H, Li K. Effects of synthesis conditions on the morphology of hydroxyapatite nanoparticles produced by wet chemical process. *Powder Technology.* 2010;203:315-21.
- [6] Zhang H, Darvell BW. Constitution and morphology of hydroxyapatite whiskers prepared using amine additives. *Journal of the European Ceramic Society.* 2010;30:2041-8.
- [7] Zhang H, Darvell BW. Synthesis and characterization of hydroxyapatite whiskers by hydrothermal homogeneous precipitation using acetamide. *Acta Biomaterialia.* 2010;6:3216-22.
- [8] Neira IS, Guitián F, Taniguchi T, Watanabe T, Yoshimura M. Hydrothermal synthesis of hydroxyapatite whiskers with sharp faceted hexagonal morphology. *J Mater Sci.* 2008;43:2171-8.
- [9] Neira IS, Kolen'ko YV, Lebedev OI, Van Tendeloo G, Gupta HS, Guitián F, et al. An effective morphology control of hydroxyapatite crystals via hydrothermal synthesis. *Crystal Growth and Design.* 2009;9:466-74.
- [10] Jinawath S, Pongkao D, Suchanek W, Yoshimura M. Hydrothermal synthesis of monetite and hydroxyapatite from monocalcium phosphate monohydrate. *International Journal of Inorganic Materials.* 2001;3:997-1001.

- [11] Zhang Hb, Zhou Kc, Li Zy, Huang Sp. Plate-like hydroxyapatite nanoparticles synthesized by the hydrothermal method. *Journal of Physics and Chemistry of Solids*. 2009;70:243-8.
- [12] Kwon SG, Hyeon T. Formation mechanisms of uniform nanocrystals via hot-injection and heat-up methods. *Small*. 2011;7:2685-702.
- [13] Tao J, Jiang W, Zhai H, Pan H, Xu R, Tang R. Structural components and anisotropic dissolution behaviors in one hexagonal single crystal of  $\beta$ -tricalcium phosphate. *Crystal Growth and Design*. 2008;8:2227-34.
- [14] Tao J, Pan H, Zhai H, Wang J, Li L, Wu J, et al. Controls of tricalcium phosphate single-crystal formation from its amorphous precursor by interfacial energy. *Crystal Growth and Design*. 2009;9:3154-60.
- [15] Rodriguez-Carvajal J. Recent Developments of the Program FULLPROF. *Commission on Powder Diffraction (IUCr) Newsletter*. 2001;26:12-9.
- [16] Dickens B, Schroeder LW, Brown WE. Crystallographic studies on the role of Mg as a stabilizing impurity in  $\beta$ - $\text{Ca}_3(\text{PO}_4)_2$  I. The crystal structure of pure  $\beta$ - $\text{Ca}_3(\text{PO}_4)_2$ . *Journal of Solid State Chemistry*. 1974;10:232-48.
- [17] Dickens B, Bowen JS, Brown WE. A refinement of the crystal structure of  $\text{CaHPO}_4$  (synthetic monetite). *Acta Cryst*. 1971;B28:797-806.
- [18] Sudarsanan K, Young RA. Significant precision in crystal structure details: Holly springs hydroxyapatite. *Acta Cryst*. 1969;B25:1534-43.
- [19] Chenot CF. Method of converting brushite to monetite crystals with controlled variation in crystal habit. In: 3927180 UP, editor. US Patent 3927180. USA: GTE Sylvania Incorporated; 1975.
- [20] Boistelle R, Astier JP. Crystallization mechanisms in solution. *Journal of Crystal Growth*. 1988;90:14-30.
- [21] Peng X, Manna L, Yang W, Wickham J, Scher E, Kadavanich A, et al. Shape control of CdSe nanocrystals. *Nature*. 2000;404:59-61.
- [22] Vereecke G, Lemaitre J. Calculation of the solubility diagrams in the system  $\text{Ca}(\text{OH})_2$ - $\text{H}_3\text{PO}_4$ - $\text{KOH}$ - $\text{HNO}_3$ - $\text{CO}_2$ - $\text{H}_2\text{O}$ . *J Crystal Growth*. 1990;104:820-32.
- [23] Zhang X, Liu J, Yu H, Yang G, Wang J, Yu Z, et al. Enhanced electrochemical performances of  $\text{LiNi}_{0.5}\text{Mn}_{1.5}\text{O}_4$  spinel via ethylene glycol-assisted synthesis. *Elect Acta*. 2010;55:2414-7.
- [24] Knetsch D, L. Groeneveld W. Alcohol as ligands. III. Complexes of Ethylene glycol with some divalent metal halides. *Inorg Chim Acta*. 1973;7:81-7.
- [25] Weng W, Baptista JL. A new synthesis of hydroxyapatite. *Journal of the European Ceramic Society*. 1997;17:1151-6.
- [26] Gopi D, Bhalaji PR, Prakash VCA, Ramasamy AK, Kavitha L, Ferreira JMF. An effective and facile synthesis of hydroxyapatite powders using oxalic acid-ethylene glycol mixture. *Current Applied Physics*. 2011;11:590-3.
- [27] Addadi L, Vidavsky N, Weiner S. Transient precursor amorphous phases in biomineralization. In the footsteps of Heinz A. Lowenstam. *Zeitschrift fur Kristallographie*. 2012;227:711-7.
- [28] Liang L, Rulis P, Ching WY. Mechanical properties, electronic structure and bonding of  $\alpha$ - and  $\beta$ -tricalcium phosphates with surface characterization. *Acta Biomaterialia*. 2010;6:3763-71.
- [29] Gao H. Application of fracture mechanics concepts to hierarchical biomechanics of bone and bone-like materials. *International Journal of Fracture*. 2006;138:101-37.
- [30] Rodríguez-Hornedo N, Murphy D. Significance of controlling crystallization mechanisms and kinetics in pharmaceutical systems. *Journal of Pharmaceutical Sciences*. 1999;88:651-60.

- [31] Jarcho M, Salsbury RL, Thomas MB, Doremus RH. Synthesis and fabrication of b-tricalcium phosphate (whitlockite) ceramics for potential prosthetic applications. *J Mater Sci.* 1979;14:142-50.
- [32] Griffith AA. The Phenomena of Rupture and Flow in Solids. *Philosophical Transactions of the Royal Society of London Series A, Containing Papers of a Mathematical or Physical Character.* 1921;221:163-98.
- [33] Inukai S, Tanma T, Orihara S, Konno M. A simple method for producing micron-sized, highly monodisperse polystyrene particles in aqueous media: Effects of impeller speed on particle size distribution. *Chemical Engineering Research and Design.* 2001;79:901-5.
- [34] Murray CB, Norris DJ, Bawendi MG. Synthesis and characterization of nearly monodisperse CdE (E = S, Se, Te) semiconductor nanocrystallites. *J Am Chem Soc.* 1993;115:8706-15.
- [35] Feldmann C. Polyol-mediated synthesis of nanoscale functional materials. *Advanced Functional Materials.* 2003;13:101-7.
- [36] Jana NR, Chen Y, Peng X. Size- and shape-controlled magnetic (Cr, Mn, Fe, Co, Ni) oxide nanocrystals via a simple and general approach. *Chem Mater.* 2004;16:3931-5.
- [37] Tao AR, Habas S, Yang P. Shape control of colloidal metal nanocrystals. *Small.* 2008;4:310-25.
- [38] Lamer VK, Dinigar RH. Theory, production and mechanism of formation of monodispersed hydrosols. *J Am Chem Soc.* 1950;72:4847-54.
- [39] Barnard AS. Modelling of nanoparticles: Approaches to morphology and evolution. *Reports on Progress in Physics.* 2010;73.
- [40] Nichols G, Byard S, Bloxham MJ, Botterill J, Dawson NJ, Dennis A, et al. A review of the terms agglomerate and aggregate with a recommendation for nomenclature used in powder and particle characterization. *Journal of Pharmaceutical Sciences.* 2002;91:2103-9.
- [41] McNaught AD, Wilkinson A. IUPAC. *Compendium of Chemical Terminology (the "Gold Book").* 2.3.1 ed: Blackwell Scientific Publications, Oxford; 1997.
- [42] Bohner M. Calcium orthophosphates in medicine: from ceramics to calcium phosphate cements. *Injury.* 2000;31 Suppl 4:37-47.





## CHAPTER 4:

# KINETICS STUDY OF THE CALCIUM PHOSPHATE PLATELETS

## GROWTH

### *Abstract*

Recently, uniform, non-agglomerated, hexagonal  $\beta$ -tricalcium phosphate ( $\beta$ -TCP) platelets (diameter  $\approx$  400–1700 nm,  $h \approx$  100–200 nm) were obtained at fairly moderate temperatures (90 - 170 °C) by precipitation in ethylene glycol. Unfortunately, the platelet aspect ratios (diameter/thickness) obtained in the latter study were too small to optimize the strength of polymer -  $\beta$ -TCP composites. Therefore, the aim of the present study was to investigate  $\beta$ -TCP platelet crystallization kinetics, and based on this, to find ways to better control the  $\beta$ -TCP aspect ratio. For that purpose, precipitations were performed at different temperatures (90 - 170 °C) and precursor concentrations (4, 16 and 32 mM). Solution aliquots were retrieved at regular intervals (10 s - 24 h), and the size of the particles was measured on scanning electron microscopy images, hence allowing the determination of the particle growth rates. The  $\beta$ -TCP platelets were observed to nucleate and grow very rapidly. For example, the first crystals were observed after 30 s at 150 °C, and crystallization was complete within 2 min. The crystal growth curves could be well-fitted with both diffusion- and reaction-controlled equations, but the high activation energies ( $\approx$  100 kJ·mol<sup>-1</sup>) pointed towards a reaction-controlled mechanism. The results revealed that the best way to increase the diameter and aspect ratio of the platelets was to increase the precursor concentration. Aspect ratios as high as 14 were obtained, but the synthesis of such particles was always associated with the presence of large fractions of monetite impurities.

Published in part as:

Galea L, Bohner M, Thuering J, Doebelin N, Ring TA, Aneziris CG, Graule T. *Growth kinetics of hexagonal sub-micrometric  $\beta$ -tricalcium phosphate particles in ethylene glycol*. **Acta Biomaterialia**, 10, 3922-3930 (2014).

## Introduction

In the previous chapter, submicrometric calcium phosphate platelets were obtained at fairly moderate temperatures (90 – 170 °C) by precipitation in ethylene glycol [1]. Of the obtained phases, two were particularly interesting for the target application in brick-and-mortar structures. The first type was highly uniform, non-agglomerated, sub-micrometric  $\beta$ -tricalcium phosphate platelets ( $\beta$ -TCP;  $\beta$ -Ca<sub>3</sub>(PO<sub>4</sub>)<sub>2</sub>). Unfortunately, the aspect ratio was relatively limited (typically below 10), and impurities (in the form of secondary phases) were found as soon as the aspect ratio reached values superior to about 5. The second phase was monetite particles (DCP; CaHPO<sub>4</sub>) with high aspect ratio (typically around 20). However, the particles were less monodisperse, less uniform, and more agglomerated than the  $\beta$ -TCP particles. Since the latter factors are of paramount importance for the synthesis of nacre-like materials, it appears more promising to focus on  $\beta$ -TCP synthesis as a first step towards the production of nacre-like materials. However, the strength improvement efficiency is strongly proportional to the aspect ratio of the reinforcement elements [2, 3]. Hence, to efficiently strengthen a biopolymer, a better control of  $\beta$ -TCP platelets growth was necessary.

Therefore, the aim of the present study was to first gain a better understanding of the growth mechanisms of  $\beta$ -TCP platelets with the hope that their aspect ratio would be more easily controlled. The chemical kinetics of the reaction was thus investigated in order to look for the factors that influence the rate of reaction [4]. Specifically, the time evolution of  $\beta$ -TCP platelets was analyzed as a function of precursor concentration and temperature. The reaction rates were calculated and compared to various growth kinetic models [5-7] in order to propose explanations to the values found.

## Theory

In 2011, Kwon and Hyeon [5] discussed the growth kinetics of uniform nanocrystals. These authors postulated that the particle growth rate could be expressed by equations (1) and (2) for reaction-controlled and diffusion-controlled reactions, respectively:

$$\frac{dr}{dt} = V_m \cdot k \cdot ([M]_b - [M]_r), \text{ (reaction-controlled)} \quad \text{Eq. 1}$$

$$\frac{dr}{dt} = \frac{D \cdot V_m}{r} \cdot ([M]_b - [M]_r), \text{ (diffusion controlled)} \quad \text{Eq. 2}$$

where  $r$  is the particle radius,  $t$  the reaction time,  $D$  the diffusion coefficient,  $V_m$  the molecular volume (molecular mass,  $MM$ , divided by the density,  $\rho$ ;  $MM = 310$  g/mol and  $\rho = 3.07$  g/cc for  $\beta$ -TCP),  $[M]_b$  the concentration in the bulk,  $[M]_r$  the solubility of the spherical particle of radius  $r$ , and  $k$  the reaction rate constant. Considering the low solubility of  $\beta$ -TCP in ethylene glycol ( $\beta$ -TCP readily precipitates at a concentration of 1.6 mM [1] whereas most experiments are performed at 16 mM), it can be assumed that  $[M]_r = 0$ . If all the particles are formed simultaneously,  $[M]_b$  is equal to the difference between the initial concentration,  $[M]_0$ , and the concentration that has been consumed by the particles already formed:

$$[M]_b = [M]_0 - n \cdot \frac{4}{3} \cdot \pi \cdot r^3 \cdot \frac{\rho}{V}, \quad \text{Eq. 3}$$

with  $n$  the number of particles and  $V$  the total volume.

Combining Equations 1 to 3 leads to reactions 4 and 5:

$$\frac{dr}{dt} = V_m \cdot k \cdot \left( [M]_0 - n \cdot \frac{4}{3} \cdot \pi \cdot r^3 \cdot \frac{\rho}{V} \right), \quad (\text{reaction-controlled}) \quad \text{Eq. 4}$$

$$\frac{dr}{dt} = \frac{D \cdot V_m}{r} \cdot \left( [M]_0 - n \cdot \frac{4}{3} \cdot \pi \cdot r^3 \cdot \frac{\rho}{V} \right) \quad (\text{diffusion-controlled}) \quad \text{Eq. 5}$$

At infinite time, i.e. when all precursors are consumed,  $[M]_b = 0$ , and the particles reach a maximum size,  $r_\infty$ , equations 4 and 5 can be written:

$$\frac{dr}{dt} = V_m \cdot k \cdot [M]_0 \cdot \left( 1 - \left( \frac{r}{r_\infty} \right)^3 \right) \quad \text{Eq. 6}$$

$$r \cdot \frac{dr}{dt} = V_m \cdot D \cdot [M]_0 \cdot \left( 1 - \left( \frac{r}{r_\infty} \right)^3 \right) \quad \text{Eq. 7}$$

The particles obtained with the present synthesis method are hexagonal prisms, with an inner diameter  $d_{hex}$  and a thickness  $h_{hex}$ . Therefore, the radius of a sphere of equivalent volume was calculated and used in Eq. 6 and 7.

$$r = \sqrt[3]{\frac{3}{4} \cdot \left( \frac{d_{hex}}{2} \right)^2 \cdot h_{hex}} \quad \text{Eq. 8}$$

In equations 6 and 7, the value of  $r_\infty$  can be estimated by calculating the mean size of the particles present at the end of the reaction. As a result, it is possible to calculate the number of particles using equation 9.

$$n = [M]_0 \cdot \frac{3}{4\pi} \cdot \frac{V}{\rho \cdot r_\infty^3} \quad \text{Eq 9}$$

The other two unknowns in equations 6 and 7, namely  $k$  and  $D$ , can be retrieved from a numerical fit of the experimental data. Then, the activation energy,  $E_a$ , can be directly calculated from the slope of  $\ln(k)=f(1/T)$  or  $\ln(D)=f(1/T)$  curves using the Arrhenius' law (Eq. 10).

$$k = k_0 \cdot \exp\left(\frac{-E_a}{RT}\right) \text{ or } D = D_0 \cdot \exp\left(\frac{-E_a}{RT}\right), \quad \text{Eq. 10}$$

where  $R$  is the ideal gas constant ( $8.314 \text{ J}\cdot\text{K}^{-1}\cdot\text{mol}^{-1}$ ) and  $k_0$  and  $D_0$  are constants.

Assuming a diffusion-controlled growth mechanism, the diffusion constants,  $D$ , can be extracted from the numerical fits of the data with the diffusion-controlled equation (Eq. 7). The Stokes-Einstein equation [8] allows calculating the size (diameter,  $d$ ) of the diffusion units

$$d = \frac{k_B \cdot T}{3 \cdot \pi \cdot D \cdot \eta} \quad \text{Eq. 11}$$

With  $k_B$  the Boltzmann constant,  $T$  the temperature and  $\eta$  the viscosity of the solution at temperature  $T$ .

## Materials and methods

### Materials and sample preparation

CaP platelets were produced using the precipitation method described in [1]. The phosphate solution was prepared by placing 140 mL of ethylene glycol ( $\text{C}_2\text{H}_6\text{O}_2$ , Reag.Ph.Eur., Art. no 85512.360, VWR, Nyon, Switzerland) in a 600 mL glass beaker and heated up to 90 - 110 °C. Then, 9.52 mL of a 0.0825 / 0.33 / 0.66 M  $\text{Na}_2\text{HPO}_4$  ( $\text{Na}_2\text{HPO}_4 \cdot 2\text{H}_2\text{O}$ , purum p.a., Art. no 71645, Fluka, Buchs, Switzerland) solution and 0.21 / 0.84 / 1.68 mL of a 1.3 M NaOH (NaOH, puriss. p.a., Art. no 71690, Fluka, Buchs, Switzerland) were added. To prepare the calcium solution, 350 mL of ethylene glycol were mixed with 0.175 / 0.700 / 1.4 g  $\text{CaCl}_2 \cdot 2\text{H}_2\text{O}$  ( $\text{CaCl}_2 \cdot 2\text{H}_2\text{O}$ , Reag.Ph.Eur., Art. no 1.02382, MERCK, Darmstadt, Germany) in a 1 L triple-neck round bottom flask connected with a coil condenser and isolated with aluminum foil. This solution was heated to 90-180 °C under intense stirring. The temperatures of both solutions were chosen such as to match the target temperatures upon mixing (ex: 350 mL at 170 °C mixed with 140 mL at 100 °C to reach 150 °C). So, it can be assumed that the achievement of a homogeneous temperature lasted as long as it takes to reach a homogeneous mixture. The phosphate solution was poured into the calcium solution within 5 seconds. In the end, each

experiment consisted of a 500mL solution containing phosphate and calcium ions in 2:3 molar ratio with a total  $[\text{Ca}^{2+}] + [\text{PO}_4^{3-}]$  ions concentration ranging from 4 mM to 32 mM. The effect of temperature was studied at a concentration of 16 mM by varying the temperature from 90 to 170 °C in 20 °C steps. In some cases, the target temperature could not be reached, so some experiments were also conducted at additional intermediary temperatures. With 4 and 32mM, reactions were only conducted at 110, 130 and 150 °C. During the experiment, 10 mL aliquots were retrieved at regular intervals (the sampling times were adapted according to the reaction temperature) and placed in a 50 mL PP tube (Art. no 525-0402, VWR, Nyon, Switzerland). These samples were rapidly cooled down by placing the tubes in an ice bath and then centrifuged at 4000 rpm for 30 min to sediment and extract the solid phase. The precipitated crystals were then dispersed and centrifuged in ethanol ( $\text{C}_2\text{H}_6\text{O}$ , absolute 99.8%, Art. no G003, Grogg, Switzerland), in demineralized water and in ethanol again. After the third washing step, the precipitate was dispersed in 3 ml of ethanol. A drop of this solution was spread over a scanning electron microscopy (SEM) aluminum sample holder and dried in air. SEM observations were performed and the size and aspect ratio of the particles were measured by image analysis of the SEM pictures (see hereafter).

At the end of the experiment, the remaining suspension was also rinsed by centrifugation as described above and a part of it was used for XRD measurements (see hereafter). The rest of the suspension was dried at 30°C under vacuum for 24h and stored.

Each experiment was repeated at least twice.

### **Characterization methods**

The particle appearance and size were analyzed by SEM. For this, the samples were coated with a 10nm thick platinum layer (60 s, 40 mV) and observed with a EVO MA25 microscope (Zeiss, Germany) using a voltage of 20 kV and a working distance of 7-8 mm. The particle size was assessed by image analysis (Image Access 11 Premium, Imagic Bildverarbeitung AG, Glattbrugg, Switzerland) of SEM pictures at 10'000 fold magnification. Pictures were taken in regions where some particles were lying flat but also standing on their edge to allow diameter and thickness measurements. A minimum of 15 crystals was used to measure the diameter and of 6 crystals to measure the thickness. Only in case of samples taken at an early reaction stage, the number of measurements had to be reduced because only a few platelets were apparent in the amorphous phase. The diameter of the hexagon prisms, octahedrons and spherical particles was defined as the diameter of the inscribed circle. The size dispersion is calculated as the standard deviation of the particle measurement divided by the average size from image analysis.

The crystalline composition was analyzed by X-ray diffraction (XRD) measurements. For this, a concentrated ethanol suspension was dried on a glass plate, scratched off and spread on a silicon single crystal sample holder to minimize preferred orientation. XRD data were collected in reflective geometry on an X-Pert diffractometer (X'Pert Pro MPD, Panalytical, Almelo, The Netherlands). Ni-filtered  $\text{CuK}_\alpha$  radiation and a step size of  $0.016^\circ$  were used to measure from  $4.01^\circ$  to  $59.99^\circ$   $2\theta$ . Due to the limited amount of sample material available, sample transparency, texture, and variable irradiated volume limited the quality of the diffraction patterns. Therefore only semi-quantitative phase analyses could be done by Rietveld refinement using the FullProf.2k software (Version 5.00) [9] and a previously determined instrument resolution function. Crystalline models for  $\beta$ -tricalcium phosphate ( $\beta$ -TCP), monetite (DCP) and chloroapatite (Cl-Ap) were taken from Schroeder et al. [10], Dickens et al. [11] and Hughes et al. [12].

## Results

### Visual observations during manipulations

After centrifugation, nothing was observed in the first aliquots retrieved at low concentration and temperature. However, a transparent gel was seen to sediment after a while, particularly at high concentrations. At longer reaction times, this gel was progressively replaced by a white sediment forming at the bottom of the vials. The ratio between the white sediment and the transparent gel increased with time. Moreover, the amount of white sediment appeared to be proportional to the reagent concentration. The typical yield of CaP powder after drying was 0.3 - 0.4 g/L.

### SEM observations

At the beginning of the reactions, the first solid identified by SEM was of undefined shape (Figure 4-1a). No faceted particles (which are called crystals further in this manuscript) were detected. The first crystals appeared after a given time which increased with decreasing temperature (Figure 4-1b). For example, a few crystals were observed after 30min of reaction at  $90^\circ\text{C}$  (Figure 4-2), whereas first crystals were already present after 30s of reaction at  $150^\circ\text{C}$  (Figure 4-1b). The crystal size increased with the reaction time, while the amount of solid with undefined shape decreased (Figure 4-1). At  $90^\circ\text{C}$ , mostly large parallelepipedic crystals were observed. Nevertheless, some hexagonal platelets were also present (Figure 4-2). Both crystals seemed to appear simultaneously and in the same proportions throughout the reaction. The amount of parallelepipedic crystal decreased with increasing temperature but increased with increasing concentration (Figure 4-3).

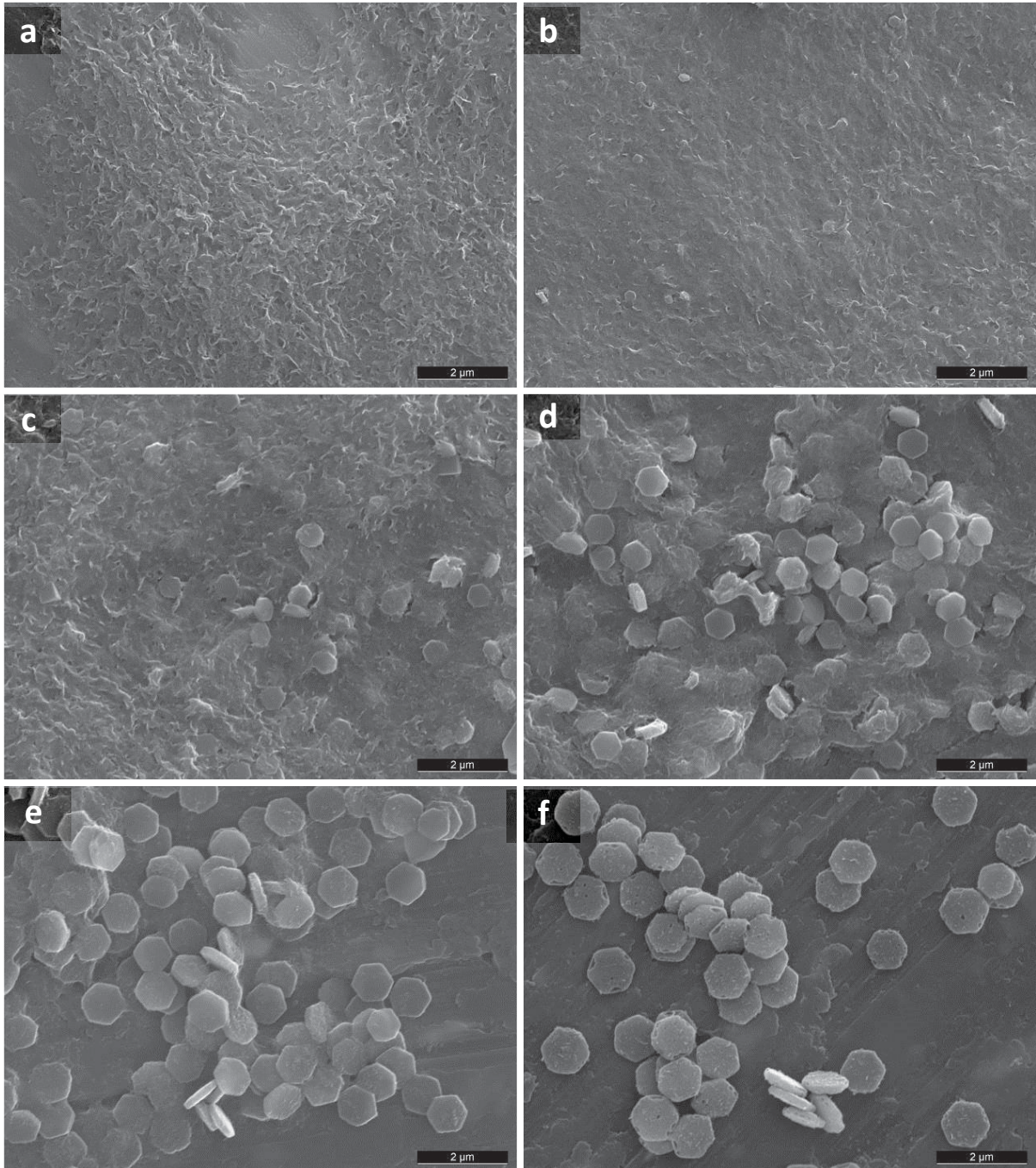


**Figure 4-1** SEM pictures of samples taken out of the reactor at 150°C at different times: a) 10s; b) 30s; c) 70s; d) 90s; e) 2min; f) 24h. The scale bars are 2μm.

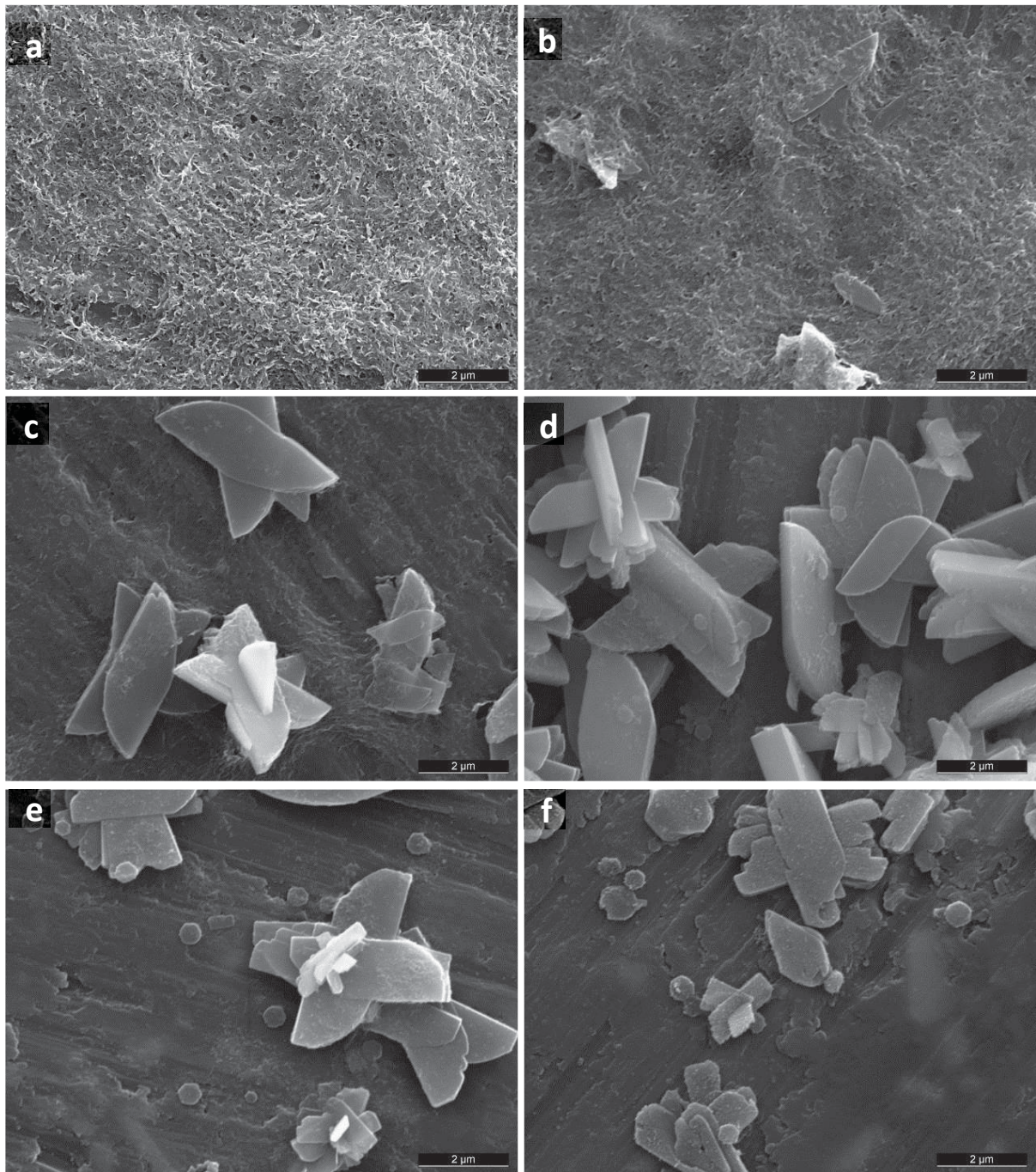


**Figure 4-2** SEM pictures of samples taken out of the reactor at 90°C at: a) 2min; b) 16min; c) 32min; d) 1h; e) 2h; f) 24h. The scale bars are 2μm



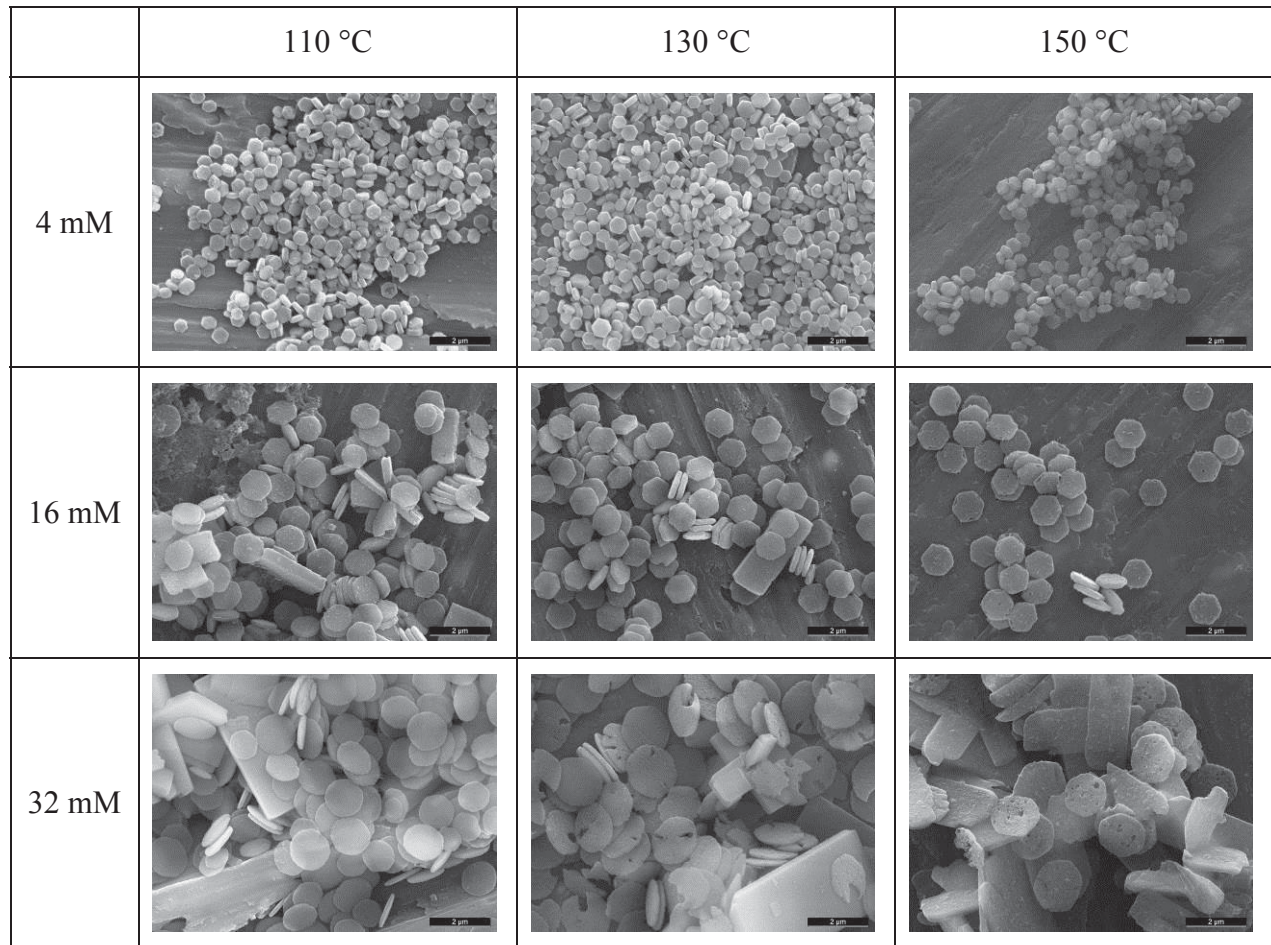


**Figure 4-3** SEM pictures of samples after complete reaction at different temperatures (110, 130, 150 °C) and concentrations (4, 16, 32 mM). The scale bar is 2  $\mu$ m for all pictures.

Figure 4-4 shows representative images of hexagonal platelets obtained at different concentrations and temperatures. In general, the diameter increased with the reagent concentration, but was not markedly affected by a change of temperature. A change of concentration also affected the aspect ratio and the shape of the particles: hexagonal prisms with well-defined edges and low aspect ratios (around 3) were noticed at low concentration, whereas thinner discs with higher aspect ratios ( $> 10$ ) were observed at high concentration. Variations in surface appearance were noticed, like presence of porosities in some samples. This was also already observed by Galea et al. [1] and attributed to the rinsing process.

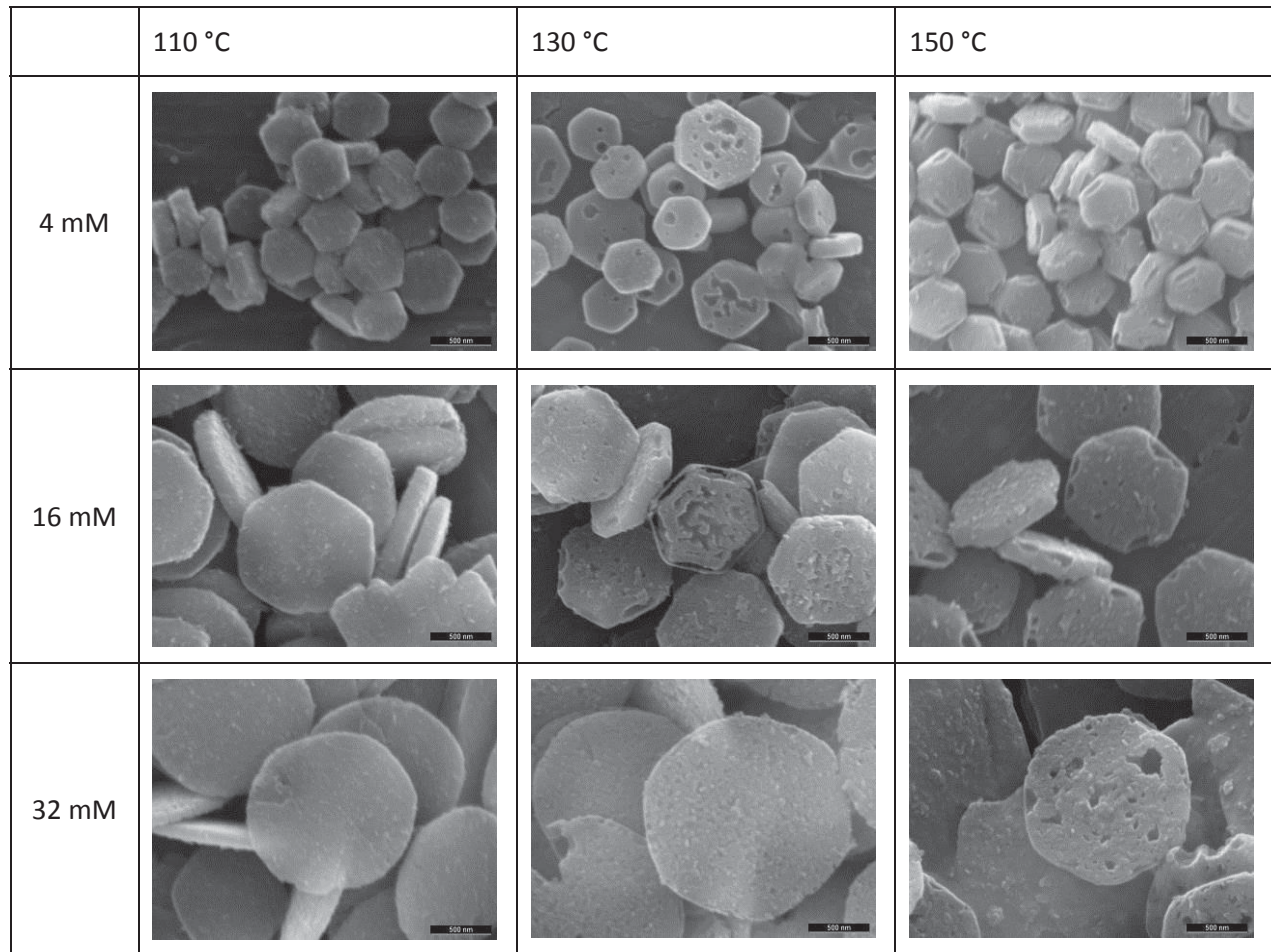


**Figure 4-4** SEM pictures of samples after complete reaction at different temperatures (110, 130, 150 °C) and concentrations (4, 16, 32 mM). The scale bar is 500nm for all pictures.

### XRD results

Rietveld refinement of XRD measurements performed on samples retrieved at the end of the synthesis reaction revealed the presence of three calcium phosphate phases:  $\beta$ -TCP, monetite (DCP,  $\text{CaHPO}_4$ ) and chloro-apatite (Cl-Ap;  $\text{Ca}_5(\text{PO}_4)_3(\text{OH},\text{Cl})$ ) (Figure 4-5). The monetite fraction was the highest at low temperature and high concentration (Table 4-1). For example, 79 wt-% DCP were measured at 90 °C and 16 mM. The DCP fraction decreased then with increasing temperature and decreasing concentration. Since the Cl-Ap content remained very low (< 10%) in all samples, a decrease in DCP content resulted in an increase in  $\beta$ -TCP content. As a result, pure  $\beta$ -TCP samples were obtained in various conditions, for example at a concentration of 4 mM at 130 °C and 150 °C, and at a concentration of 16 mM at 150 °C. Looking at the SEM images, the hexagonal prisms were identified as the  $\beta$ -TCP phase, the parallelepiped crystals as DCP and rare small elongated particles as Cl-Ap.

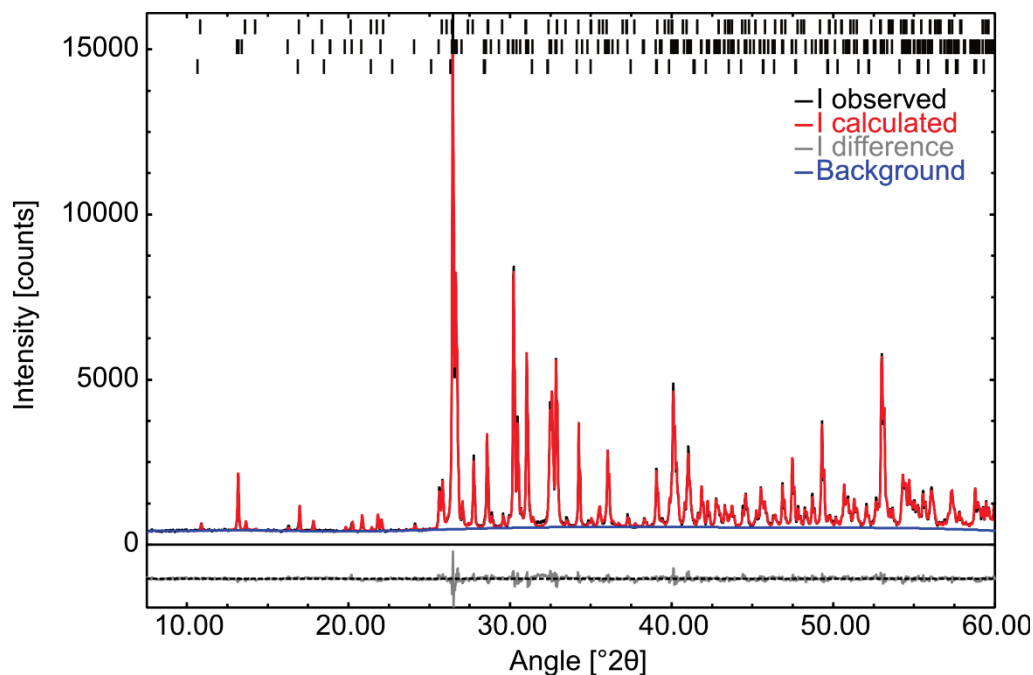


**Figure 4-5** Representative XRD diffractogram of particles synthesized at 90 °C, 16 mM for 24h showing the presence of highly crystalline  $\beta$ -TCP and DCP phases. Observed, calculated, differences and background intensities are displayed, as well as the hkl line positions for  $\beta$ -TCP (top), DCP (middle) and Cl-Ap (bottom).

**Table 4-1** Crystalline composition (wt-%) in function of temperature and concentration (Rietveld refinement of XRD diffractograms). The values are averages  $\pm$  standard deviations except when only one XRD measurement could be performed.

Concentration of precursors	Crystalline phase	Temperature				
		90 °C	110 °C	130 °C	150 °C	170 °C
4mM	$\beta$ -TCP	na	97 $\pm$ 4 %	100 %	100 $\pm$ 0 %	na
	DCP	na	3 $\pm$ 4 %	0 %	0 $\pm$ 0 %	na
	Cl-Ap	na	0 $\pm$ 0 %	0 %	0 $\pm$ 0 %	na
16mM	$\beta$ -TCP	17 $\pm$ 2 %	66 $\pm$ 5 %	93 $\pm$ 3 %	100 $\pm$ 1 %	99 $\pm$ 2 %
	DCP	79 $\pm$ 6 %	34 $\pm$ 5 %	3 $\pm$ 0 %	0 $\pm$ 0 %	0 $\pm$ 0 %
	Cl-Ap	3 $\pm$ 5 %	3 $\pm$ 0 %	2 $\pm$ 3 %	0 $\pm$ 0 %	1 $\pm$ 2 %
32mM	$\beta$ -TCP	na	55 %	72 %	90 $\pm$ 3 %	na
	DCP	na	45 %	28 %	1 $\pm$ 1 %	na
	Cl-Ap	na	0 %	0 %	9 $\pm$ 4 %	na

## Size measurements

At all reaction temperatures, the hexagonal crystals grew continuously in diameter and thickness until a plateau was reached (Figure 4-6a and b). Higher reaction temperatures strongly accelerated the nucleation and growth of the crystals, while a concentration increase had a much smaller effect (this can also be appreciated in linear scale, Figure 4-7). However, concentration markedly affected the plateau diameter value (Figure 4-6a and b). The aspect ratio tended to slightly increase during the fast crystal growth at the beginning of the reaction, but hardly varied at long reaction times (Figure 4-6c). The size dispersion was quite constant with reaction time, and was the highest at low temperature or low concentration (Figure 4-6d). The final size and aspect ratio increased with the concentration, and slightly varied with temperature changes (Figure 4-6e, f and g). The largest variations were observed between 150 and 170 °C, where the diameter and aspect ratio clearly decreased. The hexagonal platelets first decreased in diameter, without large changes of thickness (Figure 4-8a) and then became round at 170 °C (Figure 4-8b). The size dispersion at the end of the precipitation reaction was generally between 0.05 - 0.10. However, there were some exceptions (Figure 4-6h and Figure 4-8a).

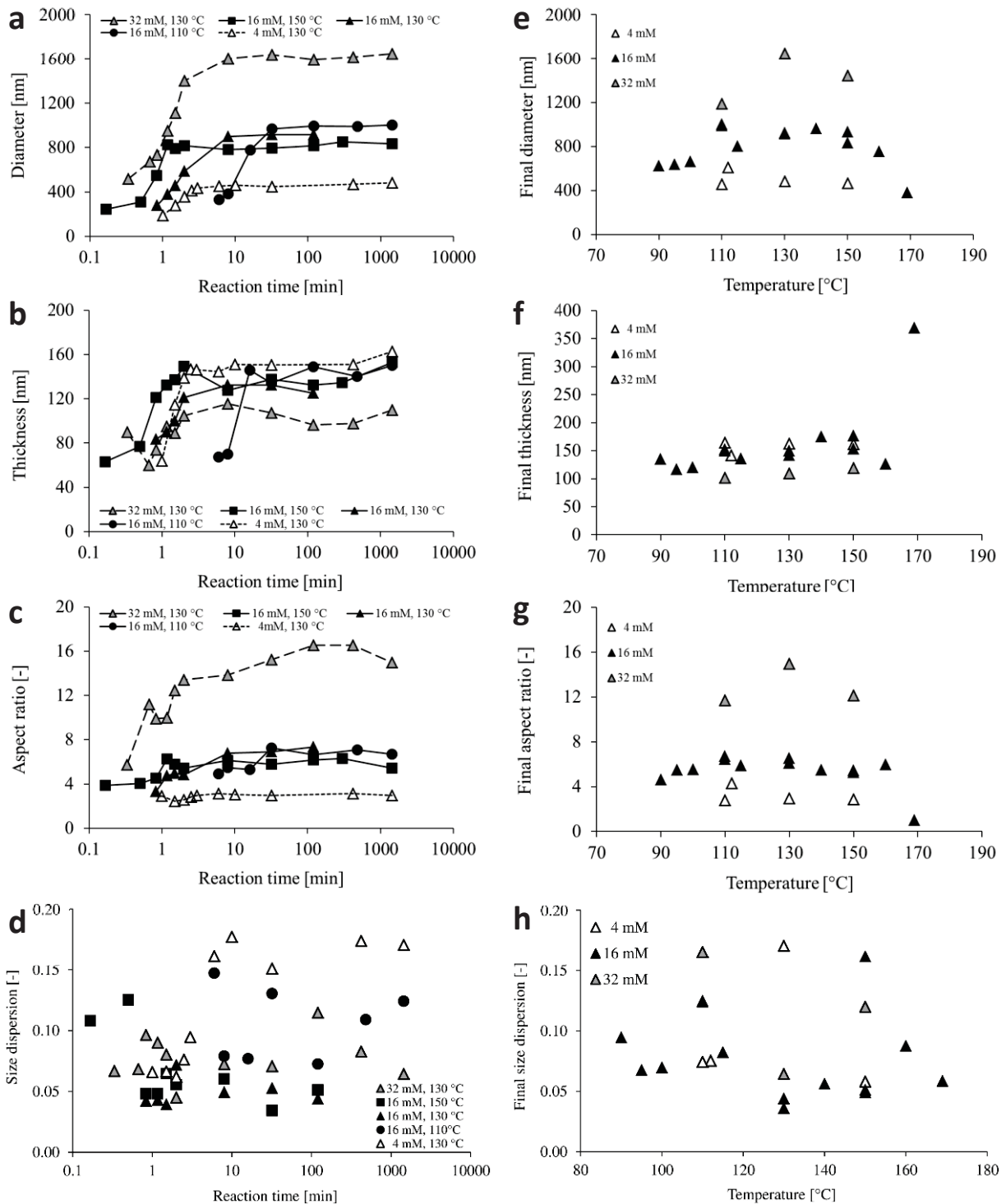


**Figure 4-6** Evolution of the platelets a) diameter, b) thickness, c) aspect ratio and d) size dispersion in function of the reaction time at different temperatures (●) 110°C, (△, ▲, ■) 130°C, (■): 150°C) and concentrations (results only at 130°C: (△) 4mM, (▲) 16mM, (▲) 32mM). Final platelets e) diameter, f) thickness, g) aspect ratio and h) size dispersion at different temperatures and concentrations.

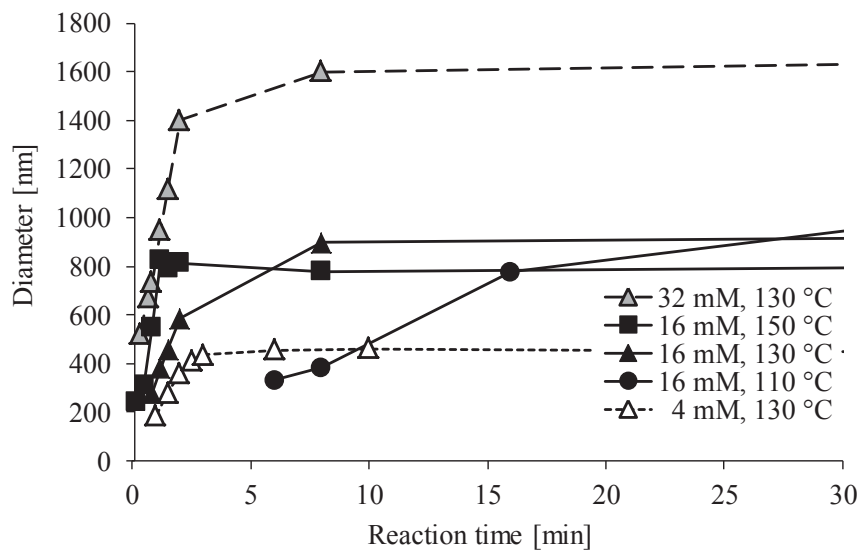


**Figure 4-7** Evolution of the platelets diameter in function of the reaction time at different temperatures ((●) 110°C, (Δ, ▲, ▲) 130°C, (■) 150°C) and concentrations (results only at 130°C: ((Δ) 4mM, (▲) 16mM, (▲) 32mM).

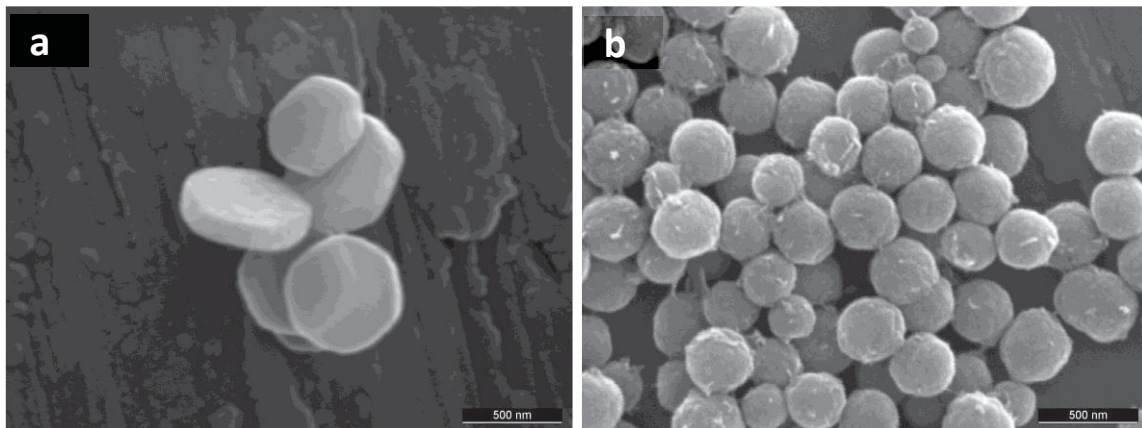


**Figure 4-8** SEM of samples after complete reaction at 16 mM and a) 160 °C; b) 170 °C. Above 150°C, the particles size and aspect ratio clearly decreases. The particles in a) are disks, whereas in b) they are spherical. Scale bars are 500 nm in a) and b).

### Kinetics calculations

$\beta$ -TCP growth was the fastest at the beginning of the reaction, when the particles were still small and the amount of precursors is high. As the precipitation continued, the precursor concentration decreased, the particle size increased and the growth rate decreased (Figure 4-9a).

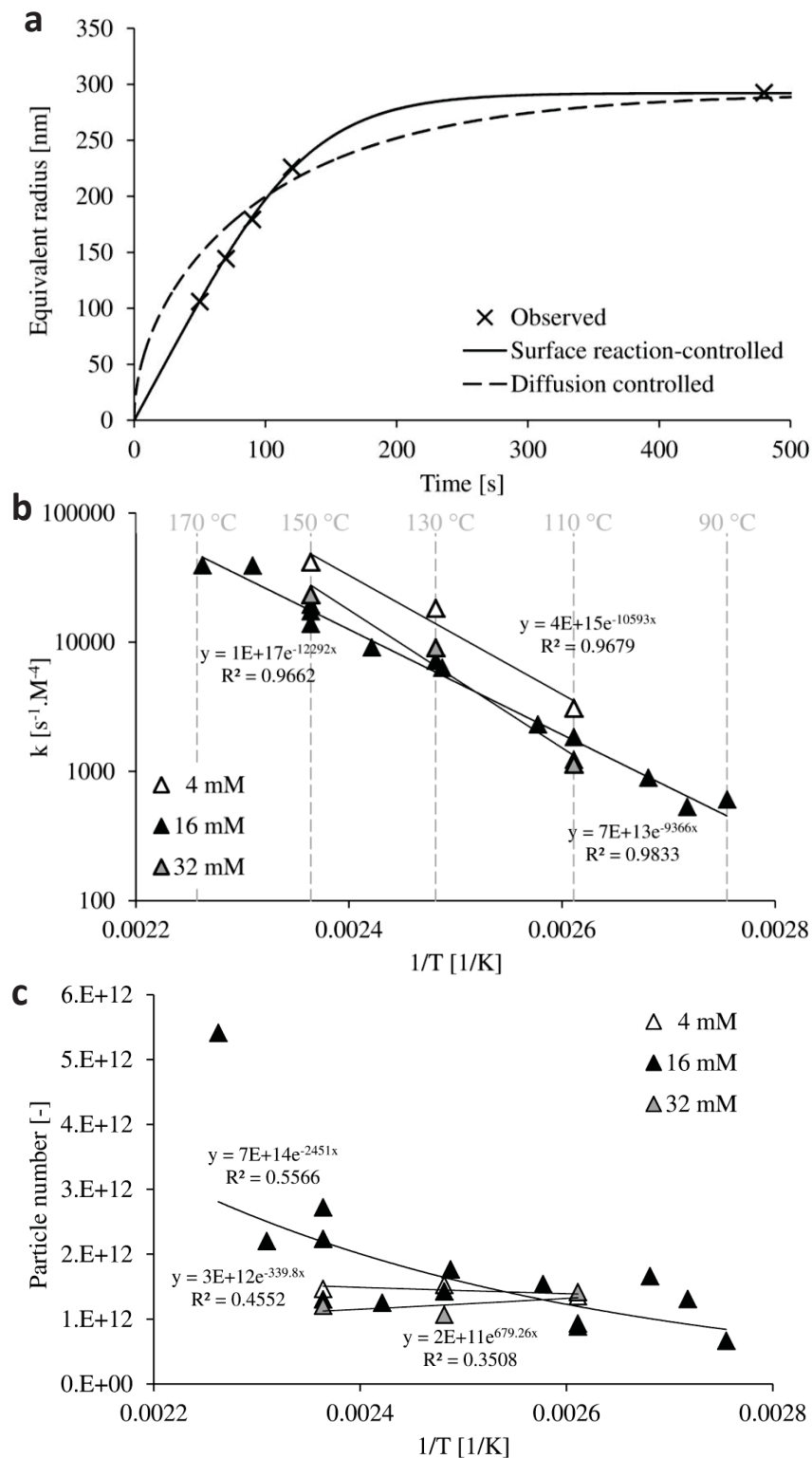


**Figure 4-9** a) Example of a fit of  $r(t)$  at 130°C, 16mM; b) reaction rate coefficient in function of  $1/T$  for ( $\Delta$ ) 4mM, ( $\blacktriangle$ ) 16mM, ( $\triangle$ ) 32mM of precursors; c) Number of particles in function of  $1/T$  for 4, 16 and 32 mM of precursors.

The observed growth curves were fitted numerically with a reaction-controlled and a diffusion-controlled model (equations 6 and 7; Figure 4-9a). Importantly, the values of  $[M_0]$  were corrected with the phase analysis from the XRD results (Table 4-1) to only consider the amounts of precursors

that were effectively used to grow the  $\beta$ -TCP particles and neglect the ions that were used to grow other crystalline phases (comparisons with uncorrected  $[M_0]$  values are presented in Figure 4-10).

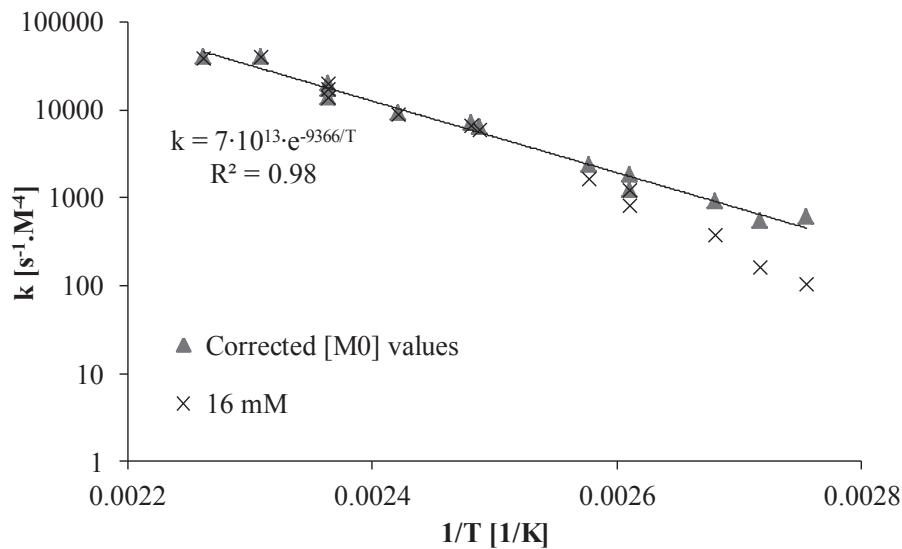


**Figure 4-10** Reaction rate coefficient in function of  $1/T$  for (x) 16 mM of precursors and for (▲) a corrected precursor concentration  $[M_0]$  according to the crystalline phase composition measured by XRD and Rietveld analysis. Without considering that a part of the precursors was used to precipitate other phases (like monetite at lower temperature), the reaction rate coefficient was clearly underestimated, leading to a non-exponential behaviour, i.e. the activation energy (proportional to the slope) decreases with an increase of temperature, which does not follow the Arrhenius law.

Both equations led to good fits, with average regression coefficients ( $R^2$ )  $> 0.94$  in both cases. Two of the 14 experiments could not be fitted properly due to a lack of experimental data point in the growing phase. Seven experiments were slightly better fitted with the diffusion-controlled equation and 5 were slightly better fitted with the surface-controlled equation, but the differences in  $R^2$  values never exceeded 0.03. Fitting the data with the surface-controlled model led to nucleation times close to zero, while using the diffusion-controlled model led to positive nucleation times, increasing up to a few minutes at low reaction temperatures (Figure 4-11).



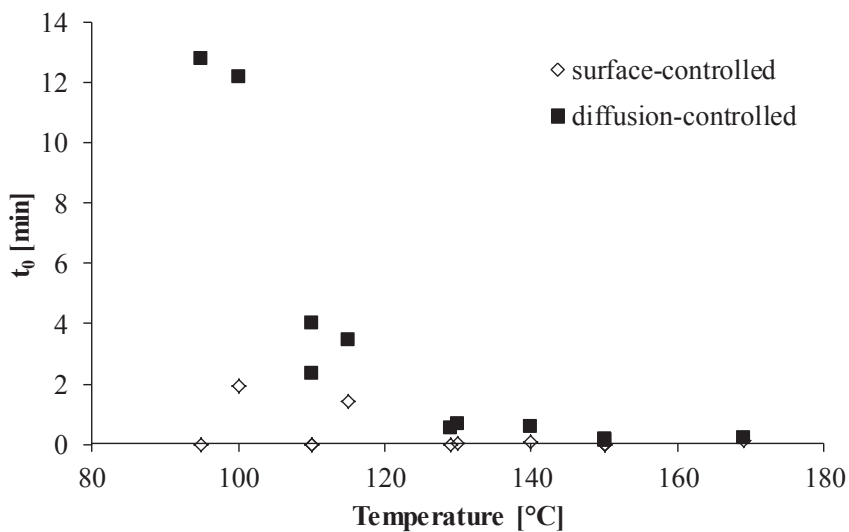


**Figure 4-11** Nucleation time calculated from the numerical fits of the data with the surface-controlled and the diffusion-controlled equations. According to the diffusion-controlled model, the lower the reaction temperature was, the later started the crystallization. No significant nucleation time increase was observed with the surface-controlled simulation.

Interestingly, the diffusion coefficients calculated with Equation 7 were extremely low, typically close to  $10^{-14}$   $\text{m}^2\cdot\text{s}$ . Such low diffusion coefficients suppose very large diffusion entities (Figure 4-12), calculated with the Stokes-Einstein equation (Eq. 11).

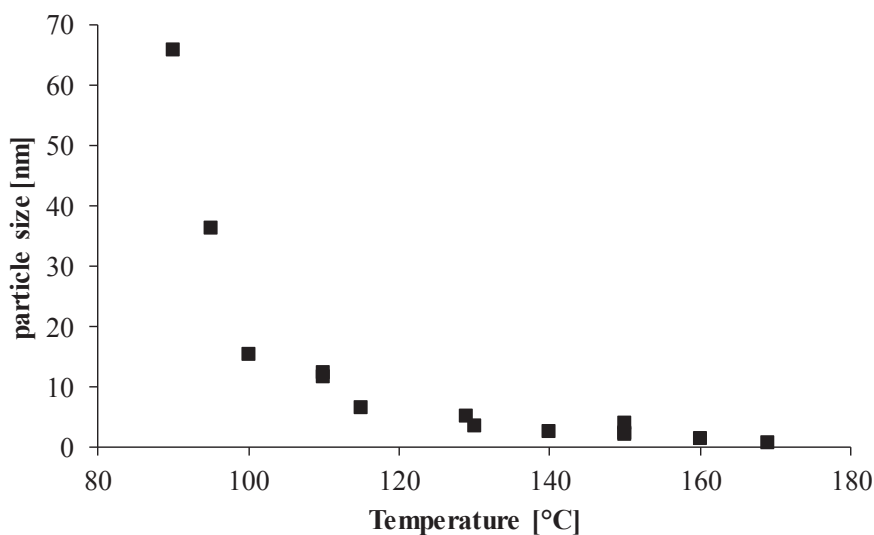


**Figure 4-12** Size of the diffusion units according to the diffusion coefficients obtained with the diffusion-controlled model.

The growth rate strongly increased with increase of temperature but was only slightly affected by the precursors' concentration (Figure 4-9b). The activation energy for the crystallization reaction was obtained by plotting the reaction constant as a function of the inverse of temperature (Figure 4-9b). Values of  $88 \pm 16$ ,  $78 \pm 3$  and  $102 \pm 19$   $\text{kJ/mol}$  were obtained at 4, 16 and 32  $\text{mM}$ .

The particle concentration was also retrieved from the numerical fits (Eq 9, Figure 4-9c). With the exception of the particles obtained at 170 °C, the particle concentration did not vary much with temperature and appeared to be independent of the initial concentration.

## Discussion

The aim of the present study was to determine the growth kinetics of  $\beta$ -TCP particles, aiming that a better control of the aspect ratio of  $\beta$ -TCP particles could eventually be achieved. For that purpose,  $\beta$ -TCP particles were produced at various concentrations (4, 16, and 32 mM) and temperatures (from 90 to 170 °C) since Levenspiel [4] mentioned that these were the two most important parameters affecting the growth kinetics of particles.

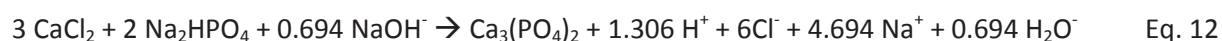
### Nucleation and assembly mechanism

In the current study, a gel-like substance was detected in the first stages of the reaction and could be separated from the supernatant by centrifugation. This observation suggests that this gel consisted of a large continuous structure, because if it was made of small individual parts, they would not sediment by centrifugation. Tao et al [13, 14] identified this phase as amorphous and suggested that  $\beta$ -TCP crystals form according to the crystallization process proposed by Gebauer and Cölfen [6]:  $\beta$ -TCP crystals nucleate within an amorphous phase and grow by solid conversion. However, as underlined by Hu et al [7], it is very difficult to differentiate between the latter mechanism and a simple dissolution-precipitation reaction. Since no TEM observations were performed in the present study to follow the occurrence and growth of  $\beta$ -TCP nuclei, it is neither possible to contradict nor to confirm the theory of Tao et al. Other nucleation mechanisms could be used to describe the nucleation of beta-calcium phosphate [15-18] but such a discussion is beyond the scope of this work.

Nevertheless, several important observations can be made. First, the various numerical fits performed in the frame of this study (Figure 4-9a) suggest that  $\beta$ -TCP particles formed very early in the synthesis reaction or, in other words, that the nucleation time was very short or even instantaneous. Indeed, even though the nucleation time was a fitting parameter, its value was mostly equal to zero in the surface-controlled model. Second, small  $\beta$ -TCP crystals were only observed at the initial stages of the reaction (Figure 4-1 and Figure 4-2). Third, the particle size distribution remained very narrow throughout the reaction (Figure 4-6d). Kwon et al. [5] referred to this phenomenon as a “burst nucleation”. In such a case, the concentration rapidly drops after particle nucleation, hence impairing further nucleation and promoting crystal growth [5]. As a consequence, all crystals reach roughly the same size at the same moment (for a given temperature) and the crystal size distribution

is very narrow all along crystal growth (Figure 4-6d). This emphasizes that the nucleation process in the present system can effectively be neglected in the kinetics study of the growing phase. Even though the data collected in this study follows Kwon's theory, a more detailed look shows that nucleation cannot stop due to a drop of concentration. Indeed, nucleation was very rapid in samples containing a 4 mM precursor concentration. So, logically, nucleation should be very intense during the consumption of at least 12 mM of the precursors in samples containing a 16 mM initial precursor concentration. Also, an increase of precursor concentration should increase the number of particles and decrease their size. However, this was not observed experimentally, suggesting that a different mechanism must occur.

So far, it was assumed that pH (or rather H/OH ratios) values were kept constant. Indeed, the  $\text{Na}_2\text{HPO}_4 / \text{NaOH}$  molar ratio (= 2.88) was kept constant throughout the experiments. However, since Tao et al. [14] mentioned that the gel had a chemical composition close to that of  $\beta$ -TCP, its formation should acidify the solution via the following reaction:



Preliminary in situ pH measurements support this explanation. From Eq. 12, the absolute amount of  $\text{H}^+$  ions released during the reaction is expected to increase with the precursors' concentration, i.e. lower pH values would be present within the precipitation reaction at high precursor concentrations. Since calcium phosphate solubility increases with a decrease of pH [19], the increase of supersaturation due to the increase in the initial precursor concentration could be annealed by the decrease of pH. This could explain why a change of concentration from 4 to 32 mM did not lead to an eightfold increase in particle concentration.

Once the crystallization reaction was completed,  $\beta$ -TCP crystals did not change in size or shape. For example, no change of crystal size and shape was observed between 2 min and 24 hours of reaction at 16 mM and 150 °C (Figure 4-1). This is surprising because Ostwald [20] predicted that small crystals should dissolve and redeposit on the surfaces of large thermodynamically more stable crystals. However, Ostwald ripening occurs when the driving force for crystallization is weak, i.e. some particles may dissolve, while others keep growing. In fact, it depends on the sensitivity of the solubility to the size of the particles. If it is high, like for nanocrystals, then the smallest easily dissolve and the largest grow more, but for larger particles the effect of Ostwald ripening is much lower [21]. In the present case, the particles were apparently large enough to keep this phenomenon low in most cases. Indeed, the size distribution tended to become broader at lower temperature and concentration (Figure 4-6d), i.e. at lower supersaturation [22]. Practically, this result suggests that longer reaction times cannot be used to enhance the platelet diameter and aspect ratio.

## Reaction kinetics

Large amounts of monetite were detected at low temperature and high concentration. However, there was no evidence that the formation of this calcium phosphate phase affected  $\beta$ -TCP precipitation and thus its kinetics. Indeed, the reaction constants obtained at low temperature did not deviate much from the regression line  $k = f(1/T)$  (Figure 4-9b). Strong effects would be expected if DCP formed before  $\beta$ -TCP, but since it was not possible to perform XRD measurements during the synthesis reaction (too small aliquots), the sequence of calcium phosphate formation could not be determined. Also, SEM measurements did not reveal a clear difference in the time of DCP and  $\beta$ -TCP formation.

The experimental data collected in this study suggests that under the used conditions  $\beta$ -TCP growth is not diffusion-controlled, but reaction-controlled, even if both model show good fits (Figure 4-9a). First, no change of reaction rate was observed with a change of concentration (Figure 4-9b), which is unexpected for a diffusion-controlled reaction. Second, the diffusion coefficients calculated with the diffusion-controlled model were clearly unrealistic. Third, the high activation energies are characteristic of surface-controlled reactions, and last, Kweon and Hyeon [5] mentioned that the growth of sub-micrometric particles is generally reaction-controlled.

In the kinetics analysis performed here, it was assumed that the retrieval time corresponded to the reaction time. However, it took a few seconds to aspirate the sample and to cool it down. Therefore, it is likely that the reaction time was slightly underestimated. Whereas it did not really matter for long reaction times or slow reactions at low temperature, it certainly mattered for aliquots retrieved within the first minute of reaction for reactions performed at high temperature. These very fast reactions also limited the number of samples that could be retrieved during crystal growth. At lower temperatures, other problems were encountered. Indeed, it was difficult to precisely control the temperature during the whole crystallization because the reactions extended over several hours.

## Control of size and aspect ratio

Temperature changes hardly influenced  $\beta$ -TCP crystal size and shape except for a strong decrease at very high temperature (Figure 4-6e-g and Figure 4-8). However, it is a useful mean to limit monetite formation (Table 4-1), accelerate  $\beta$ -TCP synthesis (Figure 4-9b), and narrow  $\beta$ -TCP size dispersion (Figure 4-6h).

The results presented in this study show that  $\beta$ -TCP platelets grew mostly in width and not in thickness (Figure 4-6). Moreover, the nucleation was apparently insensitive to concentration changes (Figure 4-9c). Therefore, a change of the precursor's concentration is expected to strongly affect  $\beta$ -

TCP aspect ratio. Indeed, increasing the concentration appeared to be the most efficient way to increase the diameter and aspect ratio of  $\beta$ -TCP platelets (Figure 4-4 and Figure 4-6). Unfortunately, the solubility of the phosphate precursor was limited and DCP and Cl-Ap precipitated at high precursor concentrations (Table 4-1). The presence of DCP at high concentration was explained by Galea et al [1] by an acidification of the solution due to  $H^+$  release from the  $Na_2HPO_4$  precursor (See Eq. 11). Indeed, DCP is stabilized at low pH [19]. Hence, more NaOH might be necessary to maintain the  $H^+$  amount independently of the concentration. A few preliminary tests were done, but increasing the  $OH^-$  amount clearly slowed down  $\beta$ -TCP growth and strongly delayed nucleation, leading to mainly amorphous samples. Also, the aspect ratio was reduced. A continuous titration over time might be a better solution, but is difficult to apply here due to the difficulties in measuring a pH value in a non-aqueous medium above 100 °C.

Since the thickness of  $\beta$ -TCP particles was hardly affected by changes of the crystallization conditions, another approach to control the particle size would be to decrease the number of particles. For example, an increase in the surface energy of the nuclei should increase the critical size, hence decreasing the nucleation rate and the number of nuclei [5]. This approach will be considered in futures experiments, with for example a solvent change, addition of foreign ions or change of precursors as Tao et al. demonstrated that this might influence the crystal face stability.

As a last note, the formation of almost spherical  $\beta$ -TCP particles at 170 °C (Figure 4-8b) has to be underlined. To the best of our knowledge, this is the first study reporting the synthesis of such shaped particles with an average particle size of  $\approx 400$ nm. In our previous article [1], the particles obtained at 170 °C resembled more to those presently obtained at 160 °C (Figure 4-8a). This difference might be explained by an improvement in the control of the temperature during the initial stages of the reaction.

## Conclusions

The precipitation of calcium and phosphate ions in ethylene glycol effectively led to the production of sub-micrometric  $\beta$ -TCP hexagonal platelets. The reaction temperature had a strong influence on the reaction rate but hardly affected the  $\beta$ -TCP platelets size ( $\varnothing \approx 600 - 1000$  nm) and aspect ratio ( $s \approx 4.5 - 6.5$ ). The precursors' concentration strongly influenced the size and aspect ratio of the platelets ( $\varnothing \approx 400 - 1700$  nm and  $s \approx 3 - 15$ ), but with no significant influence on the reaction kinetics. The analysis of the numerical fits of the growth curves revealed that the reaction was most likely reaction-controlled even though excellent fits were also obtained with a diffusion controlled model ( $R^2 > 0.94$ ). This conclusion was supported by the high activation energies (close to 80 - 100 kJ/mole)

and the very low diffusion coefficients calculated from the fits. A surprising result was the fairly constant number of particle observed in the different experiments conducted at various concentrations. As a result, the particle diameter strongly increased with an increase in precursors' concentration (5-fold increase for an 8-fold increase in concentration).

Working at high concentrations and high temperature is advantageous to rapidly produce platelets with large diameter and aspect ratio of the platelets, but high concentrations also lead to an increase of monetite and Cl-Ap by-product, i.e. inhomogeneities in composition and size. Ideal working conditions for phase-pure  $\beta$ -TCP of high aspect ratio were found at 16 mM concentration, 150 °C, and > 2 minutes reaction time. Since the maximum aspect ratio seen for pure  $\beta$ -TCP samples was limited to 5-6, it is doubtful that these platelets might be efficient reinforcement particles for brick-and-mortar composites.

## References

- [1] Galea L, Bohner M, Thuering J, Doebelin N, Aneziris CG, Graule T. Control of the size, shape and composition of highly uniform, non-agglomerated, sub-micrometer  $\beta$ -tricalcium phosphate and dicalcium phosphate platelets. *Biomaterials*. 2013;34:6388-401.
- [2] Gao H. Application of fracture mechanics concepts to hierarchical biomechanics of bone and bone-like materials. *International Journal of Fracture*. 2006;138:101-37.
- [3] Bonderer LJ, Studart AR, Gauckler LJ. Bioinspired design and assembly of platelet reinforced polymer films. *Science*. 2008;319:1069-73.
- [4] Levenspiel O. *Chemical reaction engineering*. Second Edition ed: John Wiley & Sons; 1972.
- [5] Kwon SG, Hyeon T. Formation mechanisms of uniform nanocrystals via hot-injection and heat-up methods. *Small*. 2011;7:2685-702.
- [6] Gebauer D, Cölfen H. Prenucleation clusters and non-classical nucleation. *Nano Today*. 2011;6:564-84.
- [7] Hu Q, Nielsen MH, Freeman CL, Hamm LM, Tao J, Lee JRI, et al. The thermodynamics of calcite nucleation at organic interfaces: Classical vs. non-classical pathways. *Faraday Discussions*. 2012;159:509-23.
- [8] Einstein A. On the Movement of Small Particles Suspended in Stationary Liquids Required by the Molecular-Kinetic Theory of Heat. *Annalen der Physik*. 1905;17:549-60.
- [9] Rodriguez-Carvajal J. Recent Developments of the Program FULLPROF. *Commission on Powder Diffraction (IUCr) Newsletter*. 2001;26:12-9.
- [10] Schroeder LW, Dickens B, Brown WE. Crystallographic studies of the role of Mg as a stabilizing impurity in b-Ca<sub>3</sub>(PO<sub>4</sub>)<sub>2</sub>. II. Refinement of Mg-containing b-Ca<sub>3</sub>(PO<sub>4</sub>)<sub>2</sub>. *Journal of Solid State Chemistry*. 1977;22:253-62.
- [11] Dickens B, Bowen JS, Brown WE. A refinement of the crystal structure of CaHPO<sub>4</sub> (synthetic monetite). *Acta Cryst*. 1971;B28:797-806.

- [12] Hughes JM, Cameron M, Crowley KD. Structural variations in natural F, OH, and Cl apatites. *American Mineralogist*. 1989;74:870-6.
- [13] Tao J, Jiang W, Zhai H, Pan H, Xu R, Tang R. Structural components and anisotropic dissolution behaviors in one hexagonal single crystal of b-tricalcium phosphate. *Crystal Growth and Design*. 2008;8:2227-34.
- [14] Tao J, Pan H, Zhai H, Wang J, Li L, Wu J, et al. Controls of tricalcium phosphate single-crystal formation from its amorphous precursor by interfacial energy. *Crystal Growth and Design*. 2009;9:3154-60.
- [15] Baumgartner J, Dey A, Bomans PHH, Le Coadou C, Fratzl P, Sommerdijk NAJM, et al. Nucleation and growth of magnetite from solution. *Nature Materials*. 2013;12:310-4.
- [16] Dorvee JR, Veis A. Water in the formation of biogenic minerals: Peeling away the hydration layers. *J Struct Biol*. 2013;183:278-303.
- [17] Wolf SE, Leiterer J, Kappl M, Emmerling F, Tremel W. Early homogenous amorphous precursor stages of calcium carbonate and subsequent crystal growth in levitated droplets. *J Am Chem Soc*. 2008;130:12342-7.
- [18] Habraken WJEM, Tao J, Brylka LJ, Friedrich H, Bertinetti L, Schenk AS, et al. Ion-association complexes unite classical and non-classical theories for the biomimetic nucleation of calcium phosphate. *Nature Communications*. 2013;4:Article number 1507.
- [19] Vereecke G, Lemaitre J. Calculation of the solubility diagrams in the system  $\text{Ca}(\text{OH})_2\text{-H}_3\text{PO}_4\text{-KOH-HNO}_3\text{-CO}_2\text{-H}_2\text{O}$ . *J Crystal Growth*. 1990;104:820-32.
- [20] Ostwald W. Studien uber die Bildung und Umwandlung fester Korper. *Z Phys Chem*. 1897;22:289.
- [21] Talapin DV, Rogach AL, Haase M, Weller H. Evolution of an ensemble of nanoparticles in a colloidal solution: Theoretical study. *Journal of physical chemistry B*. 2001;105:12278-85.
- [22] Sugimoto T. Preparation of monodispersed colloidal particles. *Advances in Colloid and Interface Science*. 1987;28:65-108.





## CHAPTER 5:

### STRUCTURAL DESIGN OF BIO-INSPIRED COMPOSITES BY

### SOLVENT CASTING

#### ***Abstract***

Present synthetic bone graft substitutes do not combine strength, toughness and biodegradability. Many attempts to mix ductile polymers with strong ceramic particles have already been reported, but high strength and toughness have not been combined with biodegradability. In this study, CaP platelets obtained by precipitation in ethylene glycol were mixed with chitosan solutions, casted and dried. Those particles were chosen because of their very low agglomeration, uniformity in size and shape and large aspect ratios ( $s$ ):  $\beta$ -tricalcium phosphate ( $\beta$ -TCP) platelets with  $s \approx 6$ , and dicalcium phosphate (DCP) platelets with  $s \approx 25$  were compared. Addition of  $\beta$ -TCP platelets had a negative effect on the tensile properties probably due to very low alignment during solvent evaporation. Moreover, the interfaces were too short to transfer stresses to the ceramics and the films broke through the organic phase, at even lower strength than in case of pure polymer films. The use of DCP platelets was more successful than  $\beta$ -TCP: up to 15 vol-% of platelets could be incorporated and aligned, with a positive impact on the strength of the films ( $\sigma_y = 110$  MPa and  $\sigma_t = 160$  MPa for DCP-reinforced against  $\sigma_y = 80$  MPa and  $\sigma_t = 120$  MPa for pure chitosan). Above this threshold value, alignment decreased leading to percolation and strength abruptly decreased, sometimes even below the strength of pure matrix material. Alignment of the platelets was further improved by decorating the DCP platelets with nano iron oxide particles and orienting them in a rotating magnetic field. Increase of strength was observed up to 20 vol-% ceramic (+ 20%), then percolation occurred. However, some ductility ( $\epsilon \geq 5$  %) was maintained over the all tested range (up to 25 vol-% platelets).

Publication in preparation:

Galea L, Bohner M, Erb R, Doebelin N, Aneziris CG, Studart A, Graule T. *Structural Design of Bioinspired Composites for Degradable Bone Graft Substitutes*. (2015?).

## Foreword

The general aim of this thesis is to obtain composite materials combining strength, toughness and resorbability, in particular with a nacre-inspired brick-and-mortar architecture. The two first chapters of this thesis were dedicated to the synthesis of the adequate “bricks”, i.e. calcium phosphate (CaP) platelets [1]. The two following chapters (chapters 3 and 4) focus on the assembly technique of the platelets with an organic glue and the characterization of the resulting composites, with emphasis on structure-mechanics relationship.

## Introduction

The ideal bone substitute should degrade over time and have bone-like mechanical properties at least in the first implantation stages to avoid the use of fixation devices like non-resorbable metallic screws and plates. Presently, **no synthetic material offers the combination of bioresorbability, osteoconductivity, biocompatibility and load-bearing properties**. Indeed, mechanically strong materials are generally also chemically stable, hence they rarely combine the desired biocompatibility, osteoconductivity and degradability/resorbability by living organisms in biological conditions. In contrast, biodegradable materials, such as porous CaP and resorbable polymers, are usually mechanically weak due to weak chemical bonds [2].

However, some natural materials show that combining strength, toughness and biodegradability is feasible. Despite being made of weak constituents a variety of natural composites with nano or sub-micro reinforcing phases exhibit very good mechanical properties [3-9]: bone and dentin are made of about 45 vol-% nanocrystals (2-4 nm thick, up to 100 nm long, aspect ratio 30-40) of calcium phosphate in a collagen matrix and possess tensile strengths of 70 – 150 MPa [4, 7, 10] and 52 MPa [11], respectively; nacre is made of 95 vol-% sub-micron (a few micrometers long and 200-500nm thick, aspect ratio  $\approx$  10) aragonite crystals in a protein matrix and possess a flexural strength of 70 – 210 MPa [8, 9]; enamel is made of 90 vol-% apatite crystals and has a tensile strength of 10 MPa [11]. The toughness or work of fracture of those materials generally ranges between 2 and 12 MPa·m<sup>½</sup> [4, 9, 12-14] or 1 and 10 J/m<sup>2</sup> [11], respectively. For comparison, pure components like hydroxyapatite and collagen have tensile strengths of 200 MPa [15] and 20 MPa respectively, and a toughness lower than 1 MPa·m<sup>½</sup> for pure hydroxyapatite [4].

Taking inspiration from natural materials like nacre or bone, many attempts have been done to combine brittle ceramic particles and ductile polymer matrices [16-21] in the hope of reaching

mechanical properties similar to those of bone. However, the results are still far away from the goals [22]. The main reason for the discrepancy between natural and synthetic composites is certainly the lack of control over the microstructure. Indeed, nature also uses weak components but assembles them in hierarchical architectures, with well-defined sizes, shape and arrangement of building blocks which finally generate strong and tough composites structures [23]. The relationships between the mechanical and structural properties of natural strong and tough materials like bone or nacre have been widely studied [4-9]. The size, proportion and arrangement of the different phases seem to be the result of a driven optimisation using the available materials [24].

Considering the same principles, it should be possible to design artificial composites with biocompatible and bioresorbable materials that combine strong and tough properties [25].

Synthetic “brick-and-mortar” structures similar to that of nacre have already been investigated and demonstrated the importance of controlling structural features to improve mechanical properties. However, at least one constituent, generally the reinforcement elements, was not degradable. Alumina platelets and PMMA matrix have for example been associated [26, 27], leading to strength and toughness values superior to the ones of bone (flexural strength: 200MPa, 30 MPa·m<sup>1/2</sup>). Alumina platelets have also been aligned by dip-coating combined with spin-coating of chitosan [25], or in various matrixes in a magnetic field [28]. Clay/polymer nanocomposites exhibited tensile strength up to 400 MPa with deformations close to 0.3 %, but elongations as large as 10 % for samples with a strength of 100 MPa [29]. The good results obtained in those studies not only arise from strong basic constituents, but are largely explained by a well-ordered structure of the composites, sometimes down to the nanoscale, which allowed very effective load transfer between the constituents.

The present work aimed at combining CaP platelets with biodegradable polymer matrices in a well-ordered manner. In a first step, CaP platelets combining adequate size and aspect ratio were required to reach maximum mechanical properties of the ceramic itself. CaP platelets obtained by precipitation in organic medium [1] fulfil these requirements. They are non-agglomerated, uniform and have well-defined shape and size. The platelets thickness is below 300 nm (i.e. below CaP critical thickness, assuming that  $\sigma_t$  is 1 % of E, see Chapter 2), and the aspect ratio is in the range of 3-6 for  $\beta$ -TCP platelets and of 15-25 for DCP platelets. Hence, the latter particles should be ideal for the synthesis of composites with biopolymers like chitosan (see theoretical calculations in Chapter 2). However, it was decided to also investigate the composites with  $\beta$ -TCP platelets to control the theoretical calculations. Then the CaP particles were decorated with magnetic nanoparticles to allow alignment in a magnetic field. Once embedded in an organic matrix, the magnetic orientation was

fixed during setting or drying (solvent casting). By this mean, composite materials with defined architectures over millimeter range were made from completely degradable materials.

## Experimental section

### Synthesis of resorbable ceramic platelets

Hexagonal  $\beta$ -tricalcium phosphate ( $\beta$ -TCP;  $\beta$ -Ca<sub>3</sub>(PO<sub>4</sub>)<sub>2</sub>) platelets and prismatic monetite (DCP, CaHPO<sub>4</sub>) platelets were obtained by precipitation of calcium and phosphate ions in ethylene glycol, following the procedure described in Chapter 3 and by Galea *et al.* [1]. Briefly, calcium and phosphate precursors (CaCl<sub>2</sub>·2H<sub>2</sub>O, Reag.Ph.Eur., art. n°1.02382, MERCK, Darmstadt, Germany, and Na<sub>2</sub>HPO<sub>4</sub>·2H<sub>2</sub>O, purum p.a., art. n° 71645, Fluka, Buchs, Switzerland) were dissolved in ethylene glycol (C<sub>2</sub>H<sub>6</sub>O<sub>2</sub>, Reag.Ph.Eur., art. n° 85512.360, VWR, Nyon, Switzerland) and mixed at 150 °C. The precipitate was separated by centrifugation. The particles were then characterized by scanning electron microscopy (SEM EVO MA25, Zeiss, Germany) for crystal size determination, by X-ray diffraction (XRD, X'Pert Pro MPD, Panalytical, Almelo, the Netherlands) for crystalline phase identification (Rietveld refinement) and by laser diffraction particle size analyser (LS 13 320, Beckman-Coulter, Krefeld, Germany) to determine the particle size, respectively the agglomeration rate.

### Solvent casting to prove the reinforcement efficiency of DCP platelets

Before trying to structure the ceramic platelets in a biopolymer matrix with a magnetic field, solvent casting with non-magnetized platelets was investigated. A 2 wt-% chitosan (from crab shells, highly viscous, art. n° 48165 Sigma, Saint-Louis, MO, USA) solution was prepared in 0.1 M acetic acid (art. n° 8.18755 MERCK) and mixed over night for complete dissolution. The desired amount of this solution was poured into a glass beaker. The corresponding ceramic platelets amount was dispersed in a plastic tube (art. n° 216-0154, VWR International, RADNOR, PA, USA) in 3 mL of demineralized water by thorough mixing on a vortex (art. n° 444-0202, VWR international, RADNOR, PA, USA) and 1 min ultrasonication. The platelets suspension was added to the chitosan solution. Since platelets were glued on the tube walls, the tubes were rinsed 3 times with 1 mL of demineralized water and vortexing. In total, 6 mL of water were thus added to each sample. The platelets and the hydrogel were mixed for several minutes with a static mixer at 300 RPM until complete visual homogeneity. The glass beakers were then placed in a desiccator and vacuum was applied by cycles until no more bubbles formed. The suspensions were poured into cubic Teflon molds (side dimensions: 45 mm, "Moul'flex", art. n° 1996.01, de Buyer, France) and placed again under vacuum until no more bubbles

formed. The molds were finally placed in a desiccator with silica gel and the suspensions allowed to dry for 4 days in ambient conditions, followed by drying at 40 °C for 3 additional days. Before mechanical testing, all films were heated for 2 hours at 60 °C. Tensile test samples were punched out (cut with a die) of the films in dog bone-shape (Figure 5-1) and their individual thickness measured on 3 points along the thin central part. The value of the measurement which was the closest to the breaking point (usually the lowest) was used for the strength calculation.

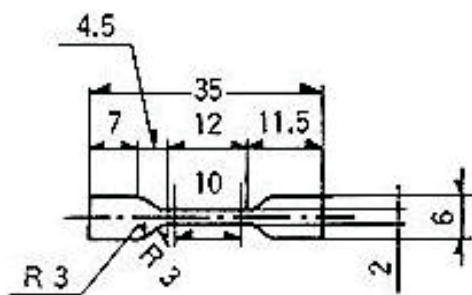


**Figure 5-1** Dimensions of the tensile test specimens punched out of chitosan or composite films, according to the norm DIN EN ISO 527-2, Type 5B. The thickness varied for each sample and was measured individually on 3 points along the thin part.

After tensile testing, the ruptured surfaces of the samples were observed by SEM with secondary electron imaging (SE). Intact samples were vertically embedded and polished for observation by back scattered electrons (BSE) for phase analysis.

Film wastes from tensile samples cutting were used for platelets alignment measurement by XRD analysis. Using a rocking curve technique [30], the angle variation of the crystals relative to the sample plane could be calculated.

### **Magnetization of the platelets**

Only DCP platelets were used for this part. Since the surface charge of the DCP platelets was not known, both positively charged and negatively charged water based ferrofluids (EMG-605 and EMG-705, Ferrotec, Bedford, USA) were tested. The 12 nm iron oxide particles in the ferrofluids are coated with cationic (EMG-605) or anionic (EMG-705) surfactant, which leads to electrostatic adsorption of the magnetic particles on oppositely charged ceramic particles. 18.75  $\mu\text{L}$  of each ferrofluid were dispersed separately in 1 mL of demineralized water and vortexed for 1 minute. 50 mg of DCP platelets were dispersed in 9 mL of demineralized water, vortexed for 1 minute, and ultrasonicated for 1 minute. The ferrofluid suspensions were then added dropwise to the stirring DCP suspensions. Mixing was pursued for 30 minutes and then centrifugation at 4000 RPM for 5 minutes allowed separating the DCP particles. Adhesion of the nanoparticles to the CaP particles was determined visually: the brown nanoparticles only sedimented in water when bound to larger particles like the

sub micro-CaP ones. Hence, a clear liquid phase with a brown sediment indicates adhesion, while a white sediment in a brown liquid phase indicates no adhesion.

The decorated platelets were then rinsed once with ethanol, centrifuged and dried overnight at 30 °C under vacuum.

The responsiveness of decorated DCP platelets in a magnetic field was investigated by observing water-based suspension under a reflected light microscope and applying a vertical magnetic field (VF) via a handheld permanent magnet.

Vertical magnetic field only induces 1D alignment, since the platelets are still free to rotate around the vertical axis. To obtain an in-plane (2D) alignment of the platelets, a vertical rotating field (VRF) [28] was required. Feasibility of planar alignment of the DCP platelets within a VRF was first tested in easily hardening matrices. The magnetized platelets were mixed with isobornyl acrylate (IBOA, art. n° 392103, Aldrich, Saint-Louis, MO, USA) with 1 vol-% 2-hydroxy-2-methylpropiophenone (art. n° 405655, Aldrich, Saint-Louis, MO, USA) as initiator and casted into lids of 2 mL-centrifugation tubes (about 8 mm in diameter, 3 mm high). The slurry was placed over a rotating magnet (50.8 x 50.8 x 25.4 mm neodymium, art. n° Q-51-51-25-N, Supermagnete, Switzerland) and exposed from the top to UV light (Omniculture Series 1000, EXFO, Mississauga, Ontario, Canada). After hardening the samples were broken transversally and observed by SEM.

Thicker samples were realized with a gelatin matrix (from bovine skin, art. n°G9391, Sigma-Aldrich, Saint-Louis, MO, USA). The magnetized platelets were vortexed with a 2 wt-% gelatin suspension at 40 °C and casted into 2 mL-centrifugation tubes placed in a warm water bath over a rotating magnet. With cooling, the gelatin hardened and the samples were subsequently freeze-dried (Hetosic, Heto lab equipment, Denmark). SEM images of cross-section were then made.

### **Maintaining the orientation during drying of an hydrogel matrix**

Magnetized DCP platelets were dispersed in a 2 wt-% chitosan solution. Films and then tensile test samples were prepared as described above with the simple solvent casting method. In addition, a rotating magnet was placed as close as possible to the molds during solvent evaporation.

A first trial was done with a vertical rotating field (VRF). It was supposed that even if the platelets would stand vertically in such a field, they should align in the rotation plane, which should then be the tensile direction.

To obtain a horizontal planar alignment of the DCP platelets compatible with the alignment already obtained from the solvent evaporation, the magnet was placed on the side of the molds and rotated around a vertical axis, such as to create a rotating field in the horizontal plane (HRF), i.e. in the drying film plane.

After drying in the rotating magnetic field, the films were characterized following the same procedure as described above for the non-magnetized films.

## Results

### Synthesis of resorbable ceramic platelets

Hexagonal platelets of  $\beta$ -TCP and prismatic platelets of monetite were obtained by precipitation at different pH values. At the highest pH (pH = 9.5 in the phosphate solution), hexagonal  $\beta$ -TCP crystals were formed, and were  $151 \pm 19$  nm thick,  $844 \pm 45$  nm in diameter and thus had an aspect ratio of  $6 \pm 1$ . The size dispersion was  $0.04 \pm 0.02$ . At a lower pH (pH = 4 in the phosphate solution), prismatic DCP crystals were obtained,  $10 \pm 3$   $\mu\text{m}$  long,  $2.3 \pm 1.6$   $\mu\text{m}$  wide,  $0.21 \pm 0.06$   $\mu\text{m}$  thick, resulting in an aspect ratio of  $48 \pm 28$  in length and  $11 \pm 5$  in width (Figure 5-2). The size dispersion of the long-axis measured by image analysis of SEM pictures was  $0.27 \pm 0.08$ . Measurements of size dispersion by laser diffraction revealed the absence of agglomerates, but the size dispersions were wider than measured on SEM images (0.4 for  $\beta$ -TCP, 0.5 for DCP).

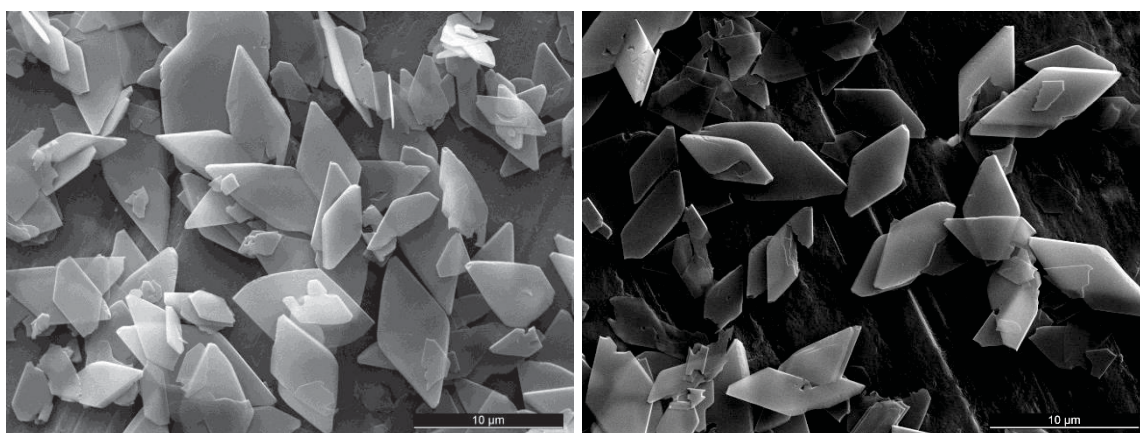


**Figure 5-2** SEM images of DCP platelets of two different batches with same conditions. Scale bars are 10  $\mu\text{m}$ .

### Solvent casting to prove the reinforcement efficiency of CaP platelets

Solvent casting with non-magnetized CaP platelets was used first. Slurries of  $\beta$ -TCP/DCP platelets and 2 wt-% chitosan solution were casted and dried to obtain composite films, generally 0.1-0.3 mm thick. Dog-bone shaped specimens were cut out of the films and tensile tested. Polished and fractured cross sections were observed by SEM.

The addition of  $\beta$ -TCP hexagonal platelets significantly decreased the mechanical performances of chitosan films. Not only the strength was decreased (Figure 5-3a), but also the stiffness and the deformation at rupture (Figure 5-3b).

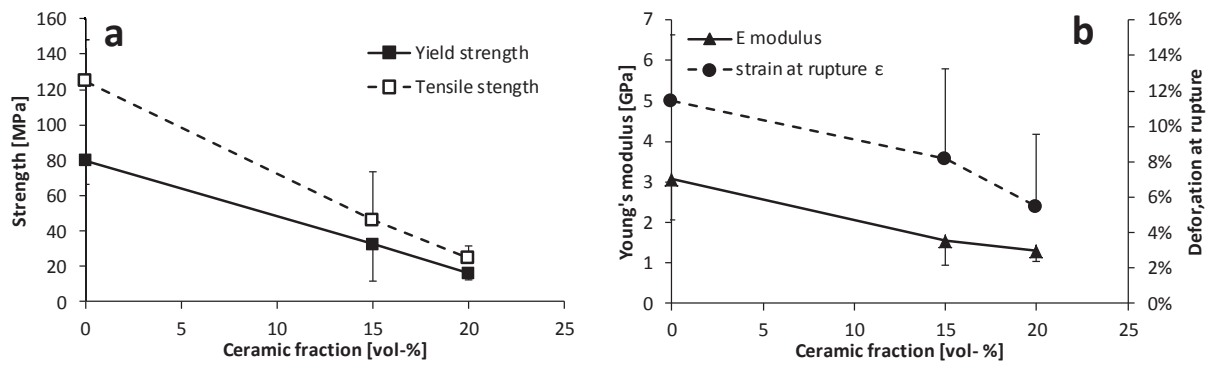


**Figure 5-3** Tensile properties of  $\beta$ -TCP reinforced chitosan in function of ceramic amount. a) the strength significantly decreases when adding  $\beta$ -TCP platelets; b) the stiffness ( $\blacktriangle$ ) and the ductility ( $\bullet$ ) of the films tended to decrease, but the trend was not significant due to large variance in the results. Remark: only half of the error bars ( $\pm 1$  SD) are represented to ease reading of the figures.

On the opposite, the addition of DCP platelets up to about 15 vol-% significantly ( $p < 0.05$ , ANOVA) increased the strength and stiffness of chitosan films (Figure 5-4a to Figure 5-4c). The increase was proportional to the ceramic volume fraction. The strain at rupture decreased with the addition of mineral platelets, but with a weak dependence on the ceramic amount (Figure 5-4d). At least 5 % of deformation were still measured in the strongest films, which is enough for the target application.

Over 15 vol-% of DCP, the stiffness further increased (Figure 5-4c), but the strength strongly decreased, even under the initial values of the pure polymeric films (Figure 5-4b).

Fractured surfaces of  $\beta$ -TCP-chitosan composite films showed poor alignment of the ceramic platelets in the film plane (Figure 5-5). No platelet seemed broken and they appeared all covered with a polymer layer. The rupture seemed to have propagated within the organic phase, without affecting the ceramic particles.



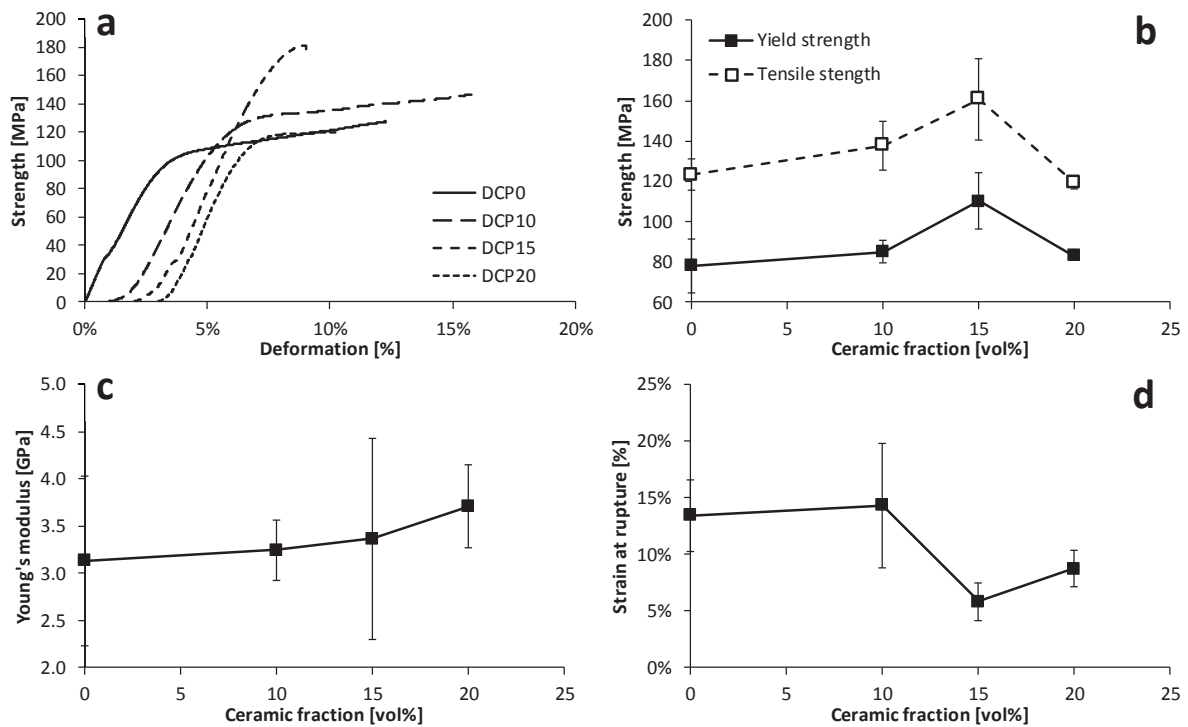


**Figure 5-4** Tensile tests performed on pure chitosan films, 10 vol-%, 15 vol-% and 20 vol-% DCP-chitosan films. a) Typical stress-strain curves of tensile tests (Note that the curves were shifted horizontally for ease of reading); b) Tensile yield strength; c) Tensile Young's modulus; d) Strain at rupture.

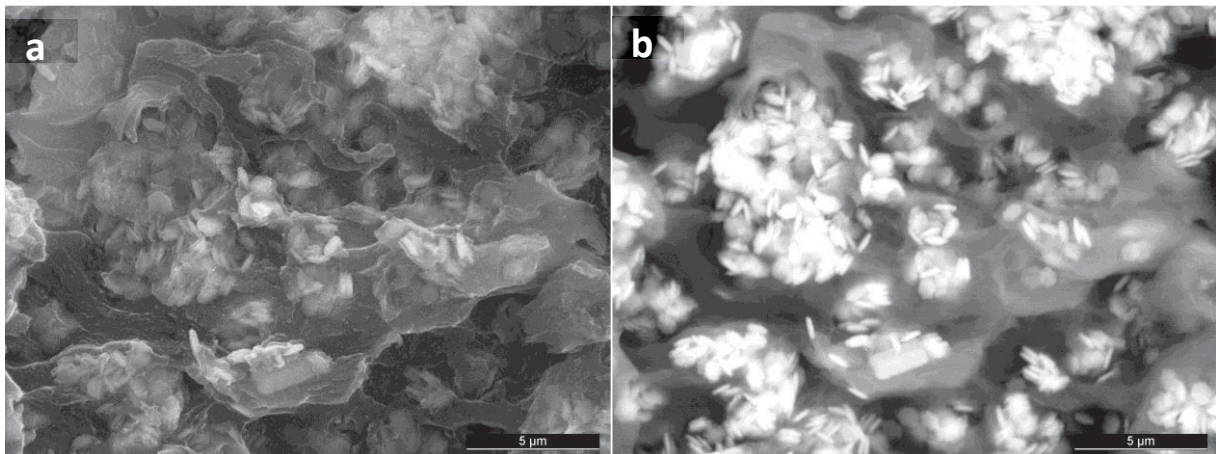


**Figure 5-5** SEM of ruptured surfaces of chitosan films reinforced with 15 vol-% of  $\beta$ -TCP platelets. a) SE image; b) BSE image.

SEM images of the fractured surfaces of DCP-chitosan samples showed a good alignment of the DCP platelets in the film plane, with some local defects like rare air bubbles, misalignment or inhomogeneities (Figure 5-6a-d). The amount of defects, especially misalignments, seemed to be the highest at 20 vol-% (Figure 5-6d). Both phases were in close contact with each other, and some polymer remnants were even found on the surface of debonded platelets (Figure 5-7). Many

defects had the shape of the platelets and many protruding platelets were observed. A few platelets appeared to be broken.

BSE images highlighted the good dispersion and alignment of the ceramic within the polymer matrix (Figure 5-6e) and holes. Platelets and polymer matrix were clearly identified by image analysis (Figure 5-6f), which confirmed the volume percentage of ceramic.

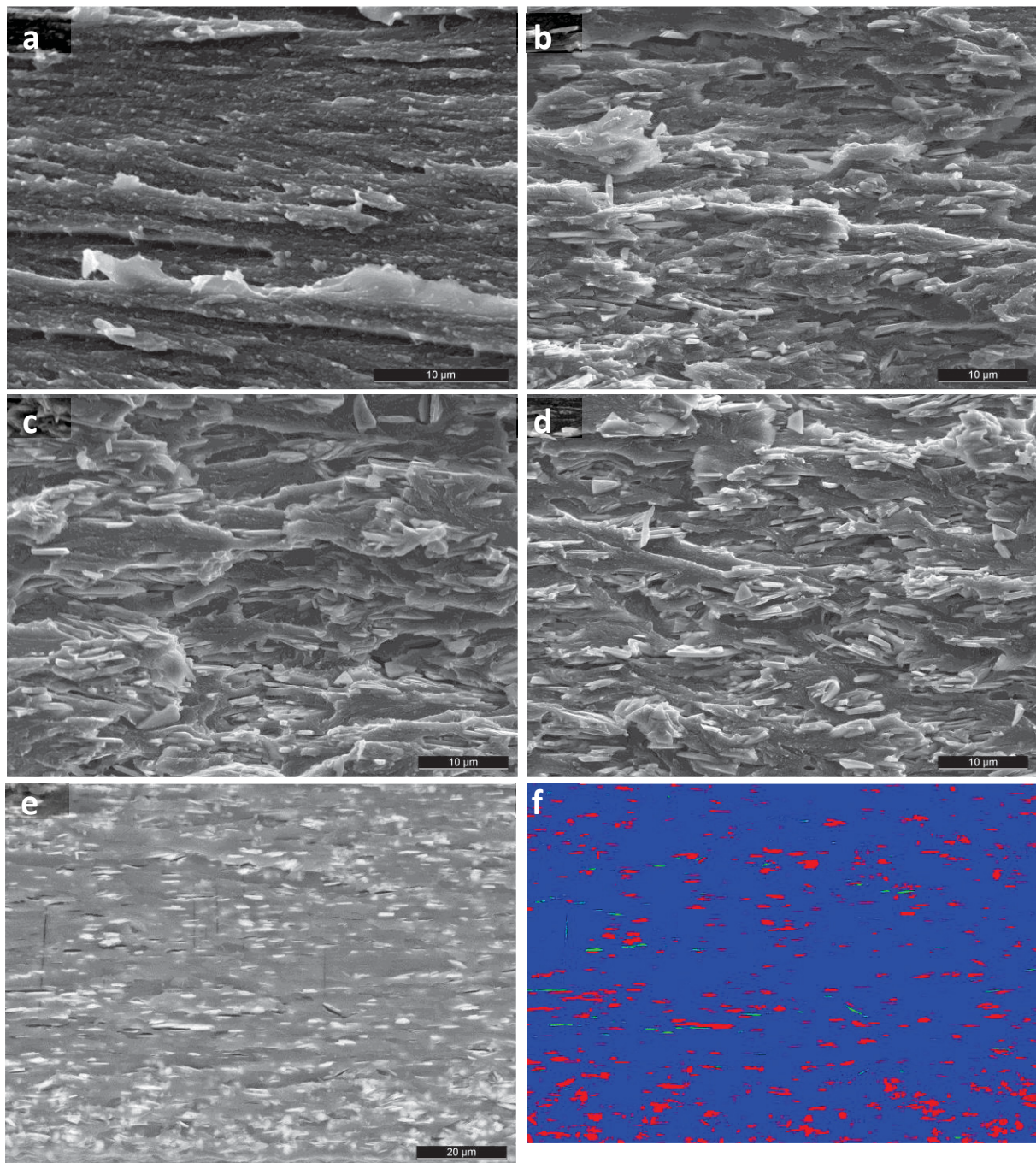


**Figure 5-6** SEM images of fracture surfaces after tensile testing of a) 0 vol-%, b) 10 vol-% and c) 15 vol-% and d) 20 vol-% DCP platelets in chitosan. Cross-section through the thickness of the films. e) BSE image of a polished cross section of a 10 vol-% sample; f) threshold analysis of picture e) with the ceramic platelets in red, the holes in green and the polymeric matrix in blue. Scale bars are 10 µm in a) to d) and 20 µm in e) and f).

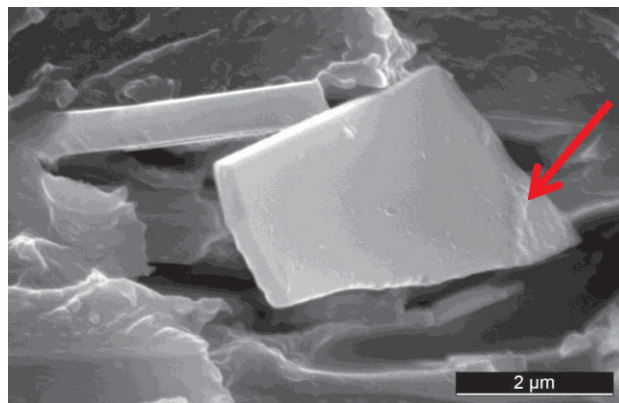


**Figure 5-7** Pieces of polymer stuck on the surface of the debonded platelets (arrow).

Rocking curve measurements by XRD showed a decrease of the platelets alignment with increasing platelets fraction (Figure 5-8). The mean angle (difference from the horizontal plane, which is  $0^\circ$ ) was  $10^\circ \pm 1^\circ$ ,  $16^\circ \pm 1^\circ$  and  $18^\circ \pm 1^\circ$  at 10 vol-%, 15 vol-% and 20 vol-%, respectively.

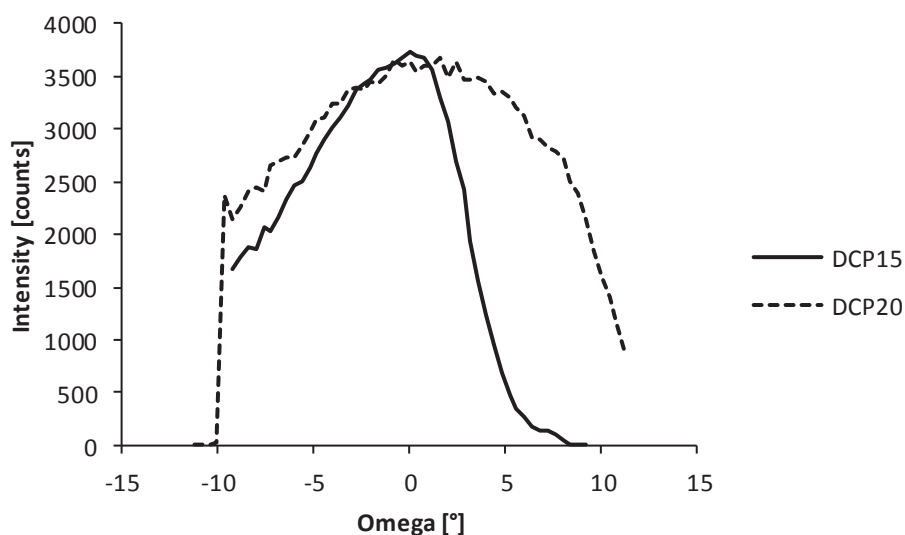


**Figure 5-8** Angle dispersion measured by XRD in rocking curve mode. The zero angle corresponds to the film plane and the mean platelet angle is calculated as the FWHM.

### Magnetization of the platelets

After mixing with negatively charged ferrofluid (EMG-705) in demineralized water, the white DCP platelets sedimented but the brown magnetic nanoparticles remained in suspension, showing no adhesion between them (Figure 5-9, left). However, positively charged magnetic nanoparticles (EMG-605) sedimented with the DCP platelets showing good binding between both (Figure 5-9, right). Hence, it can be concluded that the DCP particles were mainly negatively charged at pH 7.

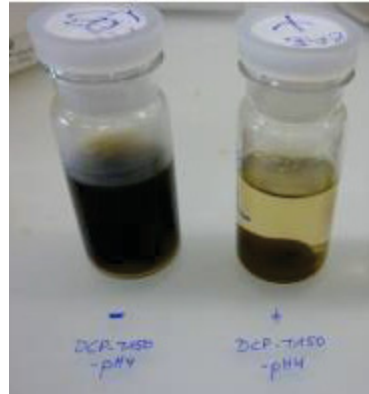


**Figure 5-9** When mixed with negatively charged ferrofluid (left flask), the DCP platelets sedimented but the magnetic nanoparticles (brown) stayed in suspension. When mixed with positively charged ferrofluid (right flask), the nanoparticles sedimented with the DCP platelets showing good binding between both.

The responsiveness of EMG 605-decorated DCP platelets to a magnetic field was verified in a water based suspension by optical microscopy observations. The EMG 605-decorated DCP platelets moved and stood up (out of the plane) when a vertical magnetic field was applied with a simple kitchen magnet (Figure 5-10).

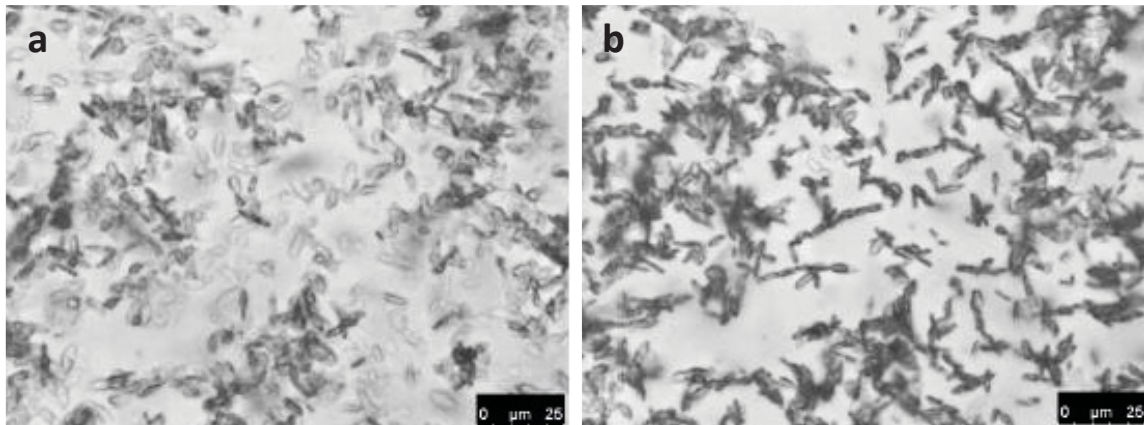


**Figure 5-10** Optical microscope pictures of magnetized DCP platelets suspended in water a) without magnetic field and b) with application of a vertical magnetic field. Scale bars are 25  $\mu\text{m}$ .

To align DCP platelets in a plane, decorated platelets were immobilized in a UV-polymerized IBOA using a VRF. The platelets strongly aligned in one planar direction (Figure 5-11).

To confirm the efficacy of the magnetic field over millimeter-size thickness, 20 vol-% of magnetized DCP platelets were mixed with a gelatin suspension (2 wt-%). The gel was hardened by cooling over a rotating magnetic field. 2D orientation was observed throughout the 3 mm thick sample (Figure 5-12).

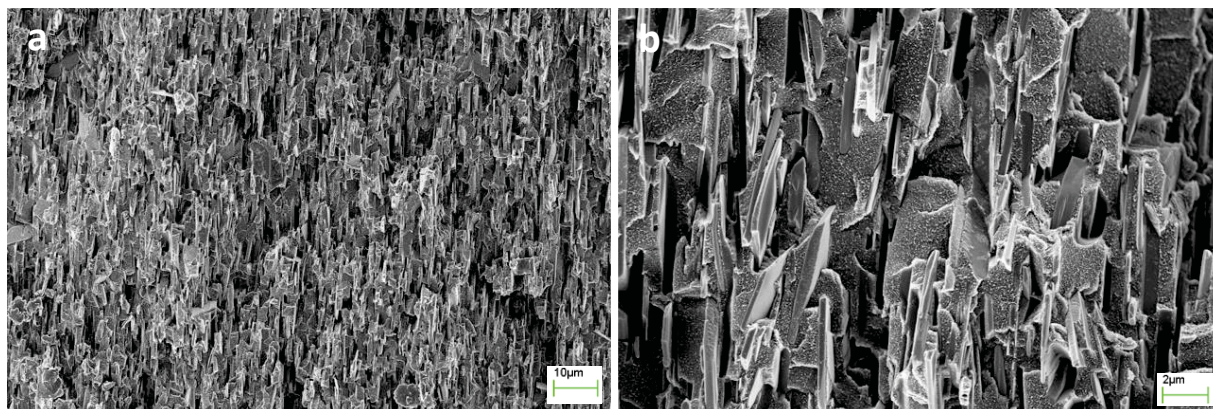


**Figure 5-11** SEM images of 20 vol-% DCP platelets in an IBOA matrix, oriented with a vertical rotating field (VRF). Cross-section perpendicular to the VRF plane. Scale bar is 10  $\mu\text{m}$  in a) and 2  $\mu\text{m}$  in b).

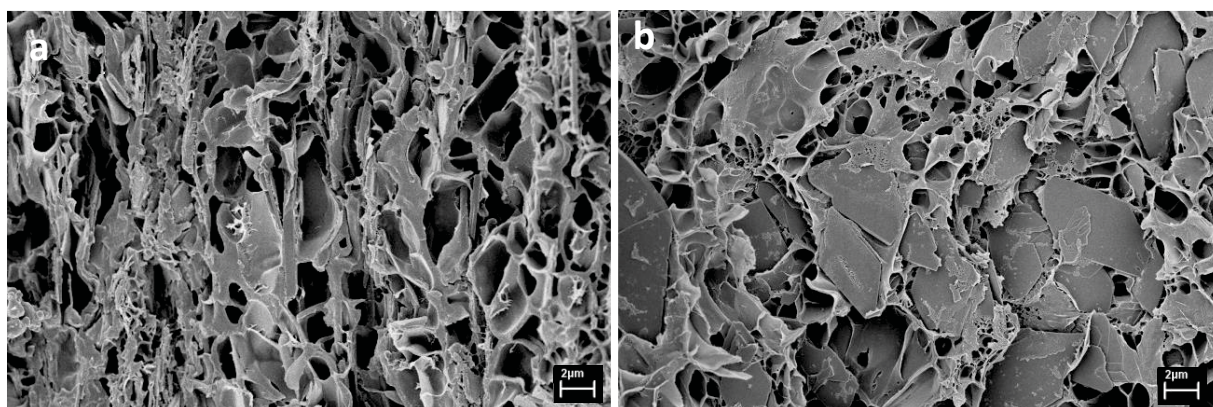


**Figure 5-12** SEM images of a freeze-dried gelatin scaffold reinforced with 10 vol-% of DCP platelets oriented with a vertical rotating magnetic field (VRF). a) perpendicular cut relative to the VRF plane; b) cut along the VRF plane. Scale bars are 2  $\mu\text{m}$ .

### Maintaining the orientation during drying of an hydrogel matrix

As seen in the previous section (Figure 5-11), the use of a VRF led to a better alignment of the ceramic platelets and postponed the misalignment threshold to higher volume fraction than with solvent casting. However, the combination of both techniques was challenging. Indeed, the vertical pressure applied by the drying film competed with the VRF and no good alignment could be reached (Figure 5-13). To overcome this problem, the magnet was placed on the side of the molds and rotated around a vertical axis, such as to create a rotating field in the horizontal plane (HRF), i.e. in the drying film plane. After drying in the rotating magnetic field, the films were prepared and characterized following the same procedures as described above for the non-magnetized films.

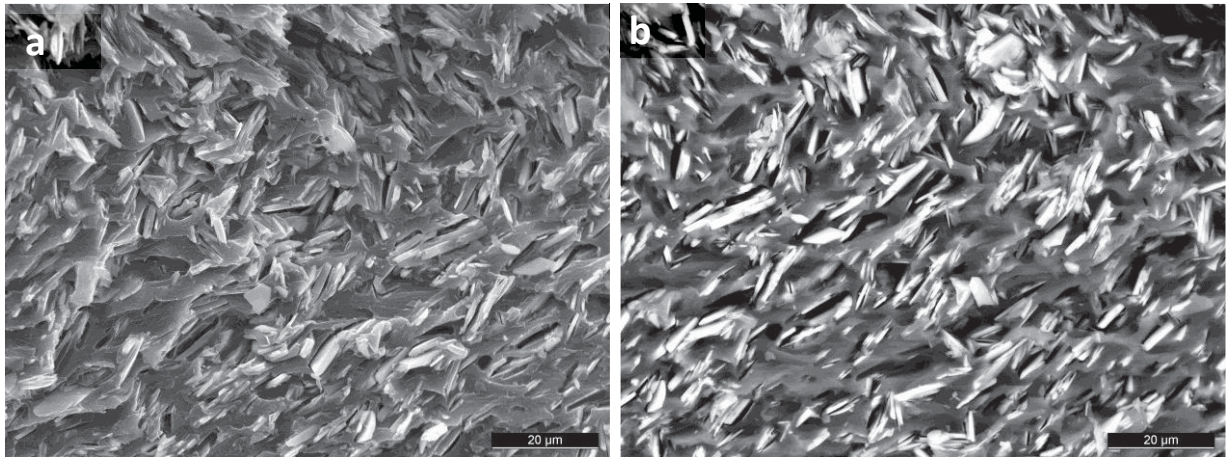


**Figure 5-13** SEM of ruptured surfaces of chitosan films reinforced with 20 vol-% of magnetized DCP platelets. The hardening process (solvent evaporation) took place over a rotating vertical field (VRF), which competed with the pressure of the drying film. a) SE image; b) BSE image. Scale bars are 20 µm.

The stiffness of the composite films tended to slightly increase with increasing ceramic fraction (Figure 5-14a). However, the results dispersion was too large to confirm this trend statistically. The tensile and yield strengths continuously increased with the ceramic fraction up to 20 vol-%. With 25 vol-% of reinforcement, the strength decreased (Figure 5-14c). The elongation at rupture was barely affected by the addition of ceramic (Figure 5-14b).

It has to be remarked that the tensile and yield strengths, the elongation at rupture and the stiffness of the pure chitosan films of the present experimental group were lower than observed in previous experiments. In consequence, for comparison of the results of previous non-magnetized and present magnetized samples, all values were reported to those of the pure polymeric films of the same batch. Hence, the stiffness increase per ceramic fraction was similar between both batches (Figure 5-14a), and reached about +25 % with 20 vol-% of ceramic. The deformation at rupture globally decreased with addition of ceramic, but with quite different results between both batches (Figure 5-14b).

Rocking curve measurements with XRD showed an increase of platelets mean angle within the composites films with increasing ceramic content. Interestingly, a strong influence of the use of a magnetic field was highlighted. Indeed, the mean angle with 25 vol-% of magnetized platelets was still lower than the mean angle of non-magnetic platelets at 20 vol-% (Figure 5-14d).

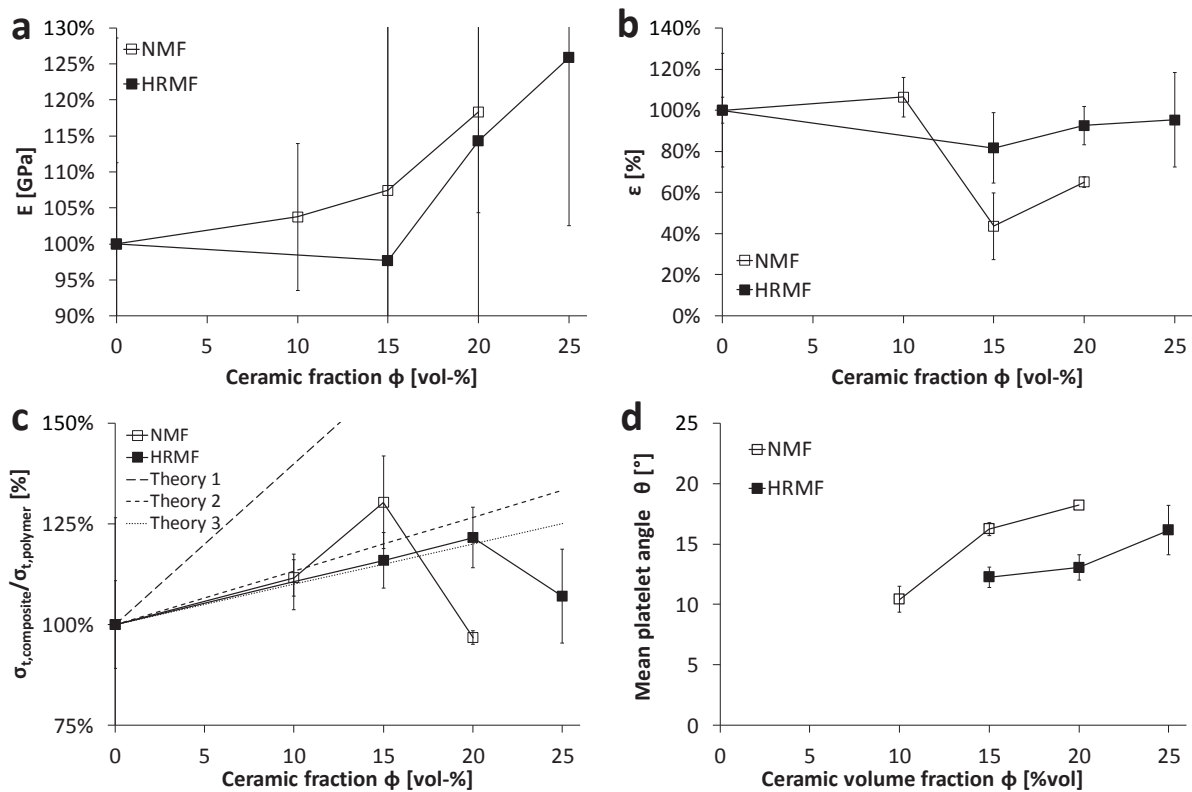


**Figure 5-14** Relative increase of a) stiffness, b) deformation at rupture and c) tensile strength in composite films compared to the pure polymer films; d) increase of mean platelets angle (measured by rocking curve) with platelets fraction with and without magnetic field. Behavior of films without magnetic field (NMF) and with rotating magnetic field (HRMF) are compared, as well as theoretical increase of strength (c) considering variables aspect ratios ( $s$ ) and interface strength ( $\tau_p$ ): Theory 1:  $s = 30$ ,  $\tau_i = \tau_m = \sigma_p/3$ ; Theory 2:  $s = 14$ ,  $\tau_i = \tau_m = \sigma_p/3$ ; Theory 3:  $s = 30$ ,  $\tau_i = 3/5 \cdot \tau_m = \sigma_p/5$ .

## Discussion

### Detrimental effect of $\beta$ -TCP platelets in chitosan

Both CaP platelets were non-agglomerated, as proved by the PSD results (Figure 3-3 and Figure 3-10, chapter 3). However, this method also showed larger size dispersion than observed by SEM. These higher values are due to artifacts from the laser diffraction measurements which accounts for spherical particles. Since the particles are elongated platelets, the measured size is an intermediate between the longest dimension and the smallest, hence, increasing the size dispersion.

According to theoretical calculations (Chapter 2), the aspect ratio of  $\beta$ -TCP platelets ( $s = 6$ ) is not high enough to efficiently reinforce a polymer matrix. Indeed, a poor or even null effect of the addition of  $\beta$ -TCP platelets on the mechanical properties of chitosan films was expected from the theoretical calculations (Chapter 2). Surprisingly, the effect of  $\beta$ -TCP platelets was even worse than expected, since a detrimental influence was observed (Figure 5-3). SEM observations of fractured

surfaces after tensile testing revealed no orientation of the platelets and no platelets surfaces exposed. This indicates a low stress transfer from the matrix to the reinforcement elements, presumably due to the too short interfaces between both phases. In consequence, the platelets rather weakened the films by creating defects that locally concentrated the stresses instead of acting as reinforcement elements. The use of a magnetic field to better orient the platelets would certainly improve the mechanical results, but the improvement rate would still be restricted due to the limited aspect ratio of the  $\beta$ -TCP platelets.

### **Efficient reinforcement with DCP platelets up to a given volume fraction**

The dimensions of the DCP platelets (Figure 5-2) were potentially much more adequate to efficiently reinforce biopolymers, by enhancing strength without leading to brittle fracture behavior. Indeed, with an aspect ratio of 30 and an interface strength of 60 MPa, the reinforcement potential can be as high as 40 % for each 10 vol-% of added ceramic. However, for an interface half that strong, it would only improve the strength by 15 % for each 10 vol-% of added ceramic (see Chapter 2 for theoretical calculations). Moreover, the magnetization experiments suggest that contrarily to that of  $\beta$ -TCP platelets, the surface of DCP platelets is negatively charged. Hence, the selection of chitosan as matrix materials was a good choice thanks to its positive charge at low pH, i.e. when dissolved. Its affinity to the negatively charged DCP platelets should thus be beneficial for the interface strength.

Tensile tests on solvent casted films confirmed efficiency of DCP platelets as reinforcement elements (Figure 5-4), with an apparently good interface (Figure 5-6a to d), as polymer remnants were observed on the surface of debonded platelets (Figure 5-7). The rupture mode was apparently mainly platelets pull-out as indicated by the numerous protruding platelets and platelets imprints in the polymer matrix. Nevertheless, the presence of broken platelets was also a sign of local high stress transfer, i.e. good and large interfaces between both phases. Indeed, the size distribution for DCP platelets was rather large (up to 0.3) and some platelets might have broken because of an aspect ratio higher than the critical value.

The highest strength, i.e. with 15 vol-% of ceramic, was comparable to the highest strength reported for cortical bone in the literature (70 - 150 MPa) [4, 7, 10]. However, the Young's modulus barely reached the lowest reported values for bone (3 - 30 GPa) [4, 7, 9, 10, 31]. It has to be noticed that other "brick-and-mortar" composites have already shown much higher strength and stiffness values [26, 32]. However, the ceramic platelets used in those studies were non-degradable materials. Composite made of biodegradable materials, like PLLA and HA have never reached such values, which is attributed to the lack of spatial arrangement of the structures.



### Threshold value for strength improvement

Platelet-reinforcement of the polymer was limited to a certain ceramic fraction. Over a threshold value, the strength decreased, as reported in the past by other authors [25, 33, 34]. Indeed, once a given limit of platelets amount was reached, defects number increased and weakened the structure, as confirmed by the SEM images of ruptured surfaces. Poor alignment obtained by simple solvent casting method led to a threshold value as low as 15 vol-%. Magnetization of the DCP platelets was then investigated in the aim to maintain their in-plane alignment during matrix solidification. The negatively charged surface of DCP platelets (not measured, but suggested by the magnetization experiments) allowed easy adhesion of iron oxide nanoparticles by electrostatic forces. Once decorated, the DCP platelets were responsive to low magnetic fields (Figure 5-10) and were easy to align in a static polymer matrix (Figure 5-11 and Figure 5-12). However, using UV polymerization was not adequate because the ceramic platelets absorb the UV, hence hindering penetration of the UV light in the core of too thick samples. Nevertheless, this experiment highlighted the potential of this structuring technique with CaP platelets. Indeed, even porous 3D scaffolds with aligned platelets were easily synthesized by freeze-drying platelets-reinforced gelatin hydrogels, confirming the potential of the magnetic alignment technique for macro objects and not only thin films.

Alignment of magnetized DCP platelets within a horizontally rotating magnetic field maintained a high in-plane orientation even during the drying of the chitosan matrix (Figure 5-14d). The higher alignment compared to simple solvent casting postponed the threshold value beyond which strength drops (Figure 5-14c and Figure 5-15). However, in the literature, this limit could be further pushed up using other alignment methods like combined gel-casting and hot-pressing [34].

The results of mechanical testing were poorly reproducible with different polymer batches, potentially due to varying characteristics of the polymer batches used, or even due to differences in samples humidity. Indeed, the samples were stored and tested by  $50 \pm 20$  % humidity. However, when normalizing all results with those of the pure chitosan films of the same batch, the results were comparable (Figure 5-14c). Moreover, in all tested composite films a few percent of deformation were observed, meaning that the rupture mode was not fragile (Figure 5-4d and Figure 5-14b).

From a mechanical point of view, reinforcement with a higher ceramic content would not be necessary, since properties close to those of cortical bone were reached with a matrix as weak as non-cross-linked chitosan. Moreover, using stronger but still ductile polymers could easily lead to higher strength and stiffness values. However, from a biological point of view, a higher ceramic fraction is desirable to optimize biocompatibility by reducing side effects of polymer degradation such as acid or polymer particle release [35]. Hence, more efficient structuring methods are necessary to maintain a good alignment of the platelets while increasing their amount.

### Fitting the experimental results with theoretical equations

As presented in Chapter 2, the increase of the composite strength ( $\sigma_{comp}$ ) as a function of the ceramic platelets fraction ( $\phi_p$ ) can be fitted with a theoretical model, taking into account the aspect ratio of the ceramic particles ( $s$ ), the critical aspect ratio of these particles ( $s_{cr}$ ), the strength of the ceramic platelets ( $\sigma_p$ ) and the strength of the polymer matrix ( $\sigma_m$ ) (Chapter 2, Equations 8 and 12). In the ideal case, when all stresses from the matrix are transmitted to the platelets, the critical aspect ratio is a function of the ceramic strength and of the interface strength ( $\tau_i$ ), which should be equal to the matrix shear strength ( $\tau_m$ ) (Chapter 2, Equation 7). However, as soon as the interface is not perfect, only a fraction  $x$  of the shear stresses is transmitted

$$\tau_i = x \cdot \tau_m \quad \text{Equation 1}$$

with  $x = [0;1]$

In consequence, the relative strength,  $\sigma_{rel} = \sigma_{comp}/\sigma_m$  (Chapter 2, Equation 13 and 14) can be expressed as

$$\sigma_{rel} = x \cdot \frac{s}{6} \cdot \phi_p + (1 - \phi_p). \quad \text{Equation 2}$$

Hence, the observed curves can be fitted up to the percolation limit by adapting variables  $x$  and  $s$ :

- 1)  $x$  from 0 to 1, is related to the interface quality ( $x = 1$ : perfect interface with maximum strength  $\tau_i = \tau_m = \sigma_m/3$ ;  $x = 0$ : no interface strength  $\tau_i = 0$ )
- 2) and  $s$ , the aspect ratio which might deviate from the SEM observations due to breakage during composite preparation for example.

The numerical fit with the perfect situation – with intact platelets of an average aspect ratio of  $s = 30$  and an interface strength as strong as the shear strength of the polymer ( $x = 1$ ,  $\tau_i = \tau_m$ ) – strongly over-estimated the experimental values (Figure 5-14c, “theory 1”).

Linear fitting with either  $x$  or  $s$  as variable were thus done. Considering a perfect interface ( $x = 1$ ), the effective aspect ratio of the platelets would be around  $s = 14$  (Figure 5-14c, “theory 2”). In the hypothesis that the aspect ratio was not affected by the composite processing ( $s = 30$ ), the interface strength was estimated at about  $\tau_i = 0.4 \cdot \tau_m$  (Figure 5-14c, “theory 3”). Hence, the interface strength  $\tau_i$  lies in between 2/5 and 1 times the matrix shear strength  $\tau_m$ , and the effective aspect ratio  $s$  is in between 14 and 30.

The interface strength could be improved to enhance the reinforcing effect of the DCP platelets, for example by surface modification of the ceramic or change of polymer. In theory, adding

20 vol-% of ceramic with  $s = 30$  and perfect interfaces ( $x = 1$ ) could increase the strength by almost 80 %.

As for the evolution of the strength with ceramic fraction, the deviation from perfect alignment of the platelets,  $\vartheta$ , (measured by XRD with the rocking curve method) also increased (Figure 5-15a). Using a magnetic field reduced the platelets mean angle achieved even at higher ceramic fraction. Since this better alignment was also linked with an increase of the maximum ceramic fraction achievable without strength drop, the link between both was investigated.

The threshold beyond which the strength drops should correspond to the percolation limit, when contacts between particles impair their alignment. Based on the aspect ratio of the reinforcing elements,  $s$ , the theoretical percolation limit,  $\phi_p$ , can be calculated in function of the platelets mean angle,  $\vartheta$  [36]:

$$\phi_p = \frac{1}{\theta \cdot s} \cdot p_c \quad \text{Equation 3}$$

where  $p_c$  is a constant (0.718) (Figure 5-15a).

Comparing the mechanical properties of samples with different ceramic fractions  $\phi$  (Figure 5-15b) and respective mean angles  $\vartheta$  (Figure 5-15a) confirmed that above the percolation limit,  $\vartheta_p$ , strength decreased. It has to be noticed that the percolation limit that best fitted the present results is for an aspect ratio smaller than 30, i.e. supporting the hypothesis that the platelets might have broken during the sample preparation process.

In parallel, since the theoretical reinforcement capacity,  $\sigma_{rel}$ , of a given fraction,  $\phi$ , of a material can be estimated from its aspect ratio [25] (Equation 2, Figure 5-14c), **the best performance of a composite obtained by a given method can be estimated based on the achieved degree of alignment.**

In the present case, improving the alignment quality by the use of a magnetic field pushed this percolation limit to 20 vol-% of ceramic. SEM observations confirmed the differences measured by XRD.

In the literature, strength increase up to ceramic contents of 27 vol-% were reached with the same method but with other materials, in particular with polymeric matrices hardening without volume change [37]. In the present case, the use of solvent evaporation induces volume changes of the matrix, which could disturb the alignment and explain why the threshold ceramic fraction was lower than 27 vol-%. Moreover, as the drying process takes place, the viscosity of the chitosan solution increases, making the action of the magnetic field even harder.

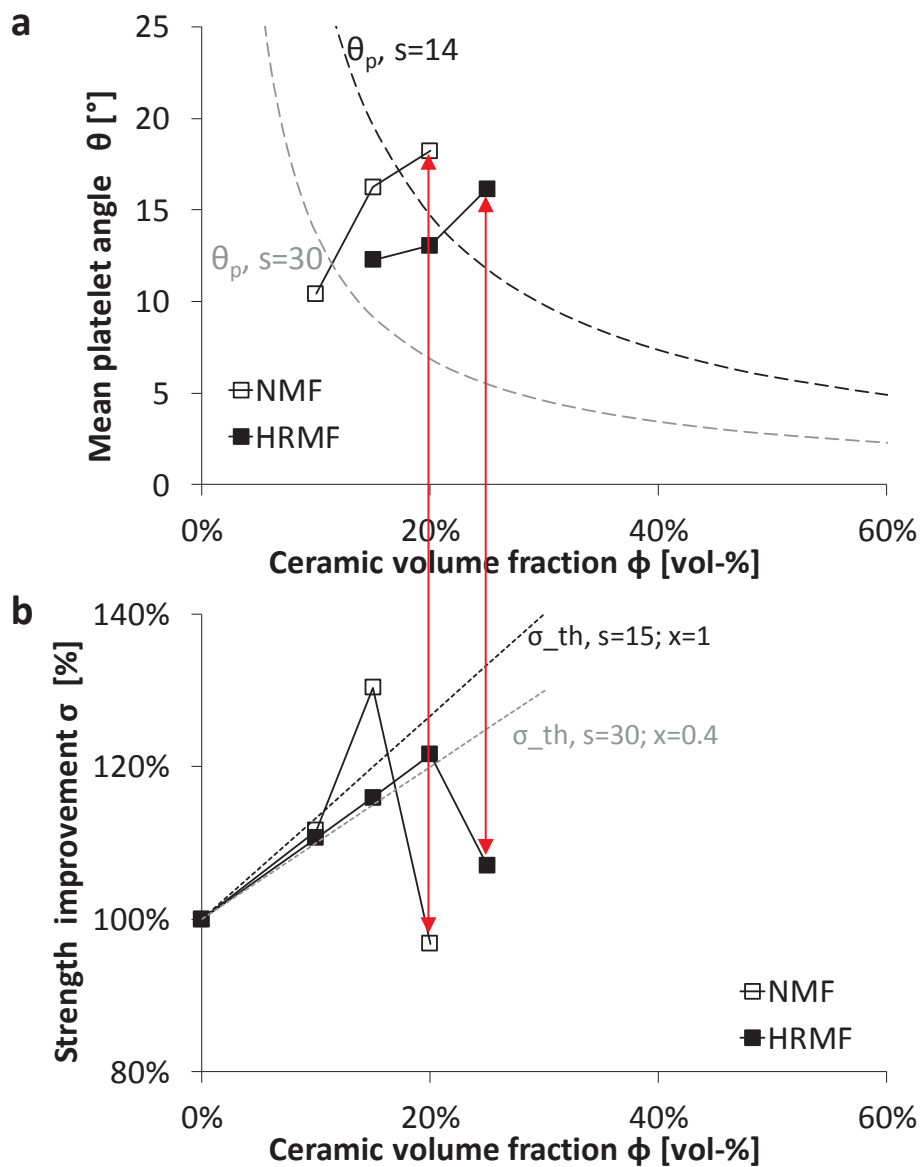


**Figure 5-15** Comparison of mean platelets angle  $\theta$  (a) and strength (b) in function of ceramic fraction without (NMF) and with magnetic alignment (HRMF). The strength decrease clearly corresponded to  $\theta$  exceeding the percolation limit for the calculated effective aspect ratio (red vertical arrows).

Even if adequate strength for bone replacement was already obtained with 15 vol-% of ceramic without magnetic orientation, the ceramic fraction should be further increased to improve the biological properties of the composite material. Indeed, CaP ceramics are highly biocompatible, without negative effect of their degradation products, while polymers may affect biocompatibility due to acid release (PLA-based polymers), or by inducing inflammation due to large particles release [35]. However, to preserve good mechanical properties, the degree of alignment has to be very high. To evaluate the suitability of a given technique, the achievable degree of alignment can be compared with the percolation limit associated to a certain particles fraction.

## Conclusions

Combination of strength, toughness and bioresorbability was reached over millimeter-size range by arranging well-defined and well-dispersed bioceramic (CaP) platelets in an organic matrix (chitosan). The use of a rotating magnetic field led to a good architectural arrangement up to 20 vol-% of reinforcement, while simple film drying by solvent evaporation already reached mechanical properties close to those of cortical bone with only 15 vol-% of ceramic. Further increase of the ceramic fraction is nevertheless necessary, not from a mechanical point of view, but from a biological point of view, to optimize the biocompatibility of the composite. Hence, better performing alignment techniques are required for further developments of bio-inspired composite materials with sub-micrometric components.

## References

- [1] Galea L, Bohner M, Thuring J, Doebelin N, Aneziris CG, Graule T. Control of the size, shape and composition of highly uniform, non-agglomerated, sub-micrometer  $\beta$ -tricalcium phosphate and dicalcium phosphate platelets. *Biomaterials*. 2013;34:6388-401.
- [2] Karageorgiou V, Kaplan D. Porosity of 3D biomaterial scaffolds and osteogenesis. *Biomaterials*. 2005;26:5474-91.
- [3] Gao H, Ji B, Jäger IL, Arzt E, Fratzl P. Materials become insensitive to flaws at nanoscale: Lessons from nature. *Proceedings of the National Academy of Sciences of the United States of America*. 2003;100:5597-600.
- [4] Ji B, Gao H. Mechanical properties of nanostructure of biological materials. *J Mech Phys Solids*. 2004;52:1963-90.
- [5] Espinosa HD, Rim JE, Barthelat F, Buehler MJ. Merger of structure and material in nacre and bone - Perspectives on de novo biomimetic materials. *Progress in Materials Science*. 2009;54:1059-100.
- [6] Norman TL, Vashishth D, Burr DB. Fracture toughness of human bone under tension. *J Biomech*. 1995;28:309-20.
- [7] Cooke FW. Bulk properties of materials. In: Ratner BD, Hoffman AS, Schoen FJ, Lemons JE, editors. *Biomaterials science - an introduction to materials in medicine*. San Diego: ACADEMIC PRESS; 1996. p. 11-21.
- [8] Hou DF, Zhou GS, Zheng M. Conch shell structure and its effect on mechanical behaviors. *Biomaterials*. 2004;25:751-6.
- [9] Currey JD, Zioupos P, Davies P, Casinos A. Mechanical properties of nacre and highly mineralized bone. *Proceedings of the Royal Society B: Biological Sciences*. 2001;268:107-11.
- [10] Roeder RK, Converse GL, Kane RJ, Yue W. Hydroxyapatite-reinforced polymer biocomposites for synthetic bone substitutes. *JOM*. 2008;60:38-45.
- [11] Healy KE. Dentin and Enamel. In "Handbook of Biomaterial Properties" Edited by J Black and G Hastings. 1998;Chapter A3:24-39.

- [12] Bechtle S, Habelitz S, Klocke A, Fett T, Schneider GA. The fracture behaviour of dental enamel. *Biomaterials*. 2010;31:375-84.
- [13] Bechtle S, Ang SF, Schneider GA. On the mechanical properties of hierarchically structured biological materials. *Biomaterials*. 2010;31:6378-85.
- [14] Jackson AP, Vincent JFV, Turner RM. The Mechanical Design of Nacre. *Proceedings of the Royal Society of London Series B Biological Sciences*. 1988;234:415-40.
- [15] Jarcho M, Bolen CH, Thomas MB, Bobick J, Kay JF, Doremus RH. Hydroxylapatite synthesis and characterization in dense polycrystalline form. *Journal of Materials Science Letters*. 1976;11:2027-35.
- [16] Bonfield W, Grynblas M, Tully AE, Bowman J, Abram J. Hydroxyapatite reinforced polyethylene--a mechanically compatible implant material for bone replacement. *Biomaterials*. 1981;2:185-6.
- [17] Shikinami Y, Okuno M. Bioresorbable devices made of forged composites of hydroxyapatite (HA) particles and poly-L-lactide (PLLA): Part I. Basic characteristics. *Biomaterials*. 1999;20:859-77.
- [18] Venkatesan J, Kim SK. Chitosan composites for bone tissue engineering - An overview. *Mar Drugs*. 2010;8:2252-66.
- [19] Baji A, Wong SC, Srivatsan TS, Njus GO, Mathur G. Processing methodologies for polycaprolactone-hydroxyapatite composites: A review. *Mater Manuf Process*. 2006;21:211-8.
- [20] Kim SS, Sun Park M, Jeon O, Yong Choi C, Kim BS. Poly(lactide-co-glycolide)/hydroxyapatite composite scaffolds for bone tissue engineering. *Biomaterials*. 2006;27:1399-409.
- [21] Hu Q, Li B, Wang M, Shen J. Preparation and characterization of biodegradable chitosan/hydroxyapatite nanocomposite rods via in situ hybridization: A potential material as internal fixation of bone fracture. *Biomaterials*. 2004;25:779-85.
- [22] Rezwani K, Chen QZ, Blaker JJ, Boccaccini AR. Biodegradable and bioactive porous polymer/inorganic composite scaffolds for bone tissue engineering. *Biomaterials*. 2006;27:3413-31.
- [23] Meyers MA, Chen PY, Lin AYM, Seki Y. Biological materials: Structure and mechanical properties. *Progress in Materials Science*. 2008;53:1-206.
- [24] Gao H. Application of fracture mechanics concepts to hierarchical biomechanics of bone and bone-like materials. *International Journal of Fracture*. 2006;138:101-37.
- [25] Bonderer LJ, Studart AR, Gauckler LJ. Bioinspired design and assembly of platelet reinforced polymer films. *Science*. 2008;319:1069-73.
- [26] Munch E, Launey ME, Alsem DH, Saiz E, Tomsia AP, Ritchie RO. Tough, bio-inspired hybrid materials. *Science*. 2008;322:1516-20.
- [27] Launey ME, Munch E, Alsem DH, Barth HB, Saiz E, Tomsia AP, et al. Designing highly toughened hybrid composites through nature-inspired hierarchical complexity. *Acta Materialia*. 2009;57:2919-32.
- [28] Erb RM, Libanori R, Rothfuchs N, Studart AR. Composites reinforced in three dimensions by using low magnetic fields. *Science*. 2012;335:199-204.
- [29] Podsiadlo P, Kaushik AK, Arruda EM, Waas AM, Shim BS, Xu J, et al. Ultrastrong and stiff layered polymer nanocomposites. *Science*. 2007;318:80-3.
- [30] Vaudin MD, Rupich MW, Jowett M, Riley Jr. GN, Bingert JF. A method for crystallographic texture investigations using standard X-ray equipment. *Journal of Materials Research*. 1998;13:2910-9.
- [31] Kokubo T, Kim HM, Kawashita M. Novel bioactive materials with different mechanical properties. *Biomaterials*. 2003;24:2161-75.

- [32] Bonderer LJ, Studart AR, Woltersdorf J, Pippel E, Gauckler LJ. Strong and ductile platelet-reinforced polymer films inspired by nature: Microstructure and mechanical properties. *Journal of Materials Research*. 2009;24:2741-54.
- [33] Libanori R, Münch FHL, Montenegro DM, Studart AR. Hierarchical reinforcement of polyurethane-based composites with inorganic micro- and nanoplatelets. *Composites Science and Technology*. 2012;72:435-45.
- [34] Bonderer LJ, Feldman K, Gauckler LJ. Platelet-reinforced polymer matrix composites by combined gel-casting and hot-pressing. Part I: Polypropylene matrix composites. *Composites Science and Technology*. 2010;70:1958-65.
- [35] Ignatius AA, Betz O, Augat P, Claes LE. In vivo investigations on composites made of resorbable ceramics and poly(lactide) used as bone graft substitutes. *J Biomed Mater Res*. 2001;58:701-9.
- [36] Lu C, Mai YW. Influence of aspect ratio on barrier properties of polymer-clay nanocomposites. *Phys Rev Lett*. 2005;95.
- [37] Libanori R, Erb RM, Reiser A, Le Ferrand H, Süess MJ, Spolenak R, et al. Stretchable heterogeneous composites with extreme mechanical gradients. *Nature Communications*. 2012;3.





## CHAPTER 6:

### BIODEGRADABLE, STRONG AND TOUGH NACRE-INSPIRED

### STRUCTURES OBTAINED BY FREEZE-CASTING

#### ***Abstract***

In the last 10 years, nacre structure has become a widespread inspiration source for the synthesis of composite materials with the idea of combining high strength and toughness. Following this natural example, synthetic materials with outstanding combination of strength and toughness have already been obtained; however ceramic contents higher than 20-25 vol-% commonly lead to disorder increase in the structure, due to percolation. To further increase the ceramic fraction, more efficient alignment methods are required to strongly orient the particles and prevent percolation. Freeze casting, or ice-templating, is a process that uses the principle of directional solidification by anisotropic freezing of a solvent. This method allows obtaining porous bulk samples with oriented microstructure and has already proved its efficient alignment potential with diverse materials, but never with fully resorbable materials.

The present work demonstrates the feasibility of using directional freezing with CaP platelets in hydrogel matrices. Volume fraction up to 50 % led apparently to proper embedding of the platelets and good spatial arrangement. Some preliminary tests were done to compress the porous lamellar samples into dense, nacre-like structures and to stabilize the chitosan matrix by acetylation. These films were then tensile tested and their properties compared with the ones obtained by solvent casting with and without magnetic alignment.

*$\beta$ -TCP platelets were posted to Philipp Hunger, in Prof. Wegst's group at Dartmouth University, Hanover, NH, to perform some preliminary freeze-casting tests.*

*Later, thorough experiments were conducted with Arto Ojuva, in Prof. Bergström's Lab at Stockholm University.*

## Introduction

In the last 10 years, nacre has become a widespread inspiration source for the synthesis of composite materials [1-3]. Indeed, it has a unique combination of high strength and toughness, despite consisting of fragile ceramic platelets and a weak organic matrix. This is mainly attributable to its highly ordered architecture [4-6]. High strength is provided by a combination of high ceramic loading, and a controlled geometry of the ceramic components: a thickness smaller than a critical value (Griffith's criterion [7]), and a high aspect ratio. However, too elongated platelets would lead to a brittle failure and an optimum value exists to preserve toughness [5]. Following similar rules, synthetic materials with outstanding combination of strength and toughness have already been obtained [1, 2, 8], however never with fully resorbable materials. Moreover, ceramic contents higher than 20-25 vol-% commonly lead to disorder increase in the structure [2, 9], due to percolation. The previous chapter of this thesis showed the possibility to obtain strong, tough and resorbable composites with solvent casting process, but reinforcement was also limited to about 20 vol-% platelet content. Unfortunately, higher ceramic volume fractions are required to ensure a high biocompatibility. To further increase the ceramic fraction, more efficient alignment methods are required to strongly orient the particles and prevent percolation.

Freeze casting, or ice-templating, is a process that uses the principle of directional solidification by anisotropic freezing of a solvent. This method allows obtaining porous bulk samples with oriented porosity. It was first reported as synthesis method in the 1950's [10]. It is ideal to study structural features like orientation and proportion of reinforcement elements [11]. However, it produces porous materials, with a honeycomb structure, made of aligned tubular pores [12]. This thesis focusing on dense materials for ease of comparison, it was intended to later flatten the obtained samples perpendicularly to the freezing direction in order to preserve the 1D alignment of the pore walls.

Freeze casting of hydrogels was proposed in the 1980's [13], and their first intended usages for biomedical applications came later [14-16], followed by freeze-cast bioceramics [17-19]. Besides pure ceramic scaffolds [18], ceramic-based composites have also been investigated [20]. As expected, the compressive strength of these composites was increased compared to pure polymer samples, but the tensile properties were not investigated. Composites with biodegradable ceramics, in particular calcium phosphates, have also been investigated but only with globular ceramic particles [21]. However, it is known that in colloidal suspensions, the alignment of plate-like particles of adequate size can be driven by the growth of ice crystals [18]. Freeze-casting of composite with well-defined

plate-like reinforcement elements has, to the best of our knowledge, only been investigated with non-degradable reinforcement materials. Hunger et al. for example, casted composites with a chitosan-alginate matrix and alumina platelets of different sizes [12]. The ceramic particles and the polymer concentrated in the interlamellar space between growing ice crystals. Due to shear forces, the platelets aligned with the freezing direction (Figure 6-1).

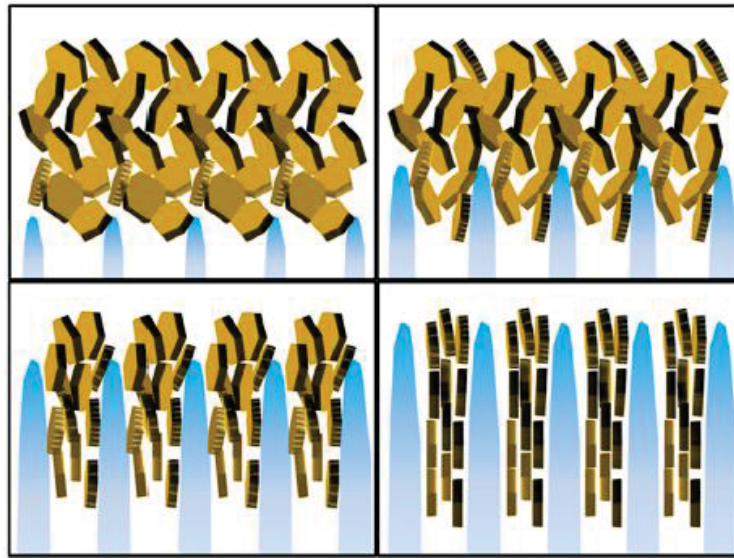


**Figure 6-1** Scheme of platelets segregation and alignment in interlamellar space between growing ice crystals from [12].

This method is thus very promising to obtain well-structured composite materials, and the next step towards strong and tough, but also biodegradable materials for bone substitution is the replacement of the non-degradable ceramic particles by degradable particles. Since such particles were successfully synthesized in the first part of this thesis [22], the way is now paved. If a global parallel alignment of the planar ice crystals – hence of the pore walls and their imbedded platelets – can be obtained, these porous structures could then be flattened to obtain dense films with in-plane reinforcement.

The aim of this chapter was hence to try to align non agglomerated and uniform CaP platelets in a chitosan matrix using freeze-casting and to show that a high spatial arrangement provides outstanding mechanical properties, even if the basic components are individually weak.

## Experimental section

### Synthesis of resorbable ceramic platelets

Prismatic platelets of  $\beta$ -tricalcium phosphate ( $\beta$ -TCP,  $\text{Ca}_3(\text{PO}_4)_2$ ) and monetite (DCP,  $\text{CaHPO}_4$ ) were obtained by precipitation of calcium and phosphate ions in ethylene glycol, following the procedure described in Chapter 3 and in Galea *et al* [22]. Briefly, calcium and phosphate precursors ( $\text{CaCl}_2 \cdot 2\text{H}_2\text{O}$ , Reag.Ph.Eur., art. n°1.02382, MERCK, Darmstadt, Germany and  $\text{Na}_2\text{HPO}_4 \cdot 2\text{H}_2\text{O}$ , purum p.a., art. n° 71645, Fluka, Buchs, Switzerland) were dissolved in ethylene glycol ( $\text{C}_2\text{H}_6\text{O}_2$ , Reag.Ph.Eur., art. n° 85512.360, VWR, Nyon, Switzerland) and mixed at 150 °C. The precipitate was separated by centrifugation at 4000 RPM for 30 minutes. The particles were then characterized by scanning electron microscopy (SEM, EVO MA25, Zeiss, Germany) for crystal size determination, by X-ray diffraction (XRD, X'Pert Pro MPD, Panalytical, Almelo, the Netherlands) for crystalline phase identification (Rietveld refinement and FullProf.2k software Version 5.00 [23]) and by laser diffraction (LS 13 320, Beckman-Coulter, Krefeld, Germany) to determine the particle size and agglomeration rate.

### Preliminary freeze-casting tests with $\beta$ -TCP-based slurries

A preliminary study with the freeze-casting method was performed at the early stages of this thesis. Hexagonal  $\beta$ -TCP platelets were sent to Prof. U. Wegst, Dartmouth University, USA. Agar was chosen as matrix material because of their large experience with this biopolymer.

A 4 wt-% agar solution was heated up to 90 °C for 24 hours before adding 0.3 g of  $\beta$ -TCP particles into 5 mL samples. The slurries were mixed for 1 minute in a high speed shear mixer at 3000 RPM. Freeze-casting at a cooling rate of 1 °/min, 10 °/min or 20 °/min (heaters off) was performed in Teflon molds. After freeze-drying, the samples were cut transversally and longitudinally for optical microscopy and SEM observations.

### Determination of adequate freeze-casting parameters for hydrogel-CaP slurries

Later, three freeze-casting units of the University of Stockholm (laboratory of Prof. L. Bergström) were used by the author to produce composites. Some experiments were first conducted with pure chitosan slurries (chitosan from crab shells, highly viscous, art. n° 48165, Sigma, Saint-Louis, MO, USA) and then with commercial CaP particles (art. nr. 21218, Sigma-Aldrich, Saint-Louis, MO, USA) to determine adequate freezing parameters.

The in-house made freeze-casting units consisted of a nitrogen vessel with a protruding copper rod for heat transfer, similar to the unit used by Deville and co-workers [24]. The copper rod was

fitted with a thermocouple and a heater, which enabled the temperature and the cooling rate to be controlled (Figure 6-2).

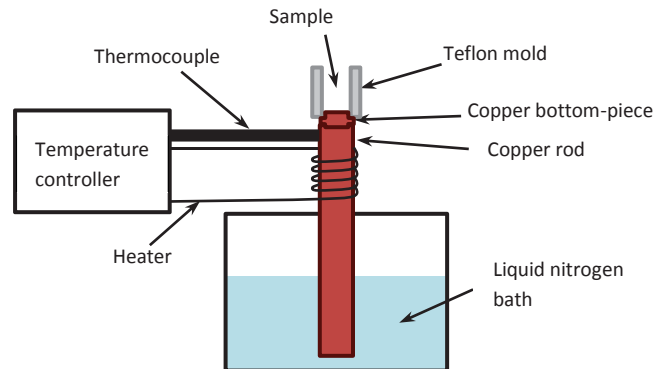


**Figure 6-2** Scheme of a freeze-casting unit.

The suspensions were casted in parallelepiped Teflon mold ( $7 \times 17 \times 28 \text{ mm}^3$ ) with a copper bottom-piece that was placed onto the protruding copper rod of the freeze-casting unit. The temperature was initially reduced to 276 °K and held at that temperature for 3 min. The suspensions were then allowed to freeze at a controlled cooling rate. When the temperature reached 233 to 193 °K, depending on the cooling rate, the frozen bodies were removed from the Teflon mold and put in a freeze-drier (Hetosic, Heto lab equipment, Denmark) for 2 days.

### Integration of CaP platelets and local planar alignment

Chitosan was chosen as the matrix material, because of its importance as biomaterial [25] and its positive charge in dissolved state which should provide a good anchoring to the negatively charged DCP platelets. Slurries with varying chitosan (1, 2 and 4 wt-% in solution) and platelets concentrations (10, 20, 30, 50, 65, 85 vol-% in final dry sample) were prepared and freeze-casted at different freezing rates (-0.5, -2, -10 and -20°C/min). The aim of this screening process was to determine the adequate parameters in order to obtain the best architectures for the later intended flattening process. More specifically, large parallel planar ice crystals, thin pore walls to induce good alignment of the platelets and as few bridges and ridges (perpendicular walls) as possible were required.

In addition, some directional freezing experiments were conducted with 50 vol-%  $\beta$ -TCP platelets (aspect ratio  $n = 6$ , [22]) in 2 wt-% alginate solutions (art. nr. A2158, Sigma, Saint-Louis, MO, USA) to favor adhesion of the negatively charged polymer on the positively charged ceramic particles.

### Attempts to globally align porosity in two directions

Once the best conditions for homogeneous and well aligned samples were found, optimization of the freezing procedure and particularly of the mold shape and configuration were performed in order to

obtain a constant 2D pore orientation throughout the sample. For this part, the samples were casted in Teflon molds with square section and removable copper inlays (Figure 6-3). The samples were characterized by SEM imaging of cross sections.

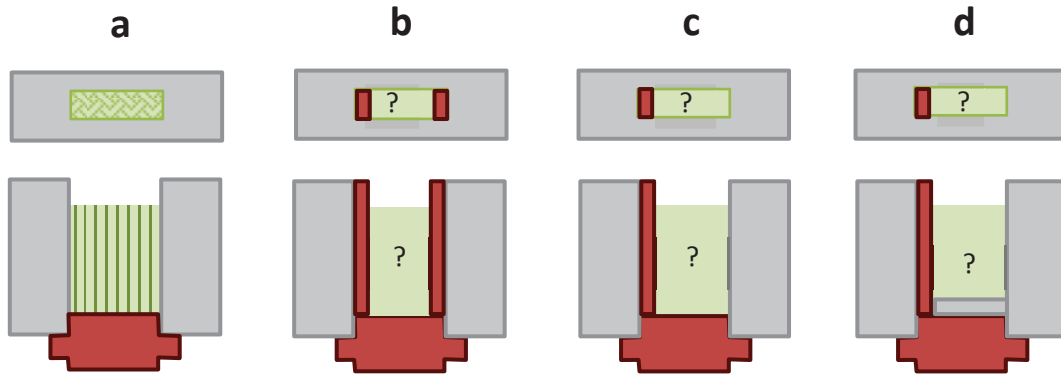


**Figure 6-3** Different mold configurations, with copper inlays covering some Teflon surfaces (top view and side cut): a) normal Teflon mold, with copper bottom piece, without inlay; b) with 2 side copper inlays; c) with only one copper side inlay; d) with only one copper side inlay and bottom insulated from the copper bottom piece. Grey = Teflon mold; red = copper parts; green = sample.

### Densification and consolidation

Later, in order to obtain dense, aligned samples, and to bind the pore walls together, the freeze-casted samples were flattened between 2 glass slides and acetylated [26, 27]. To do so, the samples were first soaked in 1M NaOH (art. n° 6771.1, Carl Roth, Karlsruhe, Germany) for 1h to neutralize acetic acid residues, rinsed in demineralized water for NaOH removal and incubated for 24h in 1M acetic anhydride ( $\geq 99\%$ , art. n° 33214, Sigma-Aldrich, Saint-Louis, MO, USA) in methanol (art. n° 322415 Sigma-Aldrich, Saint-Louis, MO, USA). Then samples were finally rinsed with methanol and ethanol, dried in vacuum at 40 °C for 24h and at 60°C for 1h.

### Tensile testing

Dog-bone shape tensile specimens were punched out of those films as described for solvent-casted films in the previous chapter. Finally, tensile tests were performed at a constant displacement speed of 0.5 mm/min (zwicki-Line Z5.0, Zwick, Kennesaw, GA, USA). XRD rocking curves were measured to evaluate the alignment degree of the DCP platelets and SEM (EVO MA25, Zeiss, Germany) observations of rupture surfaces were done as well.

## Results

### Preliminary freeze-casting tests with $\beta$ -TCP-based slurries

The agar scaffolds possessed an aligned, honeycomb-like structure and the pores had a horizontal aspect ratio of 1 to 3 (Figure 6-4).

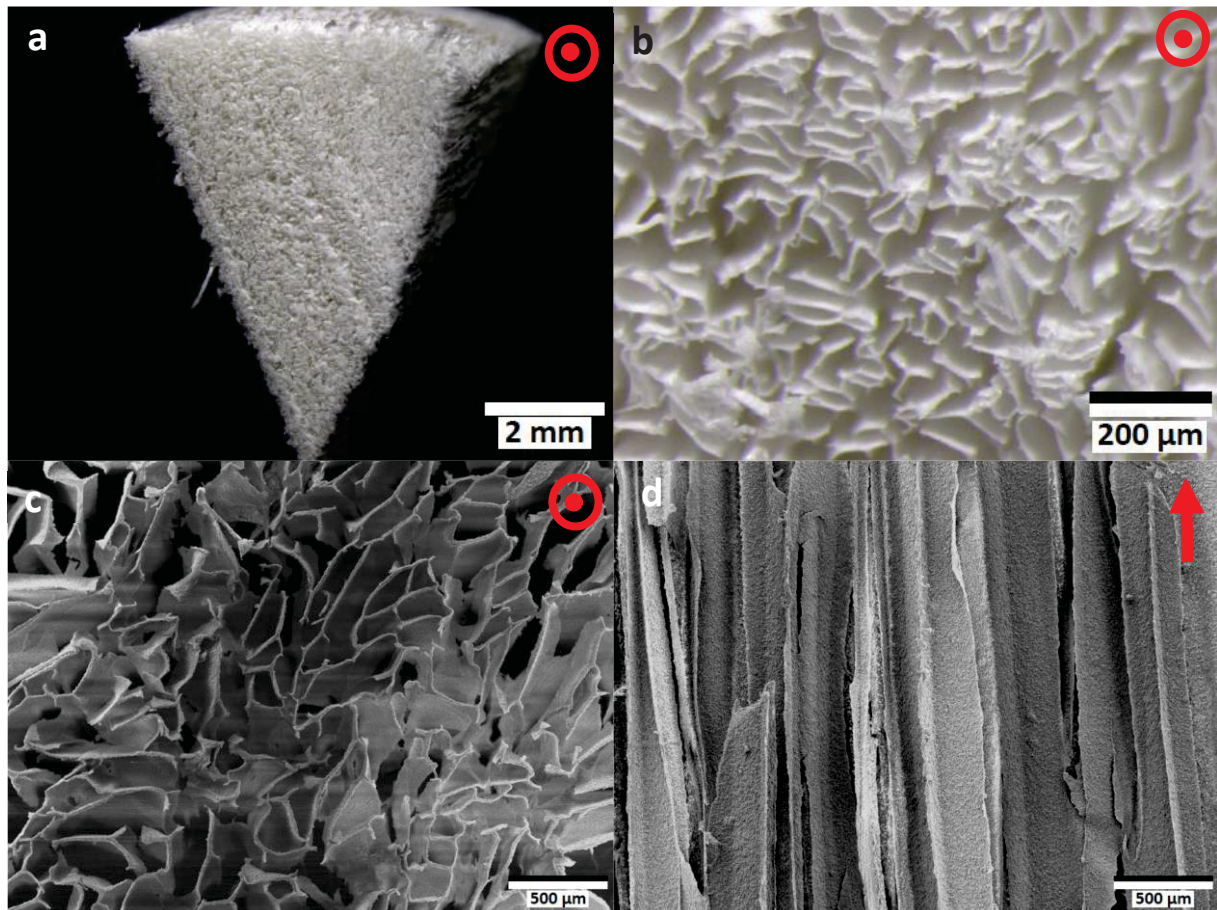


**Figure 6-4** a) and b) 4 wt-% agar, 10 °/min, transverse cross-section in optical microscope; c) transverse cross-section in SEM (scale bar = 500 μm); d) longitudinal cross-section in SEM (scale bar = 500 μm). Red arrows = freezing direction. Red arrows = freezing direction.

The platelet-alignment within the walls seemed improved in the thinner walls obtained with the faster freezing rate (Figure 6-5). The platelets were well dispersed, but the adhesion between agar and  $\beta$ -TCP looked rather poor.

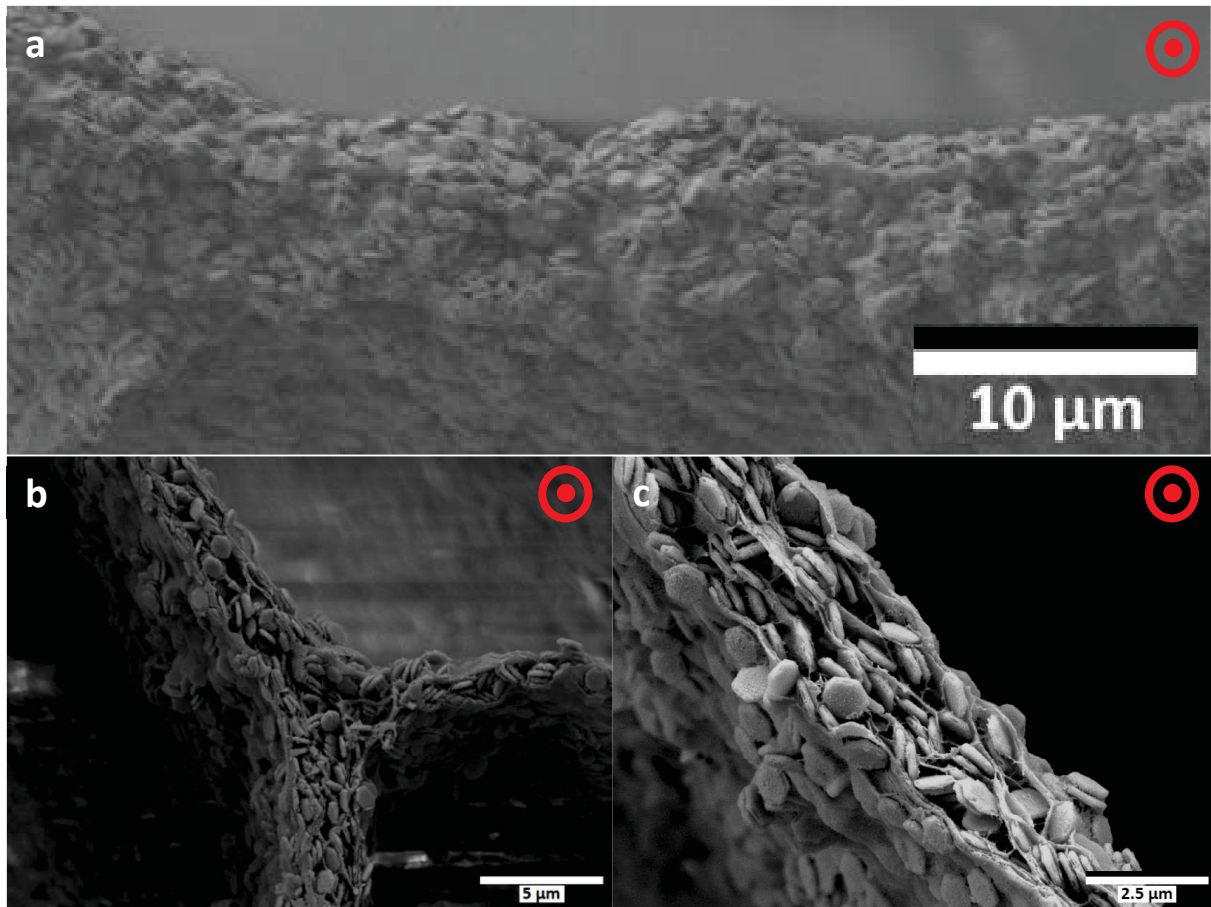


**Figure 6-5** Close-up of a transversal cross-section. Freezing rate = a)  $-1$  °/min; b) and c)  $-10$  °/min (Scale bars =  $5$   $\mu\text{m}$  and  $2.5$   $\mu\text{m}$ ). Red arrows = freezing direction.

### Determination of adequate freeze-casting parameters for hydrogel-CaP slurries

Freeze-casting of pure chitosan solutions led to porous structures which possessed very fine pore walls (Figure 6-6a and b), with ridges along the freezing direction (Figure 6-6b and c). The chitosan sheets were in average between  $0.2$  and  $1.5$   $\mu\text{m}$  thick (Figure 6-6d).

When increasing the freezing rate, the amount of bridges between pore walls increased, reducing the average pore size (Figure 6-7a), but the pore wall thickness was apparently not affected (Figure 6-7b).

Considering the difficulty to produce large amounts of CaP platelets, first trials were done with a commercial  $\beta$ -TCP powder. After freeze-casting, the ceramic particles were concentrated within the polymer walls and no large change of microstructure of the porous samples was observed (Figure 6-8). The particles seemed to be well embedded in the matrix and to slightly thicken the walls.



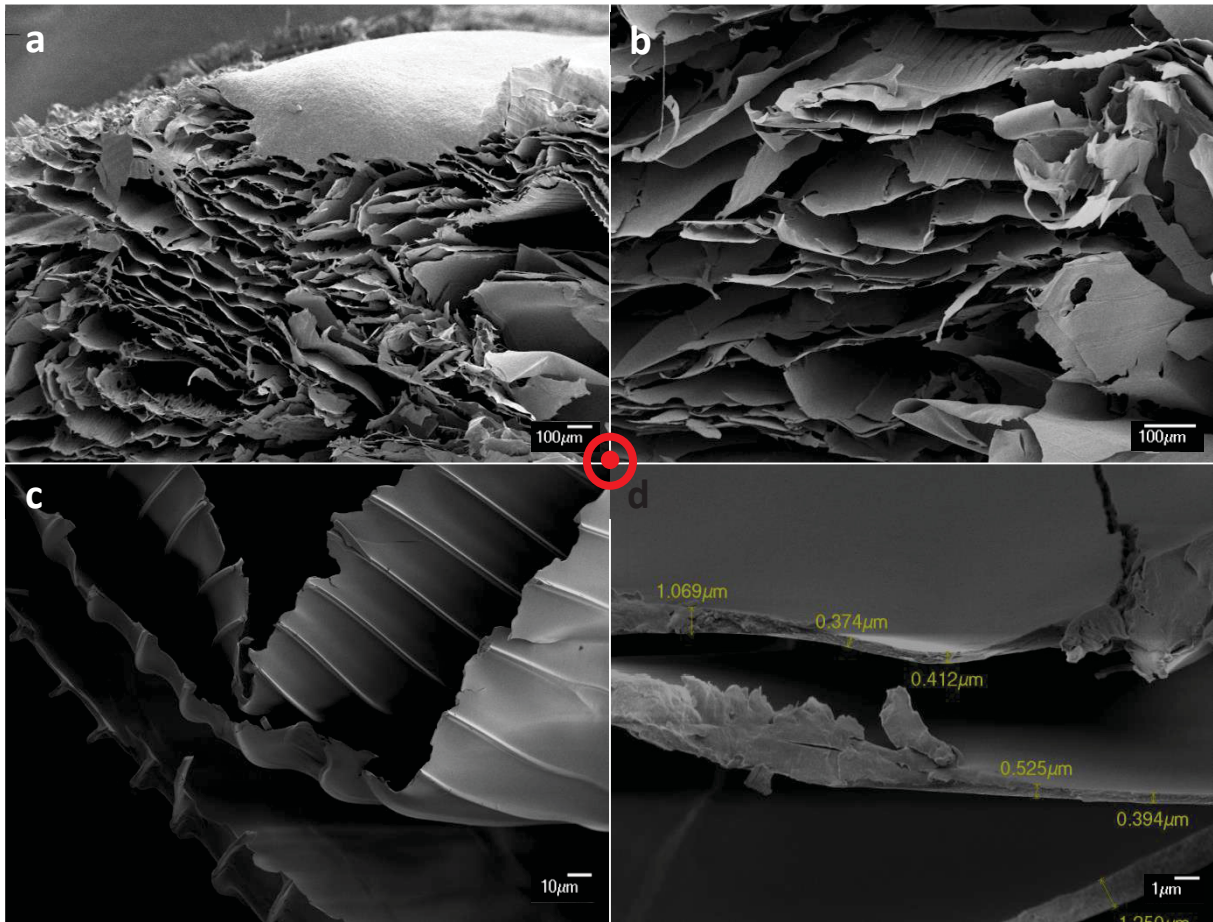


**Figure 6-6** Pure 2wt-% chitosan suspension freeze-casted at a constant speed of  $-0.5^{\circ}/\text{min}$ . a) very fine pore walls were formed (scale bar =  $100\ \mu\text{m}$ ), b) exhibiting vertical ridges (scale bar =  $100\ \mu\text{m}$ ) c) that were very regularly spaced (scale bar =  $10\ \mu\text{m}$ ). d) The chitosan sheets were in average between  $0.2$  and  $1.5\ \mu\text{m}$  thick (scale bar =  $1\ \mu\text{m}$ ). Red arrow = freezing direction.

### Integration of CaP platelets and local planar alignment

Up to 50 vol-% DCP platelets were well integrated in the chitosan walls, following the wall direction as long as the chitosan concentration was not higher than 2 wt-% in the slurry (Figure 6-9a, b, c and e). At 50 wt-% DCP and with a chitosan slurry of 2 wt-%, some bridges with protruding platelets were visible (Figure 6-9f). Beyond 50 vol-% DCP (Figure 6-9g) and 2 wt-% of chitosan (Figure 6-9d), some platelets clearly protruded out of the pore walls. A combination of low chitosan and DCP concentration is thus ideal to embed and align the platelets within the walls.

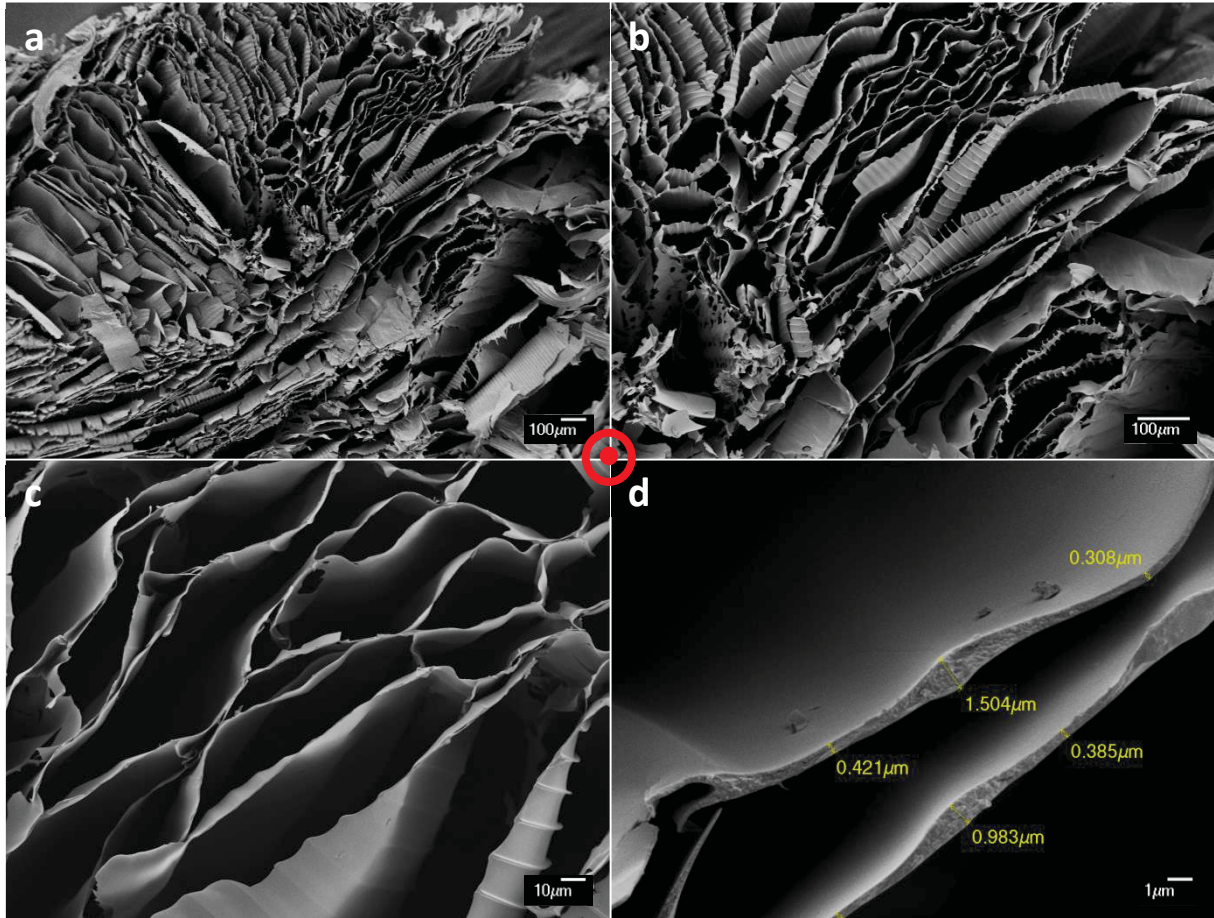


**Figure 6-7** Pure 2wt-% chitosan suspension freeze-casted at a constant speed of  $-10^{\circ}/\text{min}$ . a) and b) the pore size is smaller as with  $-0.5^{\circ}/\text{min}$  (Figure 6-6) (scale bar =  $500\ \mu\text{m}$ ) c) and the ridges are closer (scale bar =  $10\ \mu\text{m}$ ), d) but the wall thickness is similar (scale bar =  $1\ \mu\text{m}$ ). Red arrow = freezing direction for all samples. Red arrow = freezing direction.

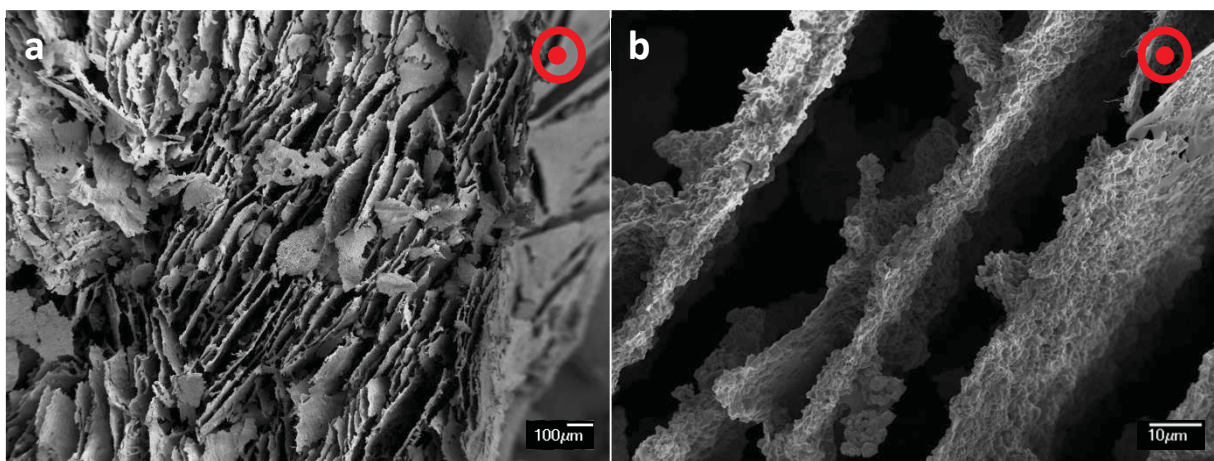


**Figure 6-8** Commercial  $\beta$ -TCP powder (15 wt-%) in a 2 wt-% chitosan slurry, freeze-casted at  $0.5\ ^{\circ}/\text{min}$ . a) SEM overview of a transverse section SEM (scale bar =  $100\ \mu\text{m}$ ) and b) close-up of the pore walls (scale bar =  $10\ \mu\text{m}$ ). Red arrow = freezing direction. Red arrows = freezing direction.

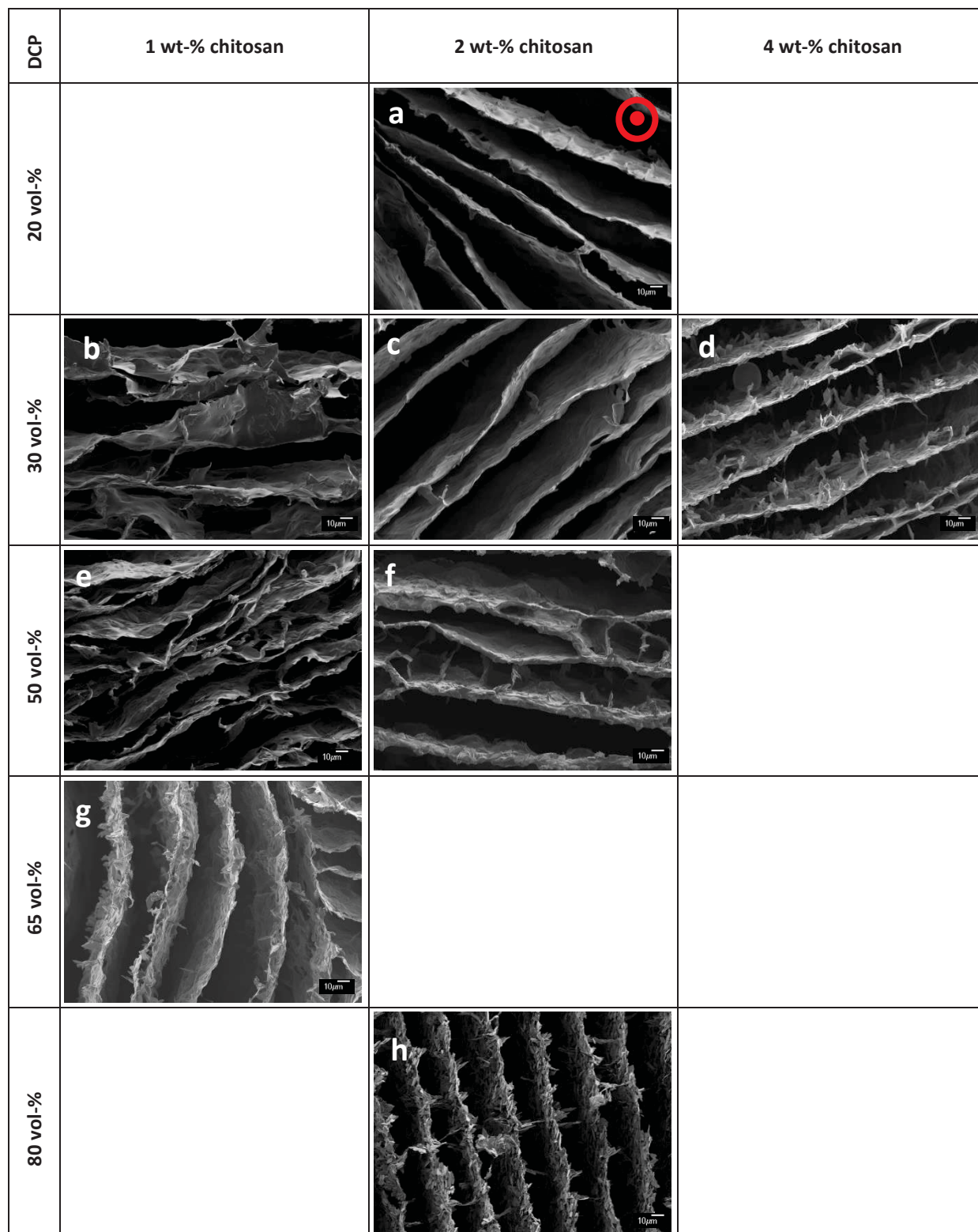


**Figure 6-9** SEM of samples obtained with a freezing rate of 2 °/min. The chitosan concentration in the slurries before drying ranged from 1 to 4 wt-% and the DCP fraction in the final dry samples ranged from 20 to 65 vol-%. The thickness of the walls and number of bridges increases with increasing chitosan and DCP concentration. Red arrow = freezing direction for all samples. Scale bar = 10 μm. a) DCP1-chit2: 20 vol-% DCP, chitosan solution at 2 wt-%; b) DCP1-chit1: 30 vol-% DCP, chitosan solution at 1 wt-%; c) DCP2-chit2: 30 vol-% DCP, chitosan solution at 2 wt-%; d) DCP4-chit4: 30 vol-% DCP, chitosan solution at 4 wt-%; e) DCP2-chit1: 50 vol-% DCP, chitosan solution at 1 wt-%; f) DCP4-chit2: 50 vol-% DCP, chitosan solution at 2 wt-%; g) DCP4-chit1: 65 vol-% DCP, chitosan solution at 1 wt-%; h) DCP15-chit2: 80 vol-% DCP, chitosan solution at 2 wt-%. Red arrow = freezing direction (same for all images).

In general, low freezing rates ( $-0.5\text{ }^{\circ}\text{C}/\text{min}$ ) led to very smooth composite walls with very few or even no ridges and large pores. In particular at 30 vol-% of DCP, using a slow freezing rate of  $0.5\text{ }^{\circ}\text{C}/\text{min}$  led to very smooth composite walls even up to 4 wt-% chitosan in the slurries (Figure 6-10a to c). Smooth walls could still be obtained at higher freezing rates if the chitosan concentration was low enough (Figure 6-10d and e and Figure 6-10g, respectively). However, increasing the freezing rate decreased the lamellae spacing and increased the number of bridges, i.e. reduced the pore size, especially at high chitosan concentration (Figure 6-10c, f, i and l). Cooling down as fast as  $20\text{ }^{\circ}\text{C}/\text{min}$  always created numerous bridges, even at low chitosan concentration (Figure 6-10j to l). These changes in microstructure with chitosan concentration and freezing rate (the formation of bridges and ridges) were also observed with other DCP concentrations, but moved towards lower freezing rates and chitosan concentrations for higher DCP content (50 vol-%, Figure 6-11a and b) and at the opposite for less reinforced samples (20 vol-%, Figure 6-11c). Hence, to avoid platelets protruding out of the walls, only one parameter can be high, either DCP concentration, chitosan concentration or freezing rate. For example at highly concentrated chitosan, slow freezing rate ( $-0.5\text{ }^{\circ}\text{C}/\text{min}$ ) and moderate DCP fraction (maximum 30 vol-%) were necessary (Figure 6-11d).

Later experiments were only performed at a freezing rate of  $0.5\text{ }^{\circ}\text{C}/\text{min}$  to accommodate even the highest platelets content in the thin pore walls and a chitosan concentration of 2 wt-% in the slurry was chosen to limit wall thickness and enhance lamella size, i.e. degree of pore alignment.

Some directional freezing experiments were also conducted with  $\beta$ -TCP platelets possessing a smaller aspect ratio of about 6 [22]. Those platelets being positively charged (see chapter 5), they require a negatively charged matrix to favor good contact and attachment between ceramic and polymer phase. Alginate was chosen for its ease of use. Aligned honey-comb-like porous structures were also obtained, as with DCP platelets and chitosan (Figure 6-12a). The anisotropic particles aligned in the plane of the walls, but some ridges and bridges between pore walls were also observed. In general, the alignment of the particles was qualitatively poorer for similar freezing rate and polymer slurry viscosity. DCP platelets with a higher aspect ratio were favored for the next experiments.

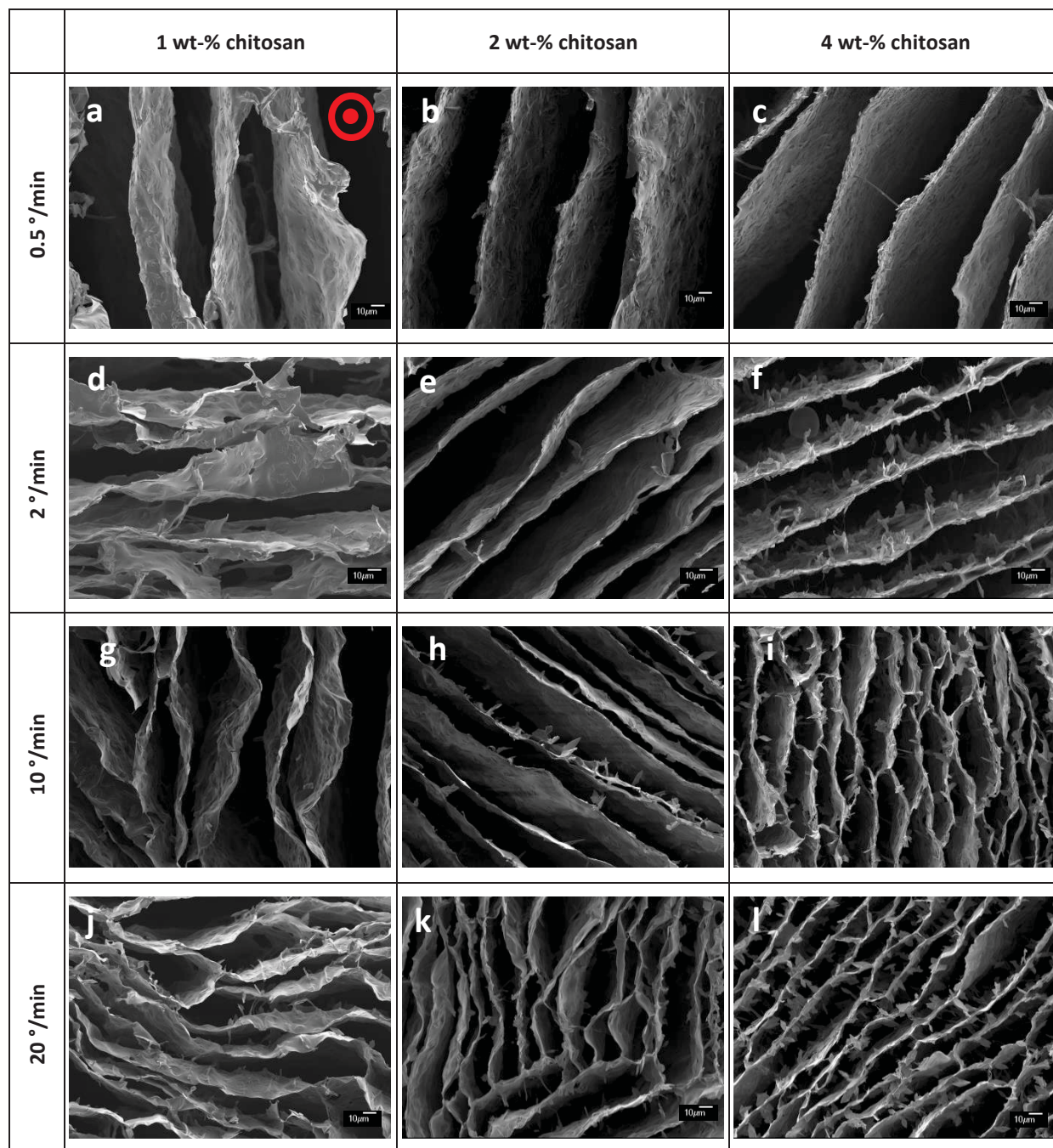


**Figure 6-10** SEM of samples freeze-casted at different freezing rate and with different chitosan concentrations, but always 30 vol-% DCP in the dry samples. The lamellae spacing decreases and the bridge number increases with increasing freezing speed and chitosan concentration. Red arrow = freezing direction for all samples. Scale bar = 10 µm. Red arrow = freezing direction (same for all images).

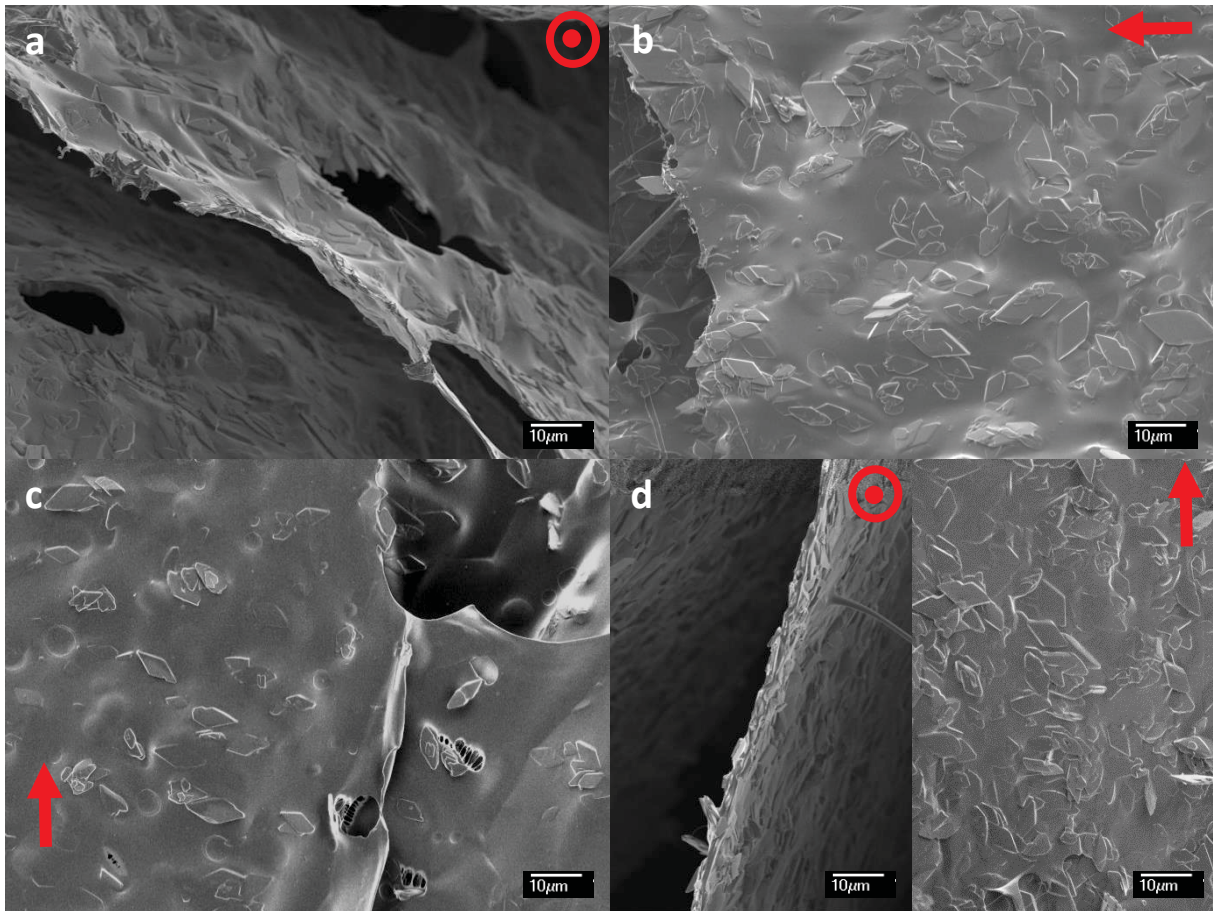


**Figure 6-11** a) and b) 50 vol-% of DCP platelets were well integrated in thin chitosan walls (1 wt-% chitosan in slurry) only when slowly directionally frozen at 0.5 °/min. c) Freezing rate as fast as 20 °/min could be applied when only 20 vol-% of DCP were integrated in chitosan from a 2 wt-% solution. d) Very concentrated chitosan solution (4 wt-%) required very slow freezing rate (0.5 °/min) and maximum 30 wt-%DCP to correctly embed the ceramic platelets. Red arrows = freezing direction.

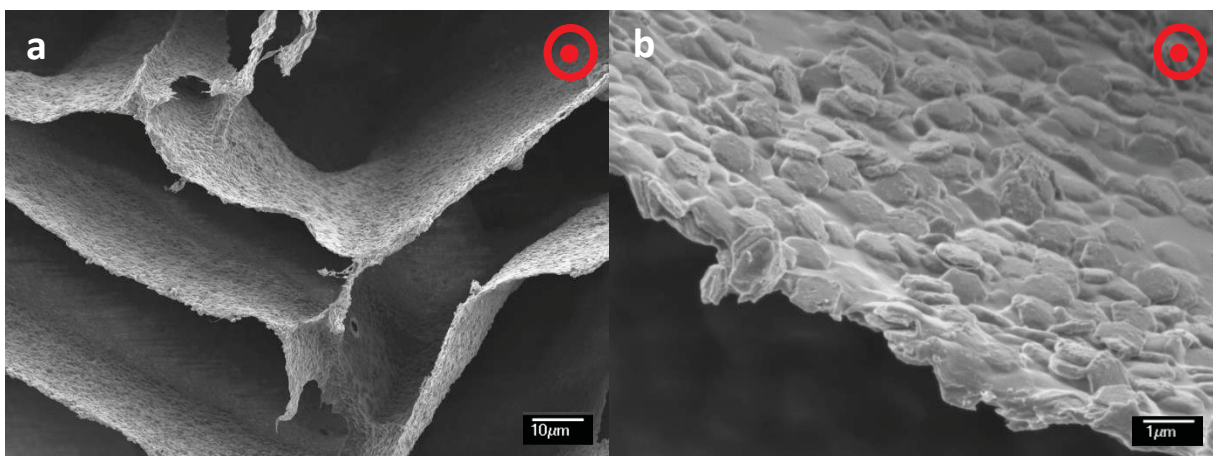


**Figure 6-12** β-TCP platelets (50 vol-%) in an alginate matrix, freeze-casted at 2 °/min. a) overview of the honeycomb-like structure on a transversal cut; b) hexagonal β-TCP platelets were mostly aligned within the plan of the pore walls. Red arrows = freezing direction.

### Attempts to globally align porosity in two directions

The next experiments aimed at obtaining parallel pore walls, i.e. parallel alignment of the embedded ceramic platelets. In order to facilitate a transverse pore orientation – in addition to the vertical freezing direction – the next samples were freeze-casted in Teflon molds with rectangle section. Some copper elements were added on the short sides of the molds to induce horizontal ice crystal growth from one or two opposite sample sides (Figure 6-3a and b). The bottom of the molds was also insulated in some cases to privilege horizontal growth compared to the vertical one (Figure 6-3c). When copper rods were inserted vertically along the short sides of the Teflon mold, the ice crystals grew horizontally from the rods (Figure 6-13). However, the existence of vertical continuous channels, i.e. a parallel alignment of the ice lamellae, could not be verified. The lower part of the sample presented the usual vertical alignment seen in the sole presence of the heat conductive copper bottom.

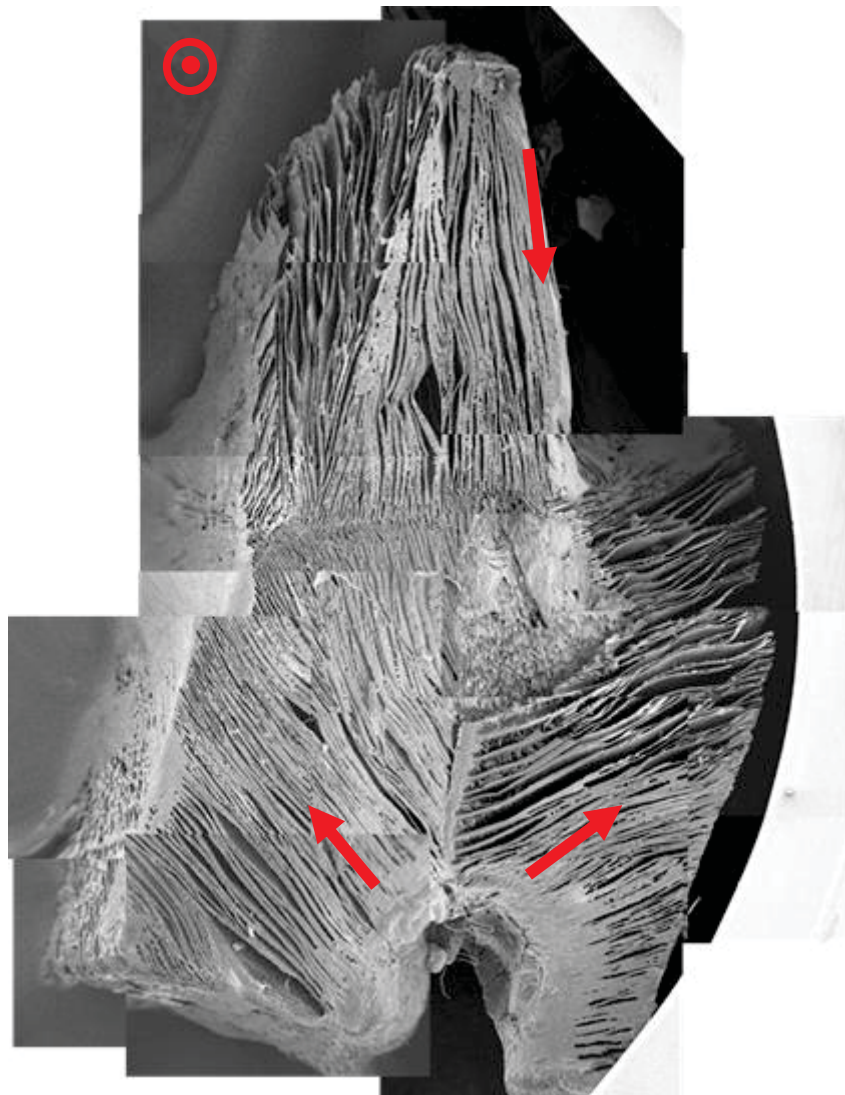


**Figure 6-13** Assembly of SEM pictures of cross-section of a sample freeze-casted in a rectangle Teflon mold with copper rods on both short sides (red arrows = freezing direction).

The use of copper inlays to cover the short sides of the molds led to nice horizontal alignment (Figure 6-14), but the center part of the sample, where growing crystals met from both sides, was disordered and a triangular zone at the bottom still grew vertically (Figure 6-14 and Figure 6-15b). To overcome the disorder in the middle, one copper side was removed. However, the resulting sample was quite inhomogeneous due to simultaneous fast growth of the ice crystals from the side and from the bottom of the mold (Figure 6-15c).

The last experiment was done in a mold with only one copper side and insulated bottom to favor the horizontal growing direction (Figure 6-15d). However, when looking at longitudinal cross-section by SEM, the honey-comb structure was purely horizontal, i.e. not different from the usual vertical freezing samples. The structure was just rotated by 90°. Grinding of the copper bottom did not led to any specific ice crystal orientation.



**Figure 6-14** Pure chitosan freeze-casted with copper inlays on both sides of the mold (configuration b). Red arrow = freezing direction.

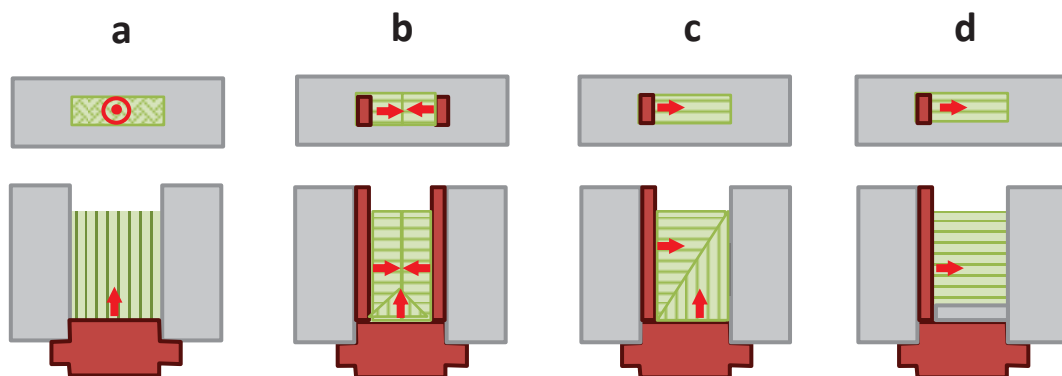


**Figure 6-15** Scheme of the orientation (red arrows = freezing directions) of the structures obtained with different mold configurations (top view and side cut): a) normal mold without inlay; b) with two copper side inlays; c) with only one copper side inlay; d) with only one copper side inlay and bottom insulated from the copper bottom piece. Red arrows = freezing direction.

In consequence, the following experiments were prepared in Teflon molds with rectangular cross-section and without special copper inlays. It has to be mentioned that the ice crystal actually never grew perfectly perpendicular to the copper surfaces, but always with a slight tilt. So neither a perfectly vertical, nor a perfectly horizontal alignment could be achieved.



### Densification and consolidation

The samples were then flattened and acetylated to glue the walls together and obtain dense, cohesive samples. Acetylation is a good way to cross-link chitosan and drastically decrease its water solubility. Acetylation was checked by FTIR (Figure 6-16). The increase of the peak at  $1650\text{ cm}^{-1}$  and the increase of the amide II band at  $1555\text{ cm}^{-1}$  were clear indications of the acetylation of chitosan, i.e. transformation into chitin [26].

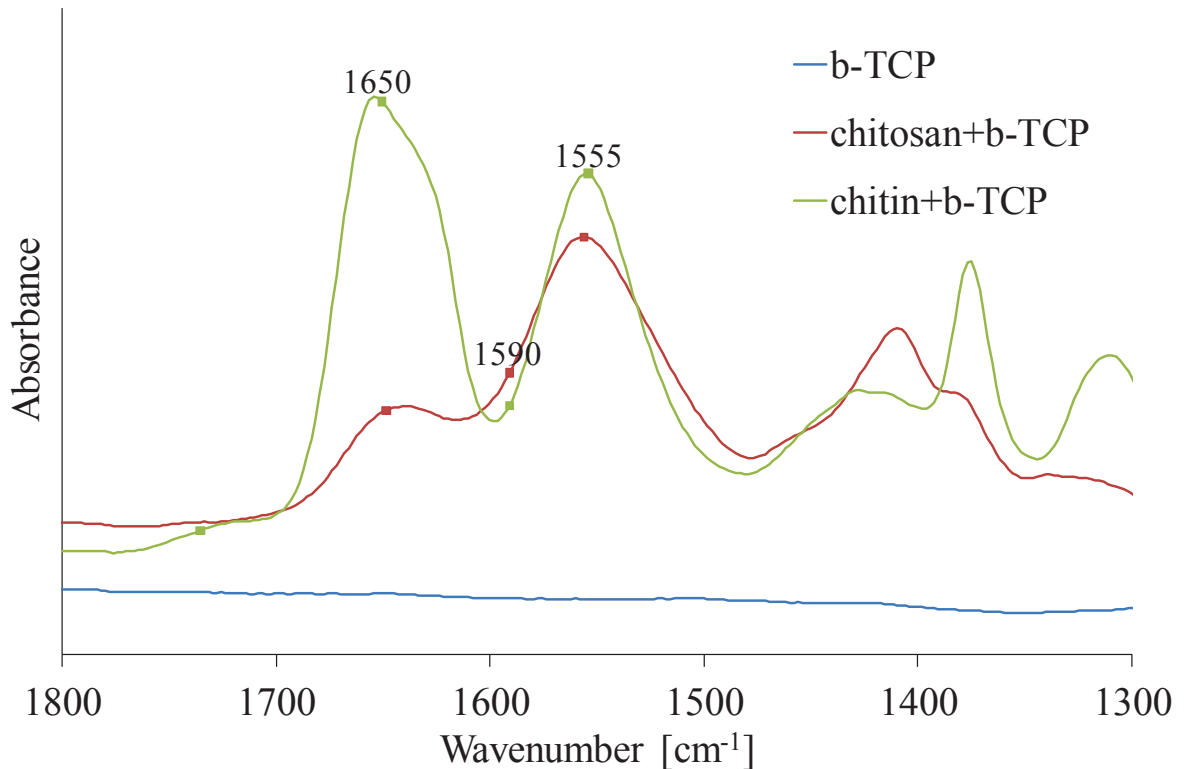


**Figure 6-16** FTIR spectra of pure  $\beta$ -TCP, chitosan +  $\beta$ -TCP after freeze-casting and chitin +  $\beta$ -TCP after acetylation.

### Tensile testing

Dog-bone shaped tensile test samples were punched out of the obtained chitin films. The tensile strength and stiffness of pure chitosan samples were very similar to values obtained from solvent casted samples (see Chapter 5). Surprisingly, the mechanical properties were not affected by the DCP platelets amount (Figure 6-17).

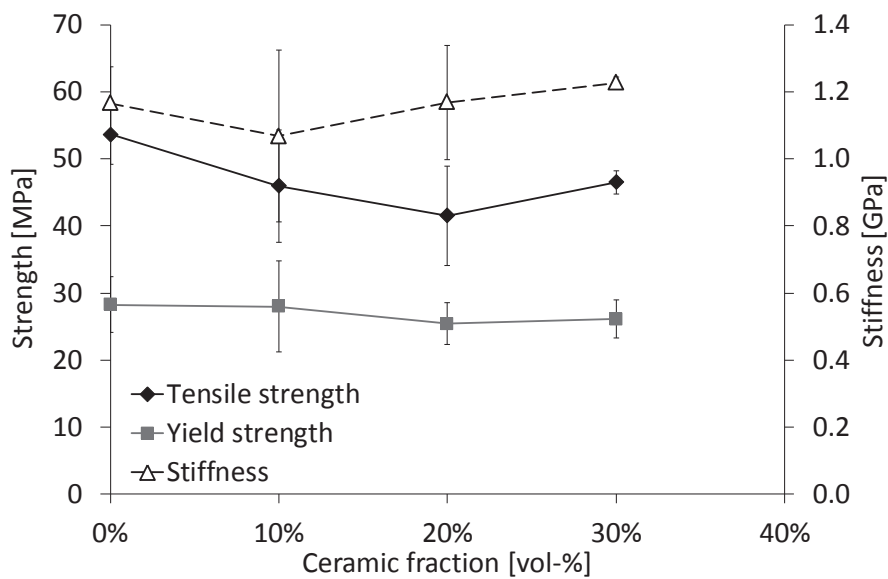


**Figure 6-17** Tensile test results for flatten and acetylated freeze-casted chitosan samples. No significant variation with DCP amount was observed.

SEM observations of cross-sections of acetylated samples provided an explanation to the unaffected mechanical properties with DCP reinforcement: no platelets were recognizable within the continuous polymeric phase (Figure 6-18). Some unacetylated and unflattened freeze-casted samples were also tensile tested, but the walls slipped against each other and delaminated with already very low tensile forces ( $< 5$  N), while high elongations were observed (a few mm).

## Discussion

The honeycomb-like structure of the preliminary agar- $\beta$ -TCP samples had thinner cell walls and smaller pore size (Figure 6-4) than in other scaffold types, like pure alginate or even composite with alginate-chitosan matrices [12]. The transversal aspect ratio of the pores was much smaller than observed in chitosan-gelatine or alginate gelatin based samples [12] and should result in superior mechanical properties. However, the walls were still much too thick to force the platelets to align (Figure 6-5). Wall thickness in the range of the platelets size might be more efficient to align the platelets within the walls, as demonstrated in [12].

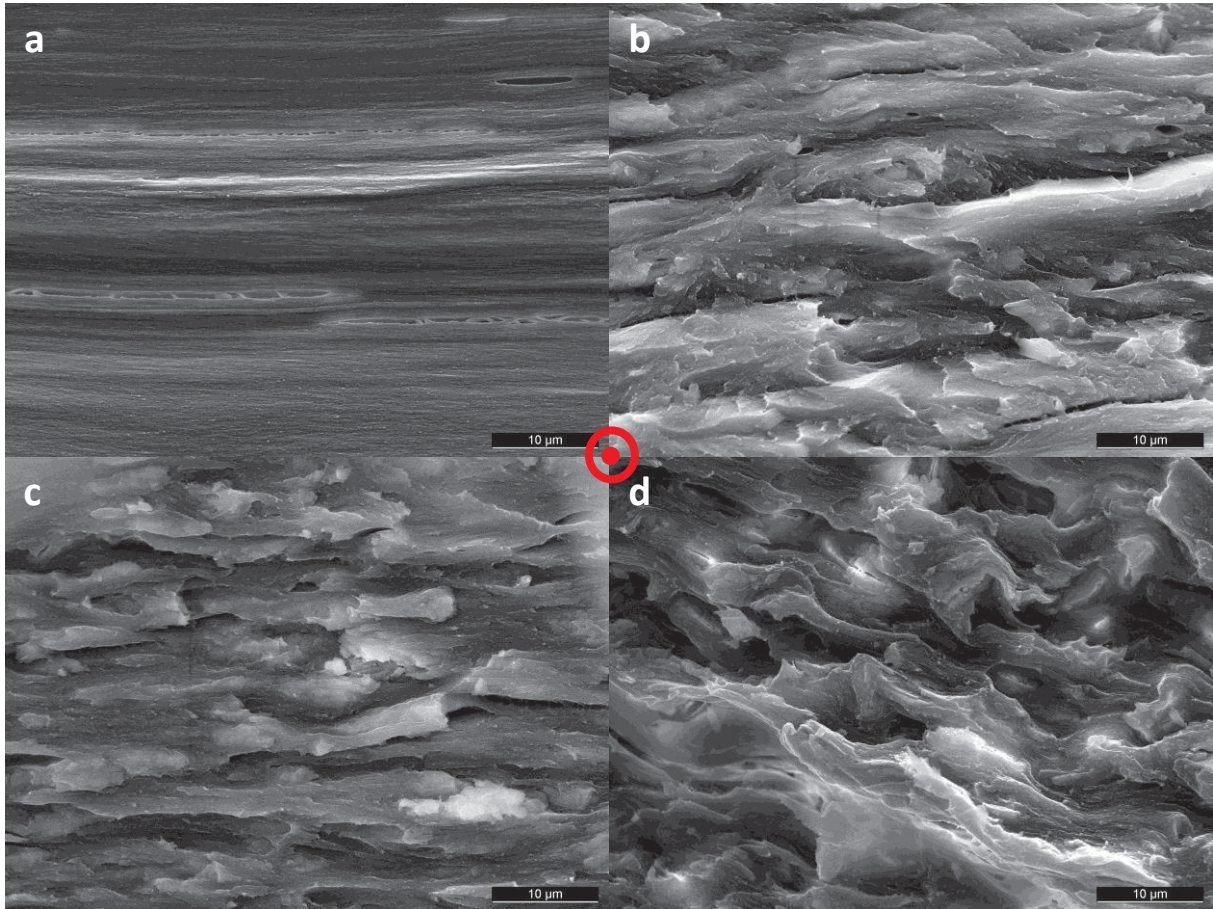


**Figure 6-18** Cross-sections of flatten freeze-casted samples after tensile testing. a) Pure chitosan; b) 10 vol-% of DCP; c) 20 vol-% of DCP; d) 30 vol-% of DCP. Scale bars = 10  $\mu\text{m}$ . Red arrow = freezing direction (same for all images).

As already shown in the literature [28], freeze-casting of pure chitosan solutions is feasible and leads to very fine pore walls, with tunable pore size by means of freezing-rate variations for example (Figure 6-6 and Figure 6-7). Adding ceramic particles in the chitosan slurries did not impair the honeycomb-like structure formation and the ceramic particles were well concentrated in the pore walls, as expected [12]. When plate-like particles were incorporated, they even aligned within the pore walls, i.e. did not protrude out of the walls (Figure 6-9a). The larger the aspect ratio of the platelets, the better they aligned in the walls (Figure 6-12 compared to Figure 6-10). Moreover, reducing the wall thickness to values similar to platelets thickness is an effective way to improve the alignment. To do so, slow freezing rates combined with low chitosan concentrations are ideal (Figure 6-10).

Attempts to force the vertical pores to align in a longitudinal plane were unsuccessful (Figure 6-13 and Figure 6-15). To obtain flat and dense samples for tensile testing, it was decided to use samples produced “classically”, i.e. only with a vertical bottom-to-top freezing direction. Acetylation was chosen as solidification mean because of its ease of application and potentially positive influence

on biological properties [26]. The acetylation of the chitosan matrix was successful; however, dissolution of the DCP platelets during the process occurred. Hence, only pure chitosan films were obtained and tested mechanically.

The good adhesion of the pore walls together due to acetylation was proved by the mechanical properties of the chitosan films that were similar to those obtained with solvent-casted films. However, no increase of strength was observed in ceramic-loaded samples because of the disappearance of the platelets during the acetylation process. The acid release during acetylation process might have dissolved the ceramic platelets. Hence, this consolidation method cannot be used with DCP filled samples. Without consolidation, the samples delaminated under tensile stresses. It is assumed that the pore walls are not perfectly aligned longitudinally in the samples, and in consequence shear forces apply on the slightly tilted layers causing easy delamination.

## Conclusions

In the idea to approach the mechanical properties of natural composites materials while using individually weak materials, it is necessary to observe a few basic bio-inspired principles, like the way the structure should look like. However, trying to also mimic the processes nature uses to make them usually leads to much too complicated and / or too slow synthesis methods to obtain samples of reasonable size. The synthesis method proposed here, i.e. using directional freezing of CaP platelets in a hydrogel matrix, successfully led to aligned, honey-comb-like porous structures. The platelets aligned within the pore walls when the pore walls were in the size-order of the platelets thickness and the alignment was better with larger aspect ratio. Ceramic content up to 50 vol% showed good alignment and embedding of the platelets within the organic matrix. Due to their lamellar structure, the actual scaffolds delaminate upon tensile testing. Further developments are under investigation to compress 2D-oriented lamellar samples into dense, nacre-like structures, and to stabilize the chitosan matrix by acetylation or any other mean that would avoid dissolution of the CaP platelets.

No mechanical testing could be performed to prove that high alignment can be artificially obtained and leads to outstanding combination of strength and toughness, like in natural composites. Demonstrating this would prove that taking inspiration from natural structures is feasible with engineered production methods, without requiring long and tedious biomimetic synthesis processes.

## References

- [1] Tang Z, Kotov NA, Magonov S, Ozturk B. Nanostructured artificial nacre. *Nat Mater*. 2003;2:413-8.
- [2] Bonderer LJ, Studart AR, Gauckler LJ. Bioinspired design and assembly of platelet reinforced polymer films. *Science*. 2008;319:1069-73.
- [3] Dimas LS, Bratzel GH, Eylon I, Buehler MJ. Tough composites inspired by mineralized natural materials: Computation, 3D printing, and testing. *Advanced Functional Materials*. 2013;23:4629-38.
- [4] Kamat S, Su X, Ballarini R, Heuer AH. Structural basis for the fracture toughness of the shell of the conch *Strombus gigas*. *Nature*. 2000;405:1036-40.
- [5] Ji B, Gao H. Mechanical properties of nanostructure of biological materials. *J Mech Phys Solids*. 2004;52:1963-90.
- [6] Barthelat F, Tang H, Zavattieri PD, Li CM, Espinosa HD. On the mechanics of mother-of-pearl: A key feature in the material hierarchical structure. *Journal of the Mechanics and Physics of Solids*. 2007;55:306-37.
- [7] Griffith AA. The Phenomena of Rupture and Flow in Solids. *Philosophical Transactions of the Royal Society of London Series A, Containing Papers of a Mathematical or Physical Character*. 1921;221:163-98.
- [8] Munch E, Launey ME, Alsem DH, Saiz E, Tomsia AP, Ritchie RO. Tough, bio-inspired hybrid materials. *Science*. 2008;322:1516-20.
- [9] Libanori R, Münch FHL, Montenegro DM, Studart AR. Hierarchical reinforcement of polyurethane-based composites with inorganic micro- and nanoplatelets. *Composites Science and Technology*. 2012;72:435-45.
- [10] Maxwell WA, Gurnick RS, Francisco AC. Preliminary investigation of the freeze casting method for forming refractory powders. NACA research memorandum 1954.
- [11] Wegst UGK, Schechter M, Donius AE, Hunger PM. Biomaterials by freeze casting. *Philos Trans R Soc A Math Phys Eng Sci*. 2010;368:2099-121.
- [12] Hunger PM, Donius AE, Wegst UGK. Platelets self-assemble into porous nacre during freeze casting. *J Mech Behav Biomed Mater*. 2013;19:87-93.
- [13] Tong Hm, Noda I, Gryte CC. CPS 768 Formation of anisotropic ice-agar composites by directional freezing. *Colloid & Polymer Sci*. 1984;262:589-95.
- [14] Schoof H, Bruns L, Apel J, Heschel I, Rau G. Einfluss des Einfriervorganges auf die Porenstruktur gefriergetrockneter Kollagenschwämme. Heidelberg, ALLEMAGNE: Müller; 1998.
- [15] Schoof H, Bruns L, Fischer A, Heschel I, Rau G. Dendritic ice morphology in unidirectionally solidified collagen suspensions. *Journal of Crystal Growth*. 2000;209:122-9.
- [16] Sum Chow K, Khor E, Chwee Aun Wan A. Porous chitin matrices for tissue engineering: Fabrication and in vitro cytotoxic assessment. *J Polym Res*. 2001;8:27-35.
- [17] Araki K, Halloran JW. Porous ceramic bodies with interconnected pore channels by a novel freeze casting technique. *Journal of the American Ceramic Society*. 2005;88:1108-14.
- [18] Deville S, Saiz E, Tomsia AP. Freeze casting of hydroxyapatite scaffolds for bone tissue engineering. *Biomaterials*. 2006;27:5480-9.
- [19] Macchetta A, Turner IG, Bowen CR. Fabrication of HA/TCP scaffolds with a graded and porous structure using a camphene-based freeze-casting method. *Acta Biomaterialia*. 2009;5:1319-27.

- [20] Zhang H, Hussain I, Brust M, Butler MF, Rannard SP, Cooper AI. Aligned two- and three-dimensional structures by directional freezing of polymers and nanoparticles. *Nature Materials*. 2005;4:787-93.
- [21] Jafarkhani M, Fazlali A, Moztarzadeh F, Mozafari M. Mechanical and structural properties of polylactide/chitosan scaffolds reinforced with nano-calcium phosphate. *Iranian Polymer Journal (English Edition)*. 2012;21:713-20.
- [22] Galea L, Bohner M, Thuering J, Doebelin N, Aneziris CG, Graule T. Control of the size, shape and composition of highly uniform, non-agglomerated, sub-micrometer  $\beta$ -tricalcium phosphate and dicalcium phosphate platelets. *Biomaterials*. 2013;34:6388-401.
- [23] Rodriguez-Carvajal J. Recent Developments of the Program FULLPROF. *Commission on Powder Diffraction (IUCr) Newsletter*. 2001;26:12-9.
- [24] Munch E, Saiz E, Tomsia AP, Deville S. Architectural control of freeze-cast ceramics through additives and templating. *Journal of the American Ceramic Society*. 2009;92:1534-9.
- [25] Venkatesan J, Kim SK. Chitosan composites for bone tissue engineering - An overview. *Mar Drugs*. 2010;8:2252-66.
- [26] Xu J, McCarthy SP, Gross RA, Kaplan DL. Chitosan film acylation and effects on biodegradability. *macromolecules*. 1996;29:3436-40.
- [27] Kubota N, Tatsumoto N, Sano T, Toya K. A simple preparation of half N-acetylated chitosan highly soluble in water and aqueous organic solvents. *Carbohydr Res*. 2000;324:268-74.
- [28] Gao H-L, Lu Y, Mao L-B, An D, Xu L, Gu J-T, et al. A shape-memory scaffold for macroscale assembly of functional nanoscale building blocks. *Materials Horizons*. 2014;1:69-73.

## Part II: Textured ceramic monoliths

### CHAPTER 7:

## MICRO-TEXTURING BY RECRYSTALLIZATION OF CALCIUM PHOSPHATE BLOCKS IN HYDROTHERMAL CONDITIONS

### ***Abstract***

A new approach to obtain textured 3D scaffolds is presented here. It consists in recrystallizing  $\alpha$ -Tricalcium Phosphate ( $\alpha$ -TCP) blocks into calcium deficient hydroxyapatite (CDHA) under hydrothermal conditions. SEM and XRD analysis revealed the appearance of fine (0.1-0.5  $\mu\text{m}$ ) CDHA needles, aligned over several hundreds of micrometers. The obtained microstructures were analogous to shell or enamel microstructures, with 5 hierarchical structure levels. Brazilian tests were used to determine the diametral tensile strength,  $\sigma_{dts}$ , and the work-of-fracture, WOF. Hydrothermal incubation significantly increased  $\sigma_{dts}$  and WOF of the ceramic blocks. These improvements were attributed to the fine and entangled crystal structure obtained after incubation leading to tortuous crack formation. Hence, refining the microstructure and texturing a ceramic material is an effective way to improve its strength and particularly its toughness. Indeed, fractured surfaces revealed intergranular tortuous crack paths, which dissipate much more energy than transgranular cracks as observed in the sintered samples.

Publication in preparation:

Galea L, Alexeev D, Bohner M, Doebelin N, Aneziris CG, Studart A, Graule T. *Hierarchical structures in calcium phosphate ceramic blocks: from aligned microfibers to toughened macro-samples*. XXX (2015).

## Introduction

Beside the challenging brick-and-mortar approach reported in the first part of this thesis, a simpler way to improve toughness of calcium phosphate based materials was investigated. Briefly, the idea was to start with monolithic ceramic blocks, as commonly used by surgeons for bone filling, and modify intrinsically their architecture to increase the work of fracture.

Nowadays CaP ceramics are widely used as bone graft substitute materials, the majority of commercial porous scaffolds being composed of  $\beta$ -tricalcium phosphate ( $\beta$ -TCP), hydroxyapatite (HA) or a blend of both phases (biphasic). These products combine high biocompatibility, adequate resorption rate and porosity for nutrient supply, vascularization, cell proliferation, and tissue infiltration. However, ceramics CaP scaffolds are very brittle (fracture toughness  $\ll 1\text{MPa}\cdot\text{m}^{1/2}$ ) and exhibit low tensile strength (typically  $< 20\text{MPa}$ ) [1, 2]. In comparison, cortical bone has a compressive strength of 100-150 MPa, a flexural strength of 135-193 MPa and a fracture toughness of 2-12  $\text{MPa}\cdot\text{m}^{1/2}$  [3]. These properties limit the use of CaP materials to indications in which the implant is not subject to mechanical loading. Cyclic dynamic loading would lead to cracking and mobilization of the surrounding bone fragments would delay or inhibit bone formation and thus impair successful healing of the defect. All CaP scaffolds commercially available can therefore only be applied in situations where either intact bone or additional metal implants protect the ceramic bone void filler from mechanical stress. The availability of novel load-bearing resorbable scaffolds would eliminate the need for additional reinforcement and widen the scope of indications. Such a scaffold should be strong enough to support normal loading applied on the bone, its elastic modulus should be similar to the one of bone to avoid stress shielding, and high toughness would be necessary to prevent catastrophic failure.

Combination of high strength and toughness is rare in engineered materials because these properties are antagonists [4]; single-phase materials are normally either strong and brittle, or tough and weak. Obtaining a combination with biodegradable materials is even more challenging because biodegradability generally implies weak chemical bonds, which are in consequence rarely mechanically strong. Moreover, biocompatibility and biodegradability strongly limit the choice of materials. Ceramics are strong, but highly brittle. Metals can be adequate in terms of toughness, but they lead to stress shielding and are, with the exception of magnesium, non-degradable. Polymers do generally not reach the required strength and their degradation products can be acidic and/or provoke an inflammatory response, both adversely affect the healing process [5].



Since no single-phase material seems to fulfill all requirements imposed by a load-bearing, resorbable bone graft substitute, the focus of researchers has shifted towards composite materials, which combine properties of materials of different nature. Unsurprisingly, reinforcement of degradable polymers by ceramic particles has already been extensively investigated [6-11]. However, in all of these studies, the problematic organic fraction remained large which might cause above-mentioned biological complications [5]. In addition, mechanical properties of such artificial composites are by far inferior to comparable natural materials [2], which is mainly attributed to poor adhesion between organic and inorganic phases [12] and above all because of the lack of a controlled architecture of the reinforcing particles within the matrix. To achieve the ideal mechanical and biological properties for a load-bearing, resorbable bone graft substitute, the materials should mainly consist of ceramic, toughened with only minor amount of polymer – provided the ceramic-polymer adhesion is good. To get close to this ideal material incorporating only thin interlayers of a tough secondary phase [3], bio-inspired structures featuring a highly organized architecture of the ceramic particles are necessary. Indeed, an organized architecture allows maintaining a low polymer content and a large contact area between polymer and ceramic particles. In fact, mechanical properties approaching those of natural composites like bone or even nacre have only been achieved with very well-controlled alignment of ceramic particles [13-15]. However, despite the highly ordered particle shape and arrangement, the polymer fraction was still much higher than the content found in nacre or even bone. Also, the ceramic particles were not degradable.

Toughening ceramic based materials by incorporating low fraction of polymer phases (“intrinsic toughening” [3, 16]) remains a very challenging approach with the present engineering methods. It is thus questionable if the toughness of pure ceramic scaffolds might not be first considerably improved by structural changes (defined as “extrinsic toughening” mechanisms in [16] and [3], but later also called “structural toughening” in this manuscript). Following this idea, the present study first goes a step backward, i.e. focusing only on the mineral part and particularly on its microstructure.

Inspiration to improve bioceramic’s toughness was taken in classical engineering approaches. Strength and toughness of structural ceramics are usually improved by microstructural developments like (a) grain size refinement [17], (b) transformation-toughening [18-21], or (c) incorporation of second phase particles [22, 23]. Refinement already proved to be also efficient in bioceramics, in particular in HA [24]. d) A last promising approach to toughen ceramics is to get inspiration from nature, i.e. to create tortuous structures [3, 25]. Tortuous structures are constituted of anisotropic particles, assembled in such a way that junctions do not align, hence deviating interparticle cracks. Its good potential was demonstrated by the recently obtained “Nacre-like Alumina” [25]. However, to the best of our knowledge, this has not been investigated yet with bioceramics. A combination of

strategies (a), grain size refinement, and (d), design of tortuous microstructures, seems adequate to increase the work-of-fracture (WOF) of resorbable CaP ceramics by inducing crack deflection. However, existing synthesis processes for CaP ceramics do not allow reaching the target structure.

Therefore, a novel approach was searched for here. CaP ceramics are commonly shaped by pressing of a dry powder or drying/setting of a slurry, followed by a heat treatment (sintering), to consolidate the structure. With such methods, the final grain size is limited by the particle size of the initial powder, hence requiring nano-powders followed by quick sintering or two-step sintering processes [26]. Hydrothermal synthesis has already shown the potential of forming fine CaP (particularly HA) particles [27-29]. However, assembly and consolidation of these particles to form fine structured blocks, either by cement reaction or sintering, leads to grain growth and finally poor improvements of mechanical properties compared to larger microstructures [24, 30, 31]. Another approach, tried in particular by Ioku et al., consisted in first compacting an  $\alpha$ -TCP powder, with or without other additives, followed by submitting the pressed forms to hydrothermal treatment [32, 33]. The obtained CDHA blocks were made of entangled rod-shape particles and were even more biodegradable and induced more bone formation than stoichiometric HA samples obtained by conventional sintering process [34]. However, the rod-shape crystal assembly was quite loose and in consequence completely disordered, without alignment.

To overcome the loose structure obtained in previous hydrothermal studies, our approach was to first solidify and densify CaP blocks, and then refine the microstructure by recrystallization (phase transformation, no isomorph transition) under hydrothermal conditions. By obtaining an **assembly of sub-micrometric particles in complex architectures**, we aimed at improving the toughness of CaP scaffolds by effective crack deflection mechanism, i.e. a structural toughening.

## Materials and Methods

Globally, the CaP block preparation consisted in 5 steps:

- 1) Powder synthesis:  $\alpha$ -TCP powder was prepared in-house by ball-milling of a calcined mixture of calcium carbonate ( $\text{CaCO}_3$ , Reag. Ph Eur., art. no 102066, Merck, Darmstadt, Germany) and calcium hydrogen phosphate ( $\text{CaHPO}_4$ , 99.95%, art. no 1548, GFS Chemicals, Columbus OH, USA) such as to obtain a calcium to phosphate molar ratio of 1.47 to avoid hydroxyapatite formation.
- 2) Cement paste preparation: The liquid phase was a 0.1 M citric acid solution ( $\text{C}_6\text{H}_8\text{O}_7 \cdot \text{H}_2\text{O}$ , Ph Eur, BP, JP, USP, E 330, FCC, Art. no 100243, Merck, Darmstadt, Germany). The powder was

added to the liquid in a 0.6:1 liquid:powder weight ratio and immediately mixed (stirrer VOS 14, art. no. 441-0026P, VWR, Dublin, Ireland) at 2000rpm for 20 seconds and then poured into cylindrical Teflon molds (8 mm diameter, 8mm height).

- 3) Setting: Setting took place at 60°C in water vapor saturated atmosphere for 72 hours.
- 4) Sintering: After unmolding, the samples were sintered at 1200 or 1500 °C for 8 hours at a heating rate of 5 °C/min and a cooling rate of -10 °C/min in a muffle furnace (LHT 02/16, Nabertherm, Germany).
- 5) Hydrothermal incubation: Hydrothermal incubation was conducted in steel autoclaves (Acid Digestion Vessel, model 4744, Parr Instruments, Moline IL, USA) with homemade inner Teflon capsules (inner volume of 45 ml), placed for 2 - 72 hours at 125 / 150 / 175 / 200 °C. The samples were placed above the water level (7 ml) on perforated Teflon plates (Figure 7-1). At the end of the incubation time, the autoclaves were cooled down for a few minutes in air, then in a water bath. The samples were finally dried for 24h at 60 °C.

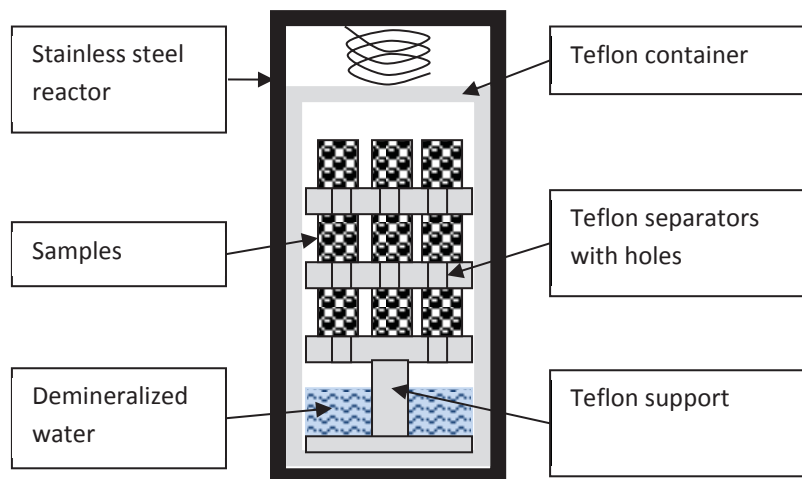


**Figure 7-1** Scheme of the hydrothermal reactor and intern positioning of samples.

During the hydrothermal treatments, the water evaporation created a pressure increase equal to the saturated vapor pressure  $P$  (Table 7-1). This increase is almost exponential with the temperature  $T$ :

$$\log_{10}(P) = A - \frac{B}{C + T} \quad \text{Equation 1}$$

with  $A = 8.14019$ ,  $B = 1810.94$  and  $C = 244.485$  for  $99 \text{ } ^\circ\text{C} < T < 374 \text{ } ^\circ\text{C}$  [35]. Hence, the pressure was 2.27, 4.64, 8.78 and 15.30 atm at 125, 150, 175 and 200 °C, respectively (Table 7-1).

**Table 7-1** Water vapor pressure in function of temperature.

Temperature [°C]	Pressure [mmHg]	Pressure [MPa]	Pressure [atm]
125	1734	0.23	2.27
150	3544	0.47	4.64
175	6655	0.89	8.78
200	11640	1.55	15.30

Alternatively, some samples were made replacing steps 2 to 4 by powder pressing, using a hydraulic press and steel molds of the same dimensions as the cement samples.

### Samples characterization

After sintering and hydrothermal incubation, all samples were weighed and their external dimensions were measured with a caliper.

From each batch, at least one sample was ground and used for X-ray diffraction (XRD) analysis. Powder datasets were collected on a PANalytical CubiX diffractometer using graphite-monochromated CuK radiation. A range from 4 to 60 ° 2 $\theta$  was scanned with a step size of 0.016 ° 2 $\theta$  and a counting time of 1 second per step. The divergence slit was used in automatic mode set to an irradiated length of 10 mm. The datasets were analyzed by Rietveld refinement using the software BGMN version 4.2.20 [36] and structure templates from Dickens et al. [37] / Schroeder et al. [38] for  $\beta$ -TCP, Mathew et al. [39] for  $\alpha$ -TCP, Sudarsanan [40] for HA (or CDHA), Dickens et al. [41] for DCP and Boudin et al. [42] for pyrophosphates ( $\beta$ -CPP). The following parameters were refined: scale factor, unit cell parameters, anisotropic peak broadening, isotropic micro-strain, and preferred orientation.

The microstructure of the samples was investigated by Scanning Electron Microscope (SEM) (LEO 1530, Carl-Zeiss SMT AG, Oberkochen, Germany). The samples were sputtered with platinum for 60 seconds at 40 mA and  $5 \cdot 10^{-7}$  mbar in a sputter coater (BAL-TEC, SCD 050) before investigation.

To determine the grain size after sintering, the samples were polished using 1000 then 2400 and finally P4000 grit Silicon Carbide abrasive paper (Reflex concept, Presi, Le Locle, Switzerland) on a polishing machine (Knuth-Rotor 2, Struers) using isopropanol as lubricant. The samples were then rinsed and thermally etched at 1300 °C for 20 min. The grain size was measured on SEM images. Hydrothermally treated samples could not be thermally etched. Those samples were embedded, polished and chemically etched with 0.1M HCl for 10s.

Tensile strength of ceramics is difficult to measure because samples preparation of brittle materials is challenging. Hence, Brazilian tests (diametral compression) were used to indirectly investigate the tensile properties of brittle materials [43]. The transverse pressure load was applied with a Zwick (zwicki-Line Z5.0, Zwick, Kennesaw, GA, USA) at a constant displacement speed of 10 mm/min. The toughness can be merely estimated from the work of fracture, but it is only a semi-quantitative method, i.e. the results are good for comparison of similar samples, but it is not an intrinsic material property.

The results were compared by ANOVA with a significance limit set at  $p < 0.01$ .

## Results

### Macroscopic observations

After the hydrothermal treatments and subsequent drying, the blocks could be manipulated without losing their integrity. They were hence weighed and measured to check their macroscopic shape and dimensions. No significant differences of diameter and height occurred during incubation, independently of the incubation conditions (time and temperature) (Figure 7-2).

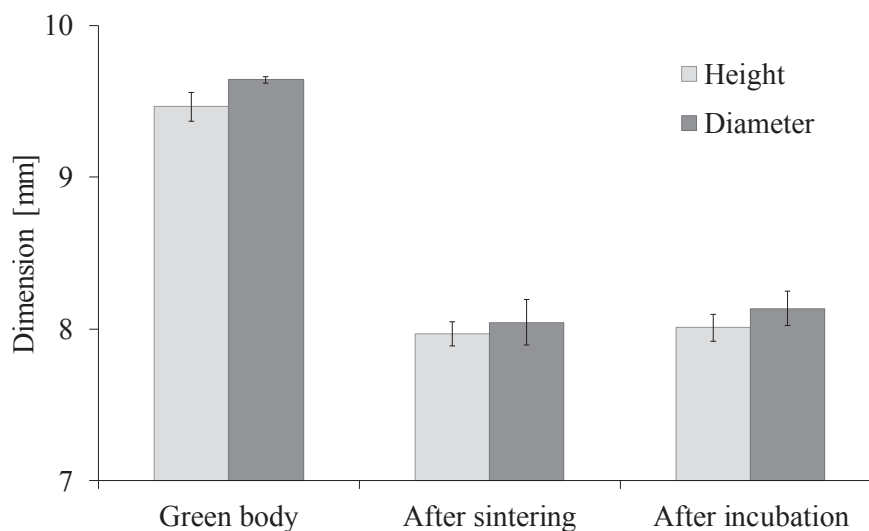


**Figure 7-2** Height and diameter of the cement blocks before sintering (green body), after sintering and after hydrothermal incubation for 8 hours at 200 °C.

### Microstructural changes (SEM)

One sample per composition/condition was broken by bending and the fractured surfaces prepared for observation by SEM. Morphology changes were observed at the microscale. Powder

pressed samples (Figure 7-3a) formed elongated crystals (Figure 7-3b), quite different from the microstructures usually obtained by cement reaction, i.e. in physiological conditions (Figure 7-3c). Powder pressed samples were directly incubated in hydrothermal conditions, without kinetic study, whereas cement samples (Figure 7-3c) were first sintered (Figure 7-3d) and then progressively incubated at different temperatures.

Recrystallization from the smooth sintered porous  $\alpha$ -TCP structure (Figure 7-4a) into fine elongated faceted structures occurred first around cracks and pores (Figure 7-4b, enlarged in Figure 7-4e). The conversion then progressed into the bulk of the  $\alpha$ -TCP initial structure (Figure 7-4c) with a linear rate strongly depending on the temperature. At the end of the reaction, the whole sample was mostly filled with needle-like crystals (Figure 7-4d). The first crystals around cracks seemed rather disoriented (Figure 7-4e), but large zones (from a few to hundreds of micrometers) with aligned crystals were later observed (Figure 7-4d and f). Semi-quantitatively, recrystallization of about 0.5  $\mu\text{m}$  from a surface (pore or crack) was measured after 2h incubation at 125 °C and progressed up to about 3  $\mu\text{m}$  after 8h. At 150 °C, the converted thickness was similar at 2h ( $\approx 0.5 \mu\text{m}$ ), but progressed already to about 5  $\mu\text{m}$  after 4h. At 175 °C, the converted thickness could only be measured after 2h (about 5  $\mu\text{m}$ ) but not at later time points because it became too thick. At longer incubation times, the phase conversion appeared complete. Large crystals were also observed at the end of the reactions, especially at the highest temperatures and on the pore surfaces (Figure 7-4f).

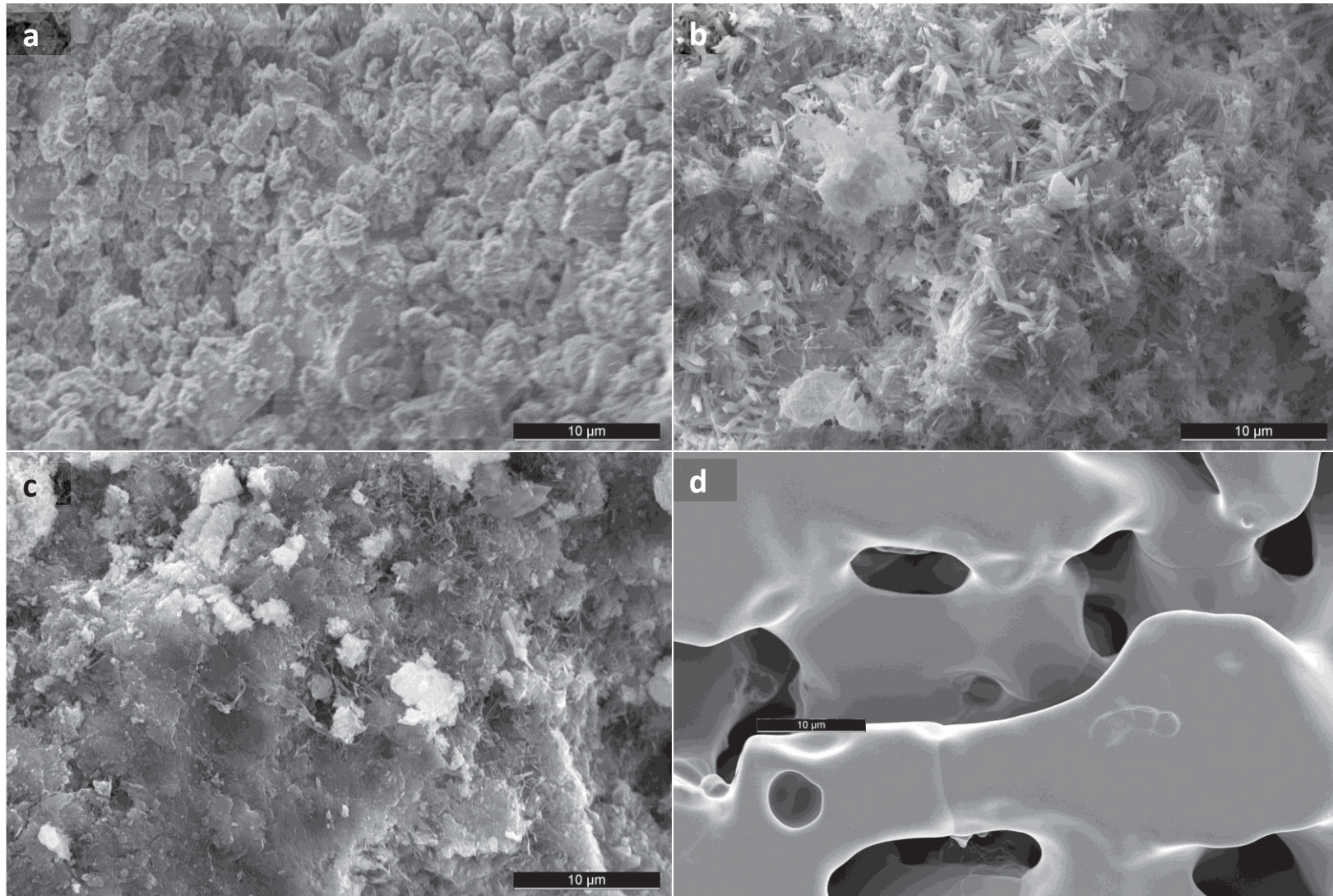


**Figure 7-3** a) Pressed sample ( $\alpha$ -TCP); b) pressed sample after hydrothermal treatment (CDHA); c) cement sample (after hydration) (CDHA); d) hydrated cement sample after sintering ( $\alpha$ -TCP).

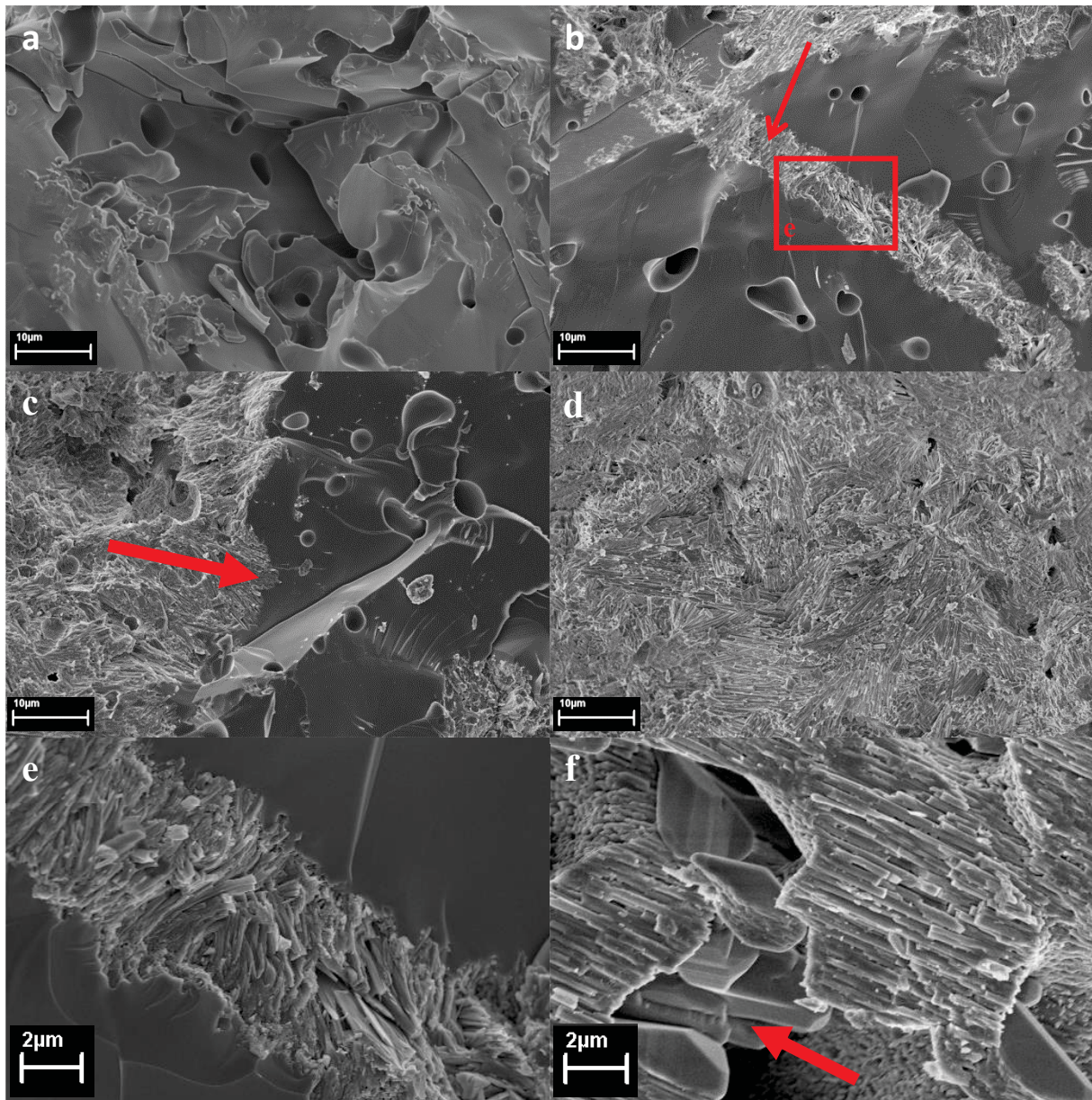


**Figure 7-4** Effect of incubation time on the microstructure as observed by SEM of broken surfaces. a) sintered  $\alpha$ -TCP; b) incubation for 2 hours at 175 °C: recrystallization into elongated hydroxyapatite crystals starts around cracks (arrow) and pores; c) incubation for 4 hours at 175 °C: further growth of the needle-like structure into the bulk in one direction (arrow); d) incubation for 8 hours at 175 °C: complete recrystallization; e) enlargement of b) on the newly formed crystals around a crack; f) large crystals (arrow) observed particularly in pores at the end of the reactions, especially at high temperature (here after 72h of incubation at 200 °C). Scale bars are 10  $\mu\text{m}$  in a to d and 2  $\mu\text{m}$  in e and f.

Differences in the location of needles were observed as a function of incubation temperature. At 125 °C, the needles completely invaded the microporosity (Figure 7-5a), but they protruded less into the initial porosity with increasing temperature (Figure 7-5b). In consequence, at low temperature the previously dense solid parts appeared more porous and also made of entangled needles (Figure 7-5c). With increasing temperature, the needles were increasingly confined to the



initial solid location, leading in consequence to more compact structures and better alignment (Figure 7-5c to f).

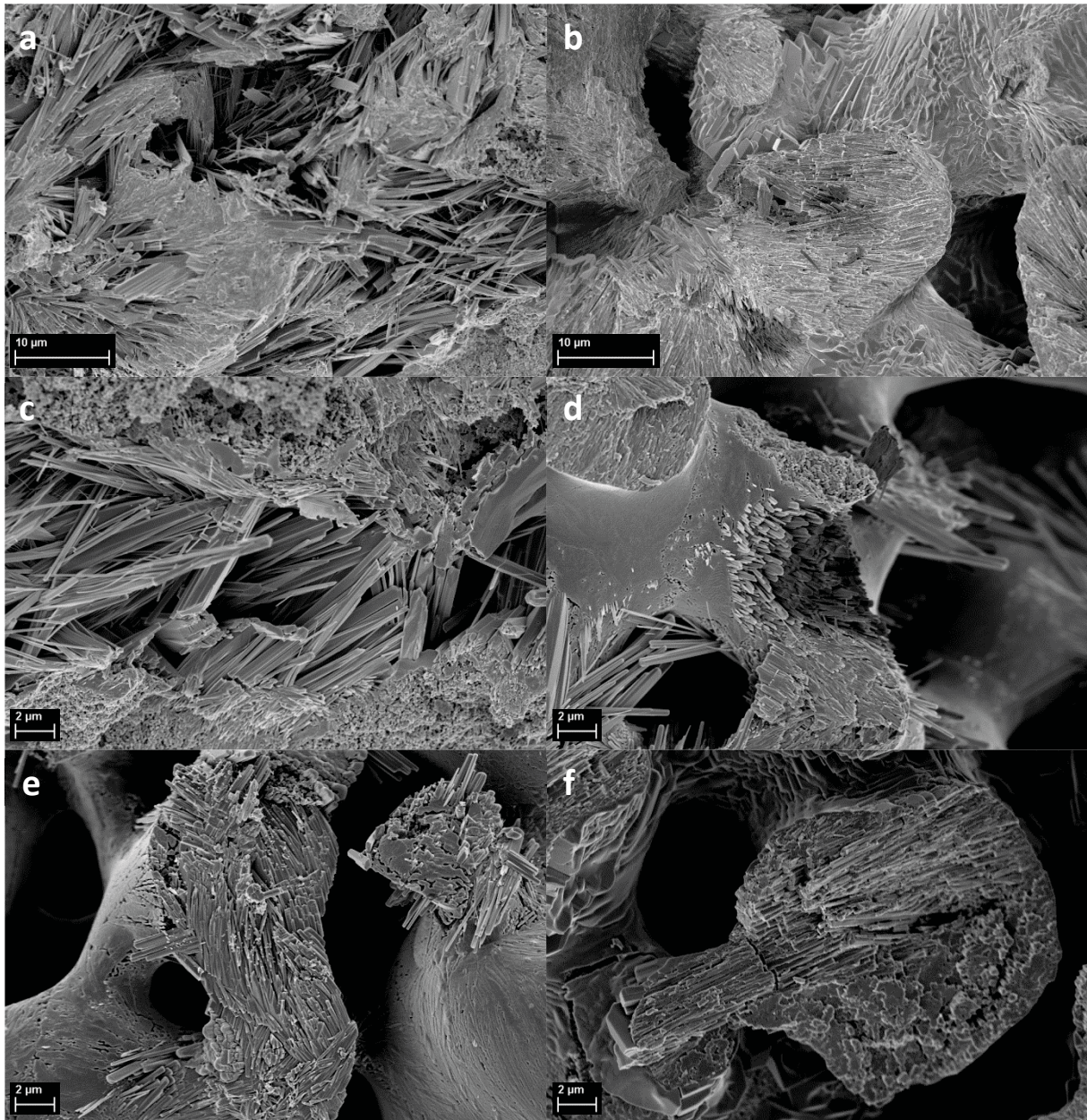


**Figure 7-5** Effect of incubation temperature on the microstructure, especially on the location of crystal growth: a) 125 °C overview, b) 200 °C overview, c) 125 °C, d) 150 °C, e) 175 °C, f) 200 °C. Scale bars are 10 µm long in a) and b) and 2 µm long in c) to f).

At low temperature, needles that grew into pores were longer and thicker than those growing into the solid phase. The opposite was observed at the highest temperature (Figure 7-6). In the pores, the average diameter of the needles was not influenced by temperature (Figure 7-6a), but the crystals were 10 times longer at 125 °C than at 200 °C (ANOVA:  $p < 0.01$ ) (Figure 7-6c). In the solid phase, both length (Figure 7-6b) and diameter (Figure 7-6d) of the needles increased with increasing incubation temperature ( $p < 0.01$ ).

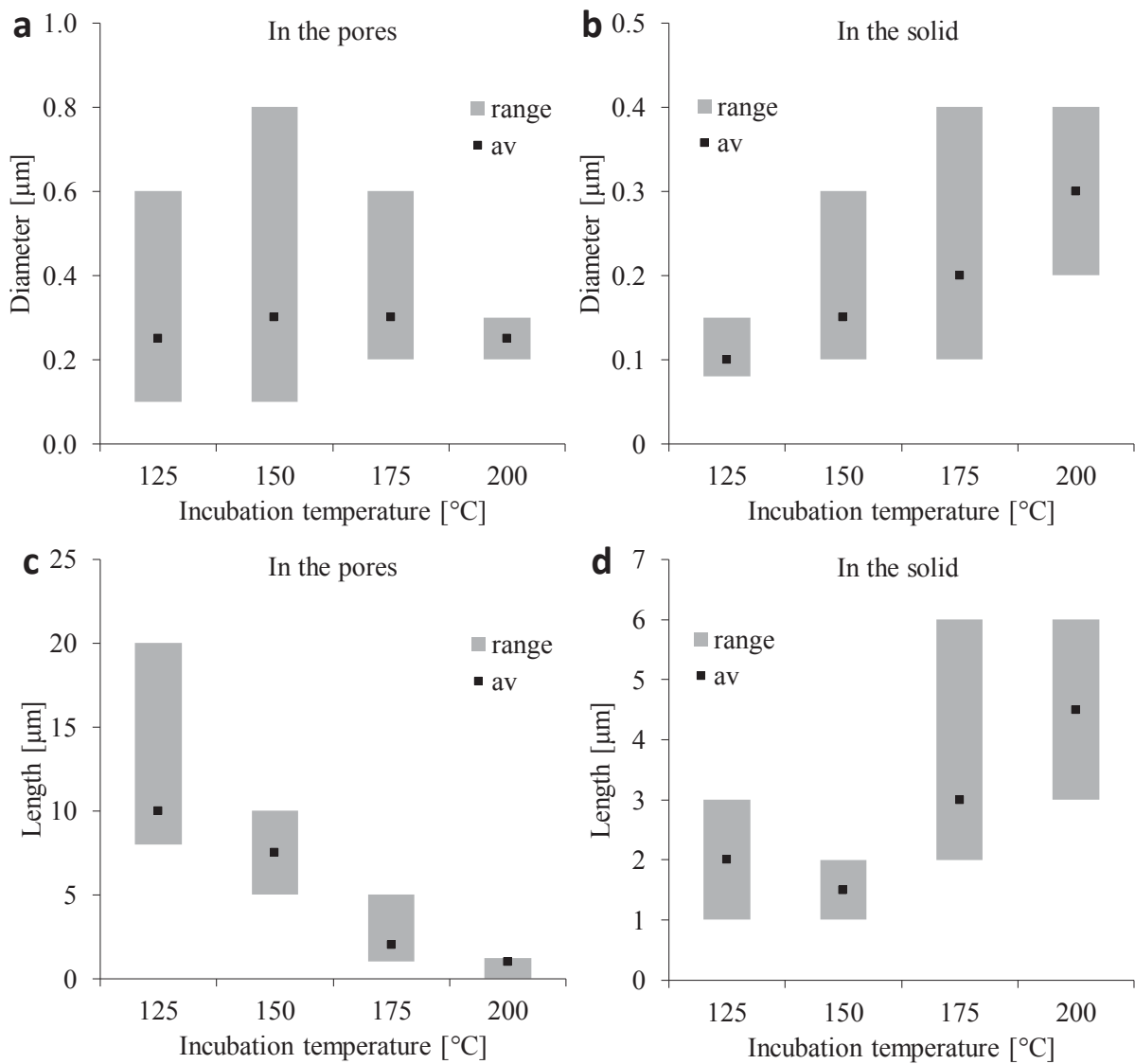


**Figure 7-6** a) and b) Diameter and c) and d) length of needle-like crystals in function of temperature and location: a) and c) in the initial porosity; b) and d) in the initial solid phase. The range (gray bar) covers the smallest to the largest measured values; the average value is represented by a black square.

Determining quantitatively the size of the oriented domains proved to be very difficult. By etching polymer-impregnated and polished surfaces, it was possible to see that domains extending over hundreds of micrometers were also surrounded by some smaller ones (Figure 7-7). For comparison, after sintering (for 8h at 1500 °C), the average grain size was about 30-100  $\mu\text{m}$ .

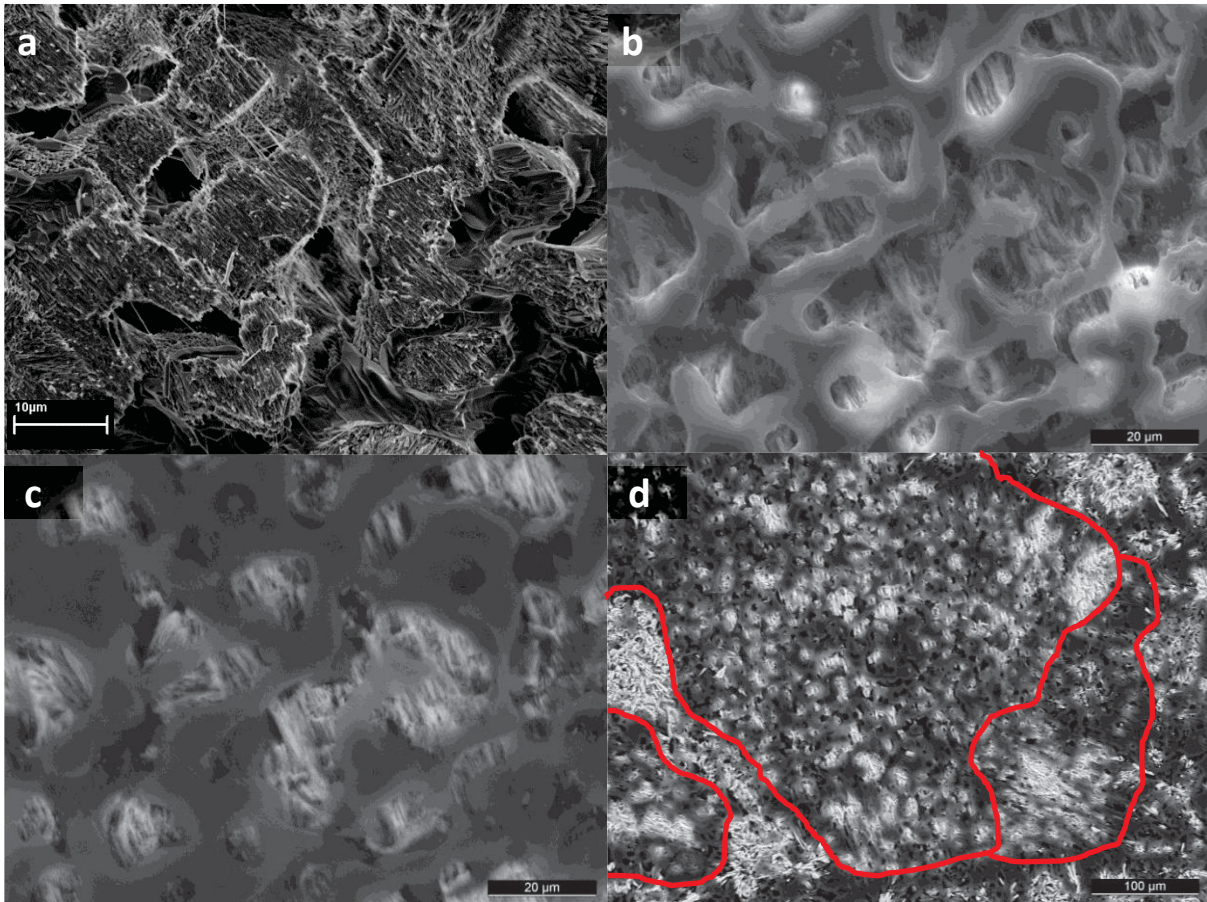


**Figure 7-7** a) The oriented domains were difficult to observe on broken or polished samples with SE because the magnification necessary to distinguish the crystals and their orientation did not allow seeing the whole oriented areas (scale bar is 10  $\mu\text{m}$  long). b) Embedding, polishing and chemically etching the samples better highlighted the needle crystals and their orientation, c) which was then better distinguished with BSE, d) and the extension of the oriented domains (red limits) was distinguishable at lower magnification. It was thus observed that oriented domains extending over hundreds of micrometers were also surrounded by smaller ones (scale bar is 100  $\mu\text{m}$  long).

### Crystalline phase conversion (XRD)

The crystalline phase conversion was characterized by Rietveld refinement of XRD data. Various phases were detected during hydrothermal conversion even though the initial 100 %  $\alpha$ -TCP blocks mainly converted into CDHA (Figure 7-8a and b).  $\beta$ -TCP and monetite (DCP) phases were also formed, in amounts depending on the incubation temperature (Figure 7-8c and d).

The conversion rate from  $\alpha$ -TCP to CDHA and DCP increased with the incubation temperature (Figure 7-8a, b and d). Increasing the temperature also accelerated and increased the formation of  $\beta$ -TCP (Figure 7-8c), but  $\beta$ -TCP disappeared over time apparently at the expense of CDHA and DCP.  $\alpha$ -TCP almost completely disappeared but CDHA and DCP continuously increased until they reached a plateau. Hence, up to 10 wt-% of DCP were detected at the end of the reactions. The global Ca/P molar ratio of the samples was checked by XRD analysis after calcination at 900  $^{\circ}\text{C}$  for 24h [44]. The

resulting composition was mixture of  $\beta$ -TCP (Ca/P = 1.5),  $\beta$ -CPP (Ca/P = 1.0) and HA (Ca/P = 1.667), corresponding to a global Ca/P molar ratio in the samples of 1.50.

Comparing XRD results and SEM observations, the needle-like crystals were identified as hydroxyapatite and the large prismatic ones (Figure 7-4f) were attributed to the monetite phase. No structural features could be identified as  $\beta$ -TCP. The powder pressed samples completely converted to CDHA upon incubation at 200 °C for 24h.

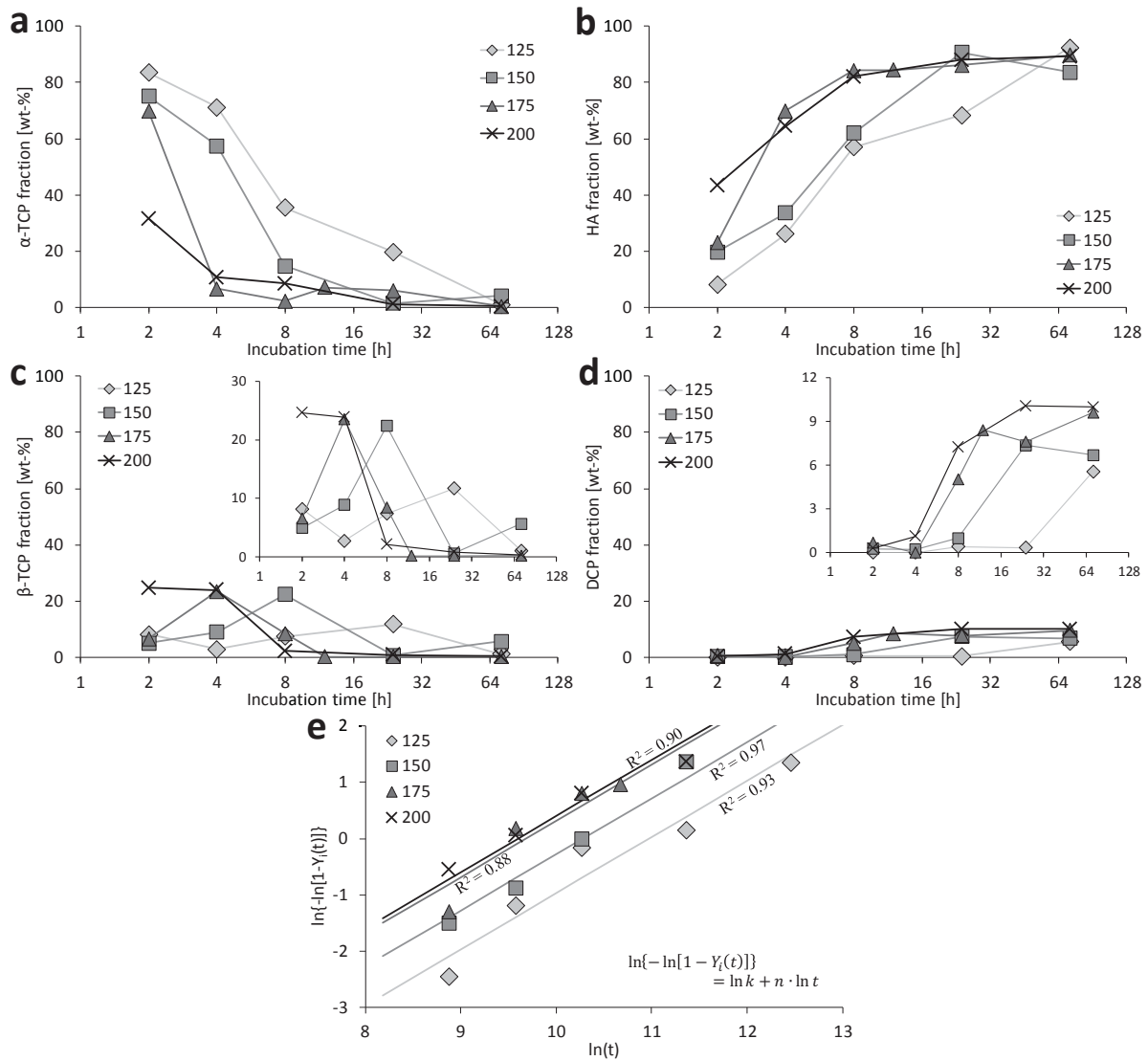


**Figure 7-8** Phase transformation (Rietveld refinement of XRD results) over incubation time at  $\blacklozenge$  125 °C,  $\blacksquare$  150 °C,  $\blacktriangle$  175 °C, and  $\times$  200 °C. a) consumption of initial  $\alpha$ -TCP phase; b) formation of hydroxyapatite (HA); c) intermediate formation and consumption of  $\beta$ -TCP (enlargement of 0 - 30 wt-%); d) formation of monetite (DCP) (enlargement of 0 - 12 wt-%); e) Avrami plot of the global phase transformation, with  $Y_i(t)$  = combined consumption of  $\alpha$ -TCP and  $\beta$ -TCP or combined formation of HA and DCP (with the slope  $n = 1$ ).

Evolution with time of all phase contents,  $Y_i(t)$  (Figure 7-8e), were fitted with the Avrami equation [45]:

$$Y_i(t) = 1 - \exp(-K_i \cdot t^{n_i}), \quad \text{Equation 2}$$

where  $K_i$  is a constant related to the formation of phase  $i$  at a given temperature and  $n_i$  is an integer. In a first step, both  $K$  and  $n$  were fitted. In a second step, only  $K$  was optimized with  $n$  set to the closest integer value found previously. All phase evolutions except that of DCP, were best fitted with  $n = 1$ . DCP was best fitted with  $n = 3$ .

The consumption and formation of all crystalline phases were fitted, and their respective regression coefficients ( $R^2$ ) calculated (Table 7-2). Whereas most of the fits were acceptable ( $R^2 > 0.80$ ), some were quite poor, in particular for the consumption of  $\beta$ -TCP at high temperatures ( $R^2 < 0.65$ ). However, fitting the sum of  $\alpha$ -TCP and  $\beta$ -TCP fractions and the sum of DCP and HA fractions led to excellent fits with regression coefficients mainly larger than 0.90 (Table 7-2 and Figure 7-8e).

The activation energy of each phase conversion was retrieved from a plot of  $K_i$  as a function of  $1/T$  using Arrhenius equation (Table 7-2). The values were close to 25 kJ/mol for  $\alpha$ -TCP consumption and HA formation, and were higher for  $\beta$ -TCP consumption ( $40 \pm 6$  kJ/mol) and DCP formation ( $119 \pm 37$  kJ/mol). In consequence, the activation energy for the combined CDHA and DCP formation or the combined  $\alpha$ -TCP and  $\beta$ -TCP consumption was  $30 \pm 5$  kJ/mol.

**Table 7-2** Parameters  $n$  and  $K$  for the Avrami fits of the phase conversions at different temperatures with the according correlation coefficients,  $R^2$ . The activation energy  $E_a$  for each phase can then be obtained with the Arrhenius equation. The minus signs indicate disappearance of phases, whereas plus signs indicate formation. Color code:  $0.7 < R^2$ ;  $0.7 < R^2 < 0.8$ ;  $0.8 < R^2 < 0.9$ ;  $0.9 < R^2$

		- $\alpha$ -TCP		+ $\beta$ -TCP		- $\beta$ -TCP		+ CDHA		+ DCP		- ( $\alpha$ -TCP + $\beta$ -TCP)		+ (CDHA + DCP)	
		n = 1		n = 1		n = 1		n = 1		n = 3		n = 1		n = 1	
		K	$R^2$	K	$R^2$	K	$R^2$	K	$R^2$	K	$R^2$	K	$R^2$	K	$R^2$
- $\ln(K_i)$	125 °C	10.66	0.95	13.14	0.84	10.78	0.77	10.84	0.94	36.69	0.98	10.97	0.93	10.97	0.93
	150 °C	9.96	0.96	11.82	0.96	9.80	0.99	10.11	0.95	32.57	0.99	10.28	0.97	10.28	0.97
	175 °C	9.70	0.26	11.23	0.76	9.13	0.87	9.94	0.51	31.01	1.00	9.69	0.88	9.69	0.88
	200 °C	9.50	0.87			8.90	0.65	9.52	0.79	31.00	0.81	9.60	0.90	9.60	0.90
$E_a$ [kJ/mol]	24 ± 4		57 ± 11		40 ± 6		26 ± 4		119 ± 37		30 ± 5		30 ± 5		

### **Mechanical properties**

The incubation time significantly influenced the mechanical properties of the ceramic blocks (ANOVA:  $p < 0.0001$ ). The fracture energy was calculated as the integral of the force-displacement curves until sample failure i.e. maximum force. Upon hydrothermal incubation at 200 °C, the diametral strength and the fracture energy (WOF) first decreased, but then increased with increasing incubation time (Figure 7-9a). From a phase transformation of about 70 % HA (after 4h of incubation) the initial strength and WOF of the sintered blocks were restored and then further increased to about 150 % of the initial value at 80 % conversion rate (8h of incubation). However, both strength and WOF decreased at longer incubation times, while HA content remained stable and DCP content increased.

The mechanical properties were investigated on samples that have just reached their maximum reaction rates. Hence, for different incubation temperatures the incubation times were also different. Higher incubation temperatures led to higher strength values ( $p < 0.0002$ , Figure 7-9b). The fracture energy was not influenced by incubation temperature, but all incubation conditions led to an average improvement of  $+ 80 \pm 40 \%$  compared to sintered samples ( $p < 0.025$ ).

Pressed samples had a very low strength that was tremendously increased upon hydrothermal treatment by a factor of about 50 (Figure 7-10). However, those samples were still weaker than previously sintered ones.

### **Fractured surfaces**

The fractured surfaces after Brazilian tests were observed by SEM. The crack paths after sintering were flat and smooth through the samples. After hydrothermal treatment, the crack paths in the dense solid parts were tortuous, particularly with increasing incubation temperatures (Figure 7-11). Indeed, the fracture planes were rather flat at 125 and 150 °C, but crack deflection around needles and bundles of needles was visible at 175 °C and obvious at 200 °C.

The crack path was difficult to evaluate in the loose structure of the samples hydrated after powder pressing. However, the fractured surface was clearly rougher than in sintered samples.

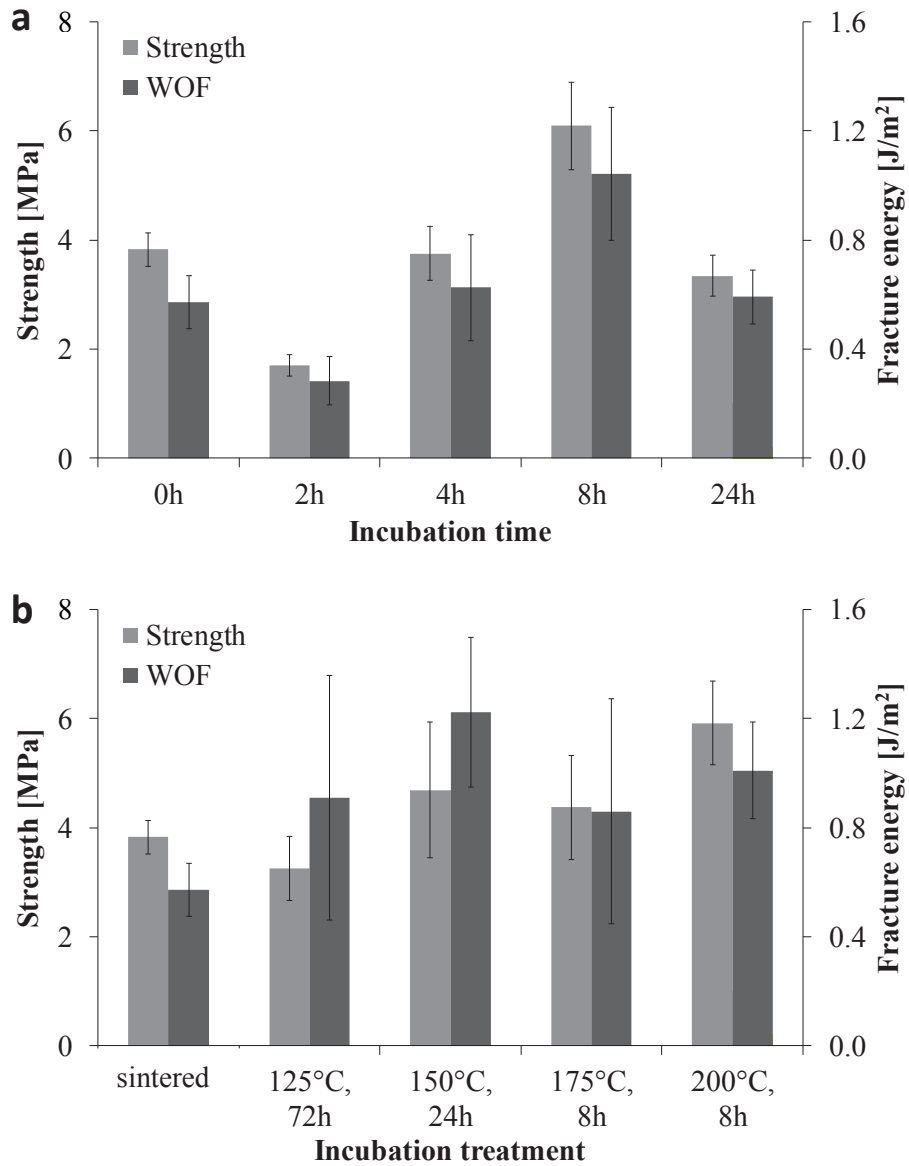


**Figure 7-9** Diametral strength and work of fracture measured by Brazilian tests a) as a function of the hydrothermal incubation time at 200°C; b) as a function of the hydrothermal incubation temperature, with hydrothermal incubation time chosen such as to obtain the HA conversion close to maximum for each temperature.

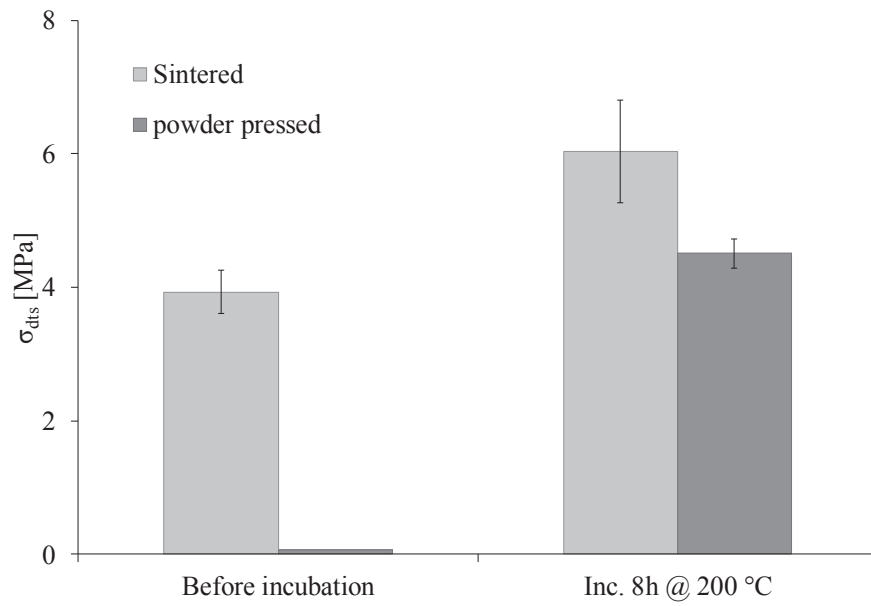


**Figure 7-10** Comparison of diametral strength improvement with incubation (for 8 hours at 200 °C) for sintered and powder pressed samples.

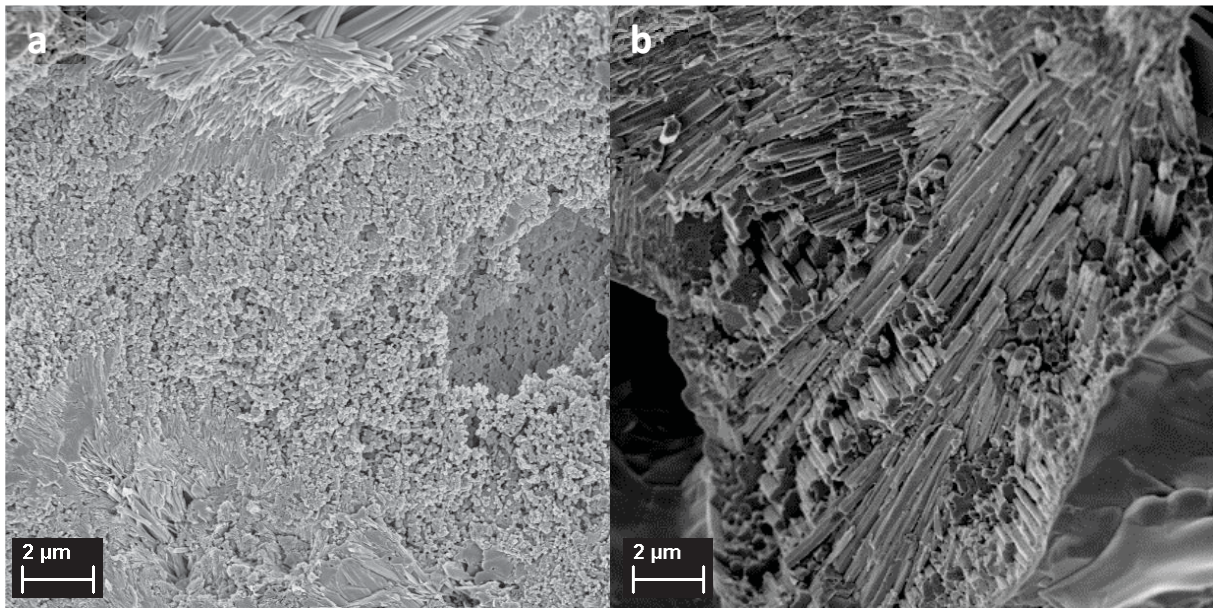


**Figure 7-11** Examples of fracture surfaces after Brazilian testing: a) with incubation at 125°C the crack path through the solid parts were rather flat. With increasing temperature, the crack paths became increasingly more tortuous, as observed in b) sample incubated at 200°C.



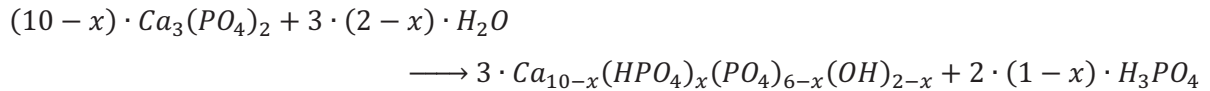
## Discussion

The aim of this study was to refine the microstructure of CaP monoliths and obtain tortuous crack paths to increase their work of fracture, i.e. their toughness. Recrystallization in hydrothermal conditions was an effective way to texture the solid at the microscale without affecting macro features like porosity and sample shape (Figure 7-2, Figure 7-5f and Figure 7-7a). Indeed, limiting direct contact with liquid water avoids extensive dissolution and reprecipitation which might provoke morphology changes at longer scale. Only with incubation at temperatures lower than 150 °C, crystals invaded the microporosity (Figure 7-5a). At high enough temperatures, even the microporosity was preserved (Figure 7-5b). However, chemical (Figure 7-8) and sub-micro structural (Figure 7-4) changes occurred in the samples.

Hydration in water vapor converted  $\alpha$ -TCP mainly into CDHA (Figure 7-8a and b), but two unexpected crystalline phases were also detected in minor concentrations by XRD:  $\beta$ -TCP (Figure 7-8c) as an intermediate and DCP (Figure 7-8d), rather simultaneously with CDHA.

The formation of  $\beta$ -TCP is unusual at such low temperature. Generally,  $\beta$ -TCP is obtained by solid state reaction above 700-800 °C and below 1120 °C, the transition temperature with  $\alpha$ -TCP [46]. Recently, a few studies reported its precipitation in non-aqueous systems. This is for example the case of Bow et al. [47] who obtained it in methanol or of Tao et al. [48] and Galea et al. [49] who obtained it by precipitation of calcium and phosphate ions in ethylene glycol at 90°C and above. When formed in organic solvents, the occurrence of  $\beta$ -TCP might be due to the absence of hydroxide groups. One study reported  $\beta$ -TCP formation in hydrothermal conditions [50]. A dissolution-reprecipitation mechanism is rather improbable since there is no reason that  $\beta$ -TCP would precipitate instead of CDHA in presence of water [51]. The high pressure (Table 7-1) might however destabilize the metastable  $\alpha$ -TCP phase, even with low input of thermal energy. Since at low temperature,  $\beta$ -TCP is thermodynamically more stable than  $\alpha$ -TCP, the allotropic phase transformation might occur (no diffusion involved).

In addition to the expected CDHA phase and the intermediate  $\beta$ -TCP phase, monetite was also present and its formation with time (Figure 7-8d) was correlated with the appearance of large prismatic crystals on SEM images (Figure 7-4f). The XRD results suggest that monetite formation was delayed compared to that of CDHA. Since DCP is more stable than CDHA at low pH [51], it indicates an acidification of the reaction milieu over time, which was confirmed by pH-paper measurements. The acidification would occur if hydroxyapatite with a Ca/P molar ratio higher than 1.5 ( $x < 1$ ) would form:



Since the Ca/P molar ratio of DCP is 1, but the overall Ca/P ratio of the samples did not differ from 1.5 over time, DCP compensated the formation of CDHA with  $x < 1$ . It is unclear whether the CDHA was depleted of its phosphate ions over time or if a newly formed phase only consisting of stoichiometric HA (Ca/P = 1.67) was formed beside an initial CDHA with Ca/P = 1.5. Buffering the pH might avoid DCP formation, but the buffering capacity of buffer solutions above their evaporation temperature is unclear.

The reaction of  $\alpha$ -TCP blocks with water vapor not only led to chemical changes, but also to microstructural changes as seen by SEM (Figure 7-4). The obtained microstructures were different from usual ones observed after hydration in physiological conditions (Figure 7-3). Whereas the sintered  $\alpha$ -TCP grains were a few micrometers large, the CDHA crystals were a few hundred of nanometers wide and up to a few micrometers long, aligned over several micrometers – or even hundreds of micrometers – (Figure 7-7). Nucleation of CDHA apparently occurred on exposed surfaces (pores and cracks), followed by unidirectional progression into the solid. These nucleation and growth mechanisms were confirmed by the outcomes of the kinetic study (Figure 7-8e and Table 7-2). Indeed, good fits of the experimental curves were obtained with Avrami's equation using a value of 1 for the  $n$  parameter, which indicate punctual nucleation and linear progression of phase conversion [52]. Using Avrami's equation, it was possible to calculate the activation energies for each phase conversion. The values obtained here for  $\alpha$ -TCP and  $\beta$ -TCP conversion into DCP and CDHA (Figure 7-8e) were only slightly above 20 kJ/mol. Usually, reactions with activation energy above 20 kJ/mol are considered to be reaction controlled. However, this value is valid for reaction in aqueous solutions and the threshold value for diffusional transport in solid even at high temperature and pressure is certainly higher. The present phase conversions might thus be diffusion controlled, with corresponding diffusion coefficients in the order of  $10^{-5}$  cm<sup>2</sup>/s. Interestingly, it is similar to diffusion of hydrogen in water at room temperature [53], and for comparison, it is about  $10^4$  times faster than hydrogen diffusion in iron ( $\alpha$ -Fe) at 25 °C [53] or about 100 times faster than carbon diffusion in  $\gamma$ -Fe at 1000 °C [54]. Hence the present diffusion coefficients are very high for diffusion of water vapor into a solid phase, even above 100 °C.

In the initially solid regions (struts), the needle-like CDHA crystals were aligned and densely packed. In the initially micropores regions, CDHA crystals were more loosely packed and less aligned. The incubation temperature affected the synthesized structures in two ways: (i) The crystal size in the initially dense parts (struts) increased with the incubation temperature (Figure 7-6). This effect is certainly related to the increase of diffusion rate with temperature (Table 7-2,  $D = \ln(k)$  in the

hypothesis of a diffusion controlled process), explaining why growth rate of CDHA increased at higher temperature. (ii) In parallel, with a high incubation temperature, recrystallization was confined to the initially dense parts whereas at lower temperature, crystals also protruded into the porosity instead of staying confined to the initial solid struts. It is hypothesized that because of a more difficult growth in the solid at lower temperature, crystallization was delocalized into the pores, leading to lack of material in the initial solid regions and in consequence also to lower densities of needles in these regions.

Interestingly, when the structure before hydrothermal incubation was not densified by sintering, entanglement between crystals was apparently less efficient, since low strength values ( $< 0.2\text{MPa}$ ) were observed previously [55, 56] and confirmed by our own results of incubation of  $\alpha$ -TCP powder-pressed samples (Figure 7-10).

Putting the present results in perspective with the values of other studies found in the literature [1, 57] it appears that the tensile properties obtained here are rather in the low range of published values. The  $\beta$ - to  $\alpha$ -TCP transition might have weakened the blocks because of internal stresses cracking the samples. This transition was necessary to ensure quick and complete phase conversion since  $\beta$ -TCP is less reactive than  $\alpha$ -TCP. It might hence be argued that the strength increase observed here is only due to closing of the cracks by recrystallization. However, if this was the case, higher improvements would have been observed at low incubation temperature since it is where crystal growth occurred in the voids. It might also be argued that the strength improvement is (only) due to the higher intrinsic strength of HA compared to  $\alpha$ -TCP (+120 %) [58]. However, the mechanical improvements measured here were sometimes higher (+150 %), implying that another mechanism is at play, like better crystal entanglement.

Beside slight improvements of tensile strength observed at 200 °C, recrystallization from large globular sintered grains into much finer and elongated crystals in well-organized features doubled the work-of-fracture ( $\approx$  toughness) (Figure 7-9). However it is not so much the twofold improvement in mechanical properties which is remarkable in the present study, but rather the change in failure mode. Indeed, cracks propagated quite linearly through the smooth sintered structures, while the textured samples showed obvious crack deflection around densely packed and aligned crystals, but also around and through crystals bundles (Figure 7-11). In other word, the reduced grain or crystal size promoted a transition from a transgranular to an intergranular cracking mode [24] and the anisotropic crystal shape, combined with changing and random orientation of bundles further enhanced crack deflection.

This toughening mechanism is very similar to what was observed in natural ceramic-based composites, where it has been designated as “extrinsic toughening” [3]. Indeed, the material itself is

not toughened at the atomic or molecular scale, like an annealed metal, but the texture and hierarchical structure of the construct increases fracture resistance by obstructing crack propagation. Micro cracking, crack bridging and crack deflection are typical extrinsic toughening mechanisms occurring in densely packed crystalline phases [3] and explaining for instance the high fracture toughness observed in bone or nacre [59]. To obtain these effects in synthetic materials, a good control of microstructure is necessary. In glass ceramics, toughness values up to  $2.7 \text{ MPa}\cdot\text{m}^{1/2}$  have been obtained [60], which is still in the lower range of cortical bone values ( $2\text{-}12 \text{ MPa}\cdot\text{m}^{1/2}$ ) [3, 61, 62], but higher than bioactive ceramics ( $0.5 \text{ MPa}\cdot\text{m}^{1/2}$ ).

The architecture of the present structures resembles those of natural ones like shells or teeth (Figure 7-12). Indeed, even if the crystal phases and chemistry are different, elongated primary crystals are densely packed and aligned within domains in those three materials. Like in enamel of shark teeth [63], the obtained structures exhibit 5 levels of hierarchy: (i) hydroxyapatite crystalline structure, (ii) in the form of needle-like crystals, (iii) aligned in bundles, (iv) which are stacked with random orientation to form (v) a macroscopic sample (Figure 7-13). It has to be noticed that the crystals observed by Enax et al. [63] in enamel of shark teeth were about 5 times thinner (Figure 7-12d and e) than the crystals observed in the present study (Figure 7-12a), but crystals and domains sizes of shells are similar to those of the present samples (Figure 7-12b and c).

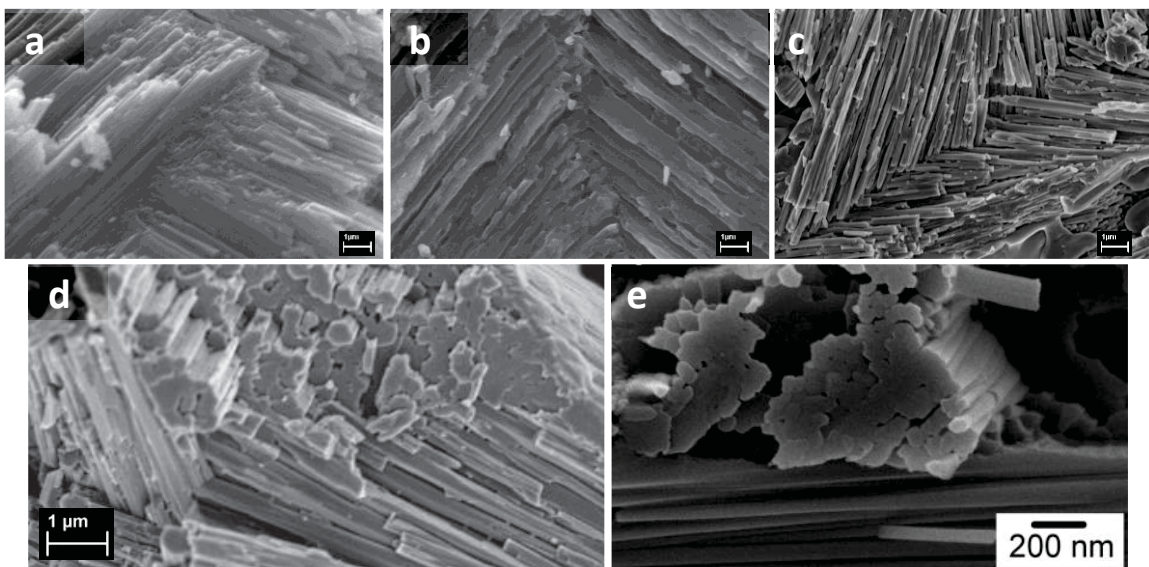


**Figure 7-12** Various SEM pictures to highlight the similarity of the microstructures obtained in the present study with natural materials. a) and d) Synthetic hydroxyapatite obtained by hydrothermal incubation for 24h at  $200^{\circ}\text{C}$ ; b) *Acanthocardia aculeate*, Mediterranean shell; c) *Aporrhais pespelecani*, Mediterranean shell; e) Enamel of shark teeth [63]. Scale bars are  $1 \mu\text{m}$  in a) to d), but  $200 \text{ nm}$  in e).

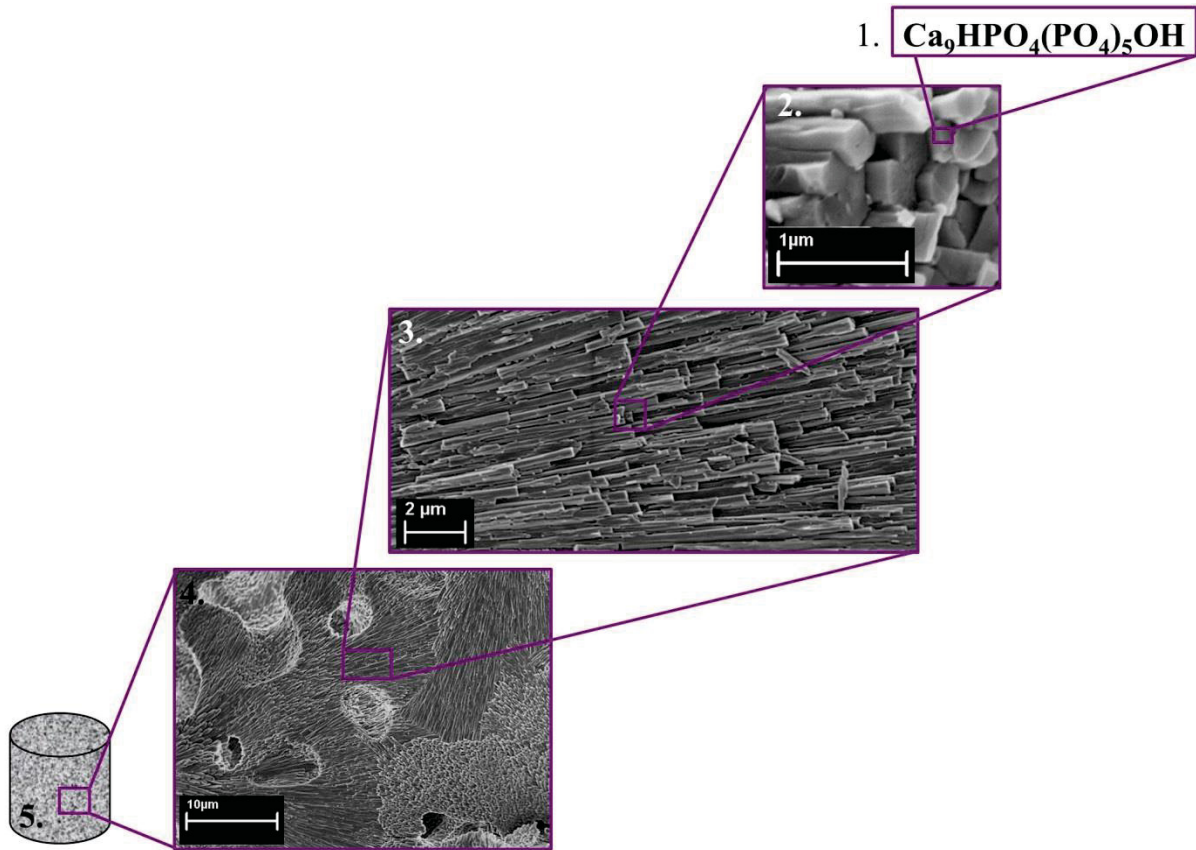


**Figure 7-13** Hierarchical structure: 1) CDHA crystalline structure 2) in the form of needles, 3) assembled in bundles, 4) stacked with random orientation, 5) to obtain a macroscopic tough ceramic.

However, there are major differences between natural materials and the materials obtained here. Natural materials present large crystalline domains whose orientation is predefined and controlled, contrarily to the present materials where the domain orientation is uncontrolled. Also organic layers are intercalated between the crystalline domains in natural composites and bring some additional toughness (defined as “intrinsic toughening” in [16]). This might be introduced by impregnating the present porous and structured bioceramics with a tough polymer. Impregnation of sintered ceramic scaffolds has already shown substantial results like for example a 7- to 13-fold increase of BCP toughness with PCL [64] or similar results with other polymers [65-68]. The toughness improvement is explained by polymer fibril extension and crack bridging which dissipate fracture energy leading to gradual rupture instead of catastrophic brittle fracture [3, 68]. However, even coated, those scaffolds were generally weaker than cortical bone and were still brittle once the polymer was degraded [3].

## Conclusions

For the first time to our knowledge, CaP ceramics with highly aligned crystals have been obtained. Complex architectures, with five hierarchical levels were reached in pure CaP ceramic blocks. This was achieved by recrystallization of sintered blocks *in situ*. The resulting crystals were much thinner than the initial sintered grains and had an elongated shape. Over a certain distance depending mainly on incubation temperature, the needles aligned, forming oriented domains. The higher the incubation temperature, the denser the crystals and aligned domains were packed.

One consequence of texturing CaP ceramics by hydrothermal treatment was a 200 % increase of work-of-fracture. The results suggest that this increase was due to a so-called “extrinsic toughening” mechanism, i.e. crack deflection, as observed in many natural examples. Interestingly, cracks were deflected at two levels: around needle-like crystals, but also around aligned domains, or bundles of crystals. Further improvement of mechanical properties would require a better control over needle size, aligned domain size and global domain orientation. To do so, more quantitative characterization techniques for the microstructure would be required. Differences in vapor pressure and diffusion rates between solid and pores might explain packing differences at different temperatures; however the whole recrystallization process is still unclear. Additives acting as growth inhibitors or accelerators, like citrates, pyrophosphates, magnesium, etc, while incubating at high temperature (200 °C) might lead to reduced but even more confined growth of CDHA crystals.

The toughness could also be further improved by incorporation of some organic phases by polymer impregnation, for example. In this case, hydrothermal incubation at low temperatures might be more adequate to preserve some porosity in between bundles, or even crystals to allow proper polymer penetration.

## References

- [1] Wagoner Johnson AJ, Herschler BA. A review of the mechanical behavior of CaP and CaP/polymer composites for applications in bone replacement and repair. *Acta Biomaterialia*. 2011;7:16-30.
- [2] Rezwan K, Chen QZ, Blaker JJ, Boccaccini AR. Biodegradable and bioactive porous polymer/inorganic composite scaffolds for bone tissue engineering. *Biomaterials*. 2006;27:3413-31.
- [3] Fu Q, Saiz E, Rahaman MN, Tomsia AP. Toward strong and tough glass and ceramic scaffolds for bone repair. *Advanced Functional Materials*. 2013;23:5461-76.
- [4] Ritchie RO. The conflicts between strength and toughness. *Nature Materials*. 2011;10:817-22.
- [5] Ignatius AA, Betz O, Augat P, Claes LE. In vivo investigations on composites made of resorbable ceramics and poly(lactide) used as bone graft substitutes. *J Biomed Mater Res*. 2001;58:701-9.

- [6] Bonfield W, Grynblas M, Tully AE, Bowman J, Abram J. Hydroxyapatite reinforced polyethylene--a mechanically compatible implant material for bone replacement. *Biomaterials*. 1981;2:185-6.
- [7] Shikunami Y, Okuno M. Bioresorbable devices made of forged composites of hydroxyapatite (HA) particles and poly-L-lactide (PLLA): Part I. Basic characteristics. *Biomaterials*. 1999;20:859-77.
- [8] Venkatesan J, Kim SK. Chitosan composites for bone tissue engineering - An overview. *Mar Drugs*. 2010;8:2252-66.
- [9] Baji A, Wong SC, Srivatsan TS, Njus GO, Mathur G. Processing methodologies for polycaprolactone-hydroxyapatite composites: A review. *Mater Manuf Process*. 2006;21:211-8.
- [10] Kim SS, Sun Park M, Jeon O, Yong Choi C, Kim BS. Poly(lactide-co-glycolide)/hydroxyapatite composite scaffolds for bone tissue engineering. *Biomaterials*. 2006;27:1399-409.
- [11] Hu Q, Li B, Wang M, Shen J. Preparation and characterization of biodegradable chitosan/hydroxyapatite nanocomposite rods via in situ hybridization: A potential material as internal fixation of bone fracture. *Biomaterials*. 2004;25:779-85.
- [12] Neuendorf RE, Saiz E, Tomsia AP, Ritchie RO. Adhesion between biodegradable polymers and hydroxyapatite: Relevance to synthetic bone-like materials and tissue engineering scaffolds. *Acta Biomaterialia*. 2008;4:1288-96.
- [13] Bonderer LJ, Studart AR, Gauckler LJ. Bioinspired design and assembly of platelet reinforced polymer films. *Science*. 2008;319:1069-73.
- [14] Munch E, Launey ME, Alsem DH, Saiz E, Tomsia AP, Ritchie RO. Tough, bio-inspired hybrid materials. *Science*. 2008;322:1516-20.
- [15] Launey ME, Munch E, Alsem DH, Barth HB, Saiz E, Tomsia AP, et al. Designing highly toughened hybrid composites through nature-inspired hierarchical complexity. *Acta Materialia*. 2009;57:2919-32.
- [16] Ritchie RO, Kinney JH, Kruzic JJ, Nalla RK. A fracture mechanics and mechanistic approach to the failure of cortical bone. *Fatigue Fract Eng Mater Struct*. 2005;28:345-71.
- [17] Shen Z, Johnsson M, Zhao Z, Nygren M. Spark plasma sintering of alumina. *Journal of the American Ceramic Society*. 2002;85:1921-7.
- [18] Hannink RHJ, Kelly PM, Muddle BC. Transformation toughening in zirconia-containing ceramics. *Journal of the American Ceramic Society*. 2000;83:461-87.
- [19] McMeeking RM, Evans AG. MECHANICS OF TRANSFORMATION-TOUGHENING IN BRITTLE MATERIALS. 5 ed 1982. p. 242-6.
- [20] Yoshimura M. Phase stability of zirconia. *American Ceramic Society Bulletin*. 1988;67:1950-5.
- [21] Masahiro A, Eiichi I, Taishi M, Masahiro H. Elastic modulus, strength and fracture toughness of alumina ceramics containing pores. *Nippon Seramikkusu Kyokai Gakujutsu Ronbunshi/Journal of the Ceramic Society of Japan*. 2002;110:554-9.
- [22] Faber KT, Evans AG. Crack deflection processes-I. Theory. *Acta Metallurgica*. 1983;31:565-76.
- [23] Zhan GD, Kuntz JD, Wan J, Mukherjee AK. Single-wall carbon nanotubes as attractive toughening agents in alumina-based nanocomposites. *Nature Materials*. 2003;2:38-42.
- [24] Wang J, Shaw LL. Nanocrystalline hydroxyapatite with simultaneous enhancements in hardness and toughness. *Biomaterials*. 2009;30:6565-72.
- [25] Bouville F, Maire E, Meille S, Van de Moortèle B, Stevenson AJ, Deville S. Strong, tough and stiff bioinspired ceramics from brittle constituents. *Nature Materials*. 2014.

- [26] Mazaheri M, Haghightzadeh M, Zahedi AM, Sadrnezhad SK. Effect of a novel sintering process on mechanical properties of hydroxyapatite ceramics. *Journal of Alloys and Compounds*. 2009;471:180-4.
- [27] Zhang H, Darvell BW. Synthesis and characterization of hydroxyapatite whiskers by hydrothermal homogeneous precipitation using acetamide. *Acta Biomaterialia*. 2010;6:3216-22.
- [28] Yoshimura M, Suda H, Okamoto K, Ioku K. Hydrothermal synthesis of biocompatible whiskers. *J Mater Sci*. 1994;29:3399-402.
- [29] Yamasaki H. Heterotopic bone formation around porous hydroxyapatite ceramics in the subcutis of dogs. *Jpn J Oral Biol*. 1990;32:190-2.
- [30] Dasgupta S, Tarafder S, Bandyopadhyay A, Bose S. Effect of grain size on mechanical, surface and biological properties of microwave sintered hydroxyapatite. *Materials Science and Engineering C*. 2013;33:2846-54.
- [31] Lahiri D, Singh V, Keshri AK, Seal S, Agarwal A. Carbon nanotube toughened hydroxyapatite by spark plasma sintering: Microstructural evolution and multiscale tribological properties. *Carbon*. 2010;48:3103-20.
- [32] Ioku K, Kawachi G, Sasaki S, Fujimori H, Goto S. Hydrothermal preparation of tailored hydroxyapatite. *J Mater Sci*. 2006;41:1341-4.
- [33] Kawachi G, Misumi H, Fujimori H, Goto S, Ohtsuki C, Kamitakahara M, et al. Fabrication of porous blocks of calcium phosphate through hydrothermal processing under glycine coexistence. *Nippon Seramikkusu Kyokai Gakujutsu Ronbunshi/Journal of the Ceramic Society of Japan*. 2010;118:559-63.
- [34] Okuda T, Ioku K, Yonezawa I, Minagi H, Gonda Y, Kawachi G, et al. The slow resorption with replacement by bone of a hydrothermally synthesized pure calcium-deficient hydroxyapatite. *Biomaterials*. 2008;29:2719-28.
- [35] Antoine C. Tensions des vapeurs: nouvelle relation entre les tensions et les températures. *Comptes Rendus des Séances de l'Académie des Sciences*. 1888;107:681-4, 778-80, 836-7.
- [36] Taut T, Kleeberg R, Bergmann J. The new Seifert Rietveld program BGMN and its application to quantitative phase analysis. *Materials Structure*. 1998;5:57-66.
- [37] Dickens B, Schroeder LW, Brown WE. Crystallographic studies on the role of Mg as a stabilizing impurity in  $\beta$ - $\text{Ca}_3(\text{PO}_4)_2$  I. The crystal structure of pure  $\beta$ - $\text{Ca}_3(\text{PO}_4)_2$ . *Journal of Solid State Chemistry*. 1974;10:232-48.
- [38] Schroeder LW, Dickens B, Brown WE. Crystallographic studies of the role of Mg as a stabilizing impurity in  $\beta$ - $\text{Ca}_3(\text{PO}_4)_2$ . II. Refinement of Mg-containing  $\beta$ - $\text{Ca}_3(\text{PO}_4)_2$ . *Journal of Solid State Chemistry*. 1977;22:253-62.
- [39] Mathew M, Schroeder LW, Dickens B, Brown WE. The crystal structure of  $\alpha$ - $\text{Ca}_3(\text{PO}_4)_2$ . *Acta Cryst*. 1977;B33:1325-33.
- [40] Sudarsanan K, Young RA. Significant precision in crystal structure details: Holly springs hydroxyapatite. *Acta Cryst*. 1969;B25:1534-43.
- [41] Dickens B, Bowen JS, Brown WE. A refinement of the crystal structure of  $\text{CaHPO}_4$  (synthetic monetite). *Acta Cryst*. 1971;B28:797-806.
- [42] Boudin S, Grandin A, Borel MM, Leclaire A, Raveau B. Redetermination of the  $\beta$ - $\text{Ca}_2\text{P}_2\text{O}_7$  structure. *Acta Cryst C*. 1993;49:2062-4.
- [43] Bouchard PO, Bay F, Chastel Y, Tovina I. Crack propagation modelling using an advanced remeshing technique. *Comput Methods Appl Mech Eng*. 2000;189:723-42.



- [44] Ishikawa K, Ducheyne P, Radin S. Determination of the Ca/P Ratio in Calcium-Deficient Hydroxyapatite Using X-Ray-Diffraction Analysis. *J Mater Sci-Mater M*. 1993;4:165-8.
- [45] Avrami M. Kinetics of phase change. I: General theory. *The Journal of Chemical Physics*. 1939;7:1103-12.
- [46] Dorozhkin SV, Epple M. Biological and medical significance of calcium phosphates. *Angew Chem Int Ed Engl*. 2002;41:3130-46.
- [47] Bow JS, Liou SC, Chen SY. Structural characterization of room-temperature synthesized nano-sized beta-tricalcium phosphate. *Biomaterials*. 2004;25:3155-61.
- [48] Tao J, Jiang W, Zhai H, Pan H, Xu R, Tang R. Structural components and anisotropic dissolution behaviors in one hexagonal single crystal of  $\beta$ -tricalcium phosphate. *Crystal Growth and Design*. 2008;8:2227-34.
- [49] Galea L, Bohner M, Thuering J, Doebelin N, Aneziris CG, Graule T. Control of the size, shape and composition of highly uniform, non-agglomerated, sub-micrometer  $\beta$ -tricalcium phosphate and dicalcium phosphate platelets. *Biomaterials*. 2013;34:6388-401.
- [50] Toyama T, Nakashima K, Yasue T. Hydrothermal synthesis of  $\beta$ -tricalcium phosphate from amorphous calcium phosphate. *Nippon Seramikkusu Kyokai Gakujutsu Ronbunshi/Journal of the Ceramic Society of Japan*. 2002;110:716-21.
- [51] Vereecke G, Lemaitre J. Calculation of the solubility diagrams in the system  $\text{Ca}(\text{OH})_2\text{-H}_3\text{PO}_4\text{-KOH-HNO}_3\text{-CO}_2\text{-H}_2\text{O}$ . *J Crystal Growth*. 1990;104:820-32.
- [52] Karamanov A, Avramov I, Arrizza L, Pascova R, Gutzow I. Variation of Avrami parameter during non-isothermal surface crystallization of glass powders with different sizes. *J Non Cryst Solids*. 2012;358:1486-90.
- [53] Cussler EL. *Diffusion - mass transfer in fluid systems*: Cambridge University Press, Cambridge, United Kingdom; 1984.
- [54] Porter DA, Easterling KE. *Phase transformations in metals and alloys*. Molly Millars Lane, Wokingham, Berkshire, England: Van Nostrand Reinhold (UK) Co. Ltd; 1981.
- [55] Wakae H, Takeuchi A, Udoh K, Matsuya S, Munar ML, LeGeros RZ, et al. Fabrication of macroporous carbonate apatite foam by hydrothermal conversion of  $\beta$ -tricalcium phosphate in carbonate solutions. *Journal of Biomedical Materials Research - Part A*. 2008;87:957-63.
- [56] Karashima S, Takeuchi A, Matsuya S, Udoh KI, Koyano K, Ishikawa K. Fabrication of low-crystallinity hydroxyapatite foam based on the setting reaction of  $\alpha$ -tricalcium phosphate foam. *Journal of Biomedical Materials Research - Part A*. 2009;88:628-33.
- [57] Charriere E, Terrazzoni S, Pittet C, Mordasini PH, Dutoit M, Lemaitre J, et al. Mechanical characterization of brushite and hydroxyapatite cements. *Biomaterials*. 2001;22:2937-45.
- [58] Liang L, Rulis P, Ching WY. Mechanical properties, electronic structure and bonding of  $\alpha$ - and  $\beta$ -tricalcium phosphates with surface characterization. *Acta Biomaterialia*. 2010;6:3763-71.
- [59] Launey ME, Buehler MJ, Ritchie RO. On the mechanistic origins of toughness in bone. *Annual Review of Materials Research* 2010. p. 25-53.
- [60] Apel E, Deubener J, Bernard A, Höland M, Müller R, Kappert H, et al. Phenomena and mechanisms of crack propagation in glass-ceramics. *J Mech Behav Biomed Mater*. 2008;1:313-25.
- [61] Currey JD, Zioupos P, Davies P, Casinos A. Mechanical properties of nacre and highly mineralized bone. *Proceedings of the Royal Society B: Biological Sciences*. 2001;268:107-11.

- [62] Ji B, Gao H. Mechanical properties of nanostructure of biological materials. *J Mech Phys Solids*. 2004;52:1963-90.
- [63] Enax J, Janus AM, Raabe D, Epple M, Fabritius HO. Ultrastructural organization and micromechanical properties of shark tooth enameloid. *Acta Biomaterialia*. 2014;10:3959-68.
- [64] Peroglio M, Gremillard L, Chevalier J, Chazeau L, Gauthier C, Hamaide T. Toughening of bio-ceramics scaffolds by polymer coating. *Journal of the European Ceramic Society*. 2007;27:2679-85.
- [65] Chen QZ, Boccaccini AR. Poly(D,L-lactic acid) coated 45S5 Bioglass®-based scaffolds: Processing and characterization. *Journal of Biomedical Materials Research - Part A*. 2006;77:445-57.
- [66] Mantsos T, Chatzistavrou X, Roether JA, Hupa L, Arstila H, Boccaccini AR. Non-crystalline composite tissue engineering scaffolds using boron-containing bioactive glass and poly(d,l-lactic acid) coatings. *Biomed Mater (Bristol)*. 2009;4.
- [67] Mouriño V, Newby P, Boccaccini AR. Preparation and characterization of gallium releasing 3-d alginate coated 45s5 bioglass® based scaffolds for bone tissue engineering. *Adv Eng Mater*. 2010;12:B283-B91.
- [68] Fu Q, Saiz E, Tomsia AP. Bioinspired strong and highly porous glass scaffolds. *Advanced Functional Materials*. 2011;21:1058-63.

## CHAPTER 8:

# TOUGHENING OF TEXTURED CALCIUM PHOSPHATE BLOCKS BY POLYMER IMPREGNATION

### ***Abstract***

*In situ* recrystallization was used in Chapter 7 to increase the strength and toughness of monolithic ceramic blocks. In the present chapter, the aim was to obtain further improvement especially of toughness by incorporation of thin layers of a tough polymer within the ceramic matrices.

More specifically, hydrothermally treated but also standard sintered ceramic blocks were impregnated with Poly( $\epsilon$ -caprolactone) (PCL). The polymer covered micro- and macropores walls and led to significant work of fracture increase thanks to polymer fibrils formation. Surprisingly, even the strength was increased when textured ceramic scaffolds were impregnated, presumably thanks to a very good contact – hence efficient stress transfer – between both phases and filling of surface defects of the ceramic. In consequence, texturing of ceramics increases toughness thanks to failure mode change; but also induces global strength increase when impregnated with a polymer thanks to large and strong binding interfaces between both phases.

*The PCL impregnation procedure was performed at the AO Foundation, Davos, Switzerland, with Dr. Marianna Peroglio.*

## Foreword

Structural changes that induce properties modification of a material are called “extrinsic” mechanisms [1, 2]. The fracture resistance of the material is unchanged, but extrinsic cracking mechanisms, which act mainly behind the crack tip, like crack bridging or deflection, are promoted. On the opposite, when the crack formation is hindered, for example by increased ductility, the toughening mechanism is “intrinsic”. Hence, integrating a second more ductile phase is an “intrinsic” toughening mechanism. Indeed, the properties are due to the materials themselves, and not to their form. Chapter 7 has shown the feasibility of increasing strength and toughness of monolithic ceramic blocks by texturing, i.e. “extrinsic” toughening. At present, further improvement might be obtained by incorporation of thin layers of a tough polymer within the ceramic matrices, i.e. “intrinsic” toughening.

## Introduction

Calcium phosphate (CaP) ceramics are widely used as bone graft substitute materials. Porous scaffolds are often made of  $\beta$ -tricalcium phosphate ( $\beta$ -TCP) or hydroxyapatite (HA) or a blend of both phases (biphasic). These ceramics are brittle (fracture toughness  $\ll 1\text{MPa}\cdot\text{m}^{1/2}$ ) and have low tensile strength (typically  $< 20\text{MPa}$ ).

One common approach in biomaterials to toughen CaP ceramics is to impregnate porous structures with a tough polymer phase [3-5]. Another approach to improve their mechanical strength and toughness, which rather comes from the classical ceramic technology, is to reduce the grain size, hence the maximum flaw size [6]. Indeed, when ceramic crystals are smaller than a critical size their fracture strength is identical to that of a perfect crystal [7, 8] and the rupture mode changes to intergranular increasing the rupture energy compared to usual transgranular failure mode of coarse-grain structures [6]. Moreover, if anisotropic crystal shape can be obtained, the cracks follow tortuous paths, increasing even further the rupture energy, i.e. the “extrinsic toughness” of the structure [1, 2, 9], as shown in the previous chapter. This is for example found in biological ceramic-based composites like nacre or bone [9] where ceramic parts have aspect ratio around 10 or 40, respectively [8, 10-15]. However, in the natural materials mentioned above, the toughness is even more increased by the integration of thin tough polymer layers in between the strong but brittle

ceramic particles. Indeed, natural composites combine both “intrinsic” and “extrinsic” toughening mechanisms [2].

Hence, the next logical step towards toughness improvement of synthetic CaP-based materials was the incorporation of a tough polymeric phase, i.e. bring some “intrinsic toughness” [1, 9], in the textured CaP monoliths obtained by hydrothermal treatment (Chapter 7).

## Materials and Methods

### Samples preparation

The synthesis of ceramic blocks was slightly different to the one described in the previous chapter. The oil-in-water emulsion process described in [16, 17] and used to produce a commercially available bone substitute (chronOS™, Synthes Biomaterials, Switzerland) was used. An in-house  $\alpha$ -TCP powder was mixed with a TCP powder (art. nr. 102143, Merck, Germany) in an 8:2 weight ratio with a propeller at 400 RPM for 30 seconds. The use of paraffin (art. nr. 107160, Merck, Dietikon, Switzerland) allowed varying the porosity of the cement. The emulsions were stabilized by the addition of an emulsifier (Cremophor EL, Art. nr 15-2015, BASF, Wädenswil, Switzerland) to the electrolyte solution made of 10 g/L polyacrylic acid sodium salt (PAA, 5.1 kDa, art. nr. 81132, Fluka, Buchs, Switzerland) and 28.4 g/L di-sodiumhydrogenphosphate ( $\text{Na}_2\text{HPO}_4$ , art. nr. 106586 Merck, Germany). The paraffin amount and the emulsifier concentration were varied (0, 3 or 10 g/L and 0.57 or 5.7 g/L, respectively) to modify the porosity and the pore size. Emulsification happened by mixing all powders and liquids together at 2000 RPM for 45 seconds. The slurries were poured into molds (10 mm diameter, 10 mm height) and setting occurred in humid environment at 60 °C for 76 h. After unmolding, the samples were immersed in petroleum ether (art. nr. 100915, Merck, Germany) for 24 h, twice, to remove most of the paraffin. After distillation at 140 °C for 8 h, the samples were calcined at 500 °C for 4 h to burn out the paraffin rests, followed by sintering at 1500 °C for 12 h and air quenching to obtain  $\alpha$ -TCP. The blocks were then incubated for 24 h at 200 °C in a saturated water vapor atmosphere (see Figure 7-1). After drying for 2 days at 60 °C, the ceramic blocks were impregnated with poly( $\epsilon$ -caprolactone) (PCL) following the well-established method of Peroglio et al. [5]: the samples were impregnated under vacuum with a 35 g/L Poly( $\epsilon$ -caprolactone) (PCL,  $M_n = 80000$  g/mol, art. nr 704067, Aldrich) solution in ethyl acetate (art. nr. 109623, ACS reagent grade, Aldrich) and then dried (slow solvent evaporation at room temperature). The impregnation-drying cycles were repeated twice.

For comparison, some samples were only sintered and directly impregnated with PCL, without intermediate hydrothermal incubation. In addition, some samples were sintered, impregnated with PCL and finally hydrothermally treated at 150 °C for 76 h. The lower incubation temperature was chosen to avoid as much as possible PCL degradation, but the reaction time had to be increased to reach the same phase conversion rate than with incubation at 200 °C for 24h.

## Characterization

All samples were weighed and measured after sintering, after incubation and after impregnation to determine their apparent porosity. X-ray diffraction provided the crystalline composition which was then used to infer the porosity. To test the mechanical properties, Brazilian tests [18] were performed. The strain energy density ( $G$ ) was calculated as integral of the force–displacement curve, at maximum force, divided by the sample section ( $d \cdot h$ ). It is a semi-quantitative estimation of the toughness to compare the samples of this study between each other. The samples were broken to reveal their inner microstructure and sputtered with carbon. Fracture surfaces were observed by scanning electron microscopy (SEM).

## Results

### Porosity and microstructure

Before sintering, the cement samples presented a fine microstructure made of small sub-micrometric platelets (Figure 8-1).

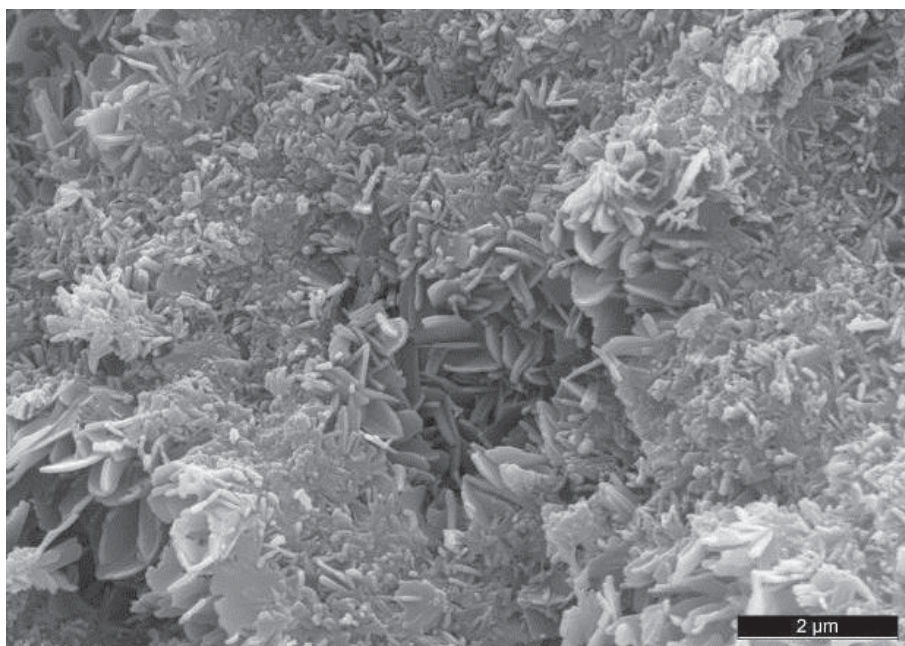


**Figure 8-1** SEM of a cement sample.

After sintering for 12 h at 1500 °C, the microstructures appeared smooth (Figure 8-2). The addition of paraffin increased the porosity. With 0g, 3g and 10g paraffin, the sintered samples were 30 %, 50 % and 70 % porous, respectively. 30 % porous samples presented similar micropores and a rather concave structure when made with both low and high emulsifier amounts (Figure 8-2a and d). When combined with a low emulsifier amount paraffin formed macropores (Figure 8-2b and c) and the micropores (inserts in Figure 8-2b and c) resembled those of only microporous samples (insert of Figure 8-2a). When paraffin was combined with a high amount of emulsifier, no macropores were formed (Figure 8-2e and f) but the microporosity was more open (inserts in Figure 8-2e and f) than without paraffin (insert in Figure 8-2d) and the structure rather convex.

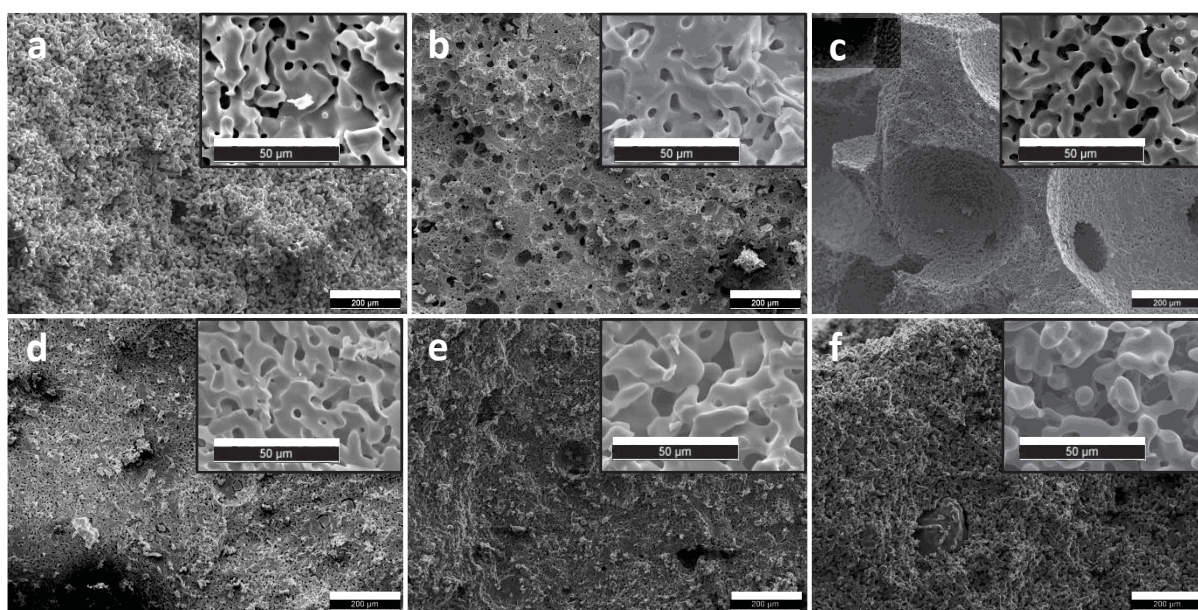


**Figure 8-2** Top (a-c): Low emulsifier concentration, bottom (d-f): High emulsifier concentration. From left to right: 0, 3 and 10 g paraffin. Scale bars are 200  $\mu\text{m}$  for the main images, and 50  $\mu\text{m}$  for the inserts.

After incubation, a weight gain after complete conversion of  $3.5 \pm 0.5$  % in average was measured, but the porosities were not changed (See chapter 7, Figure 7-2). The changes in microstructure due to recrystallization were visible on SEM images (See chapter 7, Figure 7-5), but no clear differences were observed between the different porosities. In all cases, thin and elongated crystals were obtained. Interestingly, the crystal orientation was identical in very large areas, suggesting that few nuclei determine crystal orientation and that by controlling nuclei orientation one might improve even more the mechanical properties.

For further investigations, it was decided to incubate samples at 200°C for 24h to ensure complete phase conversion and preservation of micro- and macropores.

PCL amount after impregnation and solvent evaporation was larger in macroporous samples than in microporous ones, but it was not affected by a previous hydrothermal incubation. In details,

the micro- and macroporous samples were filled with  $5.1 \pm 0.5$  and  $7.8 \pm 0.5$  vol-% PCL, respectively. This corresponds to  $7.1 \pm 0.8$  and  $19 \pm 1$  vol-% of the solid part (ceramic + polymer, without pores). Consequently, the impregnation with PCL decreased the porosity of  $15.7 \pm 0.9$  and  $11.4 \pm 0.8$  %, respectively.

PCL infiltration was visible by SEM imaging in micro- and macropores in both sintered and incubated samples (Figure 8-3) but only at the outer surfaces of the samples. Only non-incubated macroporous samples showed PCL fibrils also in the core of the samples. No PCL was visible in the nanoporosities between CaP needles.

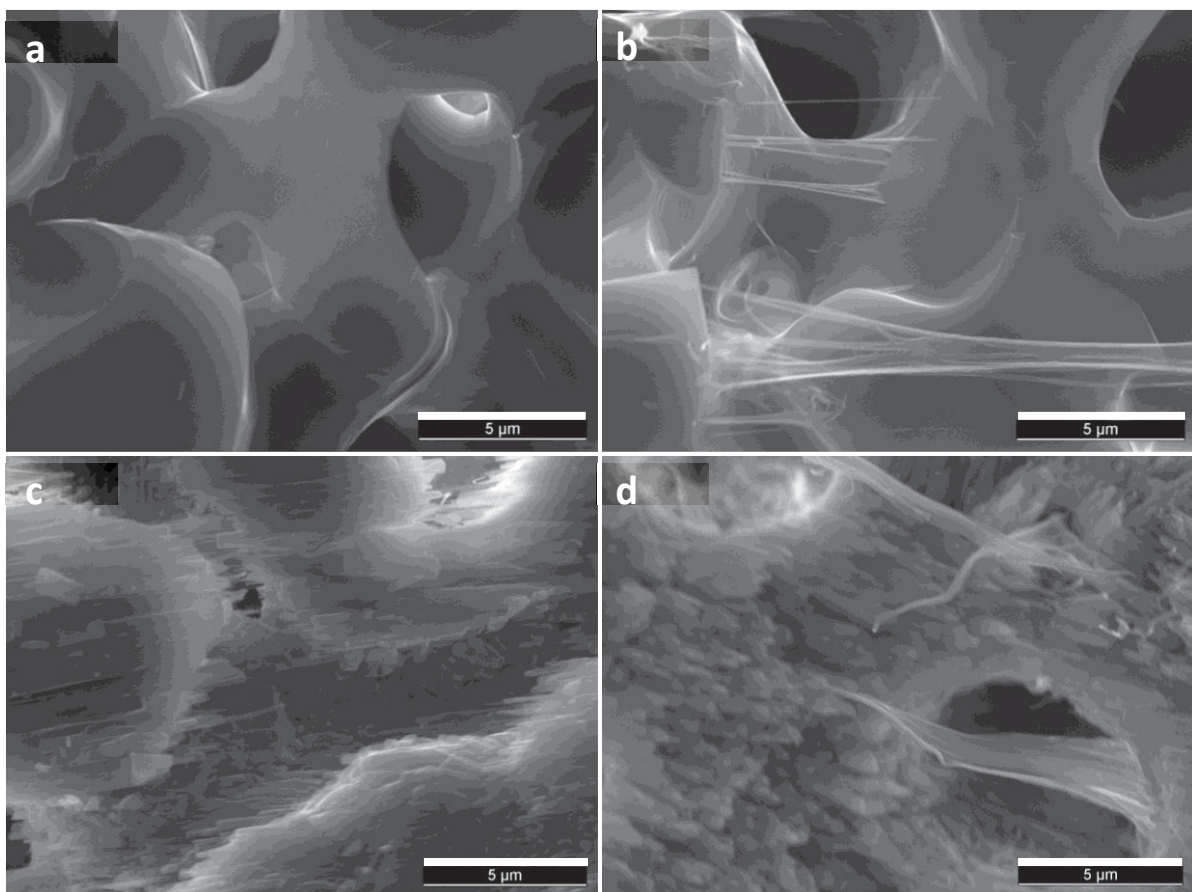


**Figure 8-3** SEM of microstructures a) after sintering, b) after sintering and PCL impregnation, c) after hydrothermal incubation and d) after hydrothermal incubation and PCL impregnation.

After rupture, the impregnated samples remained in one piece and some polymer was visible in the cracks (Figure 8-4a-c). The presence of polymer fibrils was particularly noticed in the first millimeter of thickness between broken ceramic parts, holding them together (Figure 8-4d and e) but no polymer fibrils were observed in the core of samples (Figure 8-4f), except in non-incubated macroporous samples.



## Composition

The crystalline phase after sintering was  $\alpha$ -TCP, in some cases with  $\beta$ -TCP traces. After hydrothermal incubation, independently of the porosity, the  $\alpha$ -TCP phase converted mainly to CDHA (see chapter 7, Figure 7-8). The phase conversion rate increased with time, temperature (see chapter 7, Figure 7-8) and also with porosity.

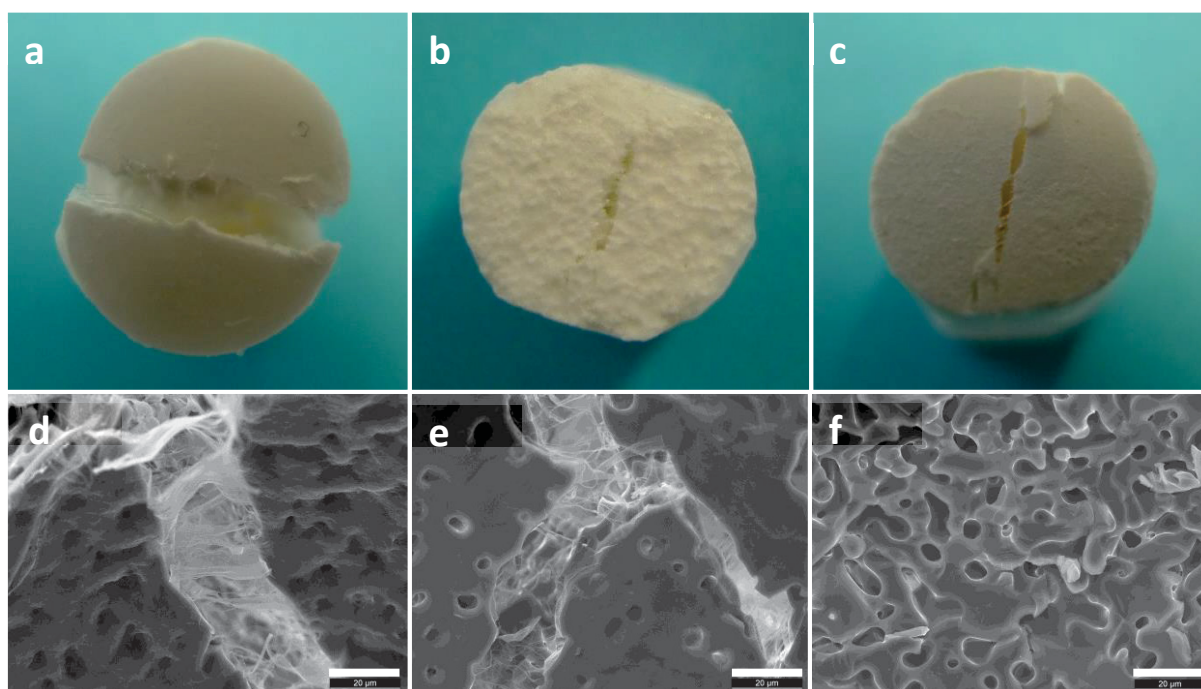


**Figure 8-4** The macroscopic integrity of the blocks was maintained (a to c) by numerous polymer fibrils formed between broken pieces of ceramics (d and e), except in the core of the samples (f).

## Mechanical properties

To limit the number of samples for mechanical testing, only samples with 30 % porosity (further named “microporous” or “micro”) and samples with 70 % porosity and macropores (“macroporous” or “macro”) were considered. Their mechanical properties were determined in the cement state, after sintering, after hydrothermal incubation at 200 °C or 150 °C, and after PCL impregnation.

For all samples, the transversal strength (measured by Brazilian test) was significantly higher after hydrothermal treatment and increased with reaction time (Figure 8-5). To ensure complete reaction and thus maximum strength increase, the incubation times were set to 24h and 76h at 200 and 150 °C respectively for further testing.

Of course, 70 % macroporous samples were weaker than 30 % microporous ones, but the strength increase with hydrothermal incubation was similar and no significant difference was noticed between incubation for 76 h at 150 °C and 24 h at 200 °C (Figure 8-6a). In parallel, the strain energy density,  $G$ , - i.e. an estimation of the toughness – increased for microporous samples at both

incubation temperatures (+ 230 % at 200 °C and + 530 % at 125 °C), but the increase (+ 50 % at 200 °C and + 180 % at 125 °C) for macroporous samples was not significant (Figure 8-6b).

PCL impregnation of sintered samples, as done by Peroglio et al. [5], had no influence on the strength of the sintered scaffolds, and the expected increase of toughness was not significant. However, PCL impregnation had a noticeable positive effect on the toughness of macroporous 200 °C-incubated samples, for which hydrothermal incubation had no effect. Surprisingly, PCL impregnation increased the strength of both micro- and macroporous samples previously incubated.

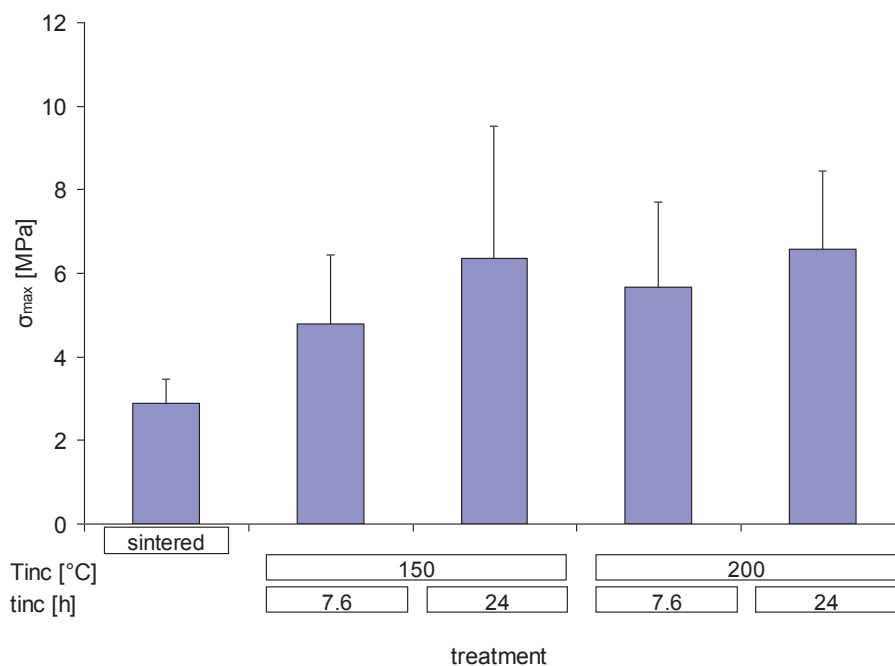


**Figure 8-5** Transversal strength measured with Brazilian testing on 30 % microporous samples.

When scaffolds were impregnated with PCL before hydrothermal treatment, the polymer had no influence, neither on strength, nor on toughness. The combined influence of incubation and polymer impregnation was thus not reached with this processing order.

## Discussion

PCL covered the surface of micro- and macropores but not easily until the core of the samples (Figure 8-4). This might explain the poor toughness improvement observed on sintered samples compared to other studies where almost a 7-fold increase in strain energy was observed [5]. It has to be mentioned that in the present study, the strain energy was only calculated up to the maximum force, not until rupture point. Since PCL fibrils maintain ceramic pieces together after rupture of the

ceramic, a lot of deformation energy was not taken into account here, because it could not be measured by Brazilian testing, contrarily to bending tests.

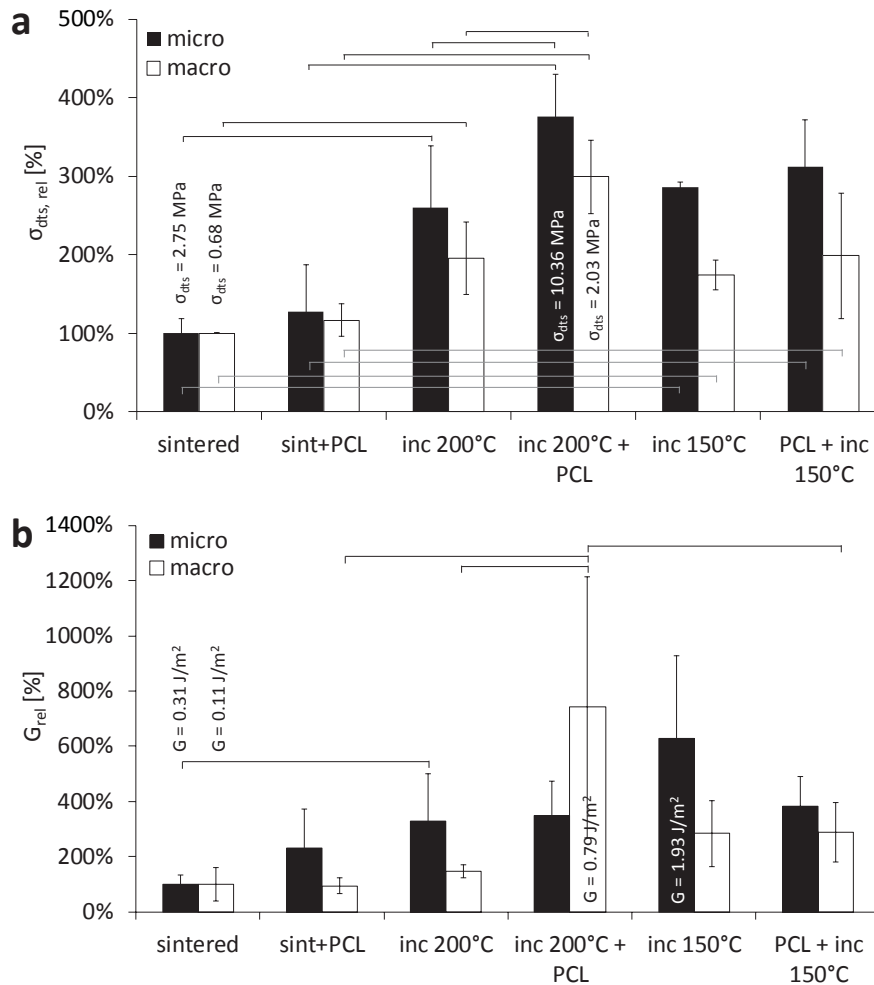


**Figure 8-6** a) Transversal strength (brasilian test) of different ceramic or composite blocks, from the left to the right: after sintering, after subsequent impregnation with PCL, after hydrothermal incubation (200 °C, 24h), after subsequent PCL impregnation, after hydrothermal incubation (150 °C, 76h, “inc2”), after hydrothermal incubation (150 °C, 76h) of previously PCL impregnated samples. b) strain energy density at maximum force is a semi-quantitative estimation of the toughness to compare the samples of this study.

However, even with this limitation, significant improvement was measured when hydrothermally treated samples were coated with PCL.

Surprisingly, a strength increase was observed with PCL impregnation of textured samples. According to the standard rule of mixture of composites, addition of a weaker material cannot increase the global strength. This increase might be explained by the filling of surface defects of the ceramic. Hence, the flaw resistance of the ceramic increases. Moreover, it implies a good stress transfer between the structural elements. Unfortunately it was not possible to verify whether PCL also penetrated between individual needles, i.e. in nanoporosities. However, even in some natural

materials the organic phases remains around the fiber bundles, but is not found around individual needles [19].

Hence, the toughness of ceramic scaffolds can be increased both by “intrinsic” or “extrinsic” toughening mechanism [1, 2], but combining both led to a surprising synergistic effect: toughening by PCL impregnation on textured samples is more efficient than on smooth sintered structures and these fine tortuous microstructures allow a high contact and thus stress transfer between both phases leading to increased strength.

The presently used method is not appropriate for measuring plastic deformation and in consequence underestimates strain energy released during breaking of non-brittle materials. The improvements of toughness observed here were therefore particularly reliable.

## Conclusions

In the aim to increase the toughness of ceramic bone scaffolds, many attempts have been made either by incorporating a tough polymer phase (“intrinsic” toughening) or by decreasing the size of ceramic particles (“extrinsic” toughening) in composites with polymer matrices. However, to our knowledge, combining both approaches has never been done before. Here, we showed first that reducing the crystal size and elongating their shape, even in monolith blocks successfully increased both strength and toughness. Then, a thin polymer phase was introduced by impregnation of porous scaffolds. Thanks to the fine and tortuous structure of the ceramic, the high contact area between both phases allowed good stress transfer and led to even more improved strength. And obviously, the toughness was synergistically improved.

## References

- [1] Ritchie RO, Kinney JH, Kruzic JJ, Nalla RK. A fracture mechanics and mechanistic approach to the failure of cortical bone. *Fatigue Fract Eng Mater Struct*. 2005;28:345-71.
- [2] Ritchie RO. The conflicts between strength and toughness. *Nature Materials*. 2011;10:817-22.
- [3] Martínez-Vázquez FJ, Pajares A, Guiberteau F, Miranda P. Effect of polymer infiltration on the flexural behavior of  $\beta$ -tricalcium phosphate robocast scaffolds. *Mater*. 2014;7:4001-18.
- [4] Zhao J, Lu X, Duan K, Guo LY, Zhou SB, Weng J. Improving mechanical and biological properties of macroporous HA scaffolds through composite coatings. *Colloids Surf B Biointerfaces*. 2009;74:159-66.
- [5] Peroglio M, Gremillard L, Chevalier J, Chazeau L, Gauthier C, Hamaide T. Toughening of bio-ceramics scaffolds by polymer coating. *Journal of the European Ceramic Society*. 2007;27:2679-85.

- [6] Wang J, Shaw LL. Nanocrystalline hydroxyapatite with simultaneous enhancements in hardness and toughness. *Biomaterials*. 2009;30:6565-72.
- [7] Griffith AA. The Phenomena of Rupture and Flow in Solids. *Philosophical Transactions of the Royal Society of London Series A, Containing Papers of a Mathematical or Physical Character*. 1921;221:163-98.
- [8] Ji B, Gao H. Mechanical properties of nanostructure of biological materials. *J Mech Phys Solids*. 2004;52:1963-90.
- [9] Fu Q, Saiz E, Rahaman MN, Tomsia AP. Toward strong and tough glass and ceramic scaffolds for bone repair. *Advanced Functional Materials*. 2013;23:5461-76.
- [10] Gao H, Ji B, Jäger IL, Arzt E, Fratzl P. Materials become insensitive to flaws at nanoscale: Lessons from nature. *Proceedings of the National Academy of Sciences of the United States of America*. 2003;100:5597-600.
- [11] Espinosa HD, Rim JE, Barthelat F, Buehler MJ. Merger of structure and material in nacre and bone - Perspectives on de novo biomimetic materials. *Progress in Materials Science*. 2009;54:1059-100.
- [12] Norman TL, Vashishth D, Burr DB. Fracture toughness of human bone under tension. *J Biomech*. 1995;28:309-20.
- [13] Cooke FW. Bulk properties of materials. In: Ratner BD, Hoffman AS, Schoen FJ, Lemons JE, editors. *Biomaterials science - an introduction to materials in medicine*. San Diego: ACADEMIC PRESS; 1996. p. 11-21.
- [14] Hou DF, Zhou GS, Zheng M. Conch shell structure and its effect on mechanical behaviors. *Biomaterials*. 2004;25:751-6.
- [15] Currey JD, Zioupos P, Davies P, Casinos A. Mechanical properties of nacre and highly mineralized bone. *Proceedings of the Royal Society B: Biological Sciences*. 2001;268:107-11.
- [16] Bohner M. Calcium phosphate emulsions: possible applications. *Key Engineering Materials*. 2001;192-195:765-8.
- [17] Bohner M, van Lenthe GH, Grunfelder S, Hirsiger W, Evison R, Muller R. Synthesis and characterization of porous beta-tricalcium phosphate blocks. *Biomaterials*. 2005.
- [18] Bouchard PO, Bay F, Chastel Y, Tovenia I. Crack propagation modelling using an advanced remeshing technique. *Comput Methods Appl Mech Eng*. 2000;189:723-42.
- [19] Enax J, Janus AM, Raabe D, Epple M, Fabritius HO. Ultrastructural organization and micromechanical properties of shark tooth enameloid. *Acta Biomaterialia*. 2014;10:3959-68.



## CHAPTER 9:

# SYNTHESIS AND OUTLOOK

Current bone substitutes not only differ chemically and mechanically from bone, but they are also structurally different. Indeed, existing bone substitutes are generally pure ceramic monoliths, with limited toughness, or composites with uncontrolled architectures, limiting their structural toughness, and sometimes also their strength.

In the aim to obtain structures with outstanding combination of strength and toughness, it can be deduced from theoretical considerations (Chapter 2) and from the experimental results of the present PhD thesis that some key features are required:

1. **Refinement** of the structure into sub-micrometric particles for crack-like flaws tolerance
2. **High aspect ratios** for high load transfer between elements
3. **High alignment** to optimize stress transfer in the load direction and to improve the **packing density**
4. **Hierarchical architectures** to increase energy absorption at failure
5. **High interface** strength between the different phases

Nacre-like “brick-and-mortar” structures obtained in the first part of this thesis particularly demonstrated the efficacy of refinement, high aspect ratio and proper alignment of reinforcement elements in polymer-matrix materials. In particular, chitosan-monetite composite films reached tensile strengths up to 160 MPa– corresponding to the higher values found in the literature for cortical bone – while still presenting deformation at rupture of about 5 %. The negative influence of a moderate interface strength was obvious when comparing the experimental results with theoretical calculations. Deeper characterization of the CaP platelets (like measurement of surface energies or electrical charges) might help selecting an appropriate polymer and improve the interface between both phases. In addition to binding improvement, many other alignment methods as those tested in the frame of this research work could be investigated. Dip-casting, centrifugation, tape-casting, spinning or extrusion, for example should be compared with the methods tested here. Indeed, as shown in Chapter 5, alignment control is the key to obtain high ceramic fractions for improved

biological properties while still leading to an efficient reinforcement. Besides improvement of interface strength, or alignment quality, the existence of an ideal aspect ratio as stated in chapter 2 should be verified experimentally. However, to do so, the fine tuning of CaP platelets size and shape should first be mastered and their production rate increased to allow screening of a large range of features.

The “monolith” structures produced in the second part of the project also highlighted the importance of particle refinement, elongated shapes, alignment – at least locally – as well as hierarchical architectures on strength and toughness improvement. Interestingly, the toughness was improved even without adding a ductile phase to the material; this is the proof that extrinsic – or structural – toughening mechanism can also be implemented in synthetic materials, as observed in natural ones. Of course, the toughness, and surprisingly also the strength, could further be increased by polymer addition.

Pores and porosity are essential for proper integration of implant materials, tissue invasion and colonization. However, it was not addressed much in this thesis, particularly in the first part. On a first hand it was decided to avoid porosity in order to ease comparison between materials, composition and structures. But on second hand, it was also deliberately decided to maximize strength with the aim to design implants for osteosynthesis applications rather than scaffolds for tissue engineering. Freeze-casting as shown in chapter 6 might be an option to introduce some porosity. Stronger polymers than hydrogels can also be shaped by this technique, like PLLA, which would provide sufficient strength to porous structures. Gas foaming in slurries as used for the solvent casting technique (chapter 5) might also be feasible and confine the ceramic parts within the pore walls. As for freeze-casting, if the thickness of the pore walls is small enough, the ceramic elements should align within the polymer, perpendicularly to the expansion forces.

In the second part of this thesis, porosity was present and due to the difficulty to produce dense CaP ceramics, not easily avoidable from the first synthesis steps. Since porosity acts as a weakening element, the differences observed thanks to structural changes might have been larger if dense samples had been produced. Contrarily to the brick-and-mortar approach, this processing way might be well adapted for porous scaffolds, but not for fixation elements.

It has to be remarked that even the most optimized synthetic biomaterials will always differ from natural materials in their incapacity to self-heal and remodel. However, materials that are osteo-integrated and are actively degraded by cellular processes also approach this phenomenon, since they take part of the bone remodeling process.

In summary, brick-and-mortar structures were achievable with strength and strain values similar to those of cortical bone but only as thin films and limited fraction of reinforcement elements



(Chapter 3 to 6). Contrarily, macroscopic CaP monoliths with hierarchical structure showed improved toughness and strength compared to conventional sintered ceramics, but still inferior to cortical bone (Chapter 7 and 8). In conclusion, obtaining strong, tough and biodegradable scaffolds for bone substitution in load-bearing location remains a compromise between macroscopic size and appropriate features, but is getting closer to success in regards to the present PhD thesis outcomes.



## LAËTITIA GALEA

Ch. des Narcisses 12  
2504 Biel/Bienne  
+41 76 615 74 48  
laetitia.galea@gmail.com

20.06.1983  
Swiss & French  
Single



## EDUCATION

---

- Doctor of Philosophy (PhD) thesis** 2011 - 2015  
at the Faculty of Mechanical, Process and Energy Engineering,  
TU Bergakademie Freiberg, Germany  
Advisor: Prof. C. G. Aneziris  
Co-advisors: Prof. T. Graule, EMPA, Dübendorf, Switzerland  
Prof. M. Böhner, RMS Foundation, Bettlach, Switzerland
- Thesis title: "Bio-inspired structured composites for load-bearing bone graft substitution"
- Master of Science (MSc)** 2002 - 2008  
in Materials Science and Engineering at Ecole Polytechnique Fédérale de  
Lausanne (EPFL), grade: 5.78/6
- Thesis title: "Obtention of nanocrystalline bone substitutes from sintered calcium phosphate bone substitutes", Powder Technology Laboratory (LTP), EPFL, in collaboration with the RMS Foundation, Bettlach
  - SVMT award 2008 for the best Master Project in Materials Science
  - Specialization in biomaterials
- Maturité Fédérale** 1998 - 2002  
CEC Nicolas-Bouvier, Geneva
- Obtained with distinction
  - Award for best grade in mathematics

## PROFESSIONAL EXPERIENCE

---

- Project manager / Senior scientist** (research projects and services) 01.2013-present
- Skeletal Substitutes Group  
RMS Foundation, Bettlach
- Scientific collaborator** (research projects and services)
- Skeletal Substitutes Group 05.2009-12.2012
  - Biomechanics Group 01.2008-04.2009  
RMS Foundation, Bettlach

## INTERNSHIPS

---

- Biomedix SA**, Geneva 04.-09.2006  
"Design of biocompatibility experiments and composition of technical files for CE marking for a gastric prosthesis"
- Ian Wark Research Institute**, University of South Australia, Adelaide 01.-03.2006  
"pH dependence of grafted polyallylamine coatings"
- RMS Foundation**, Bettlach 08.-12.2005  
"Elaboration and characterization of a calcium phosphate gel for bone repair", project for Synthes GmbH, Oberdorf

## SKILLS

---

### Languages

French	mother tongue
English	very good
German	very good
Swiss-German	good understanding

### Computer skills

Microsoft Office, Mathematica, LaTeX, Ansys, C

### Particular technical skills

Design of experiments, statistical analysis of results, Scanning Electron Microscopy (SEM), Specific Surface Analysis (SSA), calorimetry, hydrothermal treatments, mechanical testing, Particle Size Distribution (PSD) measurements, etc.

## MEMBERSHIPS AND VARIA

---

Member of the executive committee of the Swiss Society for Biomaterials and Regenerative Medicine (SSB+RM) as the young scientists and student's representative since June 2013.

Member of the Young Scientist Forum (YSF) of the European Society for Biomaterials (ESB) as the Swiss representative since September 2013.

Organization of the first Swiss Young Scientist Forum (CH-YSF) integrated in the annual conference of the SSB+RM, in parallel to co-organization of the 2014 annual conference in Basel.

July 14: creation of an independent association for young scientists active in the biomedical field in Switzerland, the "YSBM.ch" ([www.ysbm.ch](http://www.ysbm.ch), soon online).

## INTERESTS

---

Many different outdoor sports like running, cycling, bouldering, climbing, ski touring, cross-country skiing and kitesurfing.

Power yoga teacher training on going since September 2014.

## PUBLICATIONS

---

Lapczynya H., **Galea L.**, Wüst S., Bohner M., Jerban S., Sweedy A., Doebelin N., van Garderen N., Hofmann S., Baroud G., Müller R., von Rechenberg B. Effect of grain size and microporosity on the in vivo behaviour of  $\beta$ -tricalcium phosphate scaffolds (2014) *European Cells and Materials*, 28, pp. 299-319.

**Galea L.**, Bohner M., Thuering J., Doebelin N., Ring T.A., Aneziris C.G., Graule T. Growth kinetics of hexagonal sub-micrometric  $\beta$ -tricalcium phosphate particles in ethylene glycol (2014) *Acta Biomaterialia*, 10(9), pp. 3922-3930.

**Galea L.**, Bohner M., Thuering J., Doebelin N., Aneziris C.G., Graule T. Control of the size, shape and composition of highly uniform, non-agglomerated, sub-micrometer  $\beta$ -Tricalcium phosphate and dicalcium phosphate platelets (2013) *Biomaterials*, 34 (27), pp. 6388-6401.

Tadier S., **Galea L.**, Charbonnier B., Baroud G., Bohner M. Phase and size separations occurring during the injection of model pastes composed of  $\beta$ -tricalcium phosphate powder, glass beads and aqueous solutions (2013) *Acta Biomaterialia*, 10 (5), pp. 2259-2268.

Butscher A., Bohner M., Doebelin N., **Galea L.**, Loeffel O., Müller R. Moisture based three-dimensional printing of calcium phosphate structures for scaffold engineering (2013) *Acta Biomaterialia*, 9 (2), pp. 5369-5378.

Bohner M., **Galea L.**, Doebelin N. Calcium phosphate bone graft substitutes: failures and hopes (2012) *Journal of the European Ceramic Society*, 32 (11), pp. 2663-2671.

Habib M., Baroud G., **Galea L.**, Bohner M. Evaluation of the ultrasonication process for injectability of hydraulic calcium phosphate pastes (2012) *Acta Biomaterialia*, 8 (3), pp. 1164-1168.

Döbelin N., **Galea L.**, Eggenberger U., Ferreira J.M.F., Bohner M. Recrystallization of amorphized  $\alpha$ -TCP (2012) *Key Engineering Materials*, 493-494, pp. 219-224.

Tadier S., **Galea L.**, Gruenenfelder S., Bohner M. Investigation of the phase separation occurring during the injection of  $\beta$ -tricalcium phosphate - water - glass beads pastes (2012) *Key Engineering Materials*, 493-494, pp. 693-697.

**Galea L.G.**, Bohner M., Lemaître J., Kohler T., Müller R. Bone substitute: transforming  $\beta$ -tricalcium phosphate porous scaffolds into monetite (2008) *Biomaterials*, 29 (24-25), pp. 3400-3407.

## ORAL AND POSTER PRESENTATIONS

---

**L. Galea**, A. Studart, T. Graule, M. Bohner. Bioinspired Composites: Link between Alignment Control, Platelets Content and Mechanical Properties. ESB 2014, Liverpool, UK, September 2014 (Oral).

**L. Galea**, A. Ojuva, T. Graule, A. Studart, L. Bergström, M. Bohner. Biodegradable nacre-inspired materials for bone substitution. Bio-inspired materials, Potsdam, Germany, March 2014 (Poster).

**L. Galea**, N. Döbelin, R. Erb, A. Studart, T. Graule, M. Bohner. Nacre-Inspired Biodegradable Composites Approaching the Tensile Strength of Cortical Bone. MRS Fall Meeting 2013, Boston, USA, December 2013 (Oral).

**L. Galea**, M. Peroglio, D. Eglin, T. Graule, M. Bohner. Improvement of strength and toughness of porous calcium phosphate blocks by hydrothermal treatment and polymer impregnation. ESB 2013, Madrid, Spain, September 2013 (Oral).

- **SSB+RM 2013 Travel grant** to attend this conference.

**L. Galea**, J. Thuring, C.G. Aneziris, T. Graule, M. Bohner. Growth kinetics of nacre-like calcium phosphate platelets. 12th International Symposium on Biomineralization, Freiberg, Germany, August 2013 (Oral).

**L. Galea**, M. Peroglio, D. Eglin, Th. Graule, M. Bohner. Recrystallization and polymer impregnation improve strength and toughness of calcium phosphate ceramics. SSB 2013, Davos, June 2013 (Oral).

**L. Galea**, R.M. Erb, M. Bohner, A.R. Studart, T. Graule. Programming architecture into biomineral-polymer composites for bone substitution. Hybrid materials 2013, Sorrento, Italy, March 2013 (Oral).

**L. Galea**, M. Bohner, M. Niederberger, T. Graule. Beta-tricalcium phosphate platelets for load-bearing bone substitutes. MSE, Darmstadt, Germany, September 2012 (Poster).

- **SSB 2012 Travel grant** to attend this conference.

**L. Galea**, M. Bohner, M. Niederberger, T. Graule. Bioresorbable ceramic platelets for load-bearing bone substitutes. Junior Euromat, Lausanne, July 2012 (Poster).

**L. Galea**, **M. Bohner**, N. Doebelin, M. Niederberger, T. Graule. Synthesis of monodisperse hexagonal  $\beta$ -tricalcium phosphate crystals. WBC, Chengdu, China, June 2012 (Oral).

**L. Galea**, M. Bohner, O. Loeffel, S. Gruenenfelder, M. Niederberger, T. Graule. Resorbable ceramic platelets for reinforcement of bone substitutes. SSB 2012, Zurich, May 2012 (Oral).

**L. Galea**, **M. Bohner**, M. Niederberger, T. Graule. Synthesis of  $\beta$ -TCP platelets for bone substitutes. GRIBOI, Boston, USA, March 2012 (Poster).

**L. Galea**, Th. Graule, M. Bohner. Hydrothermal treatment to improve the mechanical properties of calcium phosphate ceramics. Biofuture, Ghent, Belgium, November 2011 (oral).

**S. Tadier**, **L. Galea**, S. Gruenenfelder, M. Bohner. Investigation of the phase separation occurring during the injection of  $\beta$ -tricalcium phosphate - Water - Glass beads pastes. Bioceramics, Istanbul, Turkey, November 2011 (oral).

**N. Döbelin**, **L. Galea**, U. Eggenberger, J.M.F Ferreira, M. Bohner. Recrystallization of amorphized  $\alpha$ -TCP. Bioceramics, Istanbul, Turkey, November 2011 (Oral).

**L. Galea**, N. Doebelin, M. Bohner. Effect of sintering conditions on physical properties of TCP ceramics. ESB, Dublin, Ireland, September 2011 (Poster).

**L. Galea**, N. Doebelin, M. Bohner. Effect of sintering conditions on physical properties of TCP ceramics. SSB, Yverdon-les-Bains, May 2011 (Oral).

**L. Galea**, M. Habib, G. Baroud, M. Bohner. Influence of sintering temperature, sintering type and Ca/P ratio on injectability of CaP-based pastes. ESB, Tampere, Finland, September 2010 (Oral).

**L. Galea**, M. Habib, G. Baroud, M. Bohner. Influence of particle size distribution on injectability of CaP-based pastes. SSB, Dübendorf, May 2010 (Poster).

**L. Galea**, M. Habib, G. Baroud, M. Bohner. Injectability of CaP-based pastes: Influence of sintering temperature, sintering type and Ca/P ratio. GRIBOI, Torino, Italy, March 2010 (Oral).

## STUDENT AND TRAINEE SUPERVISION

---

<b>Vivian Mouser</b> , Eindhoven University of Technology, The Netherland Internship: "Development of an automated method to produce a new bone graft substitute material by alternating layers of calcium phosphate and polymer"	08.-11.2011
<b>Katharina Thiers</b> Internship: "Precipitation of calcium phosphate particles in organic medium"	01.-09.2013
<b>Dmitriy Alexeev</b> , ETH Zurich, Switzerland Master thesis: "Recrystallization of calcium phosphate blocks through hydrothermal treatment to improve their strength and toughness"	04.-10.2013